ISSN 2522-4352

CONFERENCE PROCEEDINGS
Modern Trends In Physics

International Conference
20–22 April 2017, Baku

TABBLE OF CONTENTS

General Information 5

Organizing and advisory committee 5

A.M. Magerramov, M.A.Ramazanov, S.G.Nuriyeva, F.V.Hajiyeva.
Structure and dielectric properties of polymer nanocomposites on the basis of polypropylene and silver sulfide PP/Ag_2S 7

A.M.Maharramov, M. A.Ramazanov, Luca Di Palma, H.A.Shirinova, F.V.Hajiyeva
The influence of magnetite nanoparticles on dielectric properties of metaloxide-polymer based nanocomposite. 11

H.Ebadi.
Observation of MHD waves in Solar Spicules 14

A.SH.Abdinov, H.M.Mamedov, V.U.Mammadov, Kh.M.Ahmedova, V.J. Mammadova, L.E.Agazade.
Nano-structured solar cell based on c-Si/porous-Si/CdS/$Zn_xCd_{1-x}O$ heterostructures.....16

M.A.Ramazanov, F.V.Hajiyeva, A.B.Ahmadova, M.A.Nuriyev, A.M.Rahimli.
The influence of corona discharge on the electret properties and charge state of polymer nanocomposites based on isotactic polypropylene and titanium dioxide nanoparticles (TiO_2) 19

N.N.Heydarov, R.S.Madatov, Z.Y.Sadygov, A.Z.Sadigov, F.I.Ahmadov, S.S.Suleymanov, R.V.Valiyev, M.S.Nazarov.
New silicon photomultiplier with fast output 23

R.J.Kasumova, H.M.Mamedov, SH.A.Shamilova, G.A.Safarova, N.V.Kerimova.
Phase effects in ZnO/PM nanocomposite films, at second harmonic generation 25

S.Z.Salahova, SH.A.Topchiyeva, M.A.Ramazanov.
Dynamics of heavy metals in water and sediments in the contract area «Gurgan» of Azerbaijan sector of the Caspian Sea 28

U.F.Samedova, Sh.M.Hasanli.
Features of magnetic interaction in composites based on siderite and polymer.....32

Y.S.Gasimov, A.R.Aliyeva.
On a numerical solution of a shape optimization problem for the eigenvalues of pauli operator 35

Z.A.Samedov, U.R.Gadirova, Sh.Sh.Amirov.
Investıgatıon of theatmosphere of HD14662(F7Ib) 38

Z.H.Tagiyev, Sh.Sh.Amirov, N.V.Kerimli.
Generation of second optical harmonic in the nonlinear regime 40

A.A.Nabiyev, A. KH.Islamov, A.M.Maharramov, R.S.Ismayilova, M.N.Mirzayev, A.S.Doroshkevic, V.A.Turchenko, M.I. Rulev, A. I. Kuklin.
A study of structural and thermal properties of HDPE+ZrO_2 nanocomposites by x-ray diffraction and differential thermal analysis.....43

A.Khelashvili.
On Possible Source of the Coulomb Potential.....46

A.B.Arbuzov, R.G.Nazmitdinov, A.E.Pavlov, V.N.Pervushin, A.F.Zakharov.
Spontaneous breaking of conformal symmetry in the Standard Model.....49

A.G.Kyazim-zade, V.M.Salmanov, A.G.Huseynov, R.M.Mamedov, A.A.Salmanova, I.M.Aliyev, F. Sh.Axmedova.
Nonlinear absorption in monoselenide of gallium and indium in laser excitation.....52

A.M.Pashayev, E.Y.Salayev, B.H.Tagiyev, I.Z.Sadikhov, K.R.Allahverdiyev
Optical Spectroscopy of GaS Nanoparticles Formed via Laser Ablation.....55

A.SH.Abdinov, R.F.Babayeva
Anomalies of the kinetic phenomena in semiconducting $A^{III}B^{VI}$ compounds with a layered crystalline structure.....58

S.K.Abdullayev, M.Sh.Godjayev
Production and decay of Higgs bosons in muon colliders.....61

A.I.Ahmadov, H.M.Nagiyev, V.A.Tarverdiyeva, E.A.Dadashov
Direct inclusive gluon production in pion-proton collision.....64

Amil M. Maharramov, Rustam Sh. Shafagatov
Analysis of Typical Economic Risks in the Development of Alternative Energy Sources.....69

E.Sh. ALekperov, E.S. Garayev, S.A. Sadraddinov, S.S. Farzaliyev
Phase transition while thermal treatment of amorphous tin-alloyed $TlInS_2$ films.....72

I.G.Afandiyeva
Polarization Effects in Processes With Knocking Out Bineutrons Clusters.....77

I.Sh. Dadashov, A.N. Quliyev, Y.H.Huseynaliyev, A.A. Nabiyev, A.X. Mammadov, N.A. Hasanli
The electrical and physical properties of the system alloys Ga1-xMnxSb ($x \leq 0.25$).....80

S.J.Iqbal
Laser based fusion reaction for peaceful purpose.....82

A.B.Ismailova
The role of microscopes in biology and medicine.....86

Kamal Hussain Khan, M.K Suleymanov, M.Ajaz, Ali Zaman, H.Younis, Ya.H.Huseynaliyev
Light nuclei production in proton-Carbon and nucleus-Carbon interactions at 4.2 AGeV/c.....90

M. Dvornikov
Strong Magnetic Fields in Compact Stars as a Macroscopic Parity Violation Phenomenon.....96

M.Dvornikov, G.SH.Mehdiyeva
Long-lived Natural Plasma Structures as an Alternative Energy Source.....100

M.S.Nazarov, F.I.Ahmadov, S.S.Suleymanov, N.N.Heydarov, R.V.Valiyev, I.I.Abbasov.
Design of the radiation detector modules for security systems.....104

N.A.Huseynov.
Search for the Associated Production of a Higgs Boson and a Top Quark Pair in Multilepton Final States with the Atlas Detector.....106

O.O.Balayeva, N.F.Dadashova, M.B.Muradov, G.M.Eyvazova, E.H.Guliyev
Features of Electrical Conductivity of Composites Based on Polyvinyl Alcohol and Copper Sulfide Nanoparticles.....109

R.A.Ahmedov.
Polarization Effects in Neutron -Nucleus Collisions.....112

R.I.Khalilov, A.N.Nasibova, I.Y.Fridunbayov, N.N.Nabiyev, U.M.Qasumov.
Magnetic Nanoparticles in Plants 115

S.G.Abdulvahabova, N.Sh.Barkhalova, T.O.Bayramova.
Scattering of neutrons on nuclei at high energies 119

S.R.Figarova, M.M.Mahmudov.
Dependence of thermoelectric power of quantum well with complex profile on Fermi level 122

S.Rzayeva.
Gauge model with exotic particles 125

Sh.A.Mamedov, N.J.Huseynova.
The axial vector meson-Δ-baryon coupling constant from the hard-wall model of AdS/QCD 128

T.Inagaki.
Inflationary Cosmology in the Gauged Nambu-Jona-Lasinio Model 131

G.T.Arazov, T.G Aliyeva.
Formation and Evolution of Sustainable Dynamic System in Mathematical Models of the Theory of Population of Families of Small Bodies 135

T.C.Adorno, C.P.Gavrilov, D.M.Gitman.
General aspects on pair creation by peak electric field 138

S.M.Useynova.
Study of dielectric parameters of cyclopentanone and its concentrated binary solutions and analysis of measurement results 142

S.M.Useynova.
Measurement of ultrahigh frequencies dielectric parameters of liquids (ε' и ε'') at length of wave λ = 7,10mm (uhf). 144

Y.Murakami, K-I.Ishikawa.
The simplified construction of the Schrödinger functional scheme with the Möbius domain wall fermions 146

Y.H.Huseynaliyev, L.Y.Huseynaliyeva.
Transverse momentum physics in $^{12}C^{12}C$ interactions at the momentum 4.2AGeV/c 150

Y.M.Maharramov, A.R.Hasanova, A.M.Khalilov, A.Sh.Baloglanov, G.M.Hajiyeva.
Spectroscopic study of the stars hd142983 and hd187982 153

I.S.Ahmadov, M.A.Ramazanov, V.N.Ramazanli, N.J.Agayeva.
The interactional nature of nanoparticles with plant cell surface 156

J.S.Aliyev.
Solar Spin-Orbit Interaction: Tidal Torque 160

A.G.Alili, K.I.Alisheva.
Some parameters of planetary nebulae and determination of the total energy flux radiated by them in the region λ>912Å. 165

Yu.G.Nurullayev, B.Sh.Barkhalov, R.M.Ismayilov, K.I.Magerramova, H.O.Sadig, N.B.Mustafayev.
Thermoelectric properties of $(InTe)_{1-x}$-$(HoTe)_x$ solid solutions 169

Organizers:

- The Ministry of Education of the Azerbaijan Republic
- Baku State University (Azerbaijan)
- Joint Institute for Nuclear Research (Dubna, Russia)
- STAR-NET Regional Network for Education and Training in Nuclear Technology (Austria)
- Sapienza University of Rome (Italy)

Sponsor:

- Baku State University

Conference Site: http://www.mtphysics.org; http://www.mtphysics.az

Publisher:

Contacts: Z.Khalilov str. 23, Az1148, Baku, Azerbaijan

Web: http://publish.bsu.edu.az/en

Tel: +994 12 539 05 35

Structure and dielectric properties of polymer nanocomposites on the basis of polypropylene and silver sulfide PP/Ag_2S

A.M.MAGERRAMOV, M.A.RAMAZANOV, S.G.NURIYEVA, F.V.HAJIYEVA

Baku State University, AZ 1148, ZakhidKhalilov Str. 23, Azerbaijan, e-mail: aliyeva-s@list.ru

Abstract

This paper involves to use a combination of two synthetic methods for preparation of nanocomposite(PP/Ag_2S)based on polypropylene and silver sulphideby application of ultrasound and microemulsion techniques. The morphology of the nanocomposite and distribution of silver sulphide nanoparticles in the polymer matrix was studied by atomic force microscopy and scanning electron microscopy. It is found that, depending on the preparation method the uniform and homogeneous distribution of nanoparticles in the polymer matrix can be achieved. It has also been defined that, depending on the concentration of starting salts the sizes of nanoparticles inside the matrix change. IR and UV spectroscopy showed that with increasing concentration of nanoparticles in the polymer matrix shifts in the groups of nanoparticles were observed. The dielectric properties of polymer nanocomposites have not remained constant as a result of increase in nanoparticles concentration.

Keywords: nanocomposite, dielectric properties, dielectric loss.

1.Introduction

The preparation of nanocompositescontaining semiconductors affects their morphology and properties directly. Thus, being sensitive to the method and condition of the preparation the optical,electrical and other properties of nanocomposite materials are highly variable. In recent years, the interest for these kinds of materials has increased considerably and the study of the materials with practically important electro-physical properties has expanded considerably. Ag_2S nanoparticles have attracted widespread attention due to their unusual photoelectrical and electro-physical properties. It is widely used in various fields, such as solar cells, photodetectors and sensitive converters. It has been defined that, the electric properties of nanocomposite materials containing semiconductor nanoparticles are also different, so these kinds of nanocomposite materials have fairly high dielectric permittivity. In its turn, this leads to the application of these materials in many fields of electronics. The electrical characteristics of semiconductor nanocomposites are well correlated with concentration,volume, size and shape of nanoparticles, as well as other factors like particle/matrix interface adhesion and other possible interactions between the two phases of the semiconductor and dielectric, the supromolecular structure of the nanocomposite and the method of formation. At the interphase, between filler and matrix there exists an interphase or border layer with properties which differ from matrix and filler properties and the thickness and structure of this layer can affect to the dielectric properties of the nanocomposites[10].

This paper presents a combinational method for the synthesis of nanocomposite PP/Ag_2S based on polypropylene and silver sulphide and investigated its dielectric properties depending on Ag_2S concentration.

2.Experiments and methods

Reagents

For research used the powder of isotactic polypropylene powder (M 250000g/mol), silver nitrate (AgNO3), sodium sulfide (Na2S), toluene (C6H5CH3), C12H25SO4Na - lauryl (dodecyl) sodium sulphate, H2O - distilled water.

For the synthesis of nanocomposite PP/Ag2S was used a combinational method which combines the application of ultrasound and microemulsion methods. Were prepared aqueous solutions of 0.005 M, 0.0025 M, of the $AgNO_3$ and Na_2S salts. 0.25 g of polypropylene powder were dissolved in 50 ml of toluene. 5 ml of the respective aqueous salt solution in the presence of 0.01 g of sodium lauryl sulfate was mixed with 25 ml of toluen/PP solution. Every separately taken microemulsion (solution1)/toluene+PP and (solution2)/toluene+PP were treated by ultrasound for 20 minutes (0.6 cm diameter; Ti-tip; 20kHz; 60W/cm2) at a temperature of 300C, by means of a cooling bath. Then, a microemulsion containing (solution2)/PP+toluene was slowly added dropwise to microemulsion (solution1)/PP+toluene at 30° C and sonicated for a certain time. The resulting dispersion containing silver sulfide nanoparticles and polypropylene was vacuum evaporated in order to remove the excess of

solvent and product was poured into a glass plate to form a polymer film at room temperature. Then, by hot pressing at a temperature of fusion of the polymer at a pressure of 10 MPa obtained nanocomposite films.

Equipment

Ultrasonic processing of materials made in the instrument Sonics Vibramobil VCX 500. The morphology of the nanocomposites and distribution of nanoparticles of silver sulfide in the polymer matrix was studied by atomic force microscopy AFM (INTEGRA PRIMA) and scanning electron microscope (JEOL JSM-7600F). The XRD diffractograms of nanocomposites were examined by diffractometerRigaku Mini Flex 600s using the X-ray tube with copper anode (Cu-Kα radiation, 30 kV and mA) at room temperature. The optical characteristics of the nanocompositewere investigated by UV spectroscopySpecord250 Plus and IR spectroscopy Varian 3600 FT-IR. The measurements of dielectric permittivity and resistivity have been carried out by using theimmittancemeter MINIPI E7-20.

3.Results and discussion

The crystallographicstructure ofnanocomposites were examined by diffractometerRigaku Mini Flex 600s using the X-ray tube with copper anode (λ=1,5418 A°Cu-Kα radiation, 30 kV and mA) at room temperature.Figure 1 shows the diffraction patterns ofnanocomposites based on polypropylene and silver sulphidenanoparticles.Thephases of nanocomposites weredetermined by comparing with XRD diffraction patterns those of known minerals.

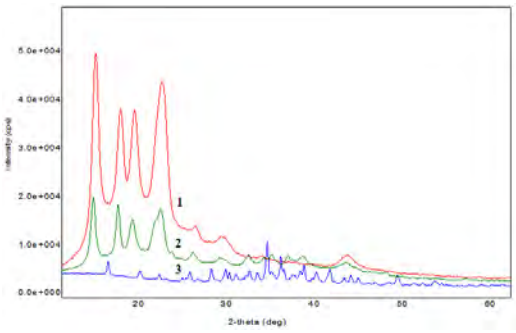

Fig. 1. XRD diffraction patterns of PP powder (1), Ag_2S nanoparticles (2) andnanocomposite based on PP/Ag_2S (3).

The diffraction patterns of pure PP powder are in good agreement with the reported data for İCDD (PDF-2/Release 2011 RDB-00-050-2397).XRD diffraction patterns show that the main peaks of 14,404(100), 17,365(040), 18,888(130), 22,093(111), 25,76(131), 29,05(141) belong to the α-PP which has monoclinic syngony.

The diffraction patterns for synthesized Ag_2S are in good agreement with the reported data for İCDD (PDF-2/Release 2011 RDB- 00-003-0844).XRD diffraction patterns gave dominant peaks 2θat 25,18(11-1); 27,62(100); 31,78(11-3); 34,43(12-1); 38,03(120); 42,99(20-2) and showed the ortorombic structure of the prepared Ag2S and are in good agreement with the reported data for Ag2S (acanthite).The lattice constants for this crystals were a= 6,880 Å, b= 6,920 Å and c=4,770 Å.

As such the presence of both dominants peaks of PP powder and Ag2S nanoparticles peaks in the nanocomposite material under study can be attributed that were prepared the PP/Ag_2S nanocomposite material.

For the investigation the distribution, shape and size of nanoparticles in a polymer matrix, Figure2 show electron microscopic images of PP/Ag2S nanocomposites obtained with various contents of silver sulphide nanoparticles(0,0025M, 0,005M, 0,01M). From the SEM images it is clear that with increasing concentration, the dimensions of silver sulphide Ag2S nanoparticles increases. It is assumed that, in the process of the formation of clusters Ag_2S nanoparticles were merged and increased in primary formed centre of crystallization.

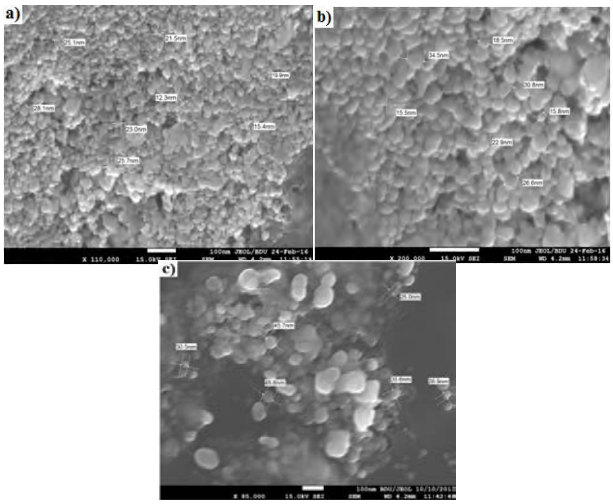

Fig.2. Electron microscope images of nanocomposites based on PP/Ag_2S at various concentration : a) 0,0025M, b) 0,005M, c) 0,01M PP/Ag_2S.

In our opinion it is due to the fact that increasing concentration of the salts solutions the most of the ions Ag+ and S2- spent on coagulation of primary formed Ag_2S nanoparticles but not on the formation of new nuclei. It is found that the shape of nanoparticles is spherical and size of the Ag_2S nanoparticles is approximately 10-50 nm.

SEM study of nanocomposites showed that the distribution of silver sulphide nanoparticles is uniform in polypropylene matrix. Also, experiments show that there is form silver sulphide nanoparticleswith small sizes in polypropylene matrix at high concentrations of starting salts.The synthesis technology allows to form homogeneous of silver sulphide nanoparticles in polypropylene matrix.

The morphology of the nanocomposite PP/Ag_2S and size of distributed Ag_2S nanoparticles was examined with a scanning atomic force microscope (AFM). Figure3 shows the 2D AFM images of the surface nanocomposites PP/Ag_2S,obtained at variousconcentrations of the starting salts $AgNO_3$ and Na_2S solutions.

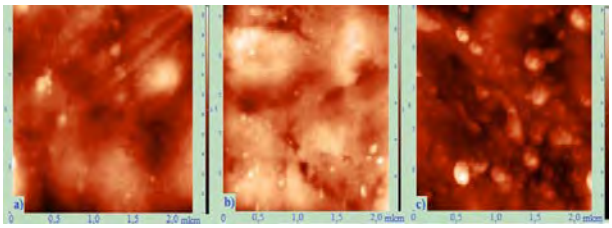

Fig. 3. Atomic force microscopic images of PP/Ag_2S nanocomposites at various concentrations of the starting salts $AgNO_3$ and Na_2S solutions: a) 0,0025M, b) 0,005M, c) 0,01M PP/Ag_2S.

AFM study shows that with increasing concentration of the starting salts in the polymer matrix the size of Ag_2S particles increases. Also it is seems that the size of Ag_2S nanoparticles changes in intervals of 20-60 nm. AFM study also showed that the nanoparticles Ag_2S distributed in the volume of PP matrix, i.e.in pores of the polymer.

The distribution histogram surface structural elements of nanocomposite materials in a particular field obtained at various concentrations shown in Figure 4.

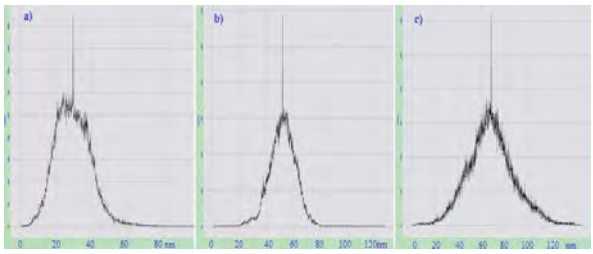

Fig. 4. Histogram of the structural elements of the nanocomposite images PP/Ag_2S obtained at different concentrations Ag_2S nanoparticles: a) 0,0025 M b) 0,005 M c) 0,01 M PP/Ag_2S.

AFM study shows that in the formation process of Ag2S nanoparticles in polymer matrix the increasing concentrations of the starting salts led to changing of surface morphology, so mean square roughness variate as shown Fig.4.

From Figure 4 seen that for the nanocomposites with different concentrations- 0,0025M, 0,005M və 0,01M of Ag2S nanoparticles the roughness of structural elements varies 20-40 nm, 40-60 nm, və 60-80 nm, respectively.This is indicated to change the surface roughness of supramolecular structure and to increasing of the structural elements of nanocomposite surface.

In general, it can be concluded that by the changing concentrations of starting salts the size and distribution of the nanoparticles can be controlled. Moreover, it is show that size interval of the silver sulfide nanoparticles is not in a wide range.

Structural changes in the formation process of Ag2S nanoparticles in polymer matrix have been investigated by the IR spectroscopy method. Figure5 shows the IR absorption spectra of the nanocomposite PP/Ag_2S obtained at variousconcentrations of the starting salts $AgNO_3$ and Na_2S solutions.

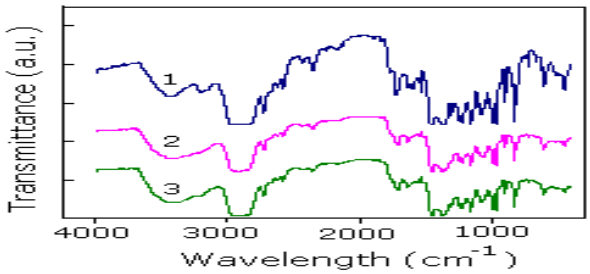

Fig. 5. IR spectra of nanocomposite PP/Ag_2S prepared from variousconcentrations of Ag_2S: 1) 0,0025 M 2) 0,005 M 3) 0,01 M

It is seen that with increasing concentrations of Ag2S some changes observed in the IR spectrum. As such with increasing concentrations of Ag2S nanoparticles, the shoulder according hydroxyl groups to the 3450-3350 cm-1 wavelength, extended and slightly shifted to the right.Also the peaks correspond to stretching vibration of C=O groups with increasing concentrations of Ag_2S nanoparticles shifted to the right side. The peaks correspond to symmetric deformation vibration of O-S-O groups with increasing concentrations of Ag_2S nanoparticles shifted to the right side.Shifting of the peaks by increasing concentrations of starting salts can coordinate with influence of Ag2S filler to the supramolecular structure.

Figure 6 shows the UV absorption spectra of nanocomposites films of PP/Ag_2S obtained on the variousconcentrations of Ag_2S.

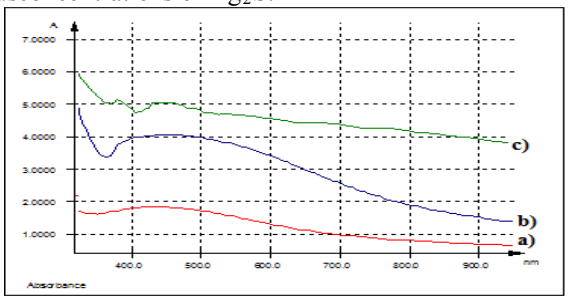

Fig.6. UV spectra nanocomposites PP /Ag_2S based on variousconcentrations of Ag_2S : a) 0,005 M b) 0,0025 M c) 0,01 M PP/Ag_2S.

From Fig.6. seen the absorption intensity increased by increasing concentration of Ag2S nanoparticles. The peak which corresponds to Ag_2S nanoparticles (445nm) by increasing concentration slightly shifted toward higher wavelength.This events which called redshiftsare indicated the increase of Ag_2S nanoparticles by the increasing of concentrations of starting salts.

Figure7 show results of investigation the dielectric permittivity ε of nanocomposites PP/Ag_2S obtained with various consentrations of silver sulphidenanoparticles(0,0025M, 0,005M, 0,01M). The dielectric permittivity ε, dielectric loss tangent tgδ of nanocomposites PP/Ag_2S have been studied in room temperature and 10^2-10^6 Hs frequency.

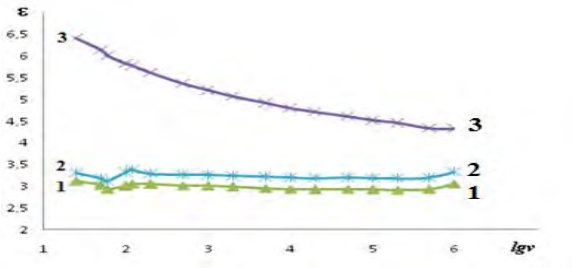

Fig.7. Dependence of permittivity ε of nanocomposites PP/Ag_2S from frequency:1) 0,0025M, 2) 0,005M, 3) 0,01M PP/Ag_2S.

Was found that increasing of Ag2S nanoparticles in polymer matrix leads to increasing of permittivity- ε . This growth is explained by formation of dipoles with adding Ag_2S nanoparticles.At the same time, it can be associated, especially at low frequencies in the interface layer between the filler and the polymer with polarization of induced electric charge.With increasing concentration of the starting salts in the polymer matrix the interfacial layer grows and this, in turn, increases polarizability, i.e.dielectric permittivity.

At figure 8 is given the graph of depends of dielectric loss tangent tgδ of nanocomposites PP/Ag_2S from frequency obtained with various concentrations of silver sulphide nanoparticles.

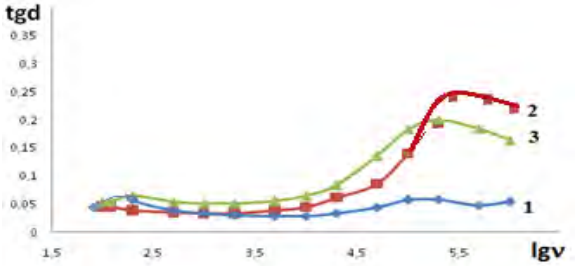

Fig.8. Dependence of dielectric loss tangent tgδ of nanocomposites PP/Ag_2S from frequency:1)0,0025M, 2)0,005M, 3) 0,01M PP/Ag_2S.

From the graphs it is shown that at low frequencies, the dielectric loss tangent tgδvalue minimal and unchanged. But with increasing of frequency the dielectric loss tangent tgδvalue is rising. It is explained by increasing of the energy scattering at the high frequencies and respectively increasing of electric conductivity.

4. Results

In this work we used a combination of two methods for producing polypropylene-based nanocomposites, by application of ultrasound and microemulsion techniques. The morphology of the nanocomposite and distribution of silver sulfide nanoparticles in the polymer matrix was studied by atomic force microscopy and scanning electron microscope. It is found that, depending on the technology for obtaining polymer nanocomposites, uniform and homogeneous distribution of nanoparticles in the polymer matrix can be achieved. It has also been defined that, depending on the concentration of starting salt the sizes of nanoparticles inside of nanocomposite change. IR and UV spectroscopy showed that with increasing concentration of nanoparticles in the polymer matrix shifts in the groups of nanoparticles were observed. The dielectric properties of polymeric nanocomposites have not remained constant as a result of increase in nanoparticles concentration.

5. References

1. B. R. Sankapal, R. S. Mane, C. D. Lokhande. Materials Chemistry and Physics,**63/3(**226–229), 2000.
2. S. S. Dhumure and C. D. Lokhande. Thin Solid Films, **240/ 1-2**(1–6), 1994.
3. I. A. Ezenwa, N. A. Okereke, and N. J. Egwunyenga, International Journal of Science and Technology, **2/ 3**(101–106), 2012.
4. T. B. Nasrallah, H. Dlala, M. Amlouk, S. Belgacem, and J.C. Bernède. Synthetic Metals, **151/ 3**(225–230), 2005.
5. J. A. Muñoz, C. Gómez, A. Ballester, M. L. Blázquez, F.González, and M. Figueroa.Journal of Applied Electrochemistry, **28/ 1**(49–56),1997.
6. M. C. Brelle and J. Z. Zhang, Journal of Chemical Physics, **108/ 8**(3119–3126), 1998.
7. A. P. Yadav and R. R. Pradhananga. Journal of Nepal Chemical Society, **15/ 9**(19–26), 1996.
8. Hodes G., Manassen J., Cahen D. Nature. **261**(403–404), 1976.
9. Kitova S, Eneva J, Panov A, Haefke H. J Imaging Sci Technol. **38**(484–488), 1994.
10. A.M.Magerramov, M.A.Ramazanov, F.V.Gadjiev. Problems of Modern Physics II. National conference, Baku, 2008, p.34

The influence of magnetite nanoparticles on dielectric properties of metaloxide- polymer based nanocomposite

[a]A. M. MAHARRAMOV, [a]M. A. RAMAZANOV, [b]LUCA DI PALMA, [a]H.A.SHIRINOVA,[a]F.V.HAJIYEVA

[a]*Baku State University,23 Z.Khalilov Street, Baku, Azerbaijan, Az-1148*
[b]*La Sapienza University of Rome, Via Eudossiana 18, Rome 00184, Italy*

Abstract
The structure and dielectric properties of the nanocompositewere investigated. The dispersion of the magnetite nanopartcles in polymer matrix was studied by scanning electron microscope(SEM, Carl Zeiss). The dielectric properties of composite materials were examined by means of E7-21 impedancespectrometre in the frequency range of 10^2 Hs -10^6Hs and over the temperature range of298°-433°K. It was shown that the introduction of magnetite (Fe_3O_4) nanoparticles into the polypropylene matrix increases the dielectric permittivity of nanocomposites. It was found that the decrease in the resistivity up to 318 K is associated with increasing ionic conductivity of the nanocomposite.

Keywords: Nanocomposite materials, polypropylene, magnetic nanoparticles, dielectric permeability, electrical resistivity

1. Introduction

One of the important branchesof nanotechnology is the creation and study of nanocomposites, representing a two-phase system of inorganic nanoparticles in a dielectric matrix [1]. The influence of a nanofiller on the properties of nanocomposites depends on the concentration and size of particles, the degree of their aggregation, and also the nature of the interfacial interactions with the polymer[2].At the boundaryof nanoparticles and polymer formed an interphase layer whichproperties differ from the filler and the polymer matrix[3]. Composite materials based on organic polymer and inorganic filler carrynot only scientific, but also undoubtedly practical interest.
At present, the interest in obtaining and investigating various types of polymer nanocomposite materials based on nanofillers has increased profoundly.Polypropylene occupies one of the first places among the filled thermoplastic polymers.Modification of polypropylenewith various nanoparticles allows the field ofits applicationto expandconsiderably.The introduction of even a small amount of nano-sized particles in polypropylene can significantly affect their physical properties, such as thermal stability, electrical conductivity etc[4].In this paper, nanocomposite materials based on isotactic polypropylene and magnetite nanoparticles are obtained and studied, their structure and dielectric properties are investigated.

2. Experimental part

2.1. Materials

Isotactic polypropylene (PP-MoplenHF500N, Homopolymer) with a 0.92g / cm^3 density at 25°C.Mw=250000, Mn =67000, Melt Mass-Flow Rate-MFR = 11,5g/10 min (230°C, 2,16 kg), melting T = 162°C.

Magnetite nanoparticles were synthesized by co-precipitation method, in an alkaline medium. The average size of the nanoparticles formed is 7-15 nm.

2.2. Methods

2.2.1 Scanning electron microscopy (SEM)

The morphology of the nanocomposites was determined by scanning electron microscopy onJeolJSM-7600 F.The sample's surfaces weresputter coated with platinum atoms prior to imaging to avoid charging. Scanning was conducted in SEI mode with a working distance of 4.5 mm.

2.2.2. Methodformeasuringdielectricproperties

The dielectric permittivity of polymer nanocomposites was measured over a wide range of frequencies using dielectric spectroscopy(MNIPIE7-20). During the test, PP+Fe_3O_4 composites' dielectric permittivity over a range of 10^2 Hz to 10^6Hz at T=298 K was measured. The sample was cut into a circle with 25 mm in diameter and the thickness of the sample was 100 μm. Measurement of the permittivity as a function of temperature was carried out at f = 10^2Hz using the same laboratory equipment. Measurement of the resistivity as a function of temperature carried out using anE7-13 A teraohmmeter.

2.3.Synthesisofnanocomposites.

Fe_3O_4 filled polymernanocomposites with 3%, 5%, 7% mass concentrations of Fe_3O_4 were prepared by using laboratory technique-magnetic stirring. Isotactic polypropylene was solved in toluene at 120°C and magnetite nanoparticleswere added to the polymer solution[5].The solution is stirred for two hours until homogeneous structure is obtained. The mixture is dried during 24 hours. Than from this samples, obtained films by

hot-pressing method under 10MPa pressure and on the melting point of polypropylene. The thickness of samples is 100μm.

3. Resultsand discussion

The scanning electron microscope image of the nanocompositesbased on PP+Fe_3O_4 is depicted in fig1. As can be seen, from the figure that, with increasing of the filler consentration, the amount of nanoparticles increases in the polymer matrix, as well as the number of agglomerates and aggregates of nanoparticles in the matrix. Thus, with a volume content of 5%, the size of magnetite nanoparticles in the matrix is 15-18 nm, with a 7% content respectly 16-20 nm.

Fig2. shows the element mapping of nanocomposites based on PP + Fe_3O_4. It is also clear from the mapping that the nanocomposite consists mainly of carbon, oxygen and iron. Platinum is detected as a result of spraying on the surface of the nanocomposite in order to eliminate the charging of the films.

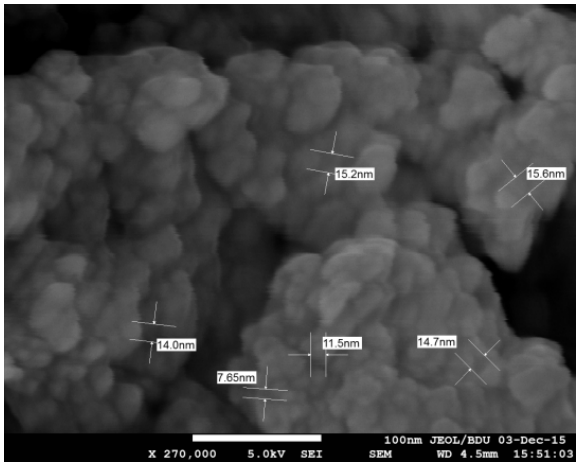

a)

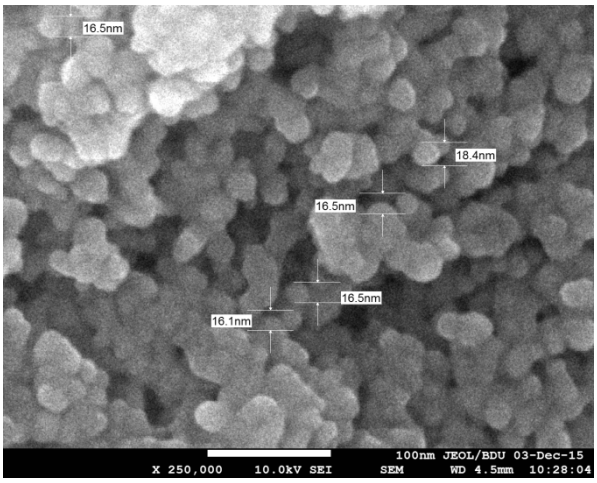

b)

Figure 1. SEM images of nanocomposites based on PP+ Fe_3O_4a) PP+ 5%Fe_3O_4 b) PP+ 7%Fe_3O_4

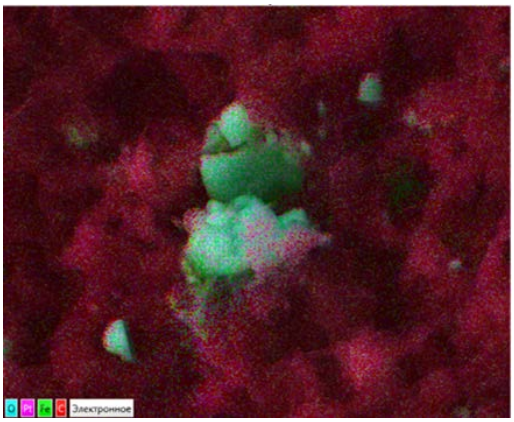

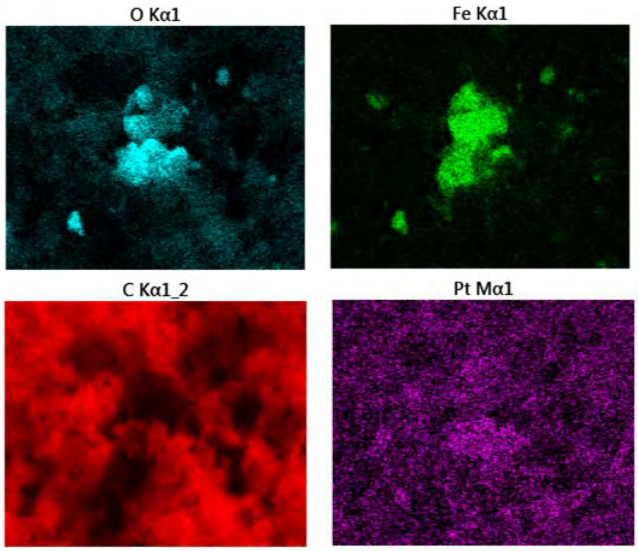

Fig.2 element mapping fornanocomposites based onPP+ Fe_3O_4

Fig3. shows the dependence of the permittivity (ε) on the frequency for the composition PP + Fe_3O_4. It can be seen from figure that with the introduction of a magnetite nanoparticle into a polypropylene matrix, the dielectric permittivity of the composite rises with increasing of filler concentration, and with increasing frequency, the value of the permittivity (ε) remains practically unchanged. At low contents Fe_3O_4 polypropylene nanoparticles, the nanoparticles play a essential role in the adjusting of the structure, by forming a relatively ordered structure in nanocomposite as center of formation [6].

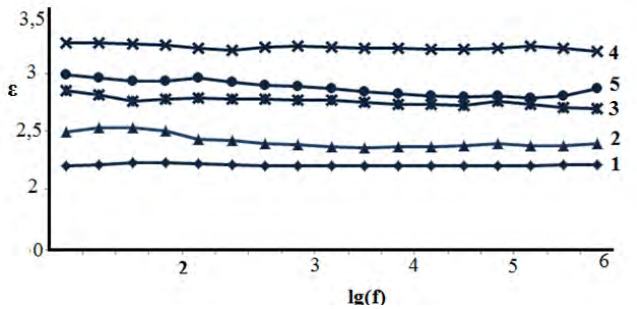

Fig3.Dependence of the dielectric constant of the composites PP+ Fe_3O_4 on frequency 1)PP 2)PP+3%Fe_3O_4 3)PP+5%Fe_3O_4 4)PP+7%Fe_3O_4 5)PP+10%Fe_3O_4

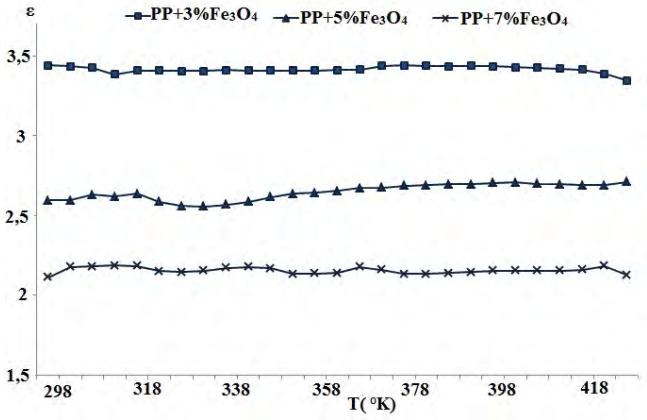

Fig.4 Dependence of the dielectric constant of the composites PP+ Fe_3O_4 on temperature

Fig4.shows the dependence of the dielectric permittivity of nanocomposites based on PP + Fe_3O_4 on the temperature measured at a frequency of 1kHz.It is shown that the value of the dielectric permittivity varies slightly with increasing of temperature [7-9].

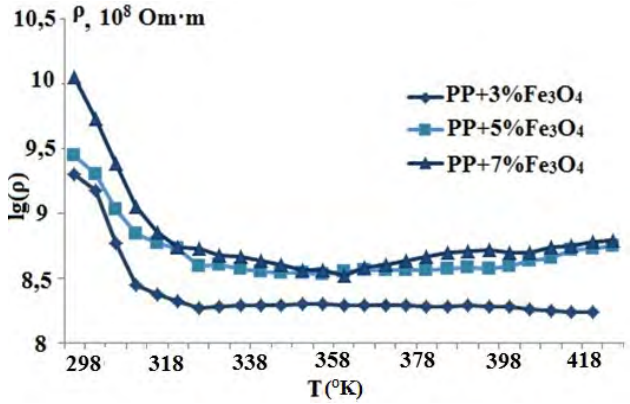

Fig.5 Dependence of the specific resistance of the nano composition PP + Fe3O4 on the temperature

In Fig5. The logarithmic dependence of the resistivity of the nanocomposite on temperature is shown.As can be seen from this graph, to a temperature of 318 K, the resistivity of the sample decreases smoothly, then remains steady to 358 K, after which a small increase in resistance occurs.In our opinion, the decrease in the resistivity up to 318 K is associated with an increase in the ionic conductivity of the nanocomposite, and the rise in the resistivity starting from 358 K is associated with the destruction of the crystalline phase of the polymer as a result of which the distance between the Fe_3O_4 nanoparticles increases.At a concentration of 3% this growth is not observed, due to the fact that a small fraction of the filler concentration does not contribute to the conductivity of the nanocomposite.

4. Conclusion:

In this paper, structures and dielectric properties of polymer nanocompositions based on isotactic polypropylene and magnetite nanoparticles were studied.It was shown that with the introduction of a magnetite nanoparticle into a polypropylene matrix, the dielectric permittivity of the composite increases with rising filler concentration, and with increasing frequency, the value of the permittivity (ε) remains practically unchanged.At low contents of Fe_3O_4 nanoparticles in polypropylene, nanoparticles play the role of the structure-forming agent.It is shown that due to the increasing consnentration of nanoparticles in the polymer matrix, a change in the supramolecular structure of the polymer takes place and a relatively ordered structure is formed, as well as the polarizing ability of the nanocompositerises.Itis also shown that with increasing temperature the value of the dielectric constant varies little.It was found that the decrease in the resistivity up to 318 K is associated with an increase in the ionic conductivity of the nanocomposite, and the rise in the resistivity starting from 358 K is associated with the destruction of the crystalline phase of the polymer as a result of which the distance between the Fe_3O_4 nanoparticles increases. It is also shown that at a 3% mass concentration of the fiber this growth is not observed, due to the fact that a small fraction of the filler concentration does not contribute to the conductivity of the nanocomposite

References

[1]P.H. Camargo, K.G.Satyanarayana, F.Wypych J.Materials Research, **12**(1-39)2009

[2]T. Hanemann, D.V. Szabó J.Materials,**3**(3468-3517)2010

[3]H.Hua, L.Onyebueke , A. Abatan, J. Minerals & Materials Characterization & Engineering,**9**(275-319), 2010

[4] A.Thabet, Y. A. Mobarak, M. Bakry, J.Engineering Sciences, **39**(377-403)2011

[5]. H. Shirinova, L. D. Palma, F.Sarasini, J.Tirillò, M. A. Ramazanov, F.Hajiyeva, D.Sannino, M. Polichetti, A.Galluzzi, J. Chemical engineering transactions **47**(103-108)2016

[6].A. M. Maharramov, M. A. Ramazanov , A. B. Ahmadova, F. V. Hajiyeva, U. A. Hasanova. J. Nanomaterials and Biostructures.**11**(365 – 372)2016

[7]. A.M.Maharramov , M.A.Ramazanov, R.A.Alizade , P.B.Asilbeyli. J.Nanomaterials and Biostructures **8**(1447 – 1454)2013.

[8].A.M.Magerramov, M.ARamazanov, F.V. HajiyevaThe Journal of American Science. 2009, 5(6), 95–101.

[9] A.M.Magerramov, M.A.Ramazanov,F.V.Hajiyeva. Journal Optoelectronics and Advanced Materials. RapidCommunications. 2008, 2(11), 743–745.

Observation of MHD waves in Solar Spicules

H. EBADI[a,b]
[a]Research Institute for Astronomy and Astrophysics of Maragheh, Maragheh, Iran
[b]Astrophysics Department, Physics Faculty, University of Tabriz, Tabriz, Iran
hosseinebadi@tabrizu.ac.ir

Abstract
We analyze the time series of oxygen line profiles (O VI 1031.93 Å and O VI 1037.61 Å) obtained from SUMER/SOHO on the solar south limb. We calculated Doppler shifts and consequently Doppler velocities in three heights 4", 14", and 24" from the limb on a coronal hole region. Then, we performed wavelet analysis with Morlet wavelet transform to determine the periods of fundamental mode and its first harmonic mode. The calculated period ratios have departures from its canonical value of 2. The density stratification and magnetic twist are two main factors which may cause these departures.

Keywords: Sun: spicules; MHD waves: period ratio

Introduction

Observation of oscillations in solar spicules may be used as an indirect evidence of energy transport from the photosphere towards the corona. Transverse motion of spicule axis can be observed by both, spectroscopic and imaging observations. The periodic Doppler shift of spectral lines have been observed from ground based coronagraphs [1]. But Doppler shift oscillations with period of 5 min also have been observed on the SOlar and Heliospheric Observatory SOHO by [2]. Direct periodic displacement of spicule axes have been found by imaging observations on Solar Optical Telescope (SOT) on Hinode. The observed transverse oscillations of spicule axes were interpreted by kink [3] and Alfven [4] waves.One of the most important functions of coronal seismology is determining the period ratio P_1/P_2 between the period P_1 of the fundamental mode and the period P_2 of its first harmonic. Different factors such as the effect of density stratification and magnetic twist can cause the deviation of the period ratio from its canonical value of 2. However, the ratio between the periods of fundamental and first harmonicsgnificantly shifted from 2, which later was explainedas a result of longitudinal density stratification in the loop. The rate of theshift allows us to estimate the density scale height in coronal loops,which can be a few times larger compared to its hydrostatic value.Observed oscillation periods can be used to estimate the Alfven speed and consequently magneticfield strength in macro-spicules. The mentioned studies in the previous paragraph are all devoted to the coronal loop transversal oscillations.To my knowledge there is no any work related to the period ratio of spicules oscillations. So, the present studyis an attempt to check this ratio observationally. We will study the same problem theoretically in our future works.

Observations and data processing

SUMER is a high-resolution normal incidence spectrograph operatingin the range 666-1610 Å (first order) and333-805Å (second order). Theangular pixel size is ~1". The spectralpixel size depends slightly on the wavelength.Contriving normally allows sub-pixel resolution. It canvary from about 45 m Å /pixel at 800 Å toabout 41m Å /pixel at 1600 Å [5].A coronal hole region in the south pole of the sun wasobserved with SUMER (detector B) on 21 Feb 1997. The pointingcoordinates were X = 0", Y = -985". The slit,which was used for observations, has the dimensions of 0.3"×120". The observation was performed-from 01:36 UT to 01:52 UT and the exposure time was 15 seconds.In Figure 1 we presented the images of the studied region which were observed by 304 Å SOHO/EIT (top) on 21 February 1997.

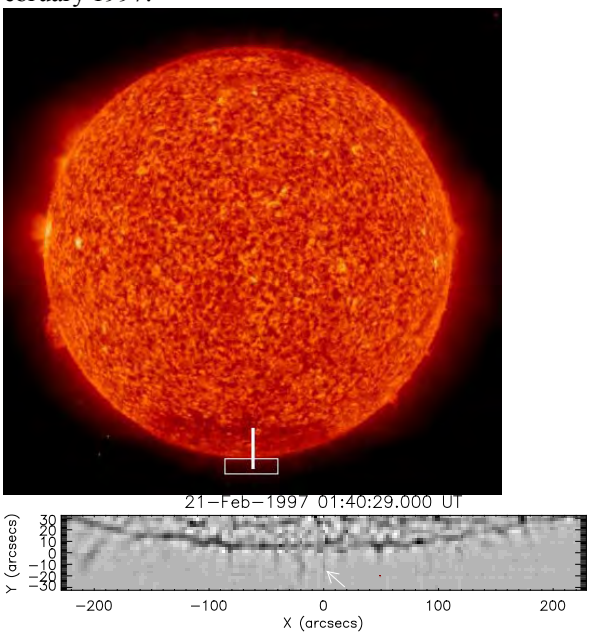

***Fig.1**: Image of the studied region which were observed by 304 Å SOHO/EIT (top) on 21 February 1997. The slit is in the North-South direction. The rectangular shows the region studied. We used the ``madmax" algorithm to enhance the finest structures (down). The white arrow shows the studied macro-spicule.*

The rectangularshows the region of south limb macro-spicules. We used the "madmax" algorithmto enhance the finest structures. As it is clear from down panel of Figure 1,the length of the studied spicule is 25 Mm which means that the studied spicule is macro-spicule.The raw data have been initially processed applying the standardprocedures for flatfield, deadtime and destretchingcorrection which can be found in the Solar Software (SSW)database. We calculated the integrated intensity for O VI (1031.93 Å) line along the SUMER slit.The limb is located in pixel

number \$86\$ and the spicule region is lied from pixel 87 to 117 which is shown in Figure 2. Moreover, we plotted integrated profile of O VI (1031.93 Å) line in Figure 2.

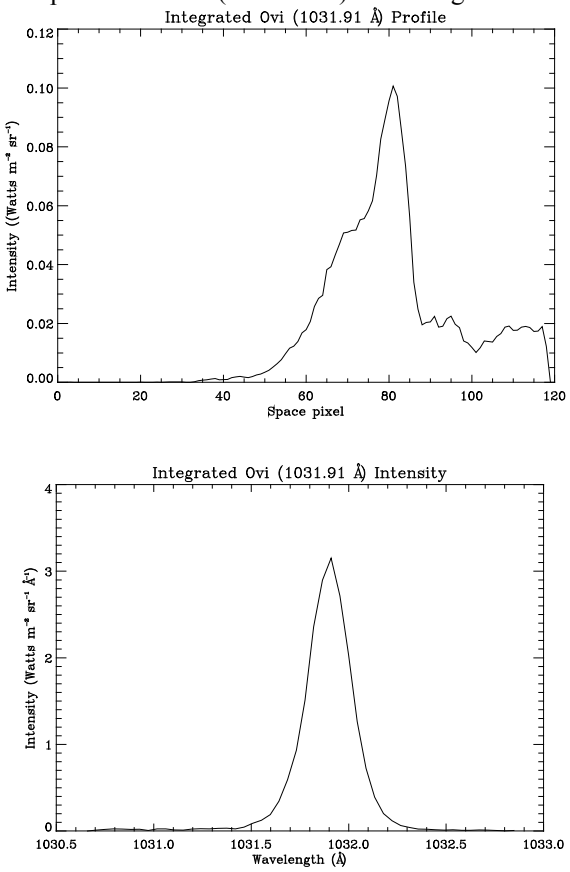

Fig. 2: *The integrated intensity along the SUMER slit for O VI (1031.93 Å) line. The spicule region is lied from pixel 87 to 117 (top panel). The integrated profile of O VI (1031.93 Å) line (down panel).*

Results and Discussions

We analyze O VI (1031.93 Å) and O VI (1037.61 Å) line profiles from the time series by fitting to a Gaussian. Then we calculated Doppler shifts and consequently Doppler velocities . We used the two stable photospheric neutral oxygen emission lines (i.e. O I (1027.43 Å) and O I (1028.16 Å)) that happen to be in the same spectral window with the O VI lines. Doppler velocities and proper wavelet analysis results are presented in Figure 3 for O VI (1031.93 Å). We perform wavelet analysis with Morlet wavelet transform in three heights for both lines.

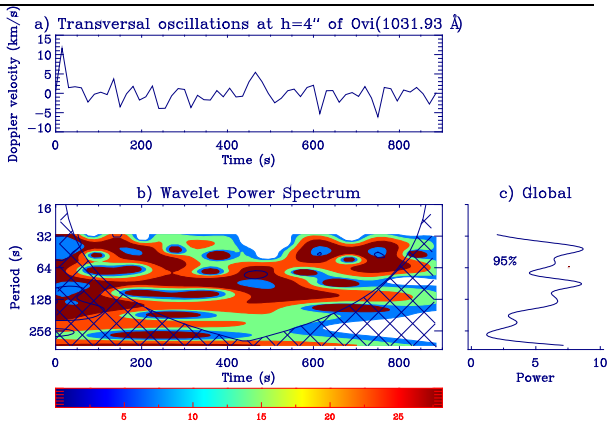

Fig. 3*: a. Doppler velocity variations of the studied spicule 4" above the limb in O VI (1031.93 Å) line. b. The wavelet power spectrum. The contour levels are chosen so that 75%, 50%, 25%, and 5% of the wavelet power is above each level, respectively. The cross-hatched region is the cone of influence, where zero padding has reduced the variance. c. The global wavelet power spectrum.*

Our findings show small departures of this value from its canonical value of 2 in both lines and three mentioned heights. In other words, they are greater than 2 in both lines in 4", 14", and 24" from the limb. These departures may be caused by the density stratification and magnetic twist which is observed in spicules. Observed oscillation periods are used to estimate the Alfven speed and consequently magnetic field strength in macro-spicules as 340 km/s and 65 G, respectively [5,6].

Refferences

[1] Nikolsky, G.M., Sazanov, A.A.: Soviet Astronomy, 10, 744 (1967)

[2] Wilhelm, K., Curdt, W., Marsch, E., Schuhle, U., Lemaire, P., Gabriel, A., Vial, J.-C., Grewing, M., Huber, M. C. E., Jordan, S. D., and 6 coauthors, Solar physics, 162, 189 (1995)

[3] Zaqarashvili, T.V., Melnik, V.N., Brazhenko, A.I., Panchenko, M., Konovalenko, A.A., Franzuzenko, A.V., Dorovskyy, V.V., Rucker, H.O.: A&A, 555, 55 (2013)

[4]De Pontieu, B., McIntosh, S.W., Carlsson, M., et al.: Science, 318, 1574 (2007)

[5]Ebadi, H., Zaqarashvili, T.V., Zhelyazkov, I.: Astrophysics and space science, 337, 33 (2012)

[6]Ebadi, H., Shahmorad, S, Vasheghani, S.: Astrophysics and space science, 361, 146 (2016)

Nano-structured solar cell based on *c*-Si/*porous*-Si/CdS/$Zn_xCd_{1-x}O$ heterostructures

A.SH.ABDINOV, H.M.MAMEDOV, V.U.MAMMADOV, Kh.M.AHMEDOVA, V.J. MAMMADOVA, L.E.AGAZADE

Faculty of Physics, Department of Physical Electronics, Baku State University, Az1148, Z.Khalilov str., 23, Baku, Azerbaijan, e-mail: mhhuseyng@bsu.edu.az; mhhuseyng@gmail.com

Abstract

Solar cells based on *c*-Si/*porous*-Si/CdS/$Zn_xCd_{1-x}O$ heterostructures are created by depositing CdS films with thickness of on *c*-Si/*porous*-Si (PS) substrates by the method of electrochemical deposition (ED). PS layers with different pores size (8-45 nm) and thickness (100-250 nm) were fabricated on p-type *c*-Si wafers using electrochemical etching. The window layers of $Zn_xCd_{1-x}O$ with different Zn content (x=0.2; 0.4; 0.5 and 0.6) is deposited onto CdS buffer layers also by ED. The morphological and structural properties of films have been studied by SEM, AFM and XRD. Photoelectrical properties of heterostructures were studied depending on the pores size of PS and Zn content in $Zn_xCd_{1-x}O$. The size of pores (10 nm) and Zn content (x=0.6) are defined, which provides the maximum efficiency (9.9 %) of solar cells.

Keywords: *porous silicon, nano-structure, heterojunction, solar cell*

1. Introduction

It is well known that the band-gap of nanostructure semiconductors can be tuned by size of nanoparticles to match the solar spectrum [1]. With the increased band-gap of the n-type material (window material) one can expect more of the incident light to pass through to the absorber and this will increase the optical path length of the incident light and thus create more electron-hole pairs. Therefore, increasing the absorption degree will stimulate an increase of the open circuit voltage and short circuit currents.

The nanostructure morphology of the absorber material would also give rise to multiple light reflections at their grain boundaries. Porous silicon (PS), is a nanostructured material, has emerged as an attractive material in the field of photoelectronics due to its broad band gap, wide optical transmission range, absorption spectrum and surface roughening. The surface roughness and lower effective refractive index, which can reduce the reflection losses of sunlight radiation, are the primary factors that enhance PS compared with c-Si [2-5]. Thus, a highly porous PS layer can enhance the efficiency of solar cells by increasing light trapping into the active region [6].

ZnO and its ternary alloys $Zn_xCd_{1-x}O$ are important semiconductor materials that may be used in solar cells [7], light-emitting diodes [8], and other optoelectronic devices [9]. The high melting and boiling points, resistance to high energy radiation of these materials makes it suitable for space applications and for the fabrication of nano-size devices.

In the present study, we demonstrate the photoelectrical properties of *c*-Si/*porous*-Si/*nanostructured*-CdS/$Zn_xCd_{1-x}O$ heterostructures depending on the pores size of PS and Zn content in $Zn_xCd_{1-x}O$ films (x=0.2; 0.4; 0.5 and 0.6) films.

2. Experiment

Before etching process p-type *c*-Si substrates (2.5 Ohm·cm resistivity and 0.2 ÷ 0.3 mm thickness) were cleaned (to remove the native oxide layer) with acetone and ethanol to remove dirt followed by etching in dilute (10%) HF acid. The anodization of *c*-Si substrate surface was carried out in Teflon chamber with platinum (Pt) cathode. HF:C_2H_6O (1:1) was used for the porous silicon formation. The anodization voltage, current density and anodization time were (20; 25; 30) V, (50; 60; 70) mA/cm^2 and 1-30 min, correspondingly. Depending on the anodization voltage, current and time PS with average porous size of ≈8-11 nm (PS1); ≈10-16 nm (PS2) and ≈30-40 nm (PS3) were prepared on the surface of *c*-Si. The thickness of PS are about 100-250 nm, depending on the anodization time.

After the PS layer formation, samples were immersed into ethyl alcohol, dried in flowing N_2 and placed into the electrochemical bath for the deposition of CdS films. Electrodeposition of the CdS films onto the *c*-Si/PS substrates was carried out at temperature of 80°C from aqueous solution containing cadmium ($CdCl_2$) and sodium ($Na_2S_2O_3$) salts (99.5% purity). The pH of solution is fixed at 6. Depending on the deposition time and substrate pores size, CdS films with different thickness (200 ÷ 1000 nm) and morphology were deposited from solution. SEM images shows that, the morphology of the CdS films can be controlled by selecting the pores size of silicon. CdS films deposited onto the PS1 shows micro-texture structure. When PS2 is used as substrate, the size of the nano-crystallites gets reduced due to controlled process of nucleation and nano-size crystallites are uniformly distributed at the surface. Size of crystallites, determined by SEM, is found as 80-190 nm. CdS films show nano-crystallite texture, with PS3. The size of the crystallites was different from each other, indicating irregular growth rate of the grains.

The electrochemical deposition of $Zn_xCd_{1-x}O$ films with different Zn content has been performed with a three electrode configuration: graphite electrode as anode, $Ag/AgCl_3$ electrode as reference electrode and *c*-Si/PS/CdS substrates as cathode. For SEM, XRD, energy dispersive spectra (EDS) and optical measurements we used the *glass*/SnO_2 substrates. Before electrodeposition, *c*-Si/PS/CdS substrates were cleaned with ethanol and deionized water and then dried in flowing N_2. At electrodeposition we used aqueous solutions of $Zn(NO_3)_2$ and $Cd(NO_3)_2$ salts (99.5% purity) with different molar fraction in solution. The solution were kept on continuous stirring for 1 hour then filtered by filter paper. The solution was homogeneous, clear, transparent and stable at room temperature. The reaction temperature was kept at 80°C. In order to investigate the electrochemistry in the deposition process of $Zn_xCd_{1-x}O$, cyclic voltammetry study was performed in the potential range of -1.6 to +1.6 V. $Zn_xCd_{1-x}O$ formation potentials were registered from cyclic voltammetry curves. The thickness of films were about 100-500 nm, depending on the anodization time. EDS data were recorded to determine the composition of Cd and Zn in deposited layers.

Morphological characterization of the $Zn_xCd_{1-x}O$ films was performed by SEM and AFM. Both the SEM and AFM images support the increase in the grain size with decreasing Zn content, calculated from the XRD data. It is established also, that the surface morphology of films depends on the pores size of PS. AFM images show that the surface roughness of the films increases with increasing pores size of PS. So, films deposited on the surface of *c*-Si/PS1/CdS substrates shows homogeneous micro-texture morphology. Particles with pyramidal shape are uniformly spread over the surface of *c*-Si/PS2/CdS substrates. It was found that, as the size of the pores increases from 10 to 30 nm, the shape of the $Zn_{0.6}Cd_{0.4}O$ nanocrystallites changes to spheres. SEM and AFM images indicated that the grain size slightly increased up to 30-45 nm.

In order to fabricate the heterojunctions, an ohmic In (or Cu) electrode, in reticulose form was evaporated on the $Zn_xCd_{1-x}O$ films with an area of ~0.82-1cm^2. An ohmic contact was performed on the side of *c*-Si wafers by evaporating an Al electrode.

3. Results and discussions

Photoelectrical properties of *c*-Si/PS/CdS/$Zn_xCd_{1-x}O$ heterostructures were investigated depending on the pores size of PS and Zn content (x) in $Zn_xCd_{1-x}O$ films. Properties of heterostructures fabricated with and without $Zn_xCd_{1-x}O$ layers were compared. All samples were found to possess high photosensitivity in the spectral range 390 – 1280 m. Illumination from the $Zn_xCd_{1-x}O$ (wide-gap material) side gives rise to a photovoltage which has the same sign over the entire photosensitivity range.

Typical spectral dependences of the photocurrent in structures with PS1 as a function of Zn content are shown in Fig. 1. Under illumination from the Si side, the spectral dependence of the photocurrent shows only one peak, at 1125 nm, due to direct interband transitions in *c*-Si (not shown in picture).

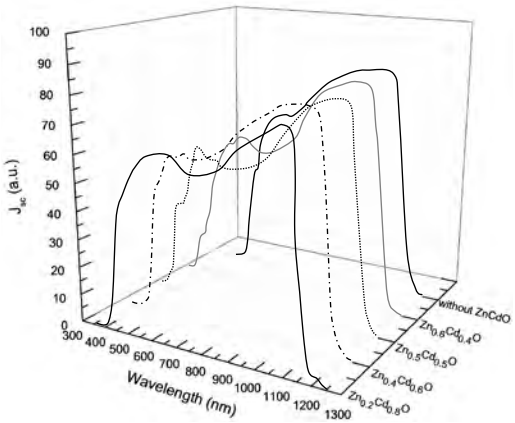

Figure 1. Spectral dependences of the photocurrent in structures c-Si/PS1/CdS/$Zn_xCd_{1-x}O$ depending on the Zn content.

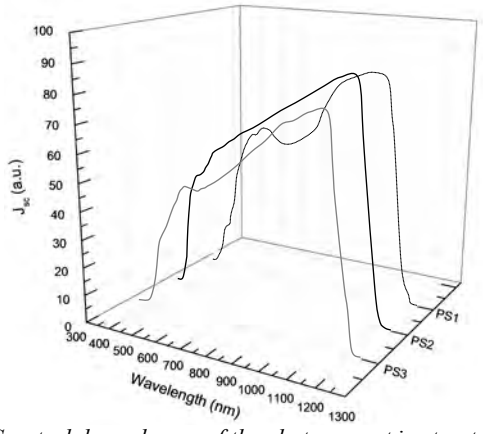

Figure 2. Spectral dependences of the photocurrent in structures c-Si/PS/CdS/ $Zn_{0.6}Cd_{0.4}O$ with PS1, PS2 and PS3

A drastically different spectral response is observed under illumination of the heterostructures from the other side, which gives rise to a short wavelength peak in the spectral dependence of the photocurrent. Short wavelength peak for heterojunctions without $Zn_xCd_{1-x}O$ layers is observed at 510 nm, which corresponds to the band gap of CdS films. The *c*-Si/PS/CdS heterojunction with 150 nm inserted $Zn_xCd_{1-x}O$ layers shows the best photoelectrical characteristics, increasing the photo-to-dark current ratio effectively by 2-5 times depending Zn content. With increasing x, the short wavelength peak shifts to shorter wavelengths, which is attribute to the increase in the band gap of $Zn_xCd_{1-x}O$ and intensity of peaks decrease with x. At x = 0.6, the peak is observed at 420 nm (Fig. 1). As seen from picture, all samples with PS1 show relatively low photosensitivity in the spectral range of 540-820 nm (table 1).

Table 1. Photoelectrical parameteres of heterojunctions c-Si/PS1/CdS/$Zn_xCd_{1-x}O$ depending on the x.

Zn content (x)	U_{oc} (mV)	J_{sc} (mA/cm^2)	FF	η, %
samples without ZnCdO	482	15.7	0.53	4.01
0.2	504	15.3	0.53	4.09
0.4	513	15.1	0.53	4.1
0.5	527	14.9	0.54	4.24
0.6	543	14.6	0.54	4.28

Table 2. Photoelectrical parameteres of heterojunctions c-Si/PS/CdS/$Zn_{0.6}Cd_{0.4}O$ with PS1, PS2 and PS3.

Porous silicon	U_{oc} (mV)	J_{sc} (mA/cm^2)	FF	η, %
PS1 (*samples with ZnCdO*)	543	14.6	0.54	4.28
PS2 (*samples without ZnCdO*)	557	21.3	0.65	7.71
PS2 (*samples with ZnCdO*)	602	23.8	0.69	9.89
PS3 (*samples with ZnCdO*)	592	19.8	0.61	7.15

It is established that the photosensitivity in this spectral region and generally in all spectral region can be controlled by selecting pores size of PS. Spectral dependences of the photocurrent in structures *c*-Si/PS/CdS/$Zn_{0.6}Cd_{0.4}O$ with PS1, PS2 and PS3 are shown in Fig. 2. As seen, a little increase of pores size leads to sharp increase of photosensitivity in all spectral regions. It is assumed that this is due to light absorption in porous silicon. With increasing pores size until 10 nm, shift of peak at 510 nm to the short wavelength region of spectrum is observed, which associated by us with the nano-structural properties of CdS films [10], i.e. band gap increasing with decrease of crystallite sizes in films. However, an increase of the optical path of light in nano-structured films leads to increase of degree of the light absorption, therefore, heterojunctions with PS2, shows greater efficiency compared heterojunctions with PS1 and PS3 (table 2).

4. Conclusion

Solar cells based on *c*-Si/PS/CdS/$Zn_xCd_{1-x}O$ heterostructures are created by depositing CdS films with thickness of on *c*-Si/PS substrates by the method of ED. PS layers with different pores size and thickness were fabricated on p-type *c*-Si wafers using electrochemical etching. The window layers of $Zn_xCd_{1-x}O$ with different Zn content is deposited onto CdS buffer layers also by ED. SEM and AFM images show that the morphological properties of CdS and $Zn_xCd_{1-x}O$ films is defined by pores size of PS. It is established that the photoelectrical parameters (U_{oc}, J_{sc}, FF and η) of solar cells can be regulated by a selecting of pores size of PS and Zn content in $Zn_xCd_{1-x}O$ films. The size of pores (10 nm) and Zn content (x=0.6) are defined, which provides the maximum efficiency (9.9 %) of solar cells.

5. References

1. Y. Kayanuma, Phys. Rev. B, **38**, 9797 (1988).
2. P. Vitanov, M. Kamenova, N. Tyutyundzhiev, M. Delibasheva, E. Goranova and M. Peneva, Thin Solid Films, **297**, 299 (1997).
3. L. Santinacci, A.-M. Gonçalves, N. Simon and A. Etcheberry, Electrochim. Acta, **56**, 878(2010).
4. V. Lehmann, J. Electrochem. Soc., **140**, 2836 (1993).
5. O. Bisi, S. Ossicini, L. Pavesi, Surface Science Reports, **38**, 1 (2000).
6. D. Oha, T.W. Kim, W.J.Chob, J. Ceram. Process. Res., **9**, 57 (2008).
7. F. Ruske, C. Jacobs, V. Sittinger, B. Szyszka, W. Werner, Thin Solid Films, **515**, 8695 (2007).
8. Ya. Alivov, J. E. Van Nostrand, D.C. Look, M.V. Chukichev, Appl. Phys. Lett., **83**, 2943 (2003).
9. G.V. Lashkarev, V.A. Karpyna, V.I. Lazorenko, A.I. Ievtushenko, I.I. Shtepliuk, V. Khranovskyy, Low Temp. Phys., **37**, 289 (2011).
10. N. Qutub, S. Sabir, Int. J. Nanosci. Nanotechnol. **8**, 111 (2012).

The influence of corona discharge on the electret properties and charge state of polymer nanocomposites based on isotactic polypropylene and titanium dioxide nanoparticles (TiO_2).

M.A.RAMAZANOV[1], F.V.HAJIYEVA[1], A.B.AHMADOVA[1], M.A.NURIYEV[2], A.M.RAHIMLI[1]

[1] *Baku State University, AZ 1148, ZakhidKhalilov Str. 23, Azerbaijan*
[2] *ANAS, Institute of Radiation Problems of Azerbaijan, AZ1143, B.Vahabzade Str., Azerbaijan*

Abstract
The paper reports of corona discharge effect on the electret properties and the charge state of nanocompositions based on isotactic polypropylene and titanium dioxide nanoparticles. It is shown that in the process of polarization under the action of a corona discharge, charges are accumulated at the interface, and these charges create a relatively large internal local field, and the polarization of the titania nanoparticle occurs in the field of this charge. Calculated the values of the local electric field that contribute to the polarization of the TiO_2 nanoparticles and found that the values of the internal local field correlate well with the values of the surface charge density measured by induction methods. The thickness of the interphase layer was calculated and it was found that with increasing titanium dioxide concentration in polypropylene, the thickness of the interphase layer increases and gets its maximum value at 1% TiO_2 concentration.
Keywords:Polypropylene, nanoparticles, nanocomposite, space charge, titanium oxide, corona discharge, thermally stimulated depolarization"

1. Introduction

Recently, metal and metal oxide filled polymer composites have proved to be a new group of structural materials optimally combining strength, electrical and thermal conductivity and other properties of metals with high chemical resistance, damping ability and technological function ability of polymers.
Recently, a great deal of attention has been attracted to polymer nanocomposites as electret materials that shown a positive effect. A promising direction is the use of nanocomposite electrets to create "smart" materials, which realise a rapid and reversible response to external influences of electric field at a relatively high temperature.
Electret properties of polymeric materials are widely used in electroacoustic devices, in air purifying devices (electret filters), in xerography (electrographic materials), etc. The main characteristics of the electret material are the magnitude of the electric charge and its stability. Polymers, as the main material for creating electrets, in many cases do not possess the necessary properties necessary for their practical application. At the same time, developing of technologies requires materials with new properties. Therefore, to obtain electret materials with given properties, it is expedient to use compositions consisting of a polymeric binder and various fillers. When polymers are filled with dispersed fillers, new structural elements appear in composite materials capable of serving as charge carriers, which causes a change in the electret characteristics of dielectrics [1-3].

In this paper, was studied the effect of corona discharge on the electret properties and the charge state of polymer nanocomposites based on PP+TiO_2.

2. The experimental part

2.1 Synthesis of nanocomposites.

The isotactic polypropylene powder (PP brand Sigma Aldrich Pcode 1001326963) was used as the polymer matrix; nanoparticle of titanium oxide as a filler. Polymer nanocomposites PP+TiO_2were prepared as follows: powders of isotactic polypropylene at a temperature of 120 C were dissolved in an organic solvent-toluene. Then, nanopowdersTiO_2 was added to the initial liquid polymer system without cooling the polymer solution at a temperature of 393 K. The mixture was transferred to a Petri dish and dried in a vacuum cabinet during the day. The preparation of films of nanocomposite samples is carried out by hot pressing at a melting point of polypropylene and a pressure of 15 MPa for 10 minutes, followed by cooling under pressure to room temperature. The thickness of the films was varied within 100 μm.

2.2 Polarization technique for polymeric nanocomposites.

Polarization of nanocomposites was carried out with the help of corona discharge. Corona discharge is realized with the help of needle-plane electrodes. The diameter of the needles is approximately 0.3 mm, and the distance between the needles and the samples of the film was 1 cm. The charging voltage $U_к$≈6-9 kV, the charging time - 5-10 min. The thickness of the samples is 100 μm. Before the beginning of the experiment, the samples were thoroughly degreased. After that, they were placed on a grounded electrode and charged at a voltage of 6 kV by a negative

corona through a system of metal needles vertically spaced 6×10-3 m from the surface of the sample.

2.3. SEM analysis

The distribution of titanium oxide nanoparticles along the depth of the polymer matrix was studied by scanning electron microscopy (SEM, Jeol JSM-767 F). The scanning was carried out in SEI mode at an accelerating voltage of 15 keV and a working distance of 4.5 mm. To eliminate the discharge, the surface of the polymer nanocomposites was covered with a 10 nm thick layer of platinum.

2.4. Method for recording thermally stimulated current.

The charge state and the activation energy of nanocomposite charges are studied by the method of thermally stimulated depolarization (TSD). The thermally stimulated current (TSC) was recorded in the temperature range 293-523 K under the condition of linear heating growth with the speed $\beta = 4$K/min.

3. Results and discussion:

In Fig.1 shows SEM images of polymer nanocomposites based on PP+TiO_2. As can be seen from Fig. 1, for small amounts of nanoparticles, the distribution of titanium nanoparticle titanium in the volume of the polymer matrix is small, and with an increase in the content, the distribution of nanoparticles is more uniform. It was also found that with increasing nanoparticle content, nanoparticle sizes increase insignificantly. Thus, with a 5%TiO_2 content in the polymer, the nanoparticle size is 10-30 nm, and at 10% -50-60 nm. Figure 2shows the EDS spectrum for nanocomposites based on PP+TiO_2. As can be seen from Figure 2, the nanocomposite consists of pure titanium dioxide. The platinum element appears on the EDS spectrum due to depositing a thin layer of platinum on the surface of the PP+TiO_2 film to eliminate the charging of

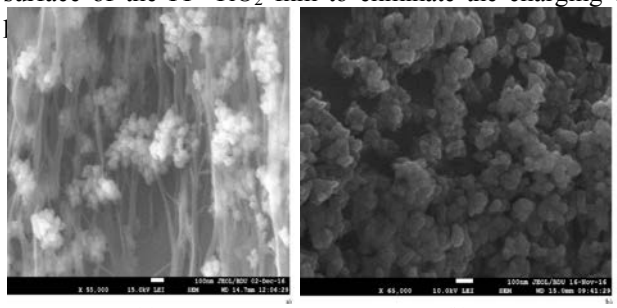

(a) (b)

Fig.1 SEMimage of nanocompositePP+TiO_2: a) PP+5%TiO_2; b) PP+10%TiO_2

Figure 3 shows the dependence of the surface density of electret charges (σ) on the storage time (τ) of polypropylene and polymer nanocomposites PP+TiO_2 at various TiO_2 contents in PP. It is seen from Fig. 3 that with increasing TiO_2content in PP, the surface density of electret charges and the storage time, measured by the induction method, reach a maximum value at1% of the volume content of TiO_2. It can be seen that the presence of titanium dioxide has a significant effect on the manifestation of the electret effect in polypropylene. The charge decreases first rapidly, then more slowly. For practical purposes, a long duration of charge conservation is probably desirable. The first studies of the dependence of σ_{eff} on time showed that σ_{eff} decreases gradually, the nature of the decreasing of$\sigma_{eff}$is different and depends on the concentration of titanium dioxide.

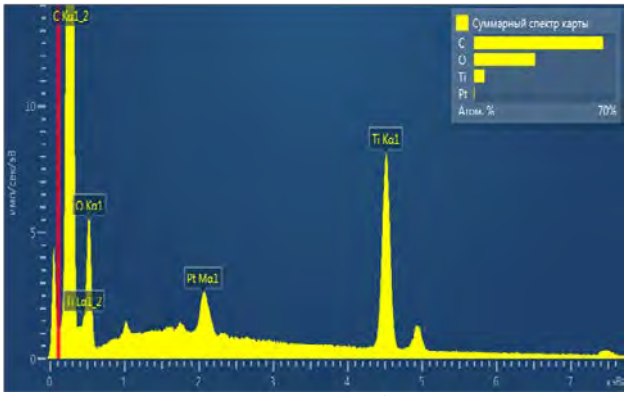

Fig.2. Energy dispersive spectra (EDS) of nanocompositePP+TiO_2.

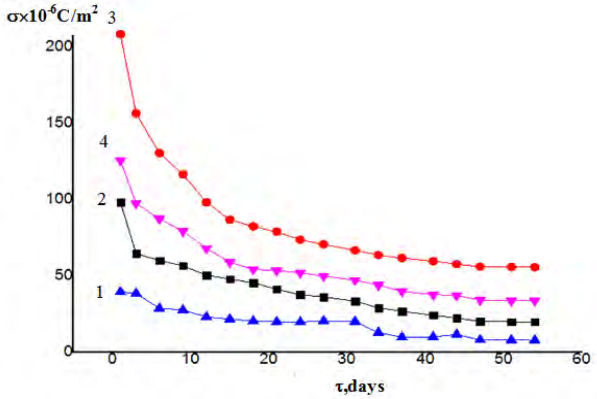

Fig.3. The dependence of the surface density of electret charges (σ) on the storage time (τ_{xp}) of polypropylene and polymer nanocomposites:1.PP; 2.PP+0,5%TiO_2; 3.PP+1%TiO_2; 4.PP+3%TiO_2;

Figure 4 shows the dependence of the surface density of electret charges (σ) on the volume content of titanium dioxide. It has been established that the value of the surface density of electret charges (σ) of polymer nanocomposites based on PP+TiO_2, depending on the concentration of titanium dioxide, varies with the extremum, i.e. increases at 1%and then decreases.

Under polarization under corona discharge conditions, in the composites due to migration polarization, charges are accumulated at the interface between phases and due to charge carrier injection followed by capture in deeper polymer traps that create a sufficiently large internal local field and in the field of these charges occurs the polarization of the titania nanoparticles.

To predict the stability of electret charges [4-6] and also to study the mechanism of their formation, we used the method of thermally stimulated depolarization. The values of the accumulated charges at the interface between the nanocomposite components are studied(Fig5).

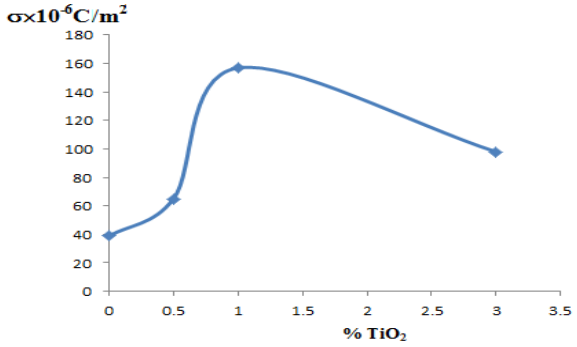

Fig.4. Dependence of the surface density of electret charges σ on the volume content of titanium oxide.

The activation energy of the maximum was calculated from the TSD curves by the method of the temperature position of the current maximums of the TSD:

$$E = k\frac{T_m(T_m - \Delta T)}{\Delta T}$$

Where T_m- is the temperature of the maximum, k -is the Boltzmann coefficient. The value of the accumulated charge during the polarization of the samples is calculated from the area of the TSD.

It can be seen from the TSD curves (Fig. 5) that for the PP+0.5%TiO_2 nanocomposite there is mainly 1 maximum at 413 K; For the nanocomposite PP+1%TiO_2 and PP+3%TiO_2, there are 2 main peaks at 373 K and 436 K, the sign of these charges for the given nanocomposite being the same, i.e. there is a polarization in the polypropylene and in the interphase layer. The maximum at 370 K is connected with traps in polypropylene, and the maximum at temperature is associated with charges in the interphase layer. The number of integral charges is calculated from the TSD curves. It is found that the value of the integral charges varies with the extremum depending on the concentration, i.e. the charge value gets its maximum value at 1% concentration of TiO_2 nanoparticles.

From the TSD curves, the activation energy of the charges of 436K maximum was calculated for the nanocomposite PP+0.5%TiO_2, PP+1%TiO_2 and PP+3%TiO_2. Table 1 shows the values of the surface density of the electret charge, the intensity of the internal field of the injected charges, the activation energy and the thickness of the interphase layer for polymer nanocomposites based on PP+TiO_2.

The thickness of the interface layer for PP+TiO_2nanocomposites was calculated using the formula

$$\delta = \frac{2ne^2}{\varepsilon_1\varepsilon_2 kT}$$

Where ε_1 and ε_2 are the permittivities of the polymer and filler, n is the concentration of charge carriers, and e is the electron charge.

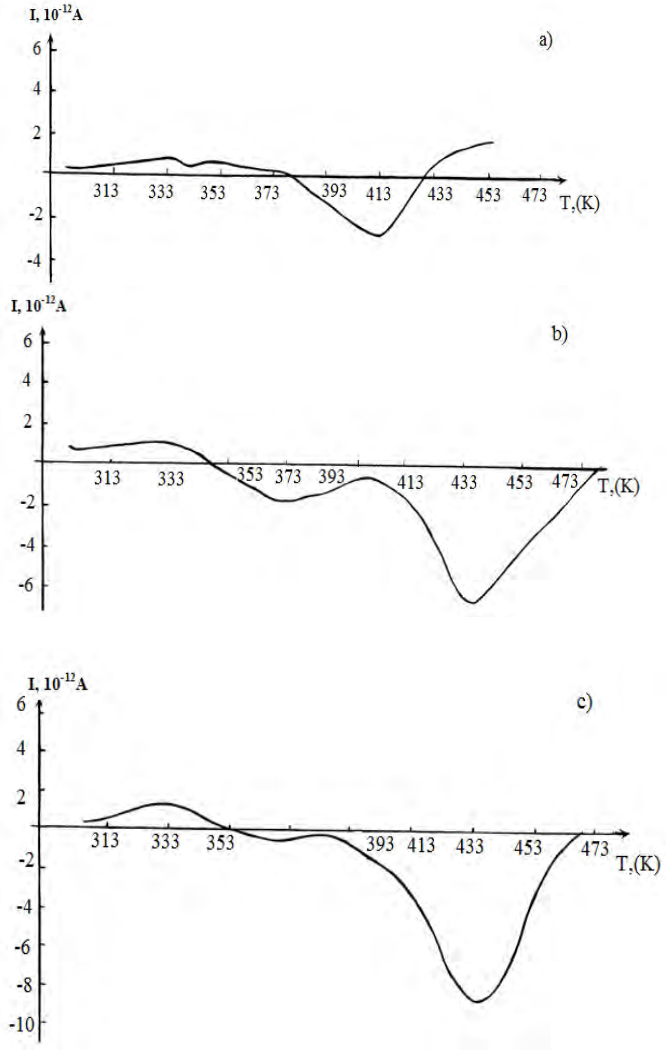

Fig.5. The TSD curves of the nanocomposite of PP+TiO_2 at concentrations of 0.5% (a), 1% (b) and 3% (c) after corona discharge polarization at T = 313K, for 4 min.

It is shown that with increasing volume content of titanium dioxide in polypropylene, the thickness of the interphase layer increases and gets its maximum value at concentrations of 1% TiO_2.

From the area of the TSD, the value of the accumulated charge is calculated during the polarization of the samples. It can be seen from the table 1 that in the process of polarization a sufficiently large amount of electric charges accumulates at the interface between the components of the nanocomposite PP+TiO2. The values of the intensity of the local electric field that contribute to the polarization of TiO_2nanoparticles are calculated. So the intensity of the internal local field of the injected charges forPP +0.5% TiO_2 is 5.2 KV/m, for the nanocomposite based on

PP+1%TiO_2 is 30.38 KV/m, and for the PP+3%TiO_2 nanocomposite is 24,05 KV/m [6,7].

Table 1. The value of the surface charge density accumulated at the interface between the components of the nanocomposites, the intensity of the internal field of the injected charges, and the energy of activation

Nanocomposite content	Number of volume charges 10^{-11}C	Surface density of volume charges 10^{-6}C/m^2
PP+0,5%TiO_2	58	4,146
PP+1% TiO_2	339,2	24,2
PP+3% TiO_2	268	19,16
Intensity of the internal field of the injected charges (KV/m)	Energy of activation (eV)	Thickness of interphase layer (nm)
5,205	1,51	0,0023
30,38	1,73	0.014
24,05	1,01	0,011

The photoluminescence spectra of nanocomposites based on PP+TiO_2 were also studied before and after corona discharge polarization (Fig. 6). It was found that the intensity of photoluminescence increases after polarization. The luminescence spectra exhibit peaks at wavelengths of 486 nm, 528 nm, 545 nm and 563 nm. It was determined that two peaks at 486 nm and 563 nm were luminescent peaks belonging to titanium oxide. At low volume contents of TiO_2 nanoparticles, the photoluminescence intensity is larger compared to the high content of nanoparticles in the polymer matrix.

This is explained by the fact that the specific surface area of the particles decreases with increasing size of the TiO_2 nanoparticles in the polymer, which in turn leads to the formation of a contacting surface of the nanoparticles with the polymer. Reducing the specific surface area of nanoparticles leads to a decrease in the interphase layer. It is also known that a decrease in the specific surface leads to a decrease in the interfacial interaction between the components of nanocomposites. It is also assumed that with a decrease in the specific surface area of TiO_2, the radiating surfaces decrease [8].

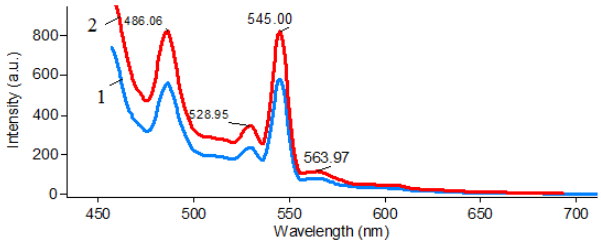

Fig. 6.Luminescence spectra of nanocomposite PP+5%TiO_2 up to (1) and after (2) polarization under the influence of corona discharge.

It is found that due to the boundary charges, a sufficiently high internal local field is created in nanocomposites based on PP+TiO_2 (Table 1), under the action of this field additional luminescent centers are excited in the nanocomposites, and as a result, the intensity of the luminescence increases. Under the local action of this field, additional luminescent centers of titanium oxide are excited in polymer nanocomposites. As a result, the intensity of the luminescence of nanocomposites based on PP+TiO_2 increases after polarization under the action of a corona discharge [9-10].

4. Conclusion:

It is shown that in the process of polarization under the action of a corona discharge, charges accumulate at the interface between phases for nanocomposites based on PP+TiO_2, and these charges create a sufficiently large internal local field, and in the field of this charge, the titanium dioxide nanoparticle polarizes. Was calculated the values of the local electrical field value that contribute to the polarization of TiO_2nanoparticles. It is found that the values of internal local fields are well correlated with the values of the surface charge density,which were measured by induction methods. The energy activation of the maximum responsible for the boundary charge varies in the range 1,01-1,73eV. The thickness of the interphase layer was calculated, and was found that with an increase of the concentration of titanium dioxide in polypropylene, the thickness of the interphase layer increases and gets its maximum value at 1% TiO_2concentrations, and then decreases. Has been found that additional luminescent centers are excited in nanocomposites due to frontier charges, and as a result, the intensity of luminescence increases.

References|

[1] G. Sesler“Electrets.” Moscow World, (1983)
[2] G.A.Luschekin“Polymer electrets.”M., (1984)
[3] O.A.Myazdrakov,V.Y.Manoylov“Electrets”, Qosenergy(1960)
[4] M.F.Galihanov,D.A.Eremeyev,R.Y.Deberdeev, Mater.Sci. **9**, 24(2003).
[5] Y.A.Gorokhovatsky, G.A.Bordovskiy“Spectroscopy of semiconductors and dialect rics”,Nauka Moscow (1991)
[6] M.A.Ramazanov,F.V.Hajiyeva,A.M.MaharramovJ.Ferro electrics**493**(1),103(2016)
[7] M. A. Ramazanov, A. S. J. Optoelectronics and Advanced Materials – Rapid Communications **7**(9-10), 789(2013)
[8] A.D.Pomogaylo, A.S.Rozenberg, I.E.Uflyand, “Metal nanoparticles in polymers”,Chemistry(2000)
[9] M.A.Ramazanov,A.S.Huseynova, F.V.Hajiyeva Journal of Ovonic Research , **11**(1), 35(2015)
[10] M.A.Ramazanov,F.V.Hajiyeva,A.M.Mahar-ramov,U.A.HasanovaJ.Ferroelectrics**507**(1),121(2017)

New silicon photomultiplier with fast output

N.N.HEYDAROV[a*], R.S.MADATOV[a], Z.Y.SADYGOV[a,b], A.Z.SADIGOV[b], F.I.AHMADOV[a,b], S.S.SULEYMANOV[a,b], R.V.VALIYEV[a], M.S.NAZAROV[a].

a-National Academy of Science of Azerbaijan -AD and IRP
b-National Nuclear Research Center, e-mail: **namiq_1991@inbox.ru**

Abstract

In this work presented a novel photomultiplier based on silicon- Micropixel Avalanche Phototransistor (MAPT) for PET scanners. MAPT include matrix of micropixels with individual quenching resistors and matrix of microtransistors with individual ballast resistors. The device has two independent signal outputs pixel output and fast output. The all micropixels connect to the common bus throat quenching resistors, and microtransistor connect to the another bus throat ballast resistors. The specific capacitance of the device decreased of 50 times when the signal are taken from fast output, that is why the response time of photodiode is rapidly increased.

Keywords
Positron emission tomography, MAPD, photodetector, MAPT

1. Introduction

Positron emission tomography (PET) - a new diagnostic technique that allows doctors to evaluate the performance of the body's tissues and organs. As against other instrumental methods of investigation, the main task of PET - to obtain a color image of chemical activity of the processes occurring in the body of the patient.The chemical processes during disease are changing and accordingly changing their color and intensity to PET, thus PET determine the illnesses on the initial stage when no structural change has not happened yet. In most cases the PET used in the diagnosis of diseases of the nervous system, heart and in oncology. The method is based on the usage of radioactive isotopes in minimal and almost harmless amounts.

Positron emission tomography is a new generation of scanners whichhave to meet high requirements such as high energy and timing resolution. They are continuously improved, due to the need to improve the image quality and shorter scanning time. Modern scanners are limited by standard photomultipliers. It is known that silicon photodiodes have an advantages such as the low operating voltage, fast response time and small size which are the key factors for PET scanners.

Thedifferent types of micropixel avalanche photodiodes (MAPD), can effectively detect a low photon flux up to single photons. However, the optical crosstalk and after pulsing effect which are manifested in the high avalanche amplifications($\approx 10^6$) and also the high specific capacitance and low response time with large sensitive area are significantly limit widespread use of MAPD with surface pixel structures. All these disadvantages significantly worsen the amplitude and time resolution of the device.

2. Experimental performance

Within the work, designed and realized a new avalanche photodetector, in which solved the MAPD's problems mentioned above. The main idea of improving these parameters of photodetector is a reducing avalanche gain and adding the amplifying element in each pixel to obtain a sufficiently high gain. So, the individual amplifying element is a bipolar microtransistor which base is connected to the pixel (Figure 1).

The microtransistor, for example n-p-n-type, may be formed directly over a small part of the area of the pixel with p-type conductivity which is made on a substrate with n-type conductivity. For instance, the microtransistor of size 5 um * 5 um can take no more than 1% of the micropixel of size 50 um * 50 um.

The new designed photodetector called Micropixel Avalanche Phototransistor (MAPT). It includes a matrix of micropixels with individual quenching resistors and matrix of microtransistors with individual ballast resistors. The device has two independent outputs: pixel output, as same asMAPD and fast output. All micropixels connected to the common metal bus by their quenching resistors, and also all microtransistors connected to the another bus by their ballast resistors. The region of avalanche amplification is spatially separated from the region of transistor amplification in order to prevent positive feedback. The fact is that when electrons injected from the emitter to avalanche region, their avalanche amplification will occur with the creation of holes that will gather at the emitter, causing a new injection of electrons. This process leads to the generation of sinusoidal oscillations, not associated with the detection of light signals.

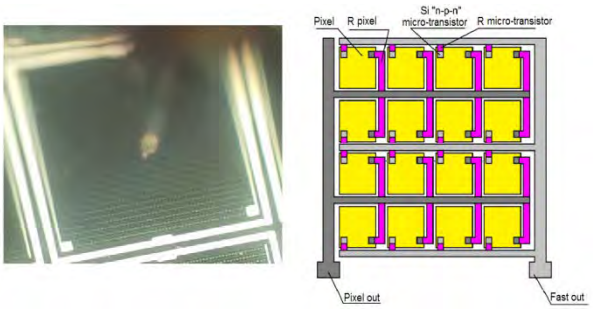

Figure 1. The photography of the photodiode on the left, the schematically view of the photodiode on the right.

The principles of operation of the MAPT are based on the specifics of the operation of the MAPD pixel in the overvoltage mode (in Geiger mode). An avalanche process in a pixel lead to increasing the voltage greater than 0.8V in the transistor base, which is sufficient to completely open the junction of the emitter-base of the microtransistor, and as a result, a large current flowing through the electric circuit of the microtransistor which isonly limited by its ballast resistor. For example, if the overvoltage is 1V, the maximum potential changing at the pixel is 2V[1;2]. The results of calculation in this case are shown in Figure 2. It seems that photocurrent J_p in the pixel circuit outstrip the J_{tr}in transistor circuit, due to the

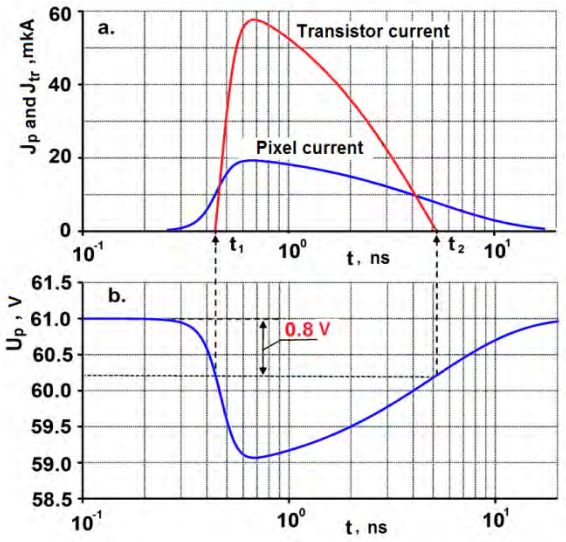

Figure 2. The dependence of single-electron photocurrents (a) and the pixel potential (b) of the MAPT from time.

beginning and the end of the latter is determined by the potential at the pixel. The microtransistor opens at that time t_t, when the avalanche process succeeds in discharging the pixel by the value of $\Delta U_{dp}=U_d-U_p(t)=0{,}8V$.. In this way, the photocurrent $J_p$in the pixel circuit and the current J_{tr} in the microtransistor circuit can be described by fallowing expressions:

$$J_p=\Delta U_{dp}/R_q \ , \quad J_{tr}=(\Delta U_{dp}-0.8)/R_{tr}$$

where $\Delta U_{dp}=U_d-U_p(t)$ – potential change in the pixel, U_d - external voltage applied to MAPT, $U_p(t)$–current potential at the pixel.

In the scientific literature are known the methods for taking a fast signal from the pixels of MAPD (or SiPM) with an independent electrode [3, 4, 5]. In our case, the device has a second independent bus for getting the signal connected to the pixels through individual resistors-"pixel out". Figure 3 shows the electrical equivalent circuit of MAPT.

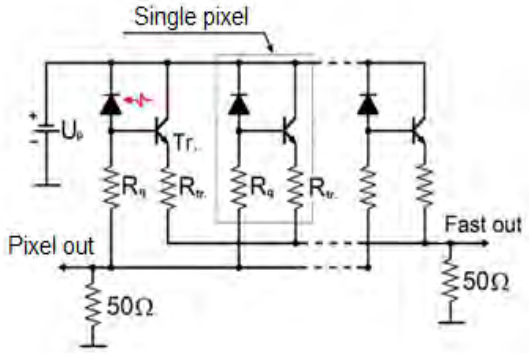

Figure 3. The electrical equivalent circuit of MAPT.

Acknowledgments

This work was supported by the Science Development Foundation under the President of the Republic of Azerbaijan Grant No.**EIF-KETPL-2-2015-1(25)-56/03/1**.

Reference

[1]- A.Sadigov, at all. 'An Iterative Model of Performance of Micropixel Avalanche Photodiodes // International Journal of Advanced Research in Physical Science (IJARPS) Volume 3, Issue 2, February 2016, PP 9-18: https://www.arcjournals.org/pdfs/ijarps/v3-i2/3.pdf .

[2]- Z.Sadygov, at all. Model of single-electron performance of micro-pixel avalanche photo-diodes. http://arxiv.org/ftp/arxiv/papers/1410/1410.2619.pdf .

[3] A.Sadigov, Patent Russian, No №2086027,

[4]- N. Pavlov. Silicon photomultiplier and readout method. Patent US, No 20130099100 A1, published 09/21/2011.

[5]- Z. Ya. Sadygov, at all. Supersensitive avalanche silicon photodiode with surface transfer of charge carriers // Nucl. Instrum. and Methods, A504 (2003), 301-303.

Phase effects in ZnO/PM nanocomposite films, at second harmonic generation

[a]R.J. KASUMOVA, [a]H.M. MAMEDOV, [a]SH.A.SHAMILOVA, [b]G.A.SAFAROVA,[a]N.V. KERIMOVA
[a]*BAKU STATE UNIVERSITY,* [b]*INSTITUTE FOR PHYSICAL PROBLEMS*
renajkasumova@gmail.com, mhhuseyng@gmail.com, shahla_shamilova@mail.ru, safarovagulnara@rambler.ru

ABSTRACT

In this paper analysis of constant-intensity approximation of nonlinear interaction of the second harmonic generation in ZnO/PMMA (polymer matrix)nanocomposite films for different concentrations of ZnO were carried out with regard to the losses and phase changes of all the interacting waves. The investigated samples were manufactured on the basis of ZnO nanoparticles embedded into polymeric matrix by the method of electrochemical deposition. The main goal of work is the exploration of the ZnO morphology and parameters of the second order susceptibilities. It is verified that the surface effects in ZnO/PMMA structures will give a larger contribution than the volume effects.

Keywords: Electrochemical deposition, generation

1. Introduction

The modern development of the microelectronics, quantum electronics and nonlinear optics requires development of new perspective nonlinear materials. As is known, it is possible to create the new sources of coherent optical radiation by the methods of nonlinear optics using crystals, which is distinguished among other transparent crystals in this region of spectrum, for its extremely high nonlinearity.

Harmonic generation is interesting for solving a number of the applied issues in UV and the extreme UV (EUV) regions of spectrum, and in obtaining the photons of high energy.

Simultaneous calculation of phase change and losses of interacting waves ispossible to make in the constant-intensity approximation (CIA)[1,2] with regard to the reverse reaction of the excited wave on pump wave. Besides, in this approximation it is found that coherent length depends on such parameters of a task as basic radiation intensity and losses in the medium in addition to mismatch of interacting waves.

In this work there are carried out the analysis of CIA of nonlinear interaction of second harmonic generation in ZnO/PMMAnanocomposite filmsfor different concentrations of ZnOwith regard to the losses and phase changes of all the interacting waves. It is verified that the surface effects in ZnO/PMMA structures will give a larger contribution than the volume effects.The factors restricting the efficiency of the process of frequency conversion have been analyzed.

2. Experiment

Polyvinylchloride(PVC) gel (dissolved in tetrahydrofuran) with thickness of 80 nm were deposited onto the surface of glass/SnO_2 substrates by centrifugation. After drying under vacuum at room temperature, the substrates were used as a cathode for deposition of ZnO.The electrochemical deposition has been performed with a three electrode configuration: graphite as anode, $Ag/AgCl_3$ electrode as reference electrode and glass/SnO_2/PVC as cathode. Total area of working electrodes (cathode) was 1×1 cm^2. At electro deposition we used aqueous solution of $Zn(NO_3)_2$. The electro deposition was carried out potentiostaticallyat -0.9, -1.2 V, -1.28 V and -1.35 V vs. Ag/AgCl for 1-2 hour.

The parameters of the task are chosen according to the conditions of existing experiments for the given ZnO structure [3, 4, 5-7]. As a fundamental beam, there are considered the output beam of a Q-switched Nd doped yttrium aluminum garnet laser generating at λ =1064 nm with 16 ps pulse duration and 10 Hz repetition rate. The fundamental beam has the s-polarization. The absolute value of the effective quadratic susceptibility for this nanocomposite films is experimentally measured in the work [4]. In bulk nonlinear materials, increasing of ZnO concentration leads to the growth of a quadratic susceptibility. In case of the nanocomposite films the opposite effect takes place.The surface effects in the films are dominant when compared to volume effects because of the size of the characteristic materials which is being reduced to nanoscale level [4]. At the ZnO concentration of 5% wt. and less, these values of the second order susceptibility $\chi_{1,2eff}$ lie in the range from 4 to 6 pm/V and are higher than analogical value for ZnO bulk which is about 2.5 pm/V. The thickness of the investigated samples is changed in the diapason $1 \div 14$ mcm [4, 8]. Experimental value of pump intensity was changed in the range $5 \div 23$ GW/cm^2 [4]. In work [5], the value for the quadratic susceptibility of ZnO/PMMA film have been obtained and is equal up to 30 pm/V, in [6] the maximal value of the second order susceptibility was found to be approximately equal to 83 pm/V.

In References[7] and [9] ,Sellmeier's coefficients are experimentally established for ZnO. Using these values of coefficients, we'll calculate the ordinary and extraordinary refractive indices in case of second harmonic generation.

Because of lack of experimentally measured value of Sellmeier's coefficients for ZnO/PMMA at different weight concentrations (of ZnOnanocrystalls inside a polymeric matrix), the same order of coefficients was supposed for the considered concentrations.

3. Theory

The efficiency $\eta_2(\ell)$ for conversion of power from the ω_1 wave to the ω_2 wave can be defined by $\eta_2(\ell) = I_2(\ell) / I_{10}$ and by neglecting reflections, we see that for the values given above, conversion efficiency is $(\delta_2 = 2\delta_1)$

$$\eta_2(\ell) = \gamma_2^2 I_{10} \ell^2 \left(t_{af}^{1s}\right)^2 \left(t_{fs}^{2p}\right)^2 \left(t_{sa}^{2p}\right)^2 \sin c^2 \lambda' \ell \exp(-2\delta_2 \ell)$$

1)where

$$\lambda'^2 = 2\Gamma^2 + \Delta^2 / 4$$

t_{af}^{1s} is the Fresneltransmission coefficient (air-film system) for second harmonic (2p) beam [4].

To study the ways of increasing frequency conversion efficiency in ZnO structure of laser radiation, we'll make the numerous calculation of the analytical expression for conversion efficiency (1) received in CIA.

Under considered case, the nonlinear material is a crystalline particle inside the polymeric film. For this case, in [4], the notion of equivalent thickness of nonlinear medium inside PMMA is being used. Here, $d_{ZnO}^{equivalent}$ shows the thickness which could have ZnOnanocrystals without PMMA as host

$$d_{ZnO}^{equivalent} = \frac{\%wt_{ZnO}}{100 - \%wt_{ZnO}} \frac{\rho_{PMMA}}{\rho_{ZnO}} \ell_{PMMA+ZnO} \qquad (2)$$

where ρ_{PMMA}, ρ_{ZnO} are densities of PMMA and ZnO, respectively, $\%wt_{ZnO}$ is the weight concentration of ZnOnanocrystals inside a polymeric matrix and $\ell_{PMMA+ZnO}$ is the thickness of ZnO/PMMA nanocomposite film.

In Equation (1) instead of ordinary thickness we used introduced equivalent thickness, according to [4]. As a result, Equation (1) can be written as

$$\eta_2(\ell eff) = \gamma_2^2 I_{10} \ell_{eff}^2 \left(t_{af}^{1s}\right)^2 \left(t_{fs}^{2p}\right)^2 \left(t_{sa}^{2p}\right)^2 \cdot \sin c^2 \lambda' \ell_{eff} \exp(-2\delta_2 \ell_{eff}) \qquad (3)$$

where

$$\ell_{eff} = d_{ZnO}^{eqiuvalent} / \cos\theta$$

$$\frac{\Delta'}{2} = \frac{2\pi}{\lambda_1} \ell (n_{2\omega} \cos\theta_{2\omega} - n_{\omega} \cos\theta_{\omega})$$

Here$\theta$is the incidence angle of laser beam, $\theta_{\omega}, \theta_{2\omega}$ are the refractive angles for fundamental and second harmonic waves, $n_{2\omega}, n_{\omega}$ are the refractive indices of the nonlinear material at frequencies 2ω and ω. The refractive indices of ZnO have been evaluated according to Sellmeier model [9].

4. Results

Estimate the dependencies of the ratio I_2 / I_{10}^2 forZnO/PMMA 1 and ZnO/PMMA 2nanocomposite films on its ZnO weight concentrations calculated by authorsin CIA (dashed curves 1 and 3, correspondingly). Here,the analogical experimental results are given (solid curves 2 and 4) from [4](see Fig. 1). As is seen from comparison of thesecurves,the good agreement between experimental and theoretical results is observed(dashed and solids curves 1, 2).

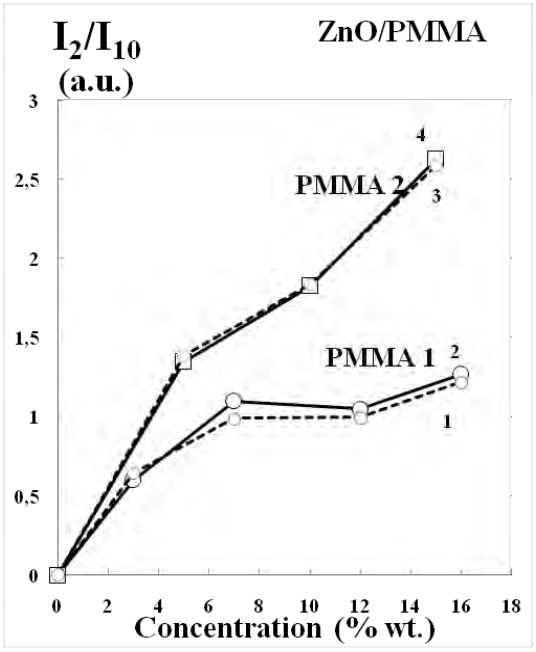

Figure1. Dependencies of the ratio I_2 / I_{10}^2 for ZnO/PMMA 1 and ZnO/PMMA 2 nanocomposite films on its ZnO weight concentrations calculated in the CIA (dashed curves 1 and 3, correspondingly). Experimental results are given (solid curves 2 and 4) from [4].The thickness of all films is equal to 1 mcm [4].

5. Conclusions

Thus, theoretical investigation of frequency conversion in ZnO/PMMA structures with account for phase effects allows one to reveal the ways of increasing conversion efficiency.The analytical method permits to estimate the expected conversion efficiency on different wavelengths of laser radiation.Thus, the numerical calculation of the efficacy obtained in CIA confirms the next fact that at higher concentrations of ZnO the films generate stronger second harmonic signal due to the larger interaction length of the nonlinear medium.

The results of carried out researches will be useful at elaborations of the modern devices of the quantum electronics and in the nanoscale optoelectronic circuitry. Method of analysis of second harmonic generation in ZnO/PMMA structures, developed in the present work, may be used for investigation ofother nanocomposite films.

6. References

1. Z.H. Tagiev, and A.S. Chirkin, Zh. Eksp. Teor. Fiz., **73** (1977) 1271-1282 [Sov. Phys. JETP,**46** (1977) 669-680].

2. Z.H. Tagiev, R.J. Kasumova, R.A. Salmanova, N.V. Kerimova, J. Opt. B: Quantum Semiclas. Opt. **3** (2001) 84-87.

3. J. Ebothe, R. Miedzinski, V. Kapustianyk, B. Turko, W. Gruhn, I.V. Kityk. XIII International Seminar on Physics and Chemistry of Solids. J. of Physics: Conf. Series **79** (2007) 012001-1-8.

4. B. Kulyk, B. Sahraoui, O.Krupka, V. Kapustianyk, V. Rudyk, E. Berdowska, S. Tkaczyk, I. Kityk. J. of Appl. Phys., 106, 093102-1-093102-6, 2009.

5. U. Neuman, R. Grunvald, U. Griebner, G. Steinmeyer, M. Scmidbauer, W. Seeber.,Appl. Phys. Letters 2005 **87** 171108-1-1711108-3.

6. X.Q. Zhang, Z.K. Tang, M. Kawasaki, A. Ohtomo, H. KoinumaJ. Phys.: Condens. Matter, 2003 **15** 5191-5196.

7. Zhong-Hong Dai, Rong-Jun Zhang, Jie Shao, Yi-Ming Chen, Yu-Xiang Zheng, Jia-Da Wu, and Liang-Yao Chen. J. of the Korean Physical Society, 2009, **55** No. 3, 1227-1232.

8. S.K. Das, M. Bock, C. O'Neill, R. Grunwald, K.M. Lee, H.W. Lee, S. Lee, F.Rotermund. Appl. Phys. Lett., 93, 181112-1-181112-3, 2008.

9. C.W. Teng, J.F. Muth, Ü. Özgür, M.J. Bergmann, H.O. Everit, A.K. Sharma, C. Jin, J. Narayan.. Applied Physics Letters, 2000, **76** No. 8, 979-981;

Dynamics of heavy metals in water and sediments in the contract area «Gurgan» of Azerbaijan sector of the Caspian Sea

S.Z. SALAHOVA[1], SH.A. TOPCHIYEVA[1], M.A. RAMAZANOV[2]
[1]*ANAS, Institute of Zoology of Azerbaijan, AZ 1073, A.Abbaszadestr.,Azerbaijan*
[2]*Baku State University, AZ 1148, Z. Xalilov str.23, Azerbaijan, e-mail: salahova.samira@gmail.com*

Abstract
Pollution of aquatic ecosystems by heavy metals is one of the global problems of modernity. For the first time for the conditions of the this region carried out comprehensive studies on the study of content migration – Fe, Ni, Hg, As, Cd, Cu, Pb, Zn in aquatic habitats that defines the novelty of research. Total index of water contamination with heavy metals create the decreasing row Fe> Zn> Cu> As> Ni> Pb> Cd, and in bottom sediments TM compounds decreases in the row Fe> Zn> Ni> Cu> Pb> As> Cd> Hg. Have been established that, the major pollutants in water of the Caspian Sea were zinc and copper. Their concentrations are constantly exceed the MPC of fish farm (zinc-0,01-0,05 mg/l, copper-0,001 mg/l), whereas in bottom sediments the excess of MPC was not observed.
Key words: heavy metals, maximum permissible concentration, sediment, total pollution index, Caspian Sea.

1. Introduction

Recently, due to pollution of the environment with products of technogenesis, heavy metals (TM) have become the object of close attention of environmental monitoring, compounds that do not undergo destruction in natural waters, but only change forms of existence and take a special position among the priority pollutants of the ecosystems of the Caspian Sea [1]. This leads to alter the migratory ability of heavy metals, toxic properties and accessibility for hydrobionts and consequently, their ecological role in water bodies. It is known that in certain concentrations they not only affect the quality of water, but also become toxic for all of the fauna and accumulate in them [2]. Heavy metals, falling into the water with the various ways, as a result of hydrolysis, sorption, desorption, complexation, precipitation and bioabsorption, pass from the aqueous phase to the bottom sediments, precipitate in the form of sparingly soluble compounds and again pass into the aqueous solution [3]. Heavy metals entering the bottom sediments as a result of the processes of sorption and sedimentation are not derived from the biogeochemical cycle of migration: only when change the physicochemical conditions, especially the redox and acid-alkaline conditions, and the vital activity of benthos, heavy metals can return to the water mass. For the Caspian Sea is particularly acute the problem of identifying the background level of the concentrations of individual pollutants in ecosystem components and assessing their impact on hydrobionts [4].
The goal of this work was obtain quantitative data for estimating the current background level of concentrations of heavy metals in the Caspian Sea.

2. The experimental part

All of the research materials were collected from 2012 through 2014 in the oil and gas field of "Gurgan" (Fig .1).

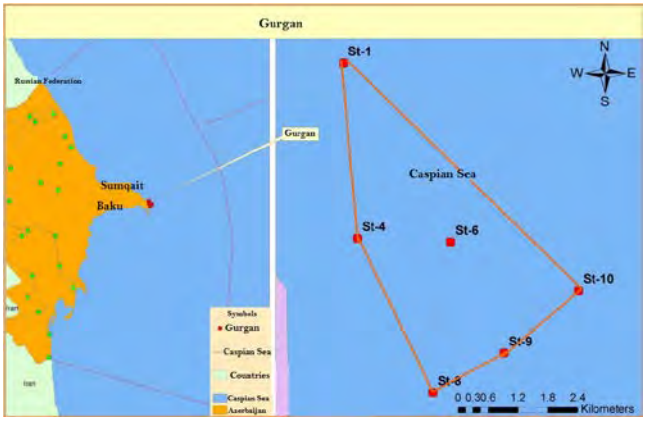

Fig.1. Scheme of distribution sampling stations in the studied fields.

Water samples were collected by using a sampler «Niskin» volume of 10 liters and for a full analysis samples taken with the two-time repetition. For sediment analysis were used samplers «Van–Veen» with an area of 0,1 m^2 and for precise of analysis samples taken with the three-fold repetition. Water samples oxidized HNO3 (k) (65%), followed by five-fold dilution. If the water polluted by petroleum product, samples were initially processed in a microwave oven firm Milestone START D (Microwave Digestion System, Italy) according to the procedure DG-EN-45 «Soil and crude oil» and DG-EN-24. Certain of the sediments samples have been dried in the oven at 35-40 °C, followed by pulverization and homogenization. According to the procedure of DG-EN-45 «Soil and crude oil» were taken 0,2 ÷ 0,25 g of samples and add 10 ml of 65% HNO3, 1ml of 1% HCl, 1 ml of 30% H2O2 reagents, according to the method DG-EN- 24 samples were taken 0.5 g with 10 ml of 65% HNO3 digestion process carried out in a microwave oven, wherein the physical parameters (temperature, time and power) are presented in Table 1. Qualitative and quantitative content of metals held by approved methods (EPA 6020 A and EPA 3051 «Inductively Coupled Plasma-Mass Spectrometry»). In the

investigated samples determination of metals produced within the limits of ppb.

Table 1.Physical properties of the oven of the company milestone start D

Step	Time	Temperature	Power
1	10 min	220 ° C	Up to 1000 Watts
2	20 min	220 ° C	Up to 1000 Watts

3. Results and discussions

During each season from 2012 to 2014, the works on a contract area of «Gurgan» held by approximately 15 - 17 stations. Samples were selected seasonally from the surface and near-bottom horizons and were analyzed approximately 50-60 samples of seawater and bottom sediments in one season. During the analyzes, we determined the content and distribution metal ions of Fe, Ni, Hg, As, Cd, Cu, Pb, Zn in water and bottom sediment on the contract area of the Caspian Sea. Tables 2-4 depicted the concentrations of metals Fe, Ni, Hg, As, Cd, Cu, Pb, Zn on the periods of studied.

Table 2.Concentration of heavy metals in the field of «Gurgan» (May2012, µg/l, M±m,p, %, n=7).

Station№	Depth (m).	Fe		Ni		Hg	As	
		E	C	E	C	E	E	C
1.	1,5	162 ± 5,58 *	146 ± 1,02	3,95 ± 0,31 *	2,91 ± 0,09	<0,1	9,0 ±5,8 **	3,0 ±2,9
	%	111		136			136	
6.	3	153,5 ± 2,95 *	145,3 ± 1,47	3,99 ± 0,37 *	3,027 ± 0,12	<0,1	3,51 ± 0,37 *	2,49 ± 0,17
	%	106		132			141	

Station№	Depth (m).	Cd		Cu		Pb		Zn	
		E	C	E	C	E		E	C
1.	1,5	0,35 ± 0,037 *	0,24 ± 0,021	3,08 ± 0,03 *	2,29 ± 0,01	4,55 ± 0,05 *	3,34 ± 0,02	150 ± 8,46 *	121 ± 6,45
	%	146		135		136		124	
6.	3	0,42 ± 0,042 *	0,31 ± 0,019	4,17 ± 0,4 *	3,05 ± 0,09	0,96 ± 0,2 *	0,40 ± 0,021	136 ± 4,35 *	114 ± 5,03
	%	136		138		240		119	

(Here and below E - experiment; C- control test; p<0,05*; p< 0,01**; p< 0,001*** - reliability, % - percentage).

Table 3.Concentration of heavy metals in the field of «Gurgan» (December2013, µg/l, M±m,p, %, n=7).

Station№	Depth (m).	Fe		Ni		Hg	As	
		E	C	E	C	E	E	C
1.	1,5	160,1± 5,50 *	146 ± 1,99	4,09 ± 0,34 *	3,14 ± 0,18	<0,1	4,19 ± 0,48	2,87 ± 0,19
	%	105		141			127	
6.	3	164,8 ± 6,5 *	148,2 ± 1,06	3,85 ± 0,27 *	3,03 ± 0,12	<0,1	3,30 ± 0,3	2,32 ± 0,17
	%	111		127			142	

Station №	Depth (m).	Cd		Cu		Pb		Zn	
		E	C	E	C	E		E	C
1.	1,5	0,40 ± 0,04 **	0,23 ± 0,021	3,85 ± 0,49 *	2,29 ± 0,157	0,49 ± 0,028 **	0,35 ± 0,022	16,63 ± 0,5 *	13,7 ± 0,81
	%	178		168		140		124	
6.	3	4,87 ± 0,033 *	3,93 ± 0,017	3,76 ± 0,44 **	2,12 ± 0,08	0,86 ± 0,13 **	0,40 ± 0,02	18,3 ± 1,57 *	11,5 ± 1,81
	%	124		177		215		159	

Table 4.Concentration of heavy metals in the field of «Gurgan» (June 2014, µg/l, M±m,p, %, n=7).

Station№	Depth (m).	Fe		Ni		Hg	As	
		E	C	E	C	E	E	C
1.	1,5	160,1± 5,50 *	146 ± 1,99	4,09 ± 0,34 *	3,14 ± 0,18	<0,1	4,19 ± 0,48	2,87 ± 0,19
	%	110		130			146	
6.	3	167,2 ± 10,5 *	141± 1,57	3,92 ± 0,32 *	3,02 ± 0,12	<0,1	3,96 ± 0,33	2,87 ± 0,16
	%	119		130			138	

Station №	Depth (m).	Cd		Cu		Pb		Zn	
		E	C	E	C	E		E	C
1.	1,5	0,40 ± 0,04 **	0,23 ± 0,021	3,85 ± 0,49 *	2,29 ± 0,157	0,49 ± 0,028 **	0,35 ± 0,022	16,63 ± 0,5 *	13,7 ± 0,81
	%	142		150		182		124	
6.	3	0,49 ± 0,036 *	0,39 ± 0,018	4,25 ± 0,24 **	3,05 ± 0,099	0,67 ± 0,11 *	0,39 ± 0,031	178,7 ± 8,1 *	151,8 ± 1,66
	%	127		139		178		118	

Iron- the average analytical concentrations in water from 2012 to 2014 declined from 0,158 mg/l to 0,148 mg/l. The maximum value of iron in the summer of 2012 reached 0,162 mg/l, the minimum - 0,149 mg/l. In December 2013, the maximum concentration of iron remained stable (0,162 mg/l), but the minimum concentration increased to 0,153 mg/l. The lowest concentrations of iron during the observed periods were recorded in the summer of 2014, where the average concentrations were in the range of 0,148 mg/l, (maximum 0,154 mg/l and minimum 0,141 mg/l). Such a decreasing of concentration can be explained with increasing of water content of rivers that flow into the Caspian Sea. The average iron concentrations in the bottom sediments in the fall of 2012 and in the summer of 2013 were 23274,3 - 20542,5 mg of element per 1 kg of dry bottom sediments, respectively. In the spring of 2014, the average concentration of iron decreased to 1984,2 mg/kg. The maximum concentrations of iron dropped from 27148 mg/kg in 2012 to 19113 mg / kg in 2014. In the fall of 2013 and in the spring of 2014, the maximum values were approximately equal and the low values of concentrations have a tendency to decrease.

Nickel- dynamics of nickel concentrations in water is a bit different, in general from 2012 to 2014 the average concentrations varied from 0,0025 mg/l to 0,0032 mg/l. The maximum concentrations in 2012 and 2013 were the same 0,0033 mg/l, and the minimum concentrations were in the range of 0,0029 - 0,0031 mg/l. The concentrations of nickel in the summer of 2014 varied from 0,0022 mg/l to 0,0029 mg/l. The results of the analysis showed that the amount of nickel in the bottom sediments decreases from 66 mg/kg at a depth of 4 meters to 51 mg/kg at a depth of 5 meters. The average content of this element in the sediment was 61,99 mg/kg.

Arsenic- the average concentrations of arsenic in the summer of 2012 and 2014 remained virtually unchanged and amounted- 0,002 mg/l - 0,009 mg/l. Thus the maximum concentrations did not exceed the maximum permissible concentration (MPC) for fisheries activities and the minimum concentrations were very low (0.002 mg/l). The mean concentrations of arsenic from autumn 2012 to spring 2014 changed and were 0,575 mg/kg - 0,516 mg/kg. The maximum values over the period were approximately 0,72 mg/kg.

Cadmium -the average concentrations of cadmium in water during the study period remained almost unchanged from 0,0001 mg/l to 0,0003 mg/l and did not exceed both the MPC of fish farm (0,5 µg/l) and the MPC of water (1 µg/l). The mean content of cadmium in the bottom sediments did not exceed 0,33 mg/kg and increased from 0,33 mg/mg to 0,39 mg/kg. In general, concentrations during the probe period ranged from 0,25 mg/kg to 0,43 mg/kg.

Copper -the mean analytical concentrations of copper in water from 2012 to 2014 were in the interval from 0,0034 mg/l to 0,0028 mg/l. The maximum concentration in the summer of 2012 reached 0,0038 mg/l, the minimum 0,0029 mg/l. In December of 2013, the maximum and minimum concentrations were almost the same 0,0039 mg/l and 0,0027 mg/l. The lowest concentrations over the observed periods were recorded in the summer of 2014, where the average concentrations were 0,0028 mg/l (maximum 0,0034 mg/l and minimum 0,0025 mg l). The average concentrations of copper in sediments did not exceed 37,75 mg/kg and varied from 35 mg/kg to 40,5 mg/kg. In turn, the concentrations for the investigation period ranged from 31 mg/kg to 45 mg/kg.

Lead - the average concentrations of lead in water from May 2012 to June 2014 dropped from 0,0009 mg/l to 0,0006 µg/l. The minimum values from 2012 to 2013 were in range 0,0006 mg/l to 0,0007 mg/l. In the summer of 2014, the concentration of lead in the water of the investigated field declined to 0,0004 mg/l. The maximum concentrations from 2012 to 2014 remained stable and were 0,0011 mg/l. The mean concentrations of lead in the bottom sediments from fall 2012 to the spring of 2011 decreased from 4,2 mg/kg to 3,5 mg/kg. The minimum values from 2012 to 2014 varied from 3,0 mg/kg to 3,8 mg/kg.

Mercury –over the research period, the concentration of mercury in water did not exceed the value of <0,0001 mg/l and did not exceed the maximum permissible concentration for fish industry. (1µg/l). In bottom sediments, the content of mercury varied from 0,004 mg/kg to 0,010 mg/kg (Fig. 2).

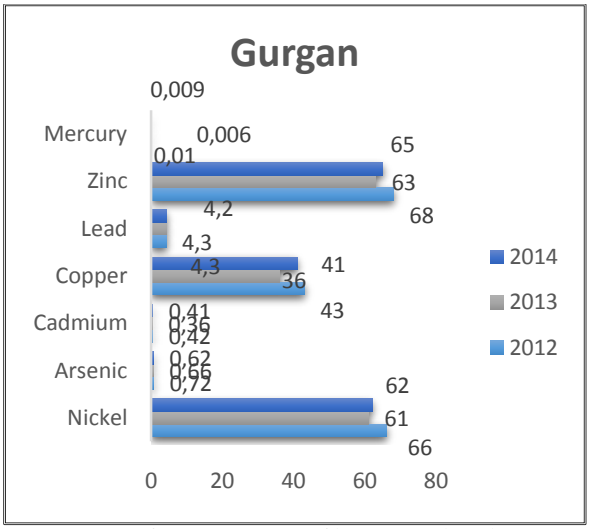

Fig.2. Dynamics of concentrations of heavy metals in bottom sediments on the oil and gas field of «Gurgan» (mg/kg).

Zinc - the dynamics of the concentrations of zinc in water is different, in general from 2012 to 2014 the average concentrations varied from 0,0142 mg/l to 0,0132 mg/l. The maximum concentration in 2012 was 0,0141 mg/l, and the minimum concentration was 0,0128 mg l. The concentration of zinc in the summer of 2014 changed in the interval of 0,0128 mg/l to 0,0137 mg/l.

The content of zinc in the bottom sediment increased in the order of increasing depth, and was in the range of 128 mg/kg. The average content of this element in bottom sediments at the oil and gas field «Gurgan» was 72,915 mg/kg.

The total pollution index of TM in sediments can be illustrated in decreasing series: Fe> Zn> Ni> Cu> Pb> As> Cd> Hg and in the water of the Caspian Sea - Fe> Zn> Cu> As> Ni> Pb> Cd. Thus, it can be said that the main pollutants in the water of the Caspian basin are zinc and copper. Their concentration continuously exceeds the MPC of fish farm (zinc-0,01-0,05 mg/l, copper-0,001 mg/l). However, in recent years, revealed decreasing the amount of iron from 0,162 mg/l to 0,141 mg/l and nickel from 0,033 mg/l to 0,022 mg/l, which is probably associated with the purification works on the area. In bottom sediments, the concentration of heavy metals did not exceed the MPC. In general, the temporary variability of the content of metal ions in water confirms the existing notion that their concentration in the waters of the Caspian Sea increases under reducing conditions, which form at the «water and soil» boundary, that facilitates the transition of metals from bottom sediments into the water, and decreases with predominance of oxidizing conditions that promote the deposition of metals from water to the bottom [5]. In turn, heavy metals being more stable in time more reliably reflect pollution of the seabed. Moreover, these sediments not be only a source of secondary pollution of rivers, but being the habitat of benthic organisms, which may have a negative effect for all of biotic components of aquatic ecosystems. Therefore, investigation of sediments becomes paramount for the determining the degree of anthropogenic pollution of seas and assessment of their initial state, which is frequently used to assess the ecological status of water objects [6].

4. Conclusion

1. In the recent years, the main pollutants in the water of the Caspian basin are zinc and copper. Their concentration continuously exceeds the MPC of fish farm (zinc-0,01-0,05 mg/l, copper-0,001 mg/l).
2. During the period of investigation, the average concentration of trace element - As remained unchanged and was in the range of 0,002-0,009 mg/l in water and 0,516-0,575 mg/kg in bottom sediments of the Caspian Sea.
3. According to the content of zinc, iron, cadmium, copper, nickel, lead, mercury and arsenic, can be composed in the bottom sediments the following decreasing series: Fe> Zn> Ni> Cu> Pb> As> Cd> Hg, and in water Fe> Zn> Cu> As> Ni> Pb> Cd.
4. In the samples of studies as compared with previous years, the amount of iron decreased from 0,162 mg/l to 0,141 mg/l and nickel from 0,033 mg/l to 0,022 mg/l, which is related with the purification works of the area that are continuing at the present time.

References

[1] A.V. Kisilev,A.A. Kurapov, V.F. Zaycev.«Ecological characteristics of the individual regions of the CaspianSea», PQTU,Astrakhan, (2008).
[2] O.A. Serebryakova, Geology, geography and global energy.**3**, 103, (2012).
[3] E.I. Melyakina, U.T. Pimenov, M.A. Musaev, A.V. Mahlun,Vestnik ASTU.**2**, 106,(2013).
[4] S.A. Huseynova, A.A. Gadzhiev,Ecology, development. **3**, 61, (2013).
[5] E.V. Chuiko, A.S. Abdusamadov, Ecology, development.**3**, 110, (2013).
[6] S. Z. Salahova, Sh. A. Topchiyeva, I. Kh. Alakbarov, Appl. Environ. Biol. Sci.**5**9, 9, (2015).

Features of magnetic interaction in composites based on siderite and polymer

U.F. SAMEDOVA, SH.M. HASANLI
Institute of Physics, National Academy of Sciences of Azerbaijan, pr. H.Javid 131, Baku, AZ_1143 Azerbaijan, neytrino7@gmail.com, hasanli_sh@rambler.ru

Abstract
We have investigated the influence of the size of magnetic particles on the magnetic characteristics of composites based on (30-50%) annealed siderite (AS) and (70- 50%) (PP). It was found that the presence of a size effect in the studied composites, namely, with a decrease in the size of magnetic particles the value of the coercive force increases, and the remanent magnetization and saturation of the magnetization decrease.

Keywords: magnetic composite, remanent magnetization, saturation, magnetic anisotropy, Curie temperature

INTRODUCTION

Nowadays, it is very actual to develop the new magnetic materials (in particular, systems containing single-domain magnetic nanoparticles), new magnetic materials are widely used in engineering, as they have a record of the magnetic parameters, or an optimal combination of magnetic and other electrical characteristics. These magnetic materials have provided the solution to many technological challenges and have made significant contribution to scientific and technical progress in the modern world.

New magnetic materials allow you to create high-performance magnetic field sensors with high sensitivity, a thin-film permanent magnets for different areas of micro-electronics, and reading data from the magnetic hard disk drives, and other devices.

The fact is that at the distances of the order of the size of the atom, or about ten atomic dimensions (about a nanometer) are expected new different magnetic effects, as a result of the fact that the range of the exchange interaction, which leads to magnetic ordering (ferromagnetic or antiferromagnetic), amounts to several interatomic distances. In the last decade, has been made some progress in the development of multilayer magnetic films and artificial magnetic structures, in which new effects arise due to the interaction of the "magnetic electron" with artificially created nanoscale structures. In accordance with the principles developed in these devices are used the combination of magnetism and electronics, therefore we can speak of the birth of a new field of magnetism and technology-a magnetoelectric [1-5]. In this paper we set the goal synthesis and study of magnetic properties of composites based on polymer (PP) and microparticles annealed siderite (Fe, Mn)CO_3.

EXPERIMENTAL METOD

This paper offered a method for the synthesis of composites. The objects of the study were taken polypropylene (PP) and annealed mineral siderite (Fe, Mn) CO_3.

It should be stressed that natural mineral siderite is not magnetic. After annealing at T = 1000^0C due to chemical changes appears magnetic properties in this material. As can be seen from X-ray (Fig.1.) after annealing appears reflexes of various metal oxides (maghemite, gamma Fe_2O_3-18%; hematite Fe_2O_3-31%), including oxide magnetite Fe_3O_4. In this case the percentage of magnetite is 53%. Composites were prepared from the homogeneous powder mixture of components by hot pressing. Contents of the components vary over a wide range (30-50%) annealed siderite (AS) and (70- 50%) (PP) respectively. A process for preparing the proposed composition of the material for making films is as follows: charge components consisting of siderite in the required amounts were weighed and ground to a particle size of 65-315 microns or less in a ball mill with porcelain balls. The mixture was then placed in a mold and hot pressed as follows: a) at the beginning mixed batch mixed at a pressure P = 1 MPa heated to the melting temperature (T = 160^0 C) for 3 minutes; b) then the pressure was raised in the press to P = 15 MPa, molten mixture is being kept at this pressure for 6 minutes; c) the composite film is cooled by the way of quenching in water. The film is more elastic with this method of cooling. The sample thickness was equal 140 mkm. To measure the electrical characteristics on the ends of the samples were applied measuring electrodes via silver paste. It is advisable to use a dielectric polypropylene (PP) becaus of a large value of its dielectric constant, and annealed siderite natural mineral (siderite) for its simplicity and cheapness of obtaining the material with magnetic properties. Note that in the joint synthesis process the components do not wet each other and ferromagnetic atoms are grouped into individual pellets.

DISCUSSION OF THE OBTAINED RESULTS

The experimental results of the magnetic parameters are given in Table 1 and in Figures 1-3. Analysis of the obtained experimental results shows the presence of a size effect, in the investigated composites.It can be seen from the table that as the size of the magnetic particles decreases, regardless of the percentage content of the components, the coercive force increases. At the same time with the percentage content of the components increases, the values of the remanent magnetization Mr and the saturation magnetization Ms grow regardless of the

particle size. Figures 1 and 2 show the temperature dependences of the remanent magnetization Mr, saturation magnetization for the investigated composites at a magnetic field value H = 4 kOe. It can be seen from Figs. 1 and 2 that, regardless of the size of the magnetic particles, the residual magnetization Mr and the saturation magnetization Ms increase with decreasing temperature.Note that coercive force as one of the main characteristics of magnetic materials determines the width of the hysteresis loop and is actually a complex indicator that depends on a large number of factors (magnetic, crystallographic and other types of anisotropy, defectiveness, external conditions, method of obtaining and processing material and so on).The growth of the coercive force with decreasing particle size is due to the decrease in the number of domain boundaries, which is associated with a decrease in the possibility of rotation of the spins in the domains and a decrease in the possibility of displacement of these boundaries.In the general case, as the particle sizes decrease, the role of the domain boundaries decreases, and magnetization reversal occurs due to the synchronous rotation of the magnetic moments, which depends on the anisotropy of the particle, the crystallographic and magnetic anisotropy.A further decrease of the particle size leads to the fact that the role of thermal fluctuations that disorient the direction of the spins in the particle increases, with which the decrease in the coercive force is attributed.At a certain size of the nanoparticle, the thermal energy (KT) begins to exceed the thermodynamic gain in energy for the orientation of the spins, the particle becomes a superparamagnetic state.

Table 1. Magnetic parameters of composite materials at room temperature

	Hc,Oe				
d,μm	***65***	***71***	***100***	***160***	***315***
30%AS+70%PP	**69**	**65.5**	**62.3**	**61.3**	**60.9**
40%AS+60%PP	**65.4**	**63.4**	**61.1**	**60.2**	**59.8**
50%AS+50%PP	**62.8**	**61.2**	**60**	**59.6**	**59.05**
	Ms,emu/cub.cm				
d,μm	***65***	***71***	***100***	***160***	***315***
30%AS+70%PP	**7.9**	**8.3**	**9**	**9.8**	**10.2**
40%AS+60%PP	**8**	**9.4**	**9.8**	**10.7**	**11**
50%AS+50%PP	**10.9**	**11**	**11.9**	**12**	**12.4**
	Mr,emu/cub.cm				
d,μm	***65***	***71***	***100***	***160***	***315***
30%AS+70%PP	**1.4**	**1.61**	**1.7**	**1.77**	**1.86**
40%AS+60%PP	**1.6**	**1.69**	**1.773**	**1.89**	**1.95**
50%AS+50%PP	**1.7**	**1.75**	**1.88**	**1.97**	**2.1**

According to [6], the main factors influencing the magnetic parameters of materials are: magnetic anisotropy, particle size, temperature (temperature fluctuation of the magnetic moments of domains), material defectiveness.The fact is that the obstacles that prevent the free movement of domain boundaries under the influence of the magnetic field in the material are microscopic pores, secondary phases, defective sections of the crystal lattice, and etc.In addition, as the temperature increases, on the one hand magnetic anisotropy decreases, in other words, both obstacles that prevent the free movement of domain walls, and forces that prevent the rotation of domain moments, are reduced, on the other hand, due to thermal energy, the forces acting on the magnetic moments of interacting atoms decrease. In view of the foregoing, the experimental results can be explained as follows. Without a magnetic field, the magnetic moments of the domains are oriented chaotically.When an external magnetic field is turned on, a certain energy barrier must be overcome to rotate the magnetic moment of the atoms in the direction of the magnetic field.

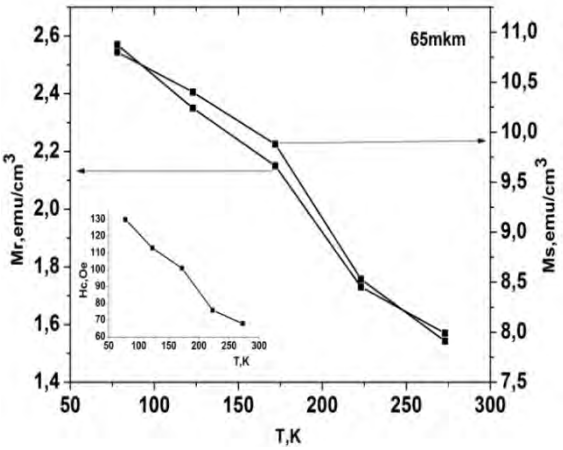

Fig 1.40% AS+60%PP
Particle size 65 microns

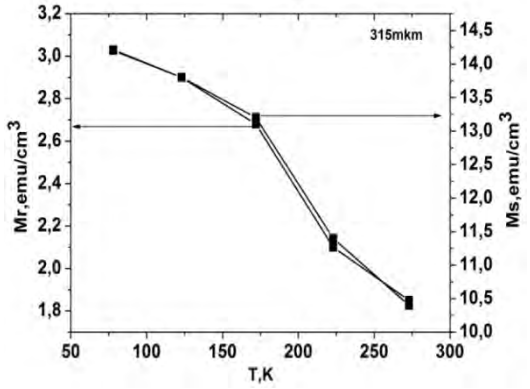

Fig 2.40% AS+60%PP
Particle size 315 microns

On the other hand, thermal energy (KT) leads to a thermal fluctuation in the amplitude of the magnetic moments of the domains. Moreover, the higher the temperature is the more (KT) and, correspondingly, the amplitude of thermal fluctuations of the magnetic moments (disordering of domains). As a result, at H = const, the values of the magnetic parameters Hc, Mr, Ms decrease with increasing temperature, which is confirmed by experimental results (see Fig. 1, 2). In particular, according to [7], taking into account the thermal fluctuations, the temperature dependence of the coercive force Hc is well described by the formula

$$H_c(T) = H_c(0)\left(1 - (T/T_B)^{1/2}\right)(1)$$

Where $-T_B$ is the blocking temperature.

For the studied composites, the blocking temperature T_B, determined by extrapolating the straight-line section of the

$H_c \sim T^{1/2}$ dependence to the point Hc = 0 on the ordinate axis is equal to T_B = 333K, 376K.Note that all the numerical values of T_B do not exceed the Curie temperature T ~800 K.

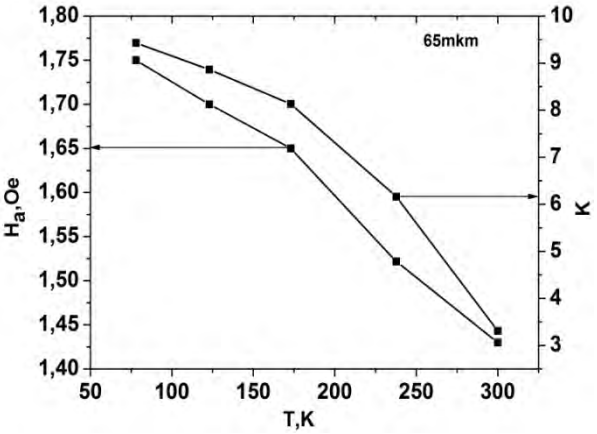

Fig. 3. 40% AS+60%PP
Particle size 65 microns

The reason for the observed growth of the coercive force Hc with decreasing temperature along with other factors can be the dependence of Hc on the magnetic anisotropy coefficient K [8].

$$H_c = \frac{2K}{M_s} \quad (2)$$

Here Ms is the spontaneous magnetization.
In turn, the magnitude of the local magnetic anisotropy of the magnetic particles Ha can be due to: the contribution of the crystallographic magnetic anisotropy, and the contribution of the anisotropy induced by the internal stresses, as well as the contribution of the anisotropy of the magnetic particles (Fig. 3). It was shown in [9] that the magnitude of the local anisotropy associated with the anisotropy of the magnetic particles depends on Ms linearly. According to [8, 10] the local anisotropy of the investigated magnetic particles should first of all be attributed to the anisotropy of the shape of these particles. The results obtained by us make it possible to assert that the magnetic characteristics of composites are affected, in addition to the shape and size of the magnetic particles.

Thus, in the presented work was studied the influence of the size of magnetic particles on the magnetic characteristics of composites based on (30-50%) annealed siderite (AS) and (70- 50%) (PP).It is established the presence of a size effect in the studied composites, namely, with a decrease in the size of magnetic particles the value of the coercive force increases, and the remanent magnetization and saturation of the magnetization decrease. It was found that, regardless of the size of the magnetic particles (with the same percentage of the components), the values of M_r, M_s and H_c increase with decreasing temperature.

REFERENCES

[1]. E.Hirota, H.Sakakima,K. Inomata.Giant Magneto-Resistance Devices. Springer, 30; 177 (2002)
[2].A. Nicola Spaldin. Magnetic Materials: Fundamentals and Applications. 2nd ed. Cambridge University Press:; 288 (2010)
[3]. S. A. Nicitin.Giant magnetoresistance. Soros Educational Journal.Vol 8 (2), p 92-98 (2004) (Russian)
[4].S.Mitani, H.Fujimori, S. Ohnuma. Spin-dependent tunneling phenomena in insulating granular systems. JMMM; 165; 141-148 (1997)
[5]. J.C.Sionczewski. Conductance and exchange coupling of two ferromagnetism separated by tunneling barrier. Phys. Rev. B; 39, (10), 6995-7002 (1989)
[6]. V.V.Pasinkov, V.S.Sorokin. Materials of electron technics. 1986. Moscow. 240 p.
[7].I.S. Jacobs, and C.P. Bean. Fine Particles; Superparamagnetism. In: Rado, G.T. and Suhl, H., Eds., Magnetism 3, Academic Press, New York, 272 (1963)
[8].E.P.Elsukov et al., J of Technical Physics, 79 (4), 125-130 (2009)
[9]. S.V.Komogorchev et al., Solid State Physics, 49 (4) 700-703 (2007)
[10]. L.N.Korotkhov et al., J of Technical Physics, 81 (4) 125-127 (2011)

On a numerical solution of a shape optimization problem for the eigenvalues of pauli operator

YUSIF S.GASIMOV[a,b], AYNURA R. ALIYEVA[c]

[a]*Azerbaijan University, Baku, Azerbaijan*
[b]*Institute of Mathematcs and Mechasnics ANAS, Baku, Azerbaijan*
[c]*Sumgait State University, Sumgayit, Azerbaijan, e-mail: gasimov.yusif@gmail.com*

Abstract

We studythe eigenvalues ofPauli operator in the variable operator definition domain. It is known thatPauli operatordescribes the motion ofa particle with spin(in differ from Schrödinger operator) in a magnetic fieldandis a generalization ofthe Schrödinger operatorin a mathematicalandquantum-physical meaning.

Keywords: *Pauli operator, extremal problem, necessary condition, variable domain.*

1. Introduction

Shape optimization is one of the young and fast developing in recent years, branches of the general optimization theory. It is stimulated by the strong relation to a number of applications in physics and engineering that makes necessary to focus on shapes instead of parameters or functions. The goal of these applications is to deform and modify the admissible shapes in order to comply with a given cost function that needs to be optimized. In this respect the problems are both classical (as isoperimetric and Newton problem of the ideal aerodynamical shape show) and the modern (reflecting the many results obtained in the last few decades) [1-3].

The characteristic point of the shape optimization problems is that the objects under investigations, indeed the competing objects are shapes (i.e. domains of E^n), instead of functions as we used to see in the traditional optimization problems. This fact adds a lot of difficulties in investigation of such problems. The first one is the lack of existence of the optimal solutions (optimal shapes). Another difficulty is related to the mathematically constructive description of the domain variation. However for the certain classes of problems under some geometric constraints on the admissible domains or when the functional that needs to be minimized has special form, an optimal solution exists [4].

Shape optimization problems for the eigenvalues received a lot of attention due their strong relations to several applications such as, for instance, stability of vibrating bodies, propagation of waves in composite media, and the thermic insulation of conductors. Some characteristics of these systems are described by the eigenvalues of the corresponding operators. For example, the eigenvalues of the Schrödinger operator

$$Hu(x) = -\Delta u(x) + q(x)u(x)$$

are energy levels of the quantum particle in the externalforce field [12], of the operators

$Lu(x) = -\Delta u(x)$ and $Lu(x) = -\Delta^2 u(x)$

are eigenfrequencies of the vibrating membrane and plate, correspondingly [11].

In its mathematical formulation the problem consists in taking a certain operator (in our case biharmonic operator) and considering its eigenvalues as functions of the domain where the problem is solved. Sometimes it is expedient to consider the domain functionals that involves eigenvalues of certain operators. These functionals also may describe this or that physical characteristics of the considered mechanical system [10].

Concerning the existence of the optimal solutions, roughly speaking, existence results for such kind of problems usually are obtained and the problem is well posed in the cases when the admissible domains satisfy some geometrical restrictions, the functional satisfies some monotonicity assumptions, or it depends only on lower part of spectrum [1].

2. Main results

As follows fromthe basic postulatesof quantum physics, eigenvalues λ_n of Pauli operatordescribethe total energy ofa quantum system(in our casean electron withspinin a magnetic field) in a state φ_n, where φ_n is an eigenfunctioncorresponding to the eigenvalue λ_n [15].

Let Ω be the set of all convex bounded closed domains from R^2 with smooth boundaries. Denote

$K = \{D \in \Omega,\ \overline{D} \in \Omega_0,\ S_D \in C^2\}$,

where Ω_0 is some convex subset of Ω, $\overline{D}$ is a closure and S_D - boundary of the domain D.

Consider the problem

$$\lambda_k(D) \to \min,\ D \in K\ . \qquad (1)$$

Here λ_k is the k-th eigenvalue of the following spectral problem

$$P\varphi = \lambda\varphi\,, \quad x \in D\,, \tag{2}$$

$$\varphi = 0\,, \quad x \in S_D\,, \tag{3}$$

where P is Pauli operator generated by the expression

$$P = P(a,v)\cdot J + \sigma B\,. \tag{4}$$

Here

$$J = \begin{pmatrix} 1 & 0 \\ 0 & 1 \end{pmatrix},\quad \sigma = \begin{pmatrix} 1 & 0 \\ 0 & -1 \end{pmatrix},\quad P = (a,v) = (-i\nabla - a)^2 + V\,,$$

i is the imaginary unit, V - smooth enough function, $\nabla = \left\{\frac{\partial}{\partial x}, \frac{\partial}{\partial y}\right\}$, $a = (a_1, a_2) \in R^2$ is a vector potential, B - magnetic field generated by a, i.e. $B = \frac{\partial}{\partial x}a_2 - \frac{\partial}{\partial y}a_1$.

If to consider these entire definitions one can obtain the following explicit form of Pauli operator in two dimensional case

$$P = \begin{pmatrix} (-i\nabla - a)^2 + a_2\frac{\partial}{\partial x} - a_1\frac{\partial}{\partial y} + V & 0 \\ 0 & (-i\nabla - a)^2 - a_2\frac{\partial}{\partial x} + a_1\frac{\partial}{\partial y} + V \end{pmatrix} =$$

$$= \begin{pmatrix} -\Delta + (2ia_1 + a_2)\frac{\partial}{\partial x} + (2ia_2 - a_1)\frac{\partial}{\partial y} + a^2 + V & 0 \\ 0 & -\Delta + (2ia_1 - a_2)\frac{\partial}{\partial x} + (2ia_2 + a_1)\frac{\partial}{\partial y} + a^2 + V \end{pmatrix} \tag{5}$$

Taking $\varphi = \begin{pmatrix} \varphi_1 \\ \varphi_2 \end{pmatrix}$, where $\varphi_1, \varphi_2 \in L_2(D)$ from (2) and (5) we get

$$\begin{aligned} &-\Delta\varphi_1 + (2ia_1 + a_2)\frac{\partial\varphi_1}{\partial x} + (2ia_2 - a_1)\frac{\partial\varphi_1}{\partial y} + \\ &+ a^2\varphi_1 + V\varphi_1 = \lambda\varphi_1, \\ &-\Delta\varphi_2 + (2ia_1 - a_2)\frac{\partial\varphi_2}{\partial x} + (2ia_2 + a_1)\frac{\partial\varphi_2}{\partial y} + \\ &+ a^2\varphi_2 + V\varphi_2 = \lambda\varphi_2. \end{aligned} \tag{6}$$

Denote $P_1 = -\Delta + (2ia_1 + a_2)\frac{\partial}{\partial x} + (2ia_2 - a_1)\frac{\partial}{\partial y} + a^2 + V$,

$P_2 = -\Delta + (2ia_1 - a_2)\frac{\partial}{\partial x} + (2ia_2 + a_1)\frac{\partial}{\partial y} + a^2 + V$.

Thus within some conditions on a we can consider eigenvalues of Pauli operator positive and numerated in increasing order considering their multiplicity $0 \le \lambda_1 \le \lambda_2 \le \ldots$.

Replacing $\varphi_i' = e^{\alpha x + \beta y}\varphi_i$, $i = 1,2$, $\alpha, \beta \in R$ after some transformations (6) we get

$$-\Delta\varphi_1 + V\varphi_1 = \left(\lambda - \frac{1}{4}a^2\right)\varphi_1 \tag{7}$$

$$-\Delta\varphi_2 + V\varphi_2 = \left(\lambda - \frac{1}{4}a^2\right)\varphi_2 \tag{8}$$

Taking $\eta = \lambda - \frac{1}{4}a^2$ from (5), (7), (8) we can rewrite the problem (2), (3) in the form

$$\begin{aligned} &\widetilde{P}\varphi = \eta\varphi, \quad x \in D, \\ &\varphi = 0\,, \quad x \in S_D\,, \end{aligned} \tag{9}$$

where $\widetilde{P} = \begin{pmatrix} -\Delta + V & 0 \\ 0 & -\Delta + V \end{pmatrix}$.

The following theorem is proved.

Theorem. In order to $D^* \in K$ provide minimum to the functional (1) subject to (2), (3) it is necessary the fulfillment of the condition

$$\max_{\varphi_k^*} \int_{S_{D^*}} \left|\nabla\varphi_k^*(x)\right|^2 \left[P_D(n(x)) - P_{D^*}(n(x))\right] ds \le 0\,,$$

for any $D \in K$. Here $\varphi_k^*(x)$ is an eigenfunction corresponding to $\lambda_k^* = \lambda_k(D^*)$ in D^*, max is taken over all eigenfuctions φ_k^* corresponded to η_k in the case of its multiplicity,

$$P_D(x) = \max_{l \in D}(x,l),\quad x \in R^2$$

is a support function of the domain D, s-is a boundary element.

On the base of this result the following algorithm is offered for the solution of the problem (9).

Algorithm.

Step 1. Chose the initial domain $D_0 \in K$ and assume that $D_i \in K$, $i = 1,2,\ldots$ are already known.

Step 2. Solve the problem (9) in D_i and find eigenfunction $\varphi_i(x)$.

Step 3. Solve the variational problem

$$\Lambda_i \to \max\,,$$

where $\Lambda_i = \int_{S_{D_i}} \left|\nabla\varphi^{(i)}\right|^2 P(n(x))ds$ and find convex positively-homogeneous function $\overline{P}_i(x)$.

Step 4. Find the auxiliary domain $\overline{D}_m$ as a subdifferential of the function $\overline{P}_i(x)$ in the point 0.

Step 5. Find the following domain from the relation $D_{i+1} = (1 - \alpha_i)D_i + \alpha_i\overline{D}_i$, where $0 < \alpha_i < 1$.

Step 6. Check up the exactness criteria. If it is not satisfied take $D_i = D_{i+1}$ and go to Step 2. Otherwise stop the iteration.

References

1. Z.Belhachmi, D.Bucur, G.Buttazzo, J.-M. Sac-Epée,Shape optimization problems for eigenvalues of elliptic operators, ZAMM-Journal of Applied Mathematics and Mechanics, **86**(3), 171(2006).
2. D.Bucur, G.Buttazzo,"Variational Methods in Shape Optimization Problems, Series: Progress in Nonlinear Differential Equations and Their Applications", Bürkhäuser, **65, (**2005).
3. D.Bucur, G.Buttazzo, I.Figueiredo, On the attainable eigenvalues of the Laplace operator, SIAM J.Math. Anal.,**30,** 527**(**1999).
4. V.F.Demyanov, A.M.Rubinov,"Basises of Non-smooth Analysis and Quazidifferential Calculas", Moscow, Nauka, (1990) (in Russian).
5. Y.S.Gasimov On some properties of the eigenvalues by the variation of the domain, Journal of Mathematical Physics, Analysis, Geometry,**10**(2)**,** 249, (2003).
6. Y.S.Gasimov, A. Nachaoui, A.A. Niftiyev, Nonlinear eigenvalue problems for p- Laplacian, Optimization Letters, **4,** 67, (2010).
7. Y.S.Gasimov On one inverse problem for defining of the domain of the plate, Appl. Comput. Math., **4**(2), 41, (2005).
8. Y.S.Gasimov, A.A.Niftiyev, On a dependence of the eigenfrequency on the form of plate under across vibrations, Problems of durability and elasticity, **64**, 91, (2002). (in Russian).
9. Y.S. Gasimov, Some shape optimization problems for the eigenvalues, J. Phys. A: Math. Theor., **41**(5), 521(2008).
10. S.H. Gould,"Variational Methods for Eigenvalue Problems", Canada: Oxford University Press/University of Toronto Press, Oxford/Toronto, (1996).
11. A.A.Niftiyev, Y.S.Gasimov,"Control by boundaries and eigenvalue problems with variable domains", Baku University Press, (2004) (in Russian).
12. V.S.Vladimirov,"Equations of Mathematical Physics", Moscow, Nauka, (1988) (in Russian).
13. H.L.Cycon, R.Froese, W.Kirsch, B.Simon,"Schrodinger Operators with Applications in Quantum Physics and Global Geometry", Moscow, Mir, 406, (1990).

Investigatıon of theatmosphere of HD14662(F7Ib)

Z.A.SAMEDOV[1,2], U.R.GADIROVA[1], Sh.Sh.AMIROV[3,4]

[1]*Shamakhi Astrophysical Observatory, Shamakhi, Azerbaijan,* ***E-mail:ulkergadirova@gmail.com, zahir.01@mail.ru***
[2]*Astrophysical department, Baku State University, AZ1148, 23, Z.Khalilov str., Baku, Azerbaijan,*
[3]*Azerbaijan Medical University, Baku,Azerbaijan,*
[4]*Khazar University,Baku,Azerbaijan*

Abstract
In this study, the atmosphere of a HD14662 (F7Ib) star has been investigated by employment of the method of atmospheric model. An effective temperature and acceleration due to gravity of the star , speed of microturbulent motion as well as quantity of eleements are determined. Values for effective temperature , acceleration due to gravity and speed of microturbulent motion were obtained as Teff = 6250 ± 200K, logg = 1.5 ± 0.2 and ξ_t=5km/sec. respectively.
Quantity of most of elements has been found to be closely to the quantity found in the Sun. In particular deficiency of element C and excess of element Na have been revealed.
Keywords:*The effective temperature, acceleration due to gravity speed of mikroturbulent movement, chemical composition.*
Pacs 98.58 Ly, *97.20.Rp*

1. Observaion material

The atmosphere of HD14662 (F7Ib) star was studied by use the model technique. Spectra obtained in the λλ 3700-5000Å region with 0,3 Å resolution and 8 Å/mm dispersion at the Kude focus of 2m telescope of Shemakhy Astrophysical Observatory(ShAO) were used. The atlas was constructed, the equivalent widths W_λ of lines were calculated and 4 spectrograms have been developed[1].

2. Atmospheric parameters: the Effective temperature, acceleration due to gravity

The effective temperature *Teff* and acceleration due to gravity logg of a star were calculated by the atmospheric model method [2]. During this process following criteria are considered:
1. Comparison of the observed and theoretical values of β index .
2. Comparison of the observed and theoretical values of [c_1] index.
3. Comparison of the observed and theoretical values of the Q index.

A diagram for determination of T_{eff} and *logg* is plotted in the Fig.1. For the atmosphere of HD14662 (F7Ib) star are chosen following parameters: T_{eff}*=6250±200K, logg=1,5±0,2.*

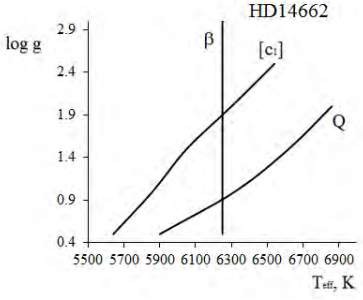

Fig 1. The T_{eff}-*logg* diagram

3. A speed of microturbulent Motion

For the analysis of chemical compositiona speed of microturbulent movement ξ_t must be known. As shown in [3] to determine the speed of microturbulent movement ξ_t an existence of specific lines for any atom and ion in the range of broadly equivalent widths W_λ is necessary. Various values are assigned to the parameter $\xi_t$and a speed of microturbulent motion associated to the case of independence of element amount versus equivalent widths of lines W_λ is chosen. Lines of FeI are of maximum number in the HD14662 (F7Ib) star.

By employment the model with basis parameters Teff = 6250K and logg = 1.5 base we calculate an amount of logε(FeI) at different values of microturbulent speed ξ_t. As can be seen from Fig.2 there is not a correllation between logε and W_λ at the value of ξ_t*=5km/sec.* The value of microturbulent movement speed equal ξ_t*=5km/sec* is determined in the atmosphere of HD14662 (F7Ib) star.

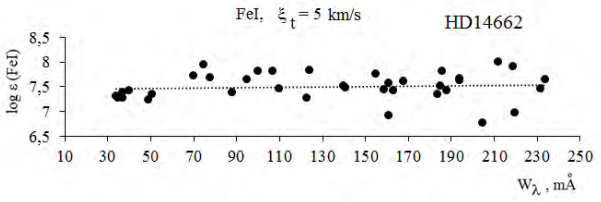

Fig. 2. Dependence of logε(*FeI*) versus W_λ at the value of ξ_t=5 km/sec

4. Chemical composition

Number of elements in the atmosphere ofHD14662(F7Ib) star are determined on the basis of atmospheric model with parameters T_{eff}*=6250K, logg=1,5,* ξ_t*=5km/sec.*Analysis of chemical composition is carried out on the base of relatively weak lines. These lines are formed at deep layers of the atmosphere, these plane parallel are in the state of

Local Thermodynamic Equilibrium (LTE). Weak lines are microturbulent and less sensitive to the errors of attenuation. Fig.3 demonstrates comparison between chemical compositions of the Sun: $\Delta\log\varepsilon=\log\varepsilon_{*}-\log\varepsilon_{\odot}$.

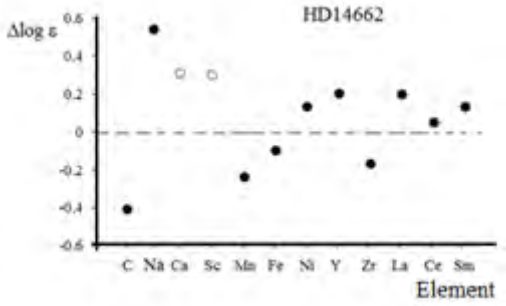

Fig. 3. Comparison of chemical composition of a HD14662 (F7Ib) star with the Sun's chemical composition

As can be seen quantities of most of elements in the atmospher ofHD14662 (F7Ib) star is close the quantity found in the Sun's atmosphere. In particular deficiency of element C and excess of element Na have been revealed.

5. Conclusions

1. Effective temperature and acceleration due to gravity in the atmoisphere of aHD14662 (F7Ib) star were determined by use the model method: $T_{eff}=6250\pm200K$, $logg=1,5\pm0,2$.

2. The speed of microturbulent movement was determined on the basis of FeI lines: $\xi_t=5$km/san.

3. The quantity of chemical elements in the star's atmosphere was determined.Quantities of most of elements in the atmospher of HD14662 (F7Ib) star is close the quantity found in the Sun's atmosphere. Deficiency of element C and excess of element Na have been revealed.

References

1. Khalilov et al. (Khalilov AM, Hasanova AR, Samedov ZA), Azerbaijan Astronomical Journal, 4, v. 6, 16-21, 2001.

2. Lyubimkov et al (Lyubimkov LS, Rachkovskaya TM, Poklad DB), Astrophysics, 52, 237 2009.

3. Lyubimkov LS, Chemical composition: Method and results of analysis, Odessa, Astroprint, 1995.

Generation of second optical harmonic in the nonlinear regime

Z.H.TAGIYEV[1], SH.SH.AMIROV[1,2], N.V.KERIMLI[1]

E-mail: phys_med@mail.ru
1.Chair of Medical Physics and Informatics at Azerbaijan Medical University
2.Department of Electronics, Telecommunications and Radio Engineering, Khazar University, Baku, Azerbaijan

Abstract

The second harmonic in the nonlinear regime is considered in the constant intensity approximation. This method has allowed to take into account reverse reaction of generated wave on the phase of fundamental one. In contrast to constant field approximation there is dependence of spatial beats of amplitude of harmonic wave versus intensity of powerful wave. It is shown that with increase in intensity of the incident pump wave, the period of spatial beats reduces and hence the width of central maximum is narrowed. The value of phase-mismatch at which the harmonic amplitude reaches maximum is a function of intensity of fundamental wave.

Key words:*second harmonic, constant intensity approximation, nonlinear regime*

1. Introduction

Up to now to investigatethe mutual interaction of waves in nonlinear media different approximations were used $[1-7]$. In the most widely used constant field approximation (CFA)[2] an amplitude and phase of fundamental wave are considered to be constant and hence reverse reaction of a new generated or amplified wave on the wave with fundamental frequency is neglected. Therefore information characterizing qualitatively the nonlinear process is partially lossed. As distinct from this approxiation the reverse reaction of generated wave on the phase of fundamental wave can be taken into account in the constant intensity approximation (CIA)$[3-5]$. In this approximation no limitation is imposed to the phases of interacting waves and this fact has allowed to take into account simultaneous influence of phase mismatch and linear losses in medium on the nonlinear processess.

2.Theory

Nonlinear interaction of waves in dissipative media is described by the set of reduced equations [3].

$$\begin{aligned}\frac{dA_1}{dz}+\delta_1 A_1 &= -i\gamma_1 A_2 A_1^* e^{i\Delta_1 z},\\ \frac{dA_2}{dz}+\delta_2 A_2 &= -i\gamma_2 A_1^2 e^{-i\Delta_2 z}.\end{aligned} \quad (1)$$

where indices “1” and “2” belong to the fundamental wave of frequency ω_1 and harmonic wave of frequency $\omega_2 = 2\omega_1$ respectively, $A_{1,2}$ –refer to the complex amplitudes of interacting waves,$\delta_{1,2}-$ are coefficients of linear losses, $\gamma_{1,2}$ −indicate nonlinear coefficients of coupling, $\Delta = k_2 - 2k_1$ is the phase mismatch,$k_{1,2}-$ are the wave numbers. Note, that the parameter Δ plays important role for the spatial distribution of electromagnetic wave over the crystal.

Solution of the system(1) in the constant intensity approximation($I_1(z) = I_1(z=0) = I_{10}$) with boundary conditions $A_1(z=0) = A_{10}$, $A_2(z=0) = 0$ is given by the following formula

$$A_2 = -i\gamma_2 A_{10}^2 z\,sinc\lambda z\, e^{-\frac{\delta_2+2\delta_1+i\Delta}{2}z} \quad (2)$$

here$\lambda^2 = 2\Gamma^2 + \{[\Delta + i(\delta_2 - 2\delta_1)]/2\}$, $\Gamma^2 = \gamma_1\gamma_2 I_{10}$, $sincx = \frac{sinx}{x}$

When $\gamma_1 = 0$ ($\Gamma = 0$) from (2) the result of constant field approximation is obtained.From this relationship is seen that unlike the constant field approximation in the constant intensity approximation amplitude of second harmonics reaches maximum at definite value of intensity I_{opt}. of fundamental wave . The optimum intensity in turn is a function of other parameters-phase difference, length of nonlinear medium , etc.

2. Results and Discussions

In the constant intensity approximation unlike the constant field approximation the argument of trigonometric function depends on the intensity (via $\Gamma^2 = \gamma_1\gamma_2 I_{10}$) of fundamental wave. When condition $\delta_2 = 2\delta_1$ for linear losses of medium satisfies the argument of trigonometric function in formuila (2) is simplified

$$\lambda z = \sqrt{2\Gamma^2 z^2 + \frac{\Delta^2 z^2}{4}} \quad (3)$$

Thus we obtain that unlike the result of constant field approximation ($\gamma_1 = 0$) the period of spatial beats of second harmonics depends on the intensity of fundamental wave. With increase of

intensity of fundamental wave the period of spatial beats decreases and hence the width of central maximum is narrowed. Maximum of amplitude of second harmonics is obtained under condition $\lambda z = \pi/2$. In other words at definite value of Δ (we denote it through Δ_m) in the phase beats along z-axis the amplitude of second harmonic reaches its maximum when

$$\frac{\Delta_m l}{2} = \left[\frac{\pi^2}{4} - 2\left(\frac{l}{l_{n/l}}\right)^2\right]^{1/2} (4)$$

As can be seen from relationship (4) in the constant intensity approximation the parameter $\frac{\Delta_m l}{2}$ characterizing the difference in wave numbers (phase mismatch) also is the function of intensity (via $\Gamma^{-2} = \gamma_1\gamma_2 I_{10}$,$l_{n/l} = \Gamma^{-1}$) of fundamental wave. In Fig.1 the dependence of reduced phase difference Φ_{max} ($\Phi_{max} = \Delta_m l/2$) on the parameter $l/l_{n/l}$is presented. Here the curve (1) corresponds to the result of constant field approximation, curves (2) and (3) refer to the results of accuratesolution and constant intensity approximation respectively. As can be seen from graphs the result of constant intensity approximation corresponds to the result of accurate calculation at $l/l_{n/l} \leq 0{,}7$, while result of constant field approximation is near to the result of exactsolution at the proximity of$l/l_{n/l} = 0$ only. When $l/l_{n/l} = 1$results of constant intensity and constant field approximations differ from the result of accurate solution as 36,7 % and 46% respectively. According to equation (2) the efficiency of conversion to second harmonics is given by ($\gamma_1 = \gamma_2$) :

$$\eta_2 = \rho^{-1}\Gamma^2(sin^2 x + sh^2 y)\cdot e^{-(\delta_2+2\delta_1)z} (5)$$

where $x = \sqrt{\rho}z(cos\varphi/2)$, $y = \sqrt{\rho}z(sin\varphi/2)$, $\rho^2 = a^2 + b^2$

$$a = 2\Gamma^2 + \frac{\Delta^2}{4} - \left(\frac{\delta_2 - 2\delta_1}{2}\right)^2, \quad b = \Delta\cdot\frac{\delta_2 - 2\delta_1}{2}, \varphi = tan^{-1}\frac{b}{a}$$

At phase matching conditions ($\Delta = 0$) expression (5) is simplified and takes the form($\delta_2 = \delta_1 = \delta$) :

$$\eta_2 = \Gamma^2 z^2 \cdot sinc^2\frac{\sqrt{8\Gamma^2 - \delta^2}z}{2}\cdot e^{-3\delta z} (6)$$

Accurate solution of the set of equations (1) at phase matching conditions ($\Delta = 0$) for the second harmonic efficiency yields [1]

$$\eta_2 = th^2\left[\frac{\Gamma}{\delta}\left(1 - e^{-\delta z}\right)\right]\cdot e^{-2\delta z} (7)$$

At phase-matching condition ($\Delta = 0$) efficiency of second harmonic in the constant field approximation is given by

$$\eta_2 = \Gamma^2 z^2 \cdot sinc^2\frac{\delta z}{2}\cdot e^{-3\delta z} (8)$$

From comparison of above equations (6) and (8) it is seen that as distinct from constant field

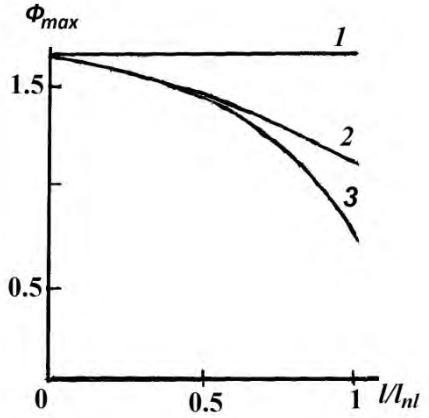

Fig.1Dependence ofΦ_{max} on the parameter $l/l_{n/l}$: 1-constant field approximation, 2- accurate solution, 3-constant intensity approximation.

approximation the argument of trigonometric function depends on the intensity of fundamental wave in the constant intensity approximation .In Fig.2. the efficiency of second harmonics is illustrated as a finction of paramater of linear losses. Here the dotted curve corresponds to the constant field approximation. Solid and dashed curves are plotted for accurate solution and constant intensity approximation respectively. Again as can be seen the result of constant intensity approximation is more near to the result of accurate solution as compared to the constant field approximation.

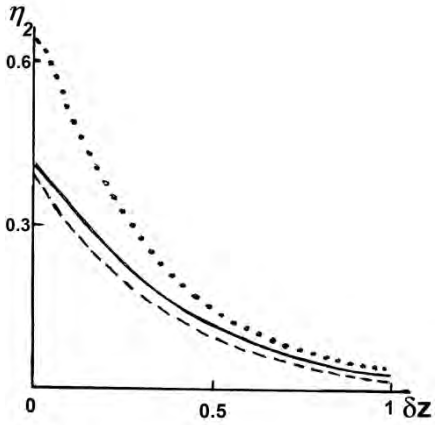

***Fig.2** Efficiency of second harmonic as a function of linear losses : Dotted curve- constant field approximation; solid curve- accurate solution; dashed curve- constant intensity approximation.*

Thus, since the result of constant intensity approximation is near to the result of accurate calculation its employment for the analysis of the process of nonlinear mutual interaction is reasonable.

References :

1. S.A.Akhmanov and R.V.Khokhlov,Problems of nonlinear Optics (in Russian), M: VINITI,1964,295 p.
2. N.Blombergen,Nonlinear Optics (in Russian) Moscow,Mir,1966,424 p.
3. Z.A.Tagiev and A.S.Chirkin.Constant intensity approximation in the theory of nonlinear waves in dispersed media (in Russian), JETF,Vol.73,issue 4,pp.1271-1282,1977.
4. Z.H.Tagiyev. Theory of nonlinear waves in the constant intensity approximation (in Russian), Baku, ELM,2003, 239p.
5. V.G.Dmitriev, A.V.Tarasov .Applied nonlinear optics. Moscow, Radio isvyaz, 1982,352 p.
6. R.J.Kasumova . Theory of nonlinear interaction of optical waves in the constant intensity approximation (in Russian). Baku, ELM,2001, 187p.
7. E.A.Ibragimov,T. K. Usmanov. Strong interaction approximation in the theory of nonlinear waves.(in Russian)JETF, Vol.86, No 5, p.1618, 1984.

A study of structural and thermal properties of HDPE+ZrO_2 nanocomposites by x-ray diffraction and differential thermal analysis

A. A. NABIYEV[a,b], A. KH. ISLAMOV[b], A. M. MAHARRAMOV[a], R. S. ISMAYILOVA[a], M. N. MIRZAYEV[a,e], A.S. DOROSHKEVIC[b,f], V.A.TURCHENKO[b], M.I. RULEV[b,d], A. I. KUKLIN[b,c]

[a]*ANAS Institute of Radiation Problems, 9 B. Vahabzade str., AZ1143 Baku, Azerbaijan*
[b]*Joint Institute for Nuclear Research, Joliot-Curie 6, 141980 Dubna, Moscow region, Russia*
[c]*Moscow Institute of Physics and Technology, MIPT,141701 Dolgoprudny, Russia*
[d]*Moscow State University,119991 Moscow, Russia*
[e]*National Nuclear Research Center, AZ1073 Baku, Azerbaijan*
[f]*Donetsk Institute for Physics and Engineering named after O.O.Galkin of the NAS of Ukraine, 03680, Nauki ave, 46, Kyiv, Ukraine*

asifnebi@jinr.ru

Abstract

X-ray diffraction (XRD) and differential thermal analysis (DTA) of HDPE+ZrO_2 nanocomposites were carried out in this work. Pure HDPE thin film, HDPE+ZrO_2 (1-20%) nanocomposites materials and ZrO_2 powder (particles of size 20-30 nm) were studied. Results of XRD analysis showed that ZrO_2 powder was crystalized both in monoclin and in cubic phase under normal conditions. The percentages of monoclinic and cubic phase was found to be 99.8% and 0.2%, respectively. The phase group and the symmetry of the ZrO_2 powder and HDPE+20%ZrO_2 nanocomposites was determined. Endothermic and exothermic effects were studied for these materials in temperature range of 25 - 160^{0}C by differential thermal analysis. Melting and crystallization temperature ranges were defined for HDPE+20% ZrO_2 nanocomposites.

Key words: *Nanocomposite, High Density Polyethylene, ZrO_2, X-ray diffraction, Differential thermal analysis, Enthalpy*

1. Introduction

In the past decade, a new generation of polymers such as ultra-high-molecular-weight polyethylene (UHMWPE) are being used as a matrix by applying nanotechnology approaches reinforcing the base polymers with nanoparticle additives in order to improve the properties of HDPE [1]. In this case it becomes possible to adjust the structure and properties of the materials in wide range due to nucleating and orientation effects, changes in conformation of macromolecules, their chemical binding to the surface of nanosize particles and “healing” of defects in the structure.

ZrO_2 is one of the interesting oxide materials which is used as nanoparticle in the base polymers in order to improve their properties. This oxide material has already found a wide range of applications in different fields such as; photonics, interferometry filter and for coating high power laser mirrors due to its hardness, optical transparency and high refractive index [2,3]. ZrO_2 is a polymorphic material existing in three cristalline forms: monoclinic, tetragonal and cubic. The monoclinic phase is stable below 1170°C , the tetragonal at the temperature range of 1170-2370°C and the cubic at over 2370°C [3,4,5,6]. However, noticeable changes accur in volume during the monoclinic to tetragonal transformation a 5% decrease when zirconium oxide is heated and conversely, a 3%-4% increase during the cooling process [7,8].

HDPE has a number of promising electrophysical [9], electret [10] and optical [11] properties in applied approaching, that make them

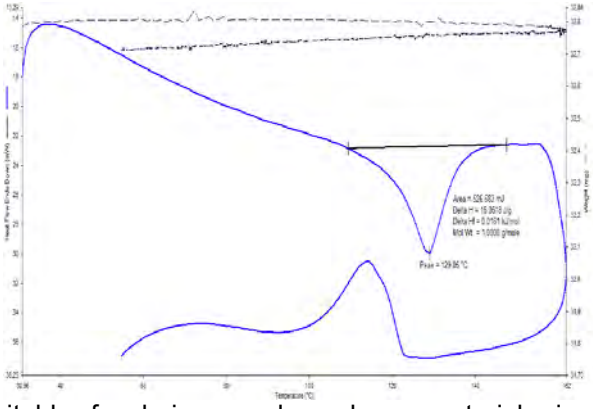

suitable for being used as base materials in development of new sensors, photovoltaic cells, various sensors, piezomaterials, etc. [12,13,14]. These types of nanocomposite materials have strong physical properties in comparison with ordinary polymers and leads to find wide application area. Polymer nanocomposites are

considered constructial and industrial materials of the 21st century.

Properties of polymers has strong dependendence on the degree of crystallization. In term the degree of crystallization dependends on crystallization [15]. The effect of nano-particles of polymer chains formed by macromolecules is theoretically and experimentally studied by researchers. There are modern main methods which are used to study the properties and structures of the polymer nanocomposites. In this study, properties of HDPE+ZrO_2 nanocomposite materials have been investigated using two methods (XRD and DTA) .

Table 1. Characteristic temperatures and melting enthalpy from DTA spectra

HDPE+ %ZrO_2	Area , mJ	Enthalpy ΔH, J/g	T_i, ^{0}C	T_m, ^{0}C	T_f, ^{0}C	ΔT	T_{cryst}, ^{0}C
0	2858.67	51.54	113	129	138	25	112.5
1	679.61	18.81	116	124	141	25	114.0
3	822.68	32.11	118	130	142	24	115.6
5	760.07	30.13	115	130	140	25	115.0
10	444.57	18.67	115	126	141	26	116.2
20	526.68	16.06	115	129	142	27	117.3

2. Experiment

The experiments has been carried out on “Perkin Elmer” STA 6000 device. This device is equipped with PolyScience analyzer and "digital temperature controller" cooling system and allows to do experiments in the temperature range of 16 - 1000 °C with thermal processing speed of 5-20 ^{0}C/min. It is given 20 mL/min speed to the system. Inert argon gas is used to prevent condensation process and to remove combustion products from the system. The standard aluminum-oxide-based pan of 177.78 mg have been used for samples. Endo and exothermic thermal effects have been proceed using “Pyris” software. Kinetic parameters are calculated using “Pyris” software, too. DTA analysis spectra are shown in Fig.1 for pure HDPE (upper) and 20% HDPE + ZrO_2 (bottom) composite materials.

As shown in Fig. 1. (upper) the melting and crystallization temperature for HDPE are 129.05 ^{o}C and 114.87 ^{o}C, respectively.

From the upper curve, it is shown that the polymer started to lose its solid form at around 85 ^{o}C. It is the glass transition temperature of HDPE. The onset melting point appears at 129.05 ^{o}C which is an endothermic process. It is noticed that, glass transition does not occure in fully crystalline polymers and they remain their structure until the melting point. For that reason, HDPE is considered as semi crystalline polymers. As the temperature increases, the rate of heat flow rises until it reached to the melting point of HDPE (129.05 ^{o}C). Then an exothermic process (energy releasing) starts until the end point at 141.1 ^{o}C. Total energy consumption between the beginning and end of melting point is 2858.669 mJ for the process. The amount of energy is equal to 51.5391 J/g. The cooling cycle and the rate of cooling temperature is 10 ^{o}C/min in the experiment. An exothermic process begins at the onset point appeared at 129.05 ^{o}C. The peak point is equal to 114.87 ^{o}C. The solidification or (re-crystallization) of HDPE ends at 85 ^{o}C. The released energy is found from the integral under the curve of cooling area. DTA analysis results for pure HDPE and 1-20% HDPE + ZrO_2 are given in Table 1. Some characteristic temperatures and melting enthalpy are calculated from DTA spectra. The definition of phase composition and type of crystal structure has been performed on the conventional X-ray diffractometer EMPYREAN (firm PANalytical) in Cu- Kα radiation with Ni filter in the room temperature (25 ^{0}C). The operation mode of the device was 40 kV voltage and 30mA current. The scanning has been done with a step of 0.026^0 and 2 s per step for 2θ. Analysis of phase composition and type of crystal structure of composite material has been performed using ICDD database. Observable diffraction lines of ZrO_2 are coincide with monoclinic structure P 21/c1 of baddeleyite described early in reference [18]. X-ray diffraction (XRD) patterns of 20% HDPE + ZrO_2 and powder ZrO_2 are shown in Fig. 2. HDPE has two diffraction peaks when 2θ is between 20° and 25°. The 2θ with corresponding crystalline lattices for HDPE are 21.67° (110) and 24.41° (200) being composed of orthorhombic crystals [16, 17]. HDPE +ZrO_2 nanocomposites and ZrO_2 have identical crystalline lattices,except for 2θ = 21.67°.

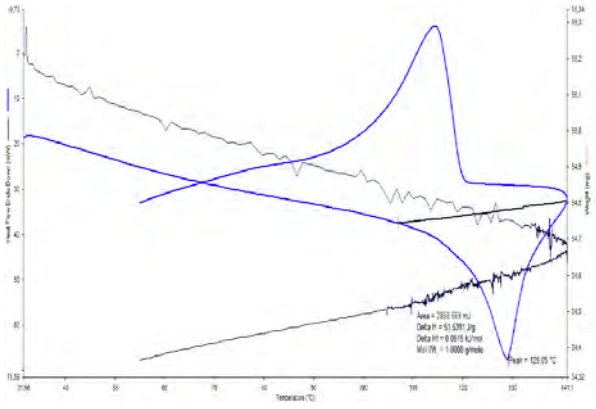

Fig. 1. DTA analysis spectra of pure HDPE (upper) and 20% HDPE + ZrO2 (bottom) polymer composite materials

As shown from the XRD graph (Figure 2), ZrO_2 does not affect the main chemical structure of HDPE. As a result, ZrO_2 and HDPE acquires monoclinic and orthorhombic phase, respectively.

Obtained XRD results are used for building monoclinic structure of ZrO_2 using Diamond software. The structure is shown in Fig. 3.

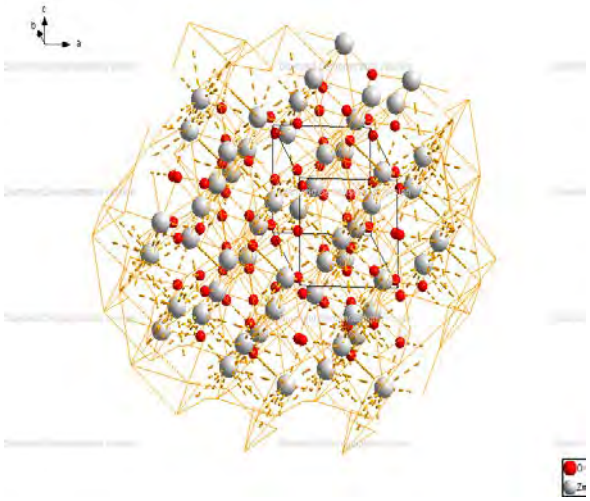

Fig. 3. Structure for monoclinic phase of ZrO_2. Oxygen atoms are shown in red and zirconium atoms in grey. The black square shows the unit cell.

3. Conclusions

It has been observed that melting and the crystallization temperature of HDPE+ZrO_2 nano-composites ranges between 125 – 131 ^{0}C and 112 – 118 ^{0}C, respectively. The temperature difference, however, ranges between 24-27 ^{0}C depending on the filler volume. The melting enthalpy has been decreased between 16 - 52 J/g depending on the filler volume. From X-ray diffraction measurements it is determined that the structure of pure ZrO_2, as well as the structure of HDPE + 20% ZrO_2 nanocomposites has monoclinic symmetry and belonged to the space group of P1 21/c1 (14). The following values have been calculated for the crystal lattice parameters: a=5.149094 Å, b=5.209923 Å, c=5.318393 Å, $\alpha=\gamma=90^0$, β=99.214710 Å, Z=4, V=140.83210 Å^3. D spacing (lattice period) for the samples ranged between 1.4 – 5.1 Å .

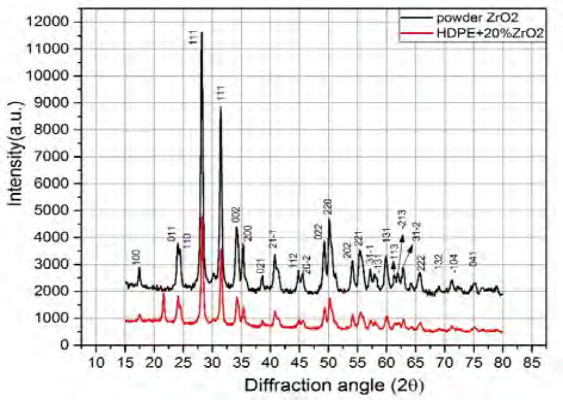

Fig. 2. X-ray diffraction (XRD) patterns of 20% HDPE + ZrO2 and pure HDPE polymer composite materials

References

[1] Selyutin G.E., Gavrilov Y.Y., Voskresenskaya E.N. et. al, Chemistry for sustainable development. **18**, 375-388, (2010).

[2] H.Q. Liu, L.L. Wang, S.G. Chen, B.S. Zou et. al., Compd. **448**, 336–339, (2008).

[3] S. Kumar, S. Bhunia, A. K. Ojha, Physica E **66**, 74–80, 2015.

[4] J.C. Garcia, L.M.R. Scolfaro, A.T. Lino at. al., J. Appl. Phys. **100**,104103–104109, (2006).

[5] Chevalier J, Gremillard L, Virkar AV at. al., *J Am Ceram Soc*; **92**: 1901–1920, (2009).

[6] Suresh A, Mayo MJ, Porter WD at. al., *J Am Ceram*; **86**: 360-362, (2003).

[7] Piconi C, Maccauro G, *Biomaterials*; 20: 1-25, (1999).

[8] Hjerppe J, Vallittu PK, Fröberg K at. al., *Dent Mater*; **25**: 166-171, (2009).

[9] Tyutnev A.P., Saenko V.S., Pozhidaev E.D. at. al., "Dielectric properties of polymers in the fields of ionizing radiation". Under ed. N.S.Kostyukova, M., Nauka, 453, (2005), book 5.

[10] Gorokhovatskiy Y.A., Aniskina L.B., Burda V.V. et. al., Proceedings of Russia pedag.university named after A.I.Gertsen, Scientific journal. - Saint-Petersbourg,№ **95**, 63-66, (2009).

[11] Guo N., Sara A. Di Benedetto at. al.,Chem. Mater., v.**22**, No4, 1567-1578.7, (2010).

[12] Yang D. Advances in nanocomposites-Synthesis, characterization and industral applications. Eds. Boreddy S. R. Reddy Rijeka. Croatia: In Tech., 857-882, (2011).

[13] Thomas Hanemann, and Dorothée Vinga Szabó, Polymer-Nanoparticle Composites: From Synthesis to Modern Applications, Materials, **3**, 3468-3517, (2010).

[14] T. Tanaka, IEEE Transactions on Dielectrics and Electrical Insulation Vol. **12**, No. 5; 914-928, (2005).

[15] By M. J. Richardson, Br. Polym. J., VoI. **1**, (1969).

[16] Inci, B. and Wagener, K.B , J. Am. Chem. Soc., **133**, 11872–11875, (2011).

[17] Liao, C.Z., Tjong, J. Macromol. Sci. B, **52**, 812–825, (2012).

[18] Arashi, H., Takeda, H., Kudoh, Y., Powder Diffraction, **1**, 265 - 275, (1986).

On Possible Source of the Coulomb Potential

ANZOR .KHELASHVILI

Inst. of High Energy Physics, Iv. Javakhishvili Tbilisi State University, University Str. 9, 0109, Tbilisi, Georgia and St.Andrea the First-called Georgian University of Patriarchate of Georgia, Chavchavadze Ave.53a, 0162, Tbilisi, Georgia.
e-mail: anzorkhelashvili@hotmail.com

Abstract
It is shown, that in Dirac's theory with central potential N=2 Witten's supersymmetry appears automatically owing to the conserved Dirac's spin-orbital operator. Generators of this algebra anticommute with spin-orbital operator. If we require their commutativity with the Dirac Hamiltonian then only Coulomb-like potential satisfies to this condition.
Keywords: *Dirac Hamiltonian, Witten's algebra, Coulomb potential.*

1. Introduction and Methodology

Since the discovery of the expanding universe through measuring the red shift of the spectral lines from distant galaxies by E. Hubble in 1929, it is considered that the early universe is in extreme conditions, i.e. high density and high temperature state. When the universe had cooled to the recombination temperature, the protons capture the free electrons and the universe is filled with neutral atoms. After the charged particles are bound in neutral atoms, the universe becomes transparent to radiation. The released photon survives for the age of the universe. A. Penzias and R. W. Wilson discovered the relic photon as the cosmic microwave background (CMB) in 1965. Nowadays the fluctuations of the Cosmic Microwave Background (CMB) is precisely observed by Planck satellite [1].

There are well-known problems in a simple big-bung cosmology, horizon problem, flatness problem, monopole problem, singularity problem and so on. Primordial inflation, an exponential expansion of the early universe, gives a solution for such cosmological problems. A broad class of the particle physics models have been proposed as practical models of the inflation theory. For example, the potential energy of the Higgs like scalar can induce the inflationary expansion in early universe. However, there is not a small possibility where composite states constructed by fermion fields dominate the energy density of the early universe [2-5].

It is considered that the fluctuation of CMB is originally generated by the quantum fluctuation of the inflaton field which induces the inflation. There is a possibility to test the model of inflation from the thermal fluctuation of CMB. Thus, we have lunched a plan to find a fermionic model of inflation and test the model by observing the CMB fluctuations. In this paper, we consider the gauged Nambu-Jona-Lasinio (gNJL) model as a simple prototype model of composite scalar. Evaluating the CMB fluctuations, we show a characteristic feature of the model. A possibility of the CP violation and the domain wall problem are discussed.

2. Conclusions

As is well known the Coulomb potential, characterizing the electrostatic interaction between charged particles, has the following form

$$V(r) = -\frac{a}{r} \qquad (1)$$

The same dependence on distance r has also the gravitational potential. This regularity is known from 18th century experimentally.

Our question is the following: What is a theoretical justification for this behavior? We mean classical as well as quantum physics. In classical physics the most popular point of view is a Gauss law, which in fact says about dimensionality of space. In quantum theory, especially in quantum field theory, propagator of massless field (photon) in the static approximation corresponds to Coulomb interaction. Indeed, the massless particle propagator is proportional to

$$\Delta \sim \frac{1}{q^2 + i\varepsilon} \Rightarrow -\frac{1}{\boldsymbol{q}^2}, \qquad F.T. \sim \frac{1}{r} \qquad (2)$$

In this report we want to propose another mechanism for arising the Coulomb potential. In this purpose we consider the Dirac Hamiltonian in the central field

$$H = \boldsymbol{\alpha} \cdot \boldsymbol{p} + \beta m + V(r) \qquad (3)$$

It is known that the total momentum $\boldsymbol{J} = \boldsymbol{l} + \frac{1}{2}\boldsymbol{\Sigma}$ commutes with above Hamiltonian. Here $\boldsymbol{l}$ is an orbital momentum operator $\boldsymbol{l} = \boldsymbol{r} \times \boldsymbol{p}$, while $\boldsymbol{\Sigma}$ - spin-matrix, $\boldsymbol{\Sigma} = diag(\boldsymbol{\sigma}, \boldsymbol{\sigma})$. Here and further we use the Dirac representation for his matrices. Besides there is one more commuting operator, so-called Dirac's spin-orbital matrix,

$$K = \beta(\boldsymbol{\Sigma} \cdot \boldsymbol{l} + 1) \qquad (4)$$

This matrix commutes also with Dirac Hamiltonian (3) for any central symmetric potential, whereas in most textbooks its commutativity with Hamiltonian is exhibited only for free particle case. I want to underline that this operator has a little attention in textbooks, mainly because it is not related to some transformation, probably.

Below we demonstrate that some interesting things may

be derived by using this matrix.

First of all remark that this matrix commutes with β and anticommutes with γ_5 matrices

$$\left[K,\beta\right]=0, \qquad \left\{K,\gamma_5\right\}=0 \tag{5}$$

By reasons specified below we will be interested in operators, which anticommute with K apart from γ_5.

Suppose that such an operator is Q. Then it is clear that the product

$$\tilde{Q}=i\frac{QK}{\sqrt{K^2}}=i\frac{QK}{|\kappa|}, \tag{6}$$

where κ is an eigenvalue of K, would also be anticommuting with K, i.e.

$$\left\{\tilde{Q},K\right\}=0, \qquad if \qquad \left\{Q,K\right\}=0 \tag{7}$$

Moreover

$$\tilde{Q}^2=Q^2$$

Let us for convenience introduce notations

$$Q=Q_1, \qquad \tilde{Q}=Q_2 \tag{8}$$

Then the derived relations can be rewritten in the following algebraic form:

$$\left\{Q_i,Q_j\right\}=2\delta_{ij}, \qquad (i,j=1,2)$$
$$\left[Q_i^2,Q_k\right]=0, \ \Rightarrow \left[h,Q_k\right]=0; \qquad (k=1,2) \tag{9}$$

Where

$$h\equiv Q_i^2 \tag{10}$$

We see, that the Witten's $N=2$ superalgebra is reproduced, where Q_1,Q_2 are generators and $h=Q_1^2=Q_2^2$ plays the role of Witten's Hamiltonian [1] .

Therefore, if we have a Dirac problem in central field the Witten's $N=2$ superalgebra appears automatically.

It is natural to ask: under what circumstances would the Dirac Hamiltonian commutative with this superalgebra? Or, equivalently, how the potential must look like in order the Dirac Hamiltonian be commuting with this superalgebra? I.e. when we have a supersymmetry of Dirac problem,

$$\left[Q_i,H\right]=0 \tag{11}$$

So, our aim is to construct the operator which anticommutes with the Dirac matrix $\left\{Q,K\right\}=0$ and at the same time, commutes with Dirac Hamiltonian (3), i.e. $\left[Q_i,H\right]=0$. The last requirement means that we must have a N=2 supersymmetry of (3).

By this aim let us make use of auxiliary theorem:

Let $\boldsymbol{\upsilon}$ be a vector with respect to the angular momentum $\boldsymbol{l}$, i.e. $\left[l_i,\upsilon_j\right]=i\varepsilon_{ijk}\upsilon_k$ or in the vector product form $\boldsymbol{l}\times\boldsymbol{\upsilon}+\boldsymbol{\upsilon}\times\boldsymbol{l}=2i\boldsymbol{\upsilon}$. Suppose also that this vector is perpendicular to $\boldsymbol{l}$. i.e. $\left(\boldsymbol{l}\cdot\boldsymbol{\upsilon}\right)=\left(\boldsymbol{\upsilon}\cdot\boldsymbol{l}\right)=0$ .Then K antcommutes with operator $\left(\boldsymbol{\Sigma}\cdot\boldsymbol{\upsilon}\right)$, which is a scalar with respect to the total momentum $\boldsymbol{J}=\boldsymbol{l}+1/2\boldsymbol{\Sigma}$.

The proof of this theorem is straightforward [2] .

It is evident that the class of anticommuting with K (so called K-odd) operators is not restricted by these operators only – any operator of kind $\hat{O}\left(\boldsymbol{\Sigma}\cdot\boldsymbol{\upsilon}\right)$, where $\hat{O}$ is commuting with K, but otherwise abbitrary, also is K-odd.

The next step is a construction of most general desired operator Q. There remains still considerable freedom of choice here because of above remark about $\hat{O}\left(\boldsymbol{\Sigma}\cdot\boldsymbol{\upsilon}\right)$. We can take $\hat{O}$ into consideration or ignore it. Let us choose as the starting point the following basis vectors at hand $\hat{\boldsymbol{r}}$ and $\boldsymbol{p}$

and probe the following combination of diagonal and antidiagonal matrices

$$Q=x_1+ix_2K\left(\Sigma\cdot p\right)+ix_3K\gamma_5 f\left(r\right) \tag{12}$$

Here the coefficients are chosen in such a way that Q be Hermitian, with $x_{1,2,3}$ arbitrary real numbers and $f\left(r\right)$ is an arbitrary real scalar function to be determined by the symmetry requirement. Moreover Q in (13) is one of Q_i -s. Calculating the commutator , and requiring commutativity we obtain

$$\left[Q,H\right]=\left(\boldsymbol{\Sigma}\cdot\hat{\boldsymbol{r}}\right)\left\{x_2V'\left(r\right)-x_3f'\left(r\right)\right\}+$$
$$+2i\beta K\gamma_5\left\{\frac{x_1}{r}-mf\left(r\right)\right\}=0 \tag{13}$$

This equality is satisfied if the coefficients of diagonal and antidiagonal matrices equal to zero separately ,i.e.

$$x_2V'\left(r\right)=x_3f'\left(r\right), \qquad x_3mf\left(r\right)=\frac{x_1}{r} \tag{14}$$

It follows from these relations that

$$V\left(r\right)=\frac{x_1}{mx_2}\frac{1}{r} \tag{15}$$

4. Conclusions

In the very general framework we have shown that **the *only central potential for which the Dirac Hamiltonian has an additional N=2 supersymmetry in the above sense***

is a COULOMB POTENTIAL, and vice versa, *from the requirement of supersymmetry of the Dirac Hamiltonian in the central potential it follows unambiguously that only the Coulomb potential satisfies this requirement.*

Can we suppose that the possible source of the Coulomb potential is the Witten's N=2 supersymmetry? It seems that Yes.

This fact manifests itself in the Dirac Hamiltonian, because it describes the spin-1/2 particles and the above-mentioned superalgebra appears in the first time.

It is evident that this result takes place also in case of scalar potential or for arbitrary combination of scalar and forth component of Lorentz vector [2].

References

1.E. Witten Nucl. Phys B.1981.v.188.p.513.

2. T. Khachidze and A. Khelashvili "Dynamical symmetry of the Kepler-Coulomb Problem in classical and Quantum Mechanics"(Non-relativistic and Relativistic) NewYork.:Nova Science Publishers, Inc., 2008.

Spontaneous breaking of conformal symmetry in the Standard Model

A.B. ARBUZOV 1,2), R.G. NAZMITDINOV 1,3), A.E. PAVLOV 4), V.N. PERVUSHIN 1), A.F. ZAKHAROV 1,5)

1) Bogoliubov Laboratory for Theoretical Physics, Joint Institute o f Nuclear Research, Dubna, 141980, Russia 2) Department o f Higher Mathematics, Dubna State University, Dubna, 141980, Russia 3) Department de Fisica, Universitat de les Illes Balears, Palma de Mallorca, E-07122, Spain 4) Moscow State Agri-Engineering University, Moscow, 127550, Russia 5) Institute o f Theoretical and Experimental Physics, Moscow, 117259, Russia
e-mail: arbuzov@theor.jinr.ru

Abstract
Radiative mechanism of conformal symmetry breaking in a conformal-invariant version of the Standard Model is considered. The Coleman-Weinberg mechanism of dimensional transmutation in this system gives rise to finite vacuum expectation values and, consequently, masses of scalar and spinor fields. A natural bootstrap between the energy scales of the top quark and Higgs boson is revealed.

Keywords: *Spontaneous symmetry breaking, the Standard Model, the Higgs mechanism*
PACS No: 11.15.Ex Spontaneous breaking of gauge symmetries 14.80.Bn Standard-model Higgs bosons 11.25.Hf Conformal field theory, algebraic structures.

1. Introduction

In spite of the Higgs boson discovery, we still do not know the origin of the electroweak energy scale. The same concerns the question about the origin of the QCD energy scale Λ_{QCD}. There is a principal difference in the treatment of these two scales in the Standard Model (SM). Namely, the electroweak scale $\sim 100\,GeV$ is provided by the value of the tachyon mass parameter in the primary SM Lagrangian, while the QCD scale is even not related to any parameter of the SM Lagrangian. It is commonly assumed that Λ_{QCD} appears due to the dimensional transmutation mechanism [1] due to the QCD conformal anomaly. Here we will discuss a modification of the Higgs mechanism [2,3], which was suggested in paper [4]. We consider a reduction of the electroweak SM to its conformal-invariant version and show that the Coleman-Weinberg (CW) mechanism of the dimensional transmutation gives rise to condensates and masses for scalar (the Higgs boson) and fermion (the top quark) fields.

The SM assumes that the spontaneous breaking of the global symmetry in the Higgs sector [1,2] happens because the presence of the tachyon-like mass term ($m^2 < 0$) in the potential

$$V_{Higgs}(\phi) = \frac{\lambda^2}{2}|\phi|^4 + m^2|\phi|^2,$$

where one component of the complex scalar doublet field acquires a non-zero vacuum expectation value $\langle\phi^0\rangle = v/\sqrt{2}$ with $v \approx 246.22\ GeV$. Note that the tachyon-like mass term is the only fundamental dimensionful parameter in the SM and it breaks the conformal symmetry explicitly. This explicit symmetry breaking leads to the very serious problem of *fine ing* (or *naturalness,* or *hierarchy)* in the renormalization of the Higgs boson mass. In fact, renormalization of the Higgs boson mass is not protected by any symmetry from running to extremely high values, e.g. to the Planck mass. On the other hand, it was found that the measured value of the Higgs boson mass makes the SM being self-consistent up to very high energies tending to the Planck mass scale [5,6,7]. Meanwhile the coincidence of the energy scales of the top quark mass and the Higgs boson one represents another puzzle in the SM.

Various dynamical mechanisms of electroweak symmetry breaking were considered in the literature, see e.g. review [8]. Most of those approaches required introduction of new interactions beyond the SM, which are restricted very much by modern experiments. In this paper we suggest to provide a radiative stability of the Higgs boson mass by ensuring by the classical scale invariance following the idea by W.Bardeen [9].

S. Coleman and E. Weinberg have shown [1] that the renormalization of several classical scale-invariant Lagrangians leads to spontaneous breaking of the scale invariance. The key reason is that those model possess an instability with respect to infrared singularities at the quantum level. In the present paper we extend the Coleman-Weinberg formalism of the radiative symmetry breaking for a system of scalar and fermion fields joined by Yukawa interactions.

2. Radiative Symmetry Breaking

Let us start at the classical level with the conformal-invariant Lagrangian describing one scalar and one fermion field:

$$L_{cl} = \frac{1}{2}\left|\partial_\mu \phi_c\right|^2 - \frac{\lambda^2}{2}\left|\phi_c\right|^2 + i\bar{\psi}_c\gamma_\mu\partial_\mu\psi_c - y\phi_c\bar{\psi}_c\psi_c,$$

where ϕ_c and ψ_c are classical massless scalar and spinor fields, respectively. This model is obviously renormalizable. At the quantum level (index c is then removed) we have to add counter terms of all possible kinds:

$$L_{c.t} = \frac{1}{2}A\left|\partial_\mu\phi\right|^2 - \frac{1}{2}B\left|\phi\right|^2 - \frac{1}{2}C\left|\phi\right|^4 +$$
$$+ iD\bar{\psi}\gamma_\mu\partial_\mu\psi - E\bar{\psi}\psi - G\phi\bar{\psi}\psi + F\phi.$$

The classical scale invariance provides the explicit condition for the mass-like counter terms B and E: they should cancel out with the relevant loop diagram contributions. Note that in the one-loop approximation the term $F\phi$ corresponds to the tadpole fermion loop diagram, i.e. $(\bar{\psi}\psi)$. The latter is proportional to the integral $\int \frac{d^4k}{i\pi^2}\frac{Tr\left(k_\mu\gamma_\mu + m_f\right)}{k^2 - m_f^2 + i0}$, which is exactly zero for a massless fermion ($m_f = 0$). However due to the CW mechanism, the classical scale invariance in such a model breaks down because of infrared instabilities in quantum loop corrections. For this reason the renormalization point should be shifted away from the origin to some finite value $\phi = M \neq 0$, where M is a finite energy scale. This is the case of *dynamical* or *spontaneous* symmetry breaking, and the classical symmetry continues guiding the system.

As the result, the so called dimensional transmutation happens: one dimensionless parameter of the classical Lagrangian can be traded for a dimensionful one. After shifting the renormalization point from $\phi = 0$, we have to perform the following steps: 1) look for the minimum of the effective potential; 2) analyze the masses of our fields in this point; 3) and test the stability of the system in the resulting potential. The latter condition should be the principal one in construction of a physical model.

As was proved by Coleman and Weinberg [1], even a pure φ^4 self-interaction of a scalar field gives rise to radiative breaking of the conformal symmetry. However, to obtain a stable solution for the effective potential minimum they added coupling to a gauge field. In our model we use instead a Yukawa coupling to a fermion field. This field yields an additional contribution to the effective potential and helps effectively to reach a stable minimum in the perturbative domain of the coupling constant values.

Let us discuss the fermion condensate $(\bar{\psi}\psi)$. Its value is proportional to the integral shown above. The latter is extremely unstable with respect to appearance of a mass of the fermion. Direct calculations show that even a tiny (but non-zero mass) makes this integral being quadratically divergent $(\bar{\psi}\psi) \sim m_f\Lambda^2$, where Λ is an ultraviolet cut-off. Then it should be renormalized by a corresponding counter term. The classical conformal symmetry condition explicitly requires the complete cancellation of this divergent loop contribution by the corresponding counter term $E(\bar{\psi}\psi)$. But the complete cancellation doesn't happen if we shift the renormalization point away from the origin.

Therefore, we make the conjecture that our model possesses a loop-back effect: i) if a non-zero value for the scalar field condensate appears (e.g. due to a quantum effect), it immediately yields a mass for the fermion; ii) the fermion field creates also a non-zero (even divergent) condensate; iii) the condensate allows to the scalar field to have a nonzero vacuum expectation value and generates its mass.

Of course, this is just a schematic description of the loop-back effect, while one has to find a stable self-consistent solution of the system as a whole. Moreover, the proper renormalization should be applied consistently for both fields. Unfortunately, the system of equations for the effective potential even at one-loop approximation is rather non-linear, and we do not have exact results. In this sense our problems is similar to the QCD one. Nevertheless, our conjecture is that the CW mechanism works for our case, and there exists a stable solution.

As the next step, we consider the conformal-invariant Lagrangian of the Higgs boson interactions

$$L_{cl} = -\frac{\lambda^2}{2}\left|\phi\right|^4 - \frac{\lambda^2}{2}\left|\phi\right|^2 - y\bar{t}\phi t,$$

where only the most intensive terms are listed: the self-interaction and the Yukawa one with the top quark. Note that we have dropped the tachyon mass term from the SM. Further, we assume that the global symmetry of the Higgs sector should be spontaneously broken in the standard way. As the result, we get a non-zero vacuum expectation value v of the Higgs field. Vacuum averaging with subsequent renormalization of the fermion operators leads to the potential of the form $V(h) = \frac{\lambda^2}{8}h^4 + \frac{y_t}{\sqrt{2}}h(\bar{t}t)$. The extremum condition for the potential $dV(h)/dh = 0$ for $h = v$ yields $v^3\frac{\lambda^2}{2} = \frac{-y_t}{\sqrt{2}}h(\bar{t}t)$. The nontrivial solution of the minimum condition leads to the standard decomposition $h = v + H$, where H represents physical excitations (the Higgs boson particles). The Yukawa coupling of top quark is $y_t \approx 0.99$ (at the tree level). The substitution $h = v + H$ into the potential defines the Higgs boson mass $m_H^2 = \frac{3\lambda^2}{2}v^2$. We stress that this relation is different from the one in the standard Higgs mechanism. Then the squared scalar particle mass can be expressed in terms of the top quark condensate: $m_H^2 = \frac{-3y_t(\bar{t}t)}{v\sqrt{2}}$. To have $m_H \approx 125\,GeV$ we need $(\bar{t}t) \approx (-122\,GeV)^3$. As discussed above, such a value of the top quark condensate does not affect the low energy QCD phenomenology. The value

of the top quark condensate in our case should correspond to a certain adjustment of the divergent tadpole loop integral renormalization. This adjustment is quite different from the fine-tuning in the Higgs boson mass renormalization. First, note that the energy scale of the top quark condensate appears to be the same as the general electroweak one given by the Higgs boson mass and vacuum expectation values. Considering the explicit examples of the radiative symmetry breaking given in [1], we find that the generated values of masses and condensates are defined by the values of the renormalization scale and the coupling constants. In fact, we substitute the tachyon mass by a single renormalization scale of the CW mechanism. This renormalization scale is not an "additional" one to the SM, in our scenario it is the only second one together with Λ_{QCD}. The value of this scale can not be derived starting from the conformal Lagrangian. Therefore, we adjust the renormalization condition to an observable as usually.

Although we have dropped the scalar field mass term from the classical Lagrangian, it re-appeared after quantization and subsequent renormalization. In fact, such a counter term in the Higgs sector is necessary. According to ref. [9], the conformal symmetry of the classical Lagrangian will lead just to the proper quantity in the mass term being consistent with all other quantum effects. A similar situation takes place in QCD: the chiral symmetry at the quark level re-appears at the hadronic level even so that the breaking is obvious [10].

3. Conclusions

In this way we suggested a mechanism of radiative breaking of the conformal symmetry in the Standard Model. This enables us to resolve the problem of the regularization of quadratically divergent tadpole loop integrals by relating them to the condensate values extracted from the experimental observations. In our construction, the top quark condensate supersedes the tachyon-like mass term in the Higgs potential. The considered mechanism allows to establish relations between condensates and masses including the Higgs boson one. In this way, we propose a simple bootstrap between the Higgs and top fields (and their condensates).

Our approach is similar to the one commonly accepted in the QCD. In fact, the conformal symmetry breaking in the QCD provides a single energy scale for the light-quark and gluon condensates as well as for the constituent quark mass. For the time being, we are not able to describe these phenomena in the QCD using only its Lagrangian. We can, however, extract the relevant scales from observables. In the same manner, the scale of the top quark mass, which appears due to the Higgs condensate, might be naturally related to the scale of its own condensate.

It is noteworthy that we consider the Higgs boson as an elementary particle, without introduction of any additional interaction beyond the SM. After the spontaneous symmetry breaking in the tree-level Lagrangian, the difference from the SM appears only in the value of the Higgs boson self-coupling constant. The latter can be extracted from the LHC data only after the high-luminosity upgrade, and it will be certainly measured at a future ear e^+e^--collider.

References

[1] P. A. R. Ade et al. [Planck Collaboration], Astron. Astrophys. **594**, A20 (2016).
[2] P. Channuie, Nucl. Phys. B **892**, 429 (2015).
[3] T. Inagaki, S. D. Odintsov, H. Sakamoto, Astrophys. Space Sci. **360**, 67 (2015).
[4] T. Inagaki, S. D. Odintsov, H. Sakamoto, Nucl. Phys. B **919**, 297 (2017).
[5] P. Channuie and C. Xiong, Phys. Rev. D **94**, 043521 (2017).
[6] Y. Nambu and G. Jona-Lasinio, Phys. Rev. **122**, 345 (1961); Phys. Rev. **124**, 246 (1961).
[7] V. A. Miransky, "Dynamical Symmetry Breaking in Quantum Field Theories", World Scientic (1993).
[8] M. Harada and K. Yamawaki, Phys. Rept. **381**, 1 (2003).
[9] K. i. Kondo, S. Shuto and K. Yamawaki, Mod. Phys. Lett. A **6**, 3385 (1991).
[10] K. i. Kondo, M. Tanabashi and K. Yamawaki, Prog. Theor. Phys. **89**, 1249 (1993).
[11] K. Kondo, M. Tanabashi and K. Yamawaki, Mod. Phys. Lett. A **8**, 2859 (1993).
[12] C. N. Leung, S. T. Love and W. A. Bardeen, Nucl. Phys. B **273**, 649 (1986).
[13] C. N. Leung, S. T. Love and W. A. Bardeen, Nucl. Phys. B **323**, 493 (1989).
[14] M. Harada, Y. Kikukawa, T. Kugo and H. Nakano, Prog. Theor. Phys. **92**, 1161 (1994).
[15] W. A. Bardeen, C. T. Hill and M. Lindner, Phys. Rev. D **41**, 1647 (1990).
[16] C. T. Hill and D. S. Salopek, Annals Phys. **213**, 21 (1992).
[17] B. Geyer and S. D. Odintsov, Phys. Rev. D **53**, 7321 (1996).
[18] B. Geyer and S. D. Odintsov, Phys. Lett. B **376**, 260 (1996).
[19] T. Inagaki, S. D. Odintsov, H. Sakamoto, in writing.
[20] S. Weinberg, Phys. Rev. Lett. **37**, 657 (1976).
[21] E. Eichten, K. D. Lane, J. Preskill, Phys. Rev. Lett. **45**, 225 (1980).
[22] W. Goldstein, Nucl. Phys. B **213**, 477 (1983); B **229**, 157 (1983).
[23] S. Hashimoto, T. Inagaki and T. Muta, Phys. Rev. D **48**, 1301 (1993).
[24] T. Inagaki, Nucl. Phys. Proc. Suppl. **37A**, 197 (1994).
[25] K. j. Hamada and M. Matsuda, Phys. Rev. D **93**, 064051 (2016).

Nonlinear absorption in monoselenide of gallium and indium in laser excitation

A.G. KYAZIM-ZADE, V.M. SALMANOV, A.G. HUSEYNOV, R.M. MAMEDOV, A.A. SALMANOVA, I.M. ALIYEV, F. SH. AXMEDOVA

Baku State University, Z.Khalilov str.23, AZ-1148, Baku, Azerbaijan , e-mail: vagif_salmanov@ yahoo.com

Abstract
Nonlinear absorption in GaSe and InSe crystals at high optical excitation intensities is experimentally studied. It is shown that the nonlinear absorption observed in InSe in the region of exciton resonance is due to the exciton-exciton interaction. The effect of filling the zones detected in GaSe at high excitation intensities leads to a change in the absorption coefficient and the refractive index. In InSe nanoparticles obtained by the chemical deposition method, a quanta-dimensional effect was observed, the dependence of the forbidden band width on the dimensions of the nanoparticles.

Keywords: GaSe, InSe, nanoparticles, nonlinear absorption,

Introduction

GaSe and InSe crystals belonging to III-V compounds have received considerable attention recently as an interesting class of nonlinear optical materials. Possessing layered structure, high polarizability, optical homogeneity and naturally mirror-like surfaces, a number of nonlinear optical phenomena such as harmonic generation, parametric light generation, electron-hole plasma and stimulated emission in the visible and terahertz region, etc., have been observed in these crystals. Investigations of dimensional quantum phenomena in these semiconductors open up great prospects for constructing on their basis new devices with a wide range of functional capabilities. Scientists have established that the ultrathin nanosilic monoselenide indium and gallium have unique properties that qualitatively distinguish it among the remaining two-dimensional crystals. In the obtained samples of indium monoselenide, the electron mobility is the highest. This material parameter is extremely important in terms of improving the performance of devices that can be created on its basis. Another interesting property of indium monoselenide is that, unlike dichalcogenide and silicon, this crystal is a so-called direct-gap semiconductor. This makes it particularly promising for use in optoelectronics. This paper is devoted to an experimental study of nonlinear absorption and quanta-dimensional effects in monoselenide gallium and indium at high optical excitation levels.

The investigated single crystals were obtained by the Bridgmen method. GaSe and InSe have a layered structure, where each layer contains two gallium (indium) and two selenium close-packed sublayers in the stacking sequence Se-Ga(In)-Ga(In)-Se. The bonding between two adjacent layers is of the Van der Waals type, while within the layer the bonding is predominantly covalent. The ingots were cleaved along the planes of layers, obtaining slices about (10÷50) μm thick. Mobility and concentration of charge carriers measured by conventional methods at room temperature were ~ 20 $cm^2/V \cdot s$, $1x10^{14}$ cm^{-3} and ~ $1.2x10^3$ $cm^2/V \cdot s$, ~ $7x10^{14}$ cm^{-3} GaSe and InSe, respectively. The samples were put into a helium cryostat equipped with a temperature controller which allows any temperature between 4.2 and 77 K to be maintained. As an excitation source, a picosecond YAG:Nd laser with a pulse duration of 30 ps were used to excite InSe crystals. In this case, both the single beam and also double beam excitation were used. As an excitation source, Rhodamine 6G dye laser (PRA, LN-107) pumped by the output of a N_2 – laser (PRA, LN-1000), tuned through the region 594-643 nm with a repetition frequency of 10 Hz and a pulse width of 1 ns was used in the case of excitation of GaSe crystals. Lower excitation intensities were obtained by means of suitable calibrated neutral filters. Transmission spectra were obtained by shifting filters from the front to the rear of the samples and checking the experimental reproductibility in the region of transparency. The output siqnals were detected by a silicon photodiode and recorded by a storage oscilloscope (Le Groy 9400).

1. Nonlinear light absorption in InSe crystals at high optical excitation

Figure 1,a illustrates dependence of the magnitude of transmission coefficient on the emission intensity for an InSe single crystal excited by laser light having an energy $\hbar\omega = 1.327eV$ (resonant excitation of exciton) at 77K. As it is seen from the figure, a nonlinear absorption in the exciton resonance region and occurrence of sample bleaching in the indicated light frequency at high excitation levels are observed. The observed bleaching saturates at the incident light intensity of ~300MW/cm^2. Diminishing of the magnitude of exciton absorption may be explained by the process of screening (Mott transition) for a high density exciton system (Fig. 1,b). The density of the electron - hole pairs in our experiment reached ~ 10^{20} cm^{-3} which exceeds the density necessary for the Mott transition in InSe (n_{Mott}=$2,5x10^{16}$ cm^{-3}). Disappearance of the exciton peak in this case may be explained by screening of the

Coulomb interaction by free charge carriers. The screening length can be defined by the following equation

$$L = \frac{\hbar}{2}\left(\frac{\pi}{3}\right)^{1/6} N^{-16} \frac{\varepsilon^{1/2}}{em^{*1/2}} \qquad (1)$$

where, ε is the dielectric constant of the crystal and m^* is the effective mass. By substituting these values from [1] it is found that, L~10A^0 which is less than the exciton radius (~37A^0).

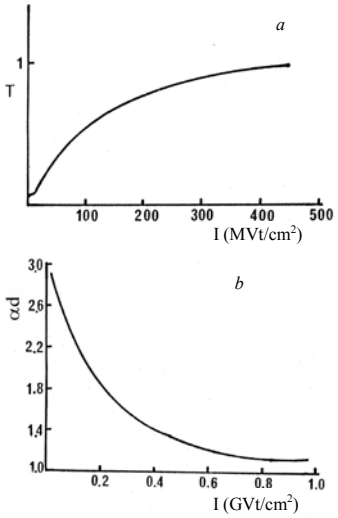

Figure 1. (a) Dependence of the transmission coefficient on the excitation intensity in InSe. (b) Dependence of the optical density on the excitation intensity.

2. Nonlinear light absorption in GaSe crystals at the fundamental absorption edge

The absorption spectra of GaSe at low (curve 1) and high (curve 2) excitation intensities are given in Fig.2,a. As it is seen from the figure, at high excitation levels, the absorption coefficient is decreased, and along with the onset of absorption is also shifted towards higher energies. The change in the absorption coefficient $\Delta\alpha$ can be obtained by direct subtraction of curves 1 and 2 in Fig.2, a. The result is plotted in Fig. 2,б. It is seen that the maximum absorption change takes place in the vicinity of the band gap. The observed nonlinear absorption near the band gap at high excitation intensities can be attributed to optical saturation effects in GaSe, i.e. electrons and holes generated by absorption of light which relax rapidly to a thermal distribution, blocking absorption states near the band edge. Effectively, this is like a shift of the band edge to higher energies with increasing laser intensity, which causes the absorption at the vicinity of the band edge to decrease. From Fig. 2,б, it is clear that, the absorption change becomes negative. Negative absorption means amplification as can be seen from Beer-Lambert's law

$$I(t) = I_0 \exp(-\alpha x) \qquad (2)$$

For α<0, the transmitted intensity is higher than the input intensity. This optical gain can give a possibility of producing a semiconductor laser based on GaSe crystals.

Coulomb electron-hole correlation effects should be taken into account which can eventually lead to the enhancement of the nonlinear absorption. Such saturation leads both to nonlinear absorption and to a strong intensity dependence of the refractive index. From the Kramers – Kronig relation [2] we may write the change in refractive index at photon energy $\hbar\omega$ as:

$$\Delta n(\hbar\omega) = \frac{hc}{\pi}\int_0^{\infty} \frac{\Delta\alpha(\hbar\omega')}{(\hbar\omega')^2 - (\hbar\omega)^2} d(\hbar\omega') \qquad (3)$$

As can be noted from Fig. 2,c the chang in the refractive index leading to nonlinear effects. $\Delta n(\omega)$ is negative at frequencies below the absorption edge and positive on the high-energy side. The laser-induced negative index change is referred to as a self-defocusing optical nonlinearity. The positive $\Delta n(\omega)$ on the high-energy side of the band gap corresponds to a self-focusing optical nonlinearity.

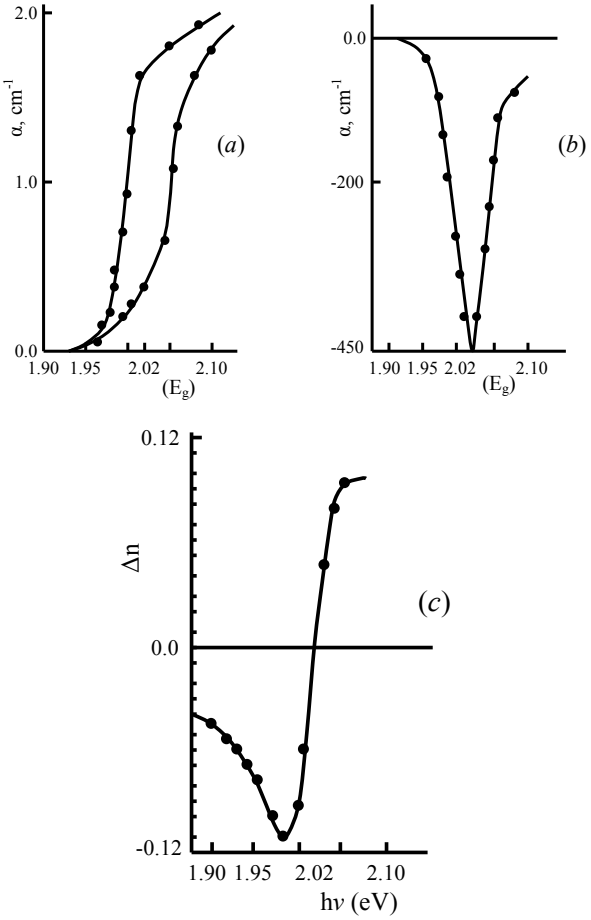

Figure 2. (a) Absorption spectra of GaSe at low (3,5 MW/cm^2, curve 1) and high (12 MW/cm^2, curve 2) intensity excitations, (б) Tha change in the absorption coefficient $\Delta\alpha$, (c) Tha change in the refractive index $\Delta n(\omega)$.

3. Quantum-dimensional effects in GaSe nanoparticles

The GaSe nanoparticles were obtained by a modified method of chemical deposition (Successive Ionic Layer Adsorption and Reaction-SILAR). Using the Debye-Scherer formula, the sizes of the nanoparticles obtained were calculated. Estimates show that the

dimensions of GaSe nanoparticles lie in the range 4÷20 nm. Using X-ray diffraction analysis (XRD), scanning electron microscopy (SEM), atomic force microscope (AFM) and energy dispersed spectroscopy X-ray (EDAX) studies conducted internal structure and the structure of the obtained samples. Images obtained with SEM show that the obtained substances consist of spherical nanocrystals that are collected in a polydisperse form (Fig.3,a). The image of the InSe nanoparticles obtained from AFM studies shows that a homogeneous particle distribution is not observed (Fig. 3,b).

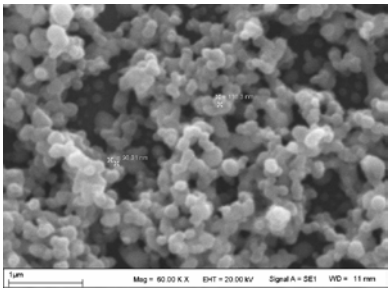

a)

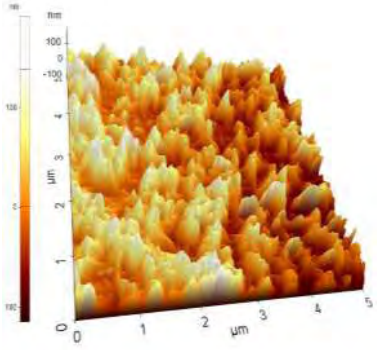

b)

Fig. 3. SEM (a) and AFM (b) images of a GaSe and InSe nanostructure grown on a glass substrate, respectively.

As is known, many mechanical, thermodynamic and electrical characteristics of a substance change in nanoparticles. Their optical properties are not an exception. It turned out that the frequency of light emitted by nanoparticles increases with decreasing size of these particles. Experiments conducted by us showed that a quasi-dimensional effect is observed in GaSe nanoparticles, the width of the forbidden band depends on the dimensions of the nanoparticles. Calculation of the width of the band gap was carried out according to the following formula [3]:

$$E_g = E_g^{(bulk)} + E_b\left(\frac{\pi a_B}{D}\right)^2 \qquad (4)$$

where Eg is the width of the band gap of nanostructures, Eg (bulk) is the width of the same substance without nanostructures, Eb is the binding energy of the exciton, the Bohr radius of the exciton, and D is the size of the nanoparticles.

The above parameters in GaSe have the following values : Eg (bulk) = 2.02 eV, Eb = 20 meV, = 37 A^0. Figure 4 shows the dependence of the width of the forbidden band of GaSe nanoparticles on the dimensions of nanoparticles. As can be seen from the figure, the quantum-size effect begins to significantly affect the width of the forbidden band when the dimensions of the nanoparticles become smaller than 10 nm.

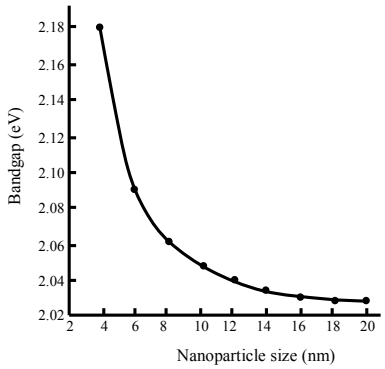

Figure 4. Dependence of the width of the forbidden band of GaSe on the dimensions of nanoparticles.

Conclusions

The exciton-exciton interaction process and screening of excitons by free carriers are the most probable mechanisms responsible for diminishing of exciton absorption in InSe at high excitation intensities. The observed nonlinear absorption near the band gap edge of the layered GaSe crystal is due to the bandfilling effect. The change in absorption effects the refractive index through the Kramers-Kronig relations, leading to nonlinear effects. Bandfilling nonlinearity can give possibility to produce semiconductor laser on the base of GaSe crystals. In the nanoparticles of GaSe, obtained by a modified method of chemical deposition, a quanta-dimensional effect was observed. Reducing the size of nanoparticles from 20 nm to 4 nm leads to an increase in the width of the forbidden band from 2.02 eV to 2.18 eV.

References

[1] G. Ottaviani, C. Canali, V.Yu. Nekrasov at all. Solid State Commun. **v.14**, 933(1974).

[2] N. Peyghambarian, S.W. Koch and A. Mysyrovicz, Introduction to semiconductor optics, Series in Solid State Physical Electronics, New Jersey, 325 (1993).

[3] Samuel S. Mao, Int. J. of Nanotechnology. **1**, 42(2004).

Optical Spectroscopy of GaS Nanoparticles Formed via Laser Ablation

A.M. PASHAYEV[1], E.Y. SALAYEV[2], B.H. TAGIYEV[1,2], I.Z. SADIKHOV[1], K.R. ALLAHVERDIYEV[1*]
[1]National Aviation Academy of Azerbaijan, Bina Mardakan prospect 30, Baku, Azerbaijan 1045
[2]Azerbaijan National Academy of Sciences, Institute of Physics, 33 H. Javid str., Baku, Azerbaijan 1143
e-mail: kerim.allahverdi@gmail.com

Abstract

Bulk single crystals of GaS were grown by Bridgman method. Nanoparticles of quasi 2-D GaS crystals were obtained by laser ablation (LA) technique and characterized by: •XRF; •GDOES; •SEM and TEM; •UV-VIS absorption spectroscopy. Nanoparticles were ablated by using the line λ = 248 nm of excimer KrF laser operated at f = 50 Hz with pulse duration τ = 4 ns and maximum energy 200 mJ. Obtained results are analyzed with respect to particle size. Absorption spectra of particles with diameter less than 18 nm turned out to be shifted in the blue range of spectra. Blue shift in the optical absorption spectra of GaS nanoparticles with decreasing the particle sizes was explained by presence of nanocrystals in the quantum size regime. These results are consistent with a perturbation of GaS band structure due to carrier confinement, resulting in a widening of the forbidden gap.

Keywords: *Nanoparticles, layered crystals, 2-D materials, gallium sulfide, absorption spectra, characterization, semiconductors, carrier confinement, laser ablation, optical band gap.*

1. Introduction

Semiconductor nanostructures are promising building blocks for future electronic and photonic devices. Nanostructures based on layer-type semiconductors, such as GaSe- type (GaS, InSe, GaTe) are of particular interest in terms of the optical, non-linear optical (NLO), solar, X-ray and particles detection applications [1-4].

For the last years our research group at the National Aviation Academy of Azerbaijan, Scientific-Research Institute of Transport and Aviacosmic Problems have been focused on layered semiconductors, specifically, GaSe, InSe and GaS due to increasing interest of their NLO and other applications (photovoltaics, particle detection etc.). We used the LA (Laser Ablation) method to obtain the nanoparticles of these materials with a given size and to examine elemental content (XRF- X-ray Fluorescence, GDOES-Glow Discharge Optical Emission Spectroscopy), structural (X-ray, TEM- Transition Electron Microscopy, and SEM- Scanning Electron Microscopy), optical (absorption in VIS- Visible) and vibrational (Raman and confocal Raman) spectroscopy.

The hierarchy of weak forces and the ability of these materials for easy cleavage together with the low density of electronic states on freshly cleaved surfaces (does not exceed ~ 10^{10} cm^{-2}, water absorbs on a surface without any reaction and forms 3- D clusters on the (0001) planes)) and existence of different polytypes and other unique properties- is one of the main reason why GaSe-type layered semiconductors were extensivley investigated since about 1960th up to the present time [1-3]. GaS crystallizes in a space group (SG) of D_{6h}^4 and the elementary unit cell consists of 2 layers of atoms in sequence of *–S-Ga-Ga-S-*. The crystals of GaS characterize by: melting point T_m= 965 ^oC (1238 K), density 3.86 gcm^{-3}, molecular weight 101.79.

2. Methodology

The starting materials were prepared by mixing quantities of high-purity (99.999%) gallium and sulfur pellets in the atomic proportion 1/1. Especially un-doped GaS crystals were grown by the Bridgman-Stockbarger method in an evacuated quartz tube (10^{-5} Torr). GaS single crystals 20 mm in diameter and 60 mm in length with yellow color were successfully obtained.From the boules (∅ 20 mm), slabs of different thickness were easily cleaved with a razor blade for further preparation of powder. Powder was obtained by grinding the single crystal plates in an agate grinder. Then the powder was pressed into a form of pellets and used as a target in the LA experiments.

Nanoparticles were grown by home built LA apparatus during stay of Prof. K. Allahverdiyev at the Institute of Material Sciences, Tsukuba University, Tsukuba, Japan (Prof. K. Allahverdiyev are indebted to Prof. S. Onari for his hospitability during stay at Tsukuba University). KrF Excimer laser at 248 nm (COHERENT COMPex 201), with the repetition frequency f = 10 Hz and pulse duration τ = 10 ns, 25 mJ and 200 mJ pulses were used and the particles were deposited at different gas pressures. The average size of grown GaS nanoparticles were controlled by a change in the pressure of the noble gases and the laser energy. In the present paper the results only for nanoparticles deposited onto the quartz plates will be presented and discussed.

Equipment, facilities and methods used in the presnt research for characterization of GaS bulk crystals and nanoparticles were as follows: •XRD- (Shimadzu XRD-600); •XRF- (Philips PW 2404); •GDOES- High Resolution HR 10000 Glow Discharge Profiler (Jobin Yvon); •very small drops of samples were dropped onto carbon support film coated copper TEM grids. JEOL-2100 HR TEM operating at 200 kV (LaB_6 filament) and equipped with an Oxford Instruments 6498 EDS system; •JEOL-JSM-6335F FEG-SEM equipped with Oxford EDS

system, operated at 20 kV and INCA software; •double-pass spectrometer (Jobin Yvon U-1000) with the photon counting system equipped with a photomultiplier (RCA-C31034) and a multichannel analyzer (Canberra Series 40) for UV-, VIS-, for the transmission measurements.

3. Results

Growth from the melt (Bridgman method) provided large single crystals sufficiently homogeneous and free of defects which allows the fabrication of samples destined for optical or transport phenomena measurements. A little thin slice of single-crystal sample was ground into powder and its XRD pattern was recorded. The results showed the presence of diffractions characteristic of hexagonal phase for GaS (D_{6h}^4 space group). The XRD pattern indicated that the as-prepared products have high crystallinity. The cell parameters are in agreement with that presented in [1]. Optical band gap of GaS measured in the present work is $\Delta E = 2.5$ eV and in good agreement with existing data [1-3]. Elemental content analysis of grown crystals are as follows: the results obtained by the GDOES confirmed nearly stoihciometry content (49.5 at % of Ga and 49.3 at% of S). XRF measurements performed on series of GaS crystals showed nearly the same content. Energy dispersive X-ray spectrometer (EDS) analysis indicated only presence of O (oxygen) element in the spectrum, indicating the high purity of grown crystals.

The average size of grown GaS nanoparticles were controlled by a change in the pressure of the noble gases and the laser energy. The size of grown particles was estimated by direct observation with a TEM operated at 200 kV. All measurements were carried out at room tempePicture presented in Fig.1)

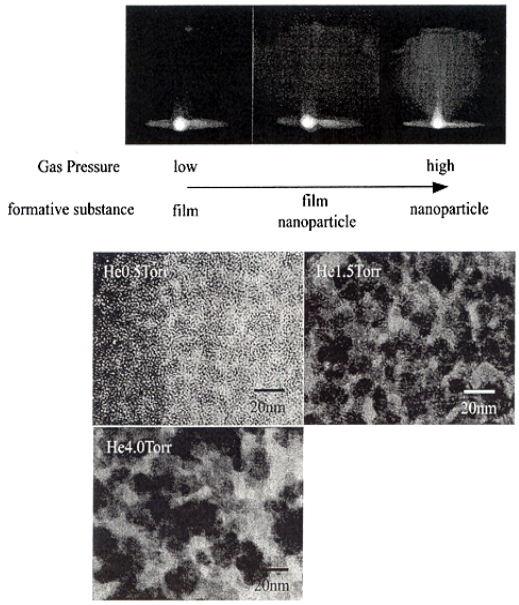

Fig.1. *Shape of plume formed during ablation in dependence on the gas pressure (less than 0.05 Torr- upper left; 0.5 Torr-middle; 1.5 Torr- right). Lower 3 pictures represent the TEM of GaS particles ablated at different He gas pressure (results are very similar to that obtained for GaSe and InSe nanoparticles* [5].

Spectral dependences of optical density of grown particles versus gas pressure (Ar and He) for GaS particles for different laser powers were built, analyzed and by using these data absorption gap versus gas pressure were built. It was established that characteristic feature of these dependences is that with increasing gas pressure optical density shifts to lower energies. It was seen that absorption gap increases with increasing pressure up to about 0.5Torr (He gas, laser pulse power 200 mJ and He gas, laser pulse power 25 mJ) and then decreases. With increasing the distance between the target and substrate gas pressure value from which the gap of particles start to decrease and shifts to higher gas pressure (at ~ 0.1 - 0.14Torr at distance 30 mm and at ~ 0.22Torr at distance 60 mm).

We associate the blue shift in the optical absorption spectra of GaS with decreasing the particle sizes to the presence of nanocrystals in the quantum size regime (nearly same as it was reported earlier for GaS and InSe [5]). According to Brus [6] ananalytical expression for the first excited electronic state of the quantum particle is:

(1)

where: the first term is the quantum energy of localization; the second term is the Coulomb attraction; the third term (smaller term) arises from Coulomb interaction in the presence of a crystalline surface; R is the radius of the particle; m_e^* and m_h^* are the effective masses of electron and hole, respectively, and e is the charge of an electron, ε is the dielectric constant at the optical frequency. The value of E represents the energy shift with respect to the value of the band gap forbulk crystal. It was shown, that for nanoparticles of GaS the combination of Coulomb term and relatively large effective masses (compared to GaAs, InSb etc.) keeps the excited state energy near the bulk forbidden gap for diameters larger than approximately 20 nm (very similar to that for GaSe and InSe).

4. Conclusions

1. High optical quality crystals of GaS were grown by the Bridgman-Stockbarger method having a size of 20 mm in diameter and 60 mm in length. The space group (D_{3h}^1) of grown crystals are in good agreement with the existing data.

2. The nanoparticles of GaS have been synthesized using LA method. The size of nanoparticles was successfully controlled by selection of the experimental parameters of rare gas species of Ar or He: at pressures lower than 0.1 Torr the particles with diameter more than 15 nm were obtained. Increasing the gas pressure more than 0.1 Torr results to formation of particles with diameter 5 nm and less (at gas pressure 1 Torr). Further increasing the pressure leads to increasing the particle sizes (12 nm at 5Torr).

3. Blue shift in the optical absorption spectra of GaS nanoparticleswith decreasing the particle sizes was explained by presence of nanocrystals in the quantum size regime. These results are consistent with a perturbation of GaSband structure due to carrier confinement, resulting in a widening of the forbidden gap.

References

1. K. Maschke, and F. Levy, "Landolt-Bornstein Numerical Data and International Relationship in Science and Technology", New Series, Group III: Crystal and Solid State Physics], Springer-Verlag, Berlin/Heidelberg/New York/Tokyo, **v**. **III/17f**, pp. 530 (1983).

2. E.Yu. Salaev, K.R. Allahverdiyev, "Dynamic and tatic nonlinear optical effects in layered gallium selenide-type crystals", Baku, Elm, (in Russian), pp. 229 (1993).

3. N.C. Fernelius, ″Properties of gallium selenide single crystals, ″Prog. Cryst. Growth Charact. Mater., **v. 28**(4), pp. 275-353 (1994).

4. G.A. Gibson, A. Chaiken, K. Nauka, C.C. Yang, R. Davidson, A. Holden, R. Bicknell, B.S. Yeh, J. Chen, H. Liao, S. Subramanian, D. Schut, J. Jasinski, Z. Liliental-Weber, "Phase-change recording medium that enables ultrahigh-density electron-beam data storage", Appl. Phys. Lett., **v. 86**(5), pp. 051902-051906 (2005).

5. A. Pashayev, B. Tunaboylu, K. Allahverdiyev, E. Salaev, B. Tagiyev, "Linear and NLO Spectroscopy of GaSe and InSe Nanoparticles Formed via Laser Ablation", XII International Conference on Atomic and Molecular Pulsed Lasers, Edited by Victor F.Tarasenko, Andrey M. Kabanov (2015), Proceedings of SPIE,**v. 9810**, pp. 981018-1 981018-12 (2016).

6. L.E. Brus, ″Electron-electron and electron-hole interactions in small semiconductor crystallites: the size dependence of the lowest excited electronic state″, J. Chem. Phys., **v. 80**, pp. 1403-1411(1984).

Anomalies of the kinetic phenomena in semiconducting $A^{III}B^{VI}$ compounds with a layered crystalline structure

A.SH. ABDINOV[1], R.F. BABAYEVA[2]

[1] *Baku State University*
[2] *Azerbaijan State Economic University*

Abstract

The dependences of the kinetic parameters on the temperature, electric field, doping, and technological pre-history of the samples of single crystals of the layered $A^{III}B^{VI}$ compounds has been studied experimentally. It is found that values of samples resistivity of with different technological pre-history are significantly different in the low-temperature region. In high-resistivity crystals the values and characteristics of the dependences of the kinetic parameters on temperature, electric field, and doping are significantly different from the theoretical concepts of the crystalline solid. It is shown that these discrepancies are caused by the presence of chaotic macroscopic defects in the crystals studied and these crystals can be represented as a composite material consisting of a low-resistivity semiconductor matrix with high-resistivity semiconducting nano-disperser with the same chemical composition.

Keywords: *kinetic parameters, electric field, temperature, doping, low-resistivity, high-resistivity, crystal, macroscopic defect.*

1. Introduction

Often in practice, the experimental results obtained in complex in chemical composition and crystalline structures, as well as irradiated by hard radiations and (or) strongly doped crystalline semiconductors does not find its full explanation on the basis of theoretical concepts of the crystalline solid [1]. This situation is even more acute in those cases when, due to various reasons, there is a partial disorder in a generally ordered crystalline substance on a macroscopic scale. However, in contrast to non-crystalline solids (for example, amorphous, vitreous, organic, polymeric, etc.) [2], in such partially-deviated from ideal crystalline substances, disorder is manifested itself as large-scale defects in the form of separate chaotic ones both in geometric dimensions and in the distribution in the volume of the investigated sample inclusions in the basically ordered in the macroscopic scale matrix.

Naturally, in such partially disordered crystalline semiconductors under certain external conditions, the behavior of the kinetic phenomena can appreciably differ from that which takes place in quasi-ordered crystalline solids. An analysis of the results obtained in the early studies [3-6] in experimental studies of the physical properties of selenides of AIIIBVI compounds with a layered crystal structure allows us to say, that single crystals of these semiconductors under certain conditions can be a vivid example for partially-disordered crystalline semiconductors, consisting of a low-resistivity (LR) matrix with chaotic high-resistivity (HR) inclusions. Moreover, at the boundaries of the LR matrix with HR inclusions, recombination barriers exist for recombination barriers, and between neighboring HR inclusions - recombination barriers for free charge carriers. However, at the present time, the influence of this type of partial non-ordering, as well as associated drift and recombination barriers on the kinetic phenomena in these semiconductors (in the crystals of $A^{III}B^{VI}$ compounds with a layered crystal structure) has not been studied at the required level.

In this paper, we report the results obtained by us in the integrated experimental study of the dependence of the kinetic parameters in pure (specially non-doped) and slightly-doped ($N \leq 10^{-1}$ at.%) with rare-earth elements (REE), namely with europium and dysprosium single crystals of gallium and indium selenides on the technological origin of the studied samples, the temperature (T), the value of the external electrical voltage (U) applied galvanic ally to the sample being studied.

2. Samples

The objects of research were single-crystal samples of n-InSe and p-GaSe grown by slow cooling at a constant temperature gradient along the ingot [7]. The initial dark resistivity (ρ_0) of n-InSe and p-GaSe crystals at 77 K) was $\sim 10^3 \div 10^7$ Ohm·cm and $\sim 3 \cdot 10^4 \div 10^8$ Ohm·cm, respectively, and the impurity content of REE in various samples of the doped crystals of n-InSe<REE> and p-GaSe<REE> was $N = 10^{-5}$, $5 \cdot 10^{-5}$; 10^{-4}; 10^{-3}; $5 \cdot 10^{-3}$; 10^{-2}; 10^{-1} at.%. The measurements were carried out at various temperatures (in the range T=77-600 K) and the intensities (E) of the galvanic ally applied external electric field to the samples (from extremely low up to $\sim 3.5 \cdot 10^3$ V/cm and $\sim 2.5 \cdot 10^3$ V/cm for p-GaSe and n-InSe, respectively).

3. Results

As a result of the experimental measurements it was established that in the high-resistivity ($\rho_0 \geq 10^4$ Ohm·cm and $\rho_0 \geq 10^5$ Ohm·cm for n-InSe and p-GaSe, respectively) crystals of semiconductors under study in the $T \leq 350$ K region, dependencies of the specific conductivity (σ), the Hall constant (R_H), and the mobility of free charge carriers (μ) on T have an anomalous course. In particular, in this temperature range with its decreasing up to 77 K the value of R_H does not change and the values of σ and μ – strongly decrease. Moreover, the course of the curves of σ_0(T) and μ(T) dependences almost coincide (Fig.1).

In addition, in the region of low temperatures (at T≤200÷250 K, depending on ρ_0 and N), specific features

of the $\mu(\rho_0)$ and $\mu(N)$, $\mu(E)$, as well as $\mu(T)$ dependences are found in crystals of both semiconductors. In particular, at 77 K the value of μ is small (sometimes it is fraction of $cm^2/V \cdot s$) and with a temperature increases by much sharper law ($\mu \sim -\frac{\Delta\varepsilon}{kT}$) than occurs when scattering of free charge carriers on impurity ions is dominated ($\mu \sim T^{3/2}$) in quasi-ordered crystalline semiconductors. In addition, the values of μ and σ decrease with increasing ρ_0, under the action of an external electric field galvanic ally applied to the sample under investigation with intensity greater than a certain boundary value increase, and with an increase in the doping level (with increasing N) change monotonically. In this case, the dependence $\sigma(E)$ is observed in the region of low temperatures, starts at considerably lower values of E, and has a completely different character (Fig. 2) than the predicted by corresponding theory for $\sigma(E)$ dependence in the case of heating of free charge carriers by an electric field in quasi-ordered crystalline semiconductors [8].

We also revealed that the influence of doping with selected REE on the kinetic parameters of single crystals of semiconductors under study is manifested only at low concentrations of the impurity introduced (for $N<10^{-2}$ at.%). At that, this influence lies in the changes in the absolute values of μ and σ, as well as in the behavior of the curves of the dependence $\sigma(T)$, $\mu(T)$, σ(E), μ(E) and σ(N), μ(N). For the same values of N the dependence of σ and μ on the chemical nature of the introduced impurity was not observed. Also it has been established that all complex of the influence of the REE doping on σ and μ is only found in the region $T \leq$200-250 K (for different species, depending on N).

In contrast to the low-temperature region, in the high-temperature region in the semiconductors under study the dependence of the kinetic parameters on T is satisfactorily obeyed regularities of the kinetic properties of quasi-ordered crystalline semiconductors.

It should be noted that under other identical conditions, with a decrease in ρ_0, the course of the curves of the temperature dependence of the kinetic parameters in these materials also approaches the predicted by the theory for quasi-ordered crystalline semiconductors.

4. Discussion

On the basis of a comparative analysis of the experimental data obtained it is shown that the above mentioned specific features of the dependencies of the kinetic parameters in the materials under study cannot be explained unambiguously only in the framework of the existing theories of the kinetic properties of quasi-ordered crystalline semiconductors, and most likely due to the presence of drift barriers in their free energy bands. It is assumed that the anomalies of kinetic phenomena discovered by us, in particular the anomaly in the Hall coefficient, the electrical conductivity and the mobility of free charge carriers in the region of low temperatures, i.e. significantly sharper, more accurately, activation growth with T, decrease with increasing of the initial dark resistivity, non-monotonic dependence on the REE doping level, and other "anomalous" features from the point of view of the theory of kinetic phenomena in crystalline semiconductors, features of the mobility of free charge carriers, the effect of the values of ρ_0 and N on the course of the dependences of the kinetic parameters on different

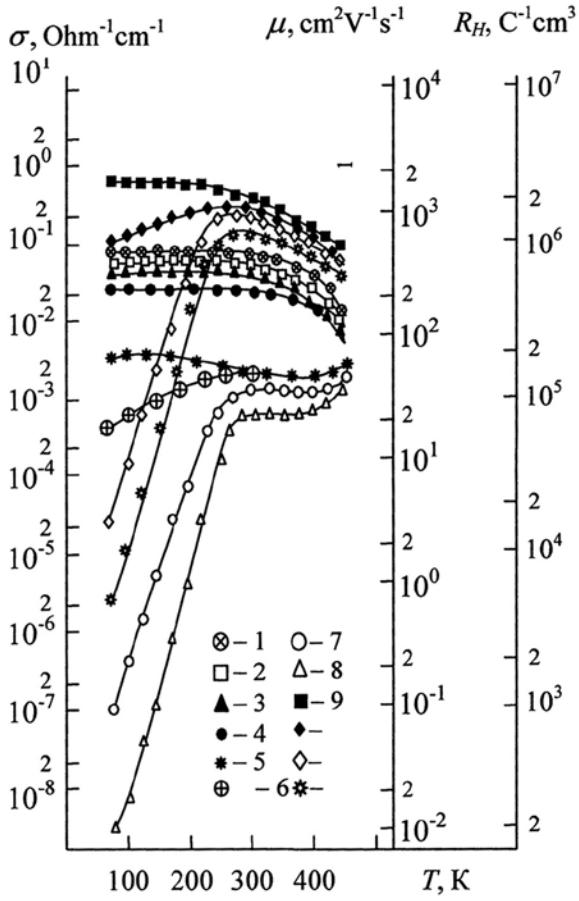

Fig.1.The temperature dependence of the Hall coefficient (R_H) (curves 1-4), electrical conductivity (σ) (curves 5-8), and the mobility of free charge carriers (μ) (curves 9-12) in n-InSe crystals with different initial specific electric conductivity(σ_0). σ_0, $Ohm^{-1} \cdot cm^{-1}$: 1, 3, 5 – $2 \cdot 10^{-3}$; 2, 4, 6 - $2 \cdot 10^{-4}$; 7, 8, 9 - $2 \cdot 10^{-5}$; 10, 11, 12 - $6 \cdot 10^{-6}$

external factors in single crystals of selenides of $A^{III}B^{VI}$ compounds with a layered crystalline structure, are primarily due to their partial disorder and can be satisfactorily explained on the basis of the dependence of ρ_0 on the degree of disorder, as well as by the change in the dimensions of the drift barriers in free energy bands of the investigated samples with T and N. On the basis of the activation nature of the discovered dependence of μ on T, from the slope of the curves of $\mu(T)$ dependences the values of the energy height of these drift barriers ($\Delta\varepsilon_i$) were determined, which at 77 K turned out to be for different samples (depending on the values of ρ_0 and N) of gallium and indium selenide single crystals ~0.05÷0.15 eV and ~0.10÷0.20 eV, respectively.

The dependence of the mobility of free charge carriers on the intensity (E) of the external electric field in high-resistivity pure and slightly-doped with REE ($N \leq 10^{-2}$ at.%) single crystals of selenides of $A^{III}B^{VI}$ compounds with a

layered crystalline structure is not related to the heating of the charge carriers by a strong electric field, but is caused by variation of the degree of spatial in homogeneity (disorder) of the investigated sample, correspondingly the magnitude of the drift barriers in its free energy bands by the excess charge of the injected current carriers [9].

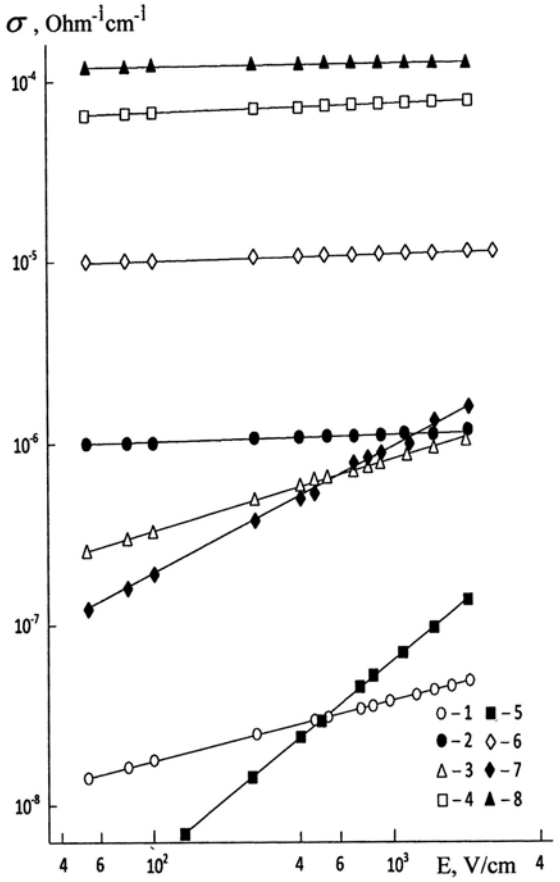

Fig. 2. Dependence of the electric conductivity on the electric field intensity in gallium monoselenide (curves 1, 2, 5, 6) and indium monoselenide (curves 3, 4, 7, 8) crystals with different ρ_0 (curves 1-4) and N (curves 5-8).
T=77 K, ρ_0, Ohmcm: 1 - 10^8; 2 - $5\cdot10^5$; 3 - $8\cdot10^6$; 4 - $2\cdot10^4$ N, at.%: 5 -$5\cdot10^{-4}$; 6-10^{-1}; 7 – $5\cdot10^{-3}$; 8 - 10^{-1}

In our opinion, independence of the kinetic phenomena from the chemical nature of the introduced impurity, the manifestation of their dependences only on the level of doping with REE, first of all, may be due to the fact that the ions of the introduced impurity first (at small values of *N*) in consequence of segregation are skipping around the large-scale defects and intensify, and then gradually spreading throughout the volume, reduce the degree of disorder in the sample.

As for the reasons for the formation, nature and origin of the HR inclusions in the semiconductors under study, they can be very diverse - the stratification of the crystal structure; presence of several modifications and (or) polytypics of the compound; segregation of the metallic component of this compound along the ingot during the growth of its single crystal; mechanical damage due to shearing from large ingots, giving the necessary geometric shape and providing current contacts of individual samples. However, for all the above mentioned and other possible cases, firstly, the dominant factor is precisely the lamination of the crystal structure (the weak Van-der-Waals bond between neighboring natural layers), and secondly, both in chemical composition and by the crystal structure these inclusions do not differ from the basic matrix. Only their specific resistivity is much greater than that of the basic matrix.

5. Conclusion

In conclusion, we can say that for elucidate the mechanisms of the kinetic phenomena in semiconductors of the type of single crystals of AIIIBVI compounds selenides with a layered crystal structure, it is necessary to present them as a crystalline semiconductor, consisting of a low-resistivity (LR) matrix with chaotic high-resistivity (HR) inclusions, and having local energy levels in the forbidden band, differing in origin, nature, and parameters. More accurately, these crystals in general can be represented as a nano-composite materials [10-13], consisting of a low-resistivity semiconductor matrix with a chaotic semiconductor nano-disperser of the same chemical composition. Moreover, the magnitude and character of the dependencies of the kinetic parameters on external factors in this "nano-composite" can be varied by varying the level of doping with rare-earth elements at small amounts of the introduced impurity. The observed influence of doping with REE is not associated with intra-center impurity

References

[1] K. Zeiger “Physics of Semiconductors”, Mir, Moscow, 1977 (in Russian).
[2] N. Mott, E. Davis “Electronic Processes in Non-Crystalline Substances”. V. I and V. II, Mir, Moscow, 1982 (in Russian).
[3] Brandt N.B., Kovalyuk Z.D., Kulbachinsky V.A., FTP, **22** (9), 1567 (1988) (in Russian).
[4] Abdinov A.Sh., Babayeva R.F., Rzayev R.M., Inorganic Materials, **48** (8), 892 (2012) (in Russian).
[5] Abdinov A.Sh., Kyazymzadeh A.G, Akhmedov A.A., FTP, **12** (9), 1759 (1978) (in Russian).
[6] Babayeva R.F., Proceedings of the NAS of Azerbaijan, Series of Physics and Mathematics and Tehn. Sciences, Physics and Astronomy, **XXIX** (5), 202 (2009) (in Russian).
[7] Huseynov A.M., Sadikhov T.I., In: Electrophysical properties of semiconductors and gas-discharge plasma, Baku: ASU. - 1989. - P. 42 (in Russian).
[8] E.Konewell “Kinetic properties of semiconductors in strong electric fields”, Mir, Moscow, 1970 (in Russian).
[9] M.Lampert, P.Mark “Injection currents in solids”, Mir, Moscow, 1977 (in Russian).
[10] Peng H., Meister S., Chan C.K., Zhang X.F., Cui Y., Nano Letters, **7** (1), 199 (2007).
[11] Late D.J., Liu B., Matte H.S., Rao C.N., Dravid V.P., Advanced Functional Materials, **22** (9), 1894 (2012) (in Russian).
[12] Rybkovskiy D.V., Vorobyev I.V., Osadchiy A.V., Obraztsova E.D., Journal of Nanoelectronics and Optoelectronics, **7**, 65 (2012).
[13] Rybkovskiy D.V., Osadchy A.V., Obraztsova E. D., Journal of Nanoelectronics and Optoelectronics, **8**, 110 (2013).

E-mail: abdinov_axmed@yahoo.com; Babaeva-Rena@yandex.ru

Production and decay of Higgs bosons in muon colliders

[1,a)]S. K. ABDULLAYEV, [2,b)]M. SH. GODJAYEV

[1,2)]*Faculty of Physics, Department of Theoretical Physics, Baku State University,*
Az 1148, *Baku, Azerbaijan, Z.Khalilov str.*, 23, *e-mail:* [a)]*sabdullayev@bsu.edu.az* , [b)]*m_qocayev@mail.ru*

Abstract

In the framework of the Standard Model the processes of resonant Higgs boson production in arbitrarily polarized muon-antimuon collisions are investigated: $\mu^-\mu^+ \to H^* \to Zf\bar{f}$ and $\mu^-\mu^+ \to H^* \to Wf\bar{f}'$, where $f\bar{f}\,(f\bar{f}')$ is a pair of fundamental fermions. Analytic expressions for the cross sections of spiral processes are obtained, and the possibility of obtaining information on the Higgs boson CP-parity is investigated.

Keywords: *Standard model, Higgs boson, left and right coupling constants, Weinberg parameter, spiral amplitudes, helicity.*

1. Introduction

As is known, the scalar Higgs boson was recently opened at the Large Hadron Collider (LHC) by ATLAS and CMS collaborations [1, 2]. In this regard, the theoretical interest in the various channels of production and decay of this boson has greatly increased. In this paper we study the processes of the resonant Higgs boson production in arbitrarily polarized muon-antimuon collisions:

$$\mu^- + \mu^+ \to H^* \to Z + f + \bar{f}\,, \qquad (1)$$

$$\mu^- + \mu^+ \to H^* \to W + f + \bar{f}'\,, \qquad (2)$$

where $f\bar{f}\,(f\bar{f}')$ is a pair of fundamental fermions.

2. Theory

The cross section of the reaction $\mu^-\mu^+ \to \Phi^* \to Zf\bar{f}$. The Feynman diagram for the process (1) is shown in Fig. 1. The 4-momentum of particles are shown over the diagram. In addition to the standard CP-even Higgs boson H, CP-odd A-boson is also discussed in the literature [3]. In this connection, we have considered the Φ-boson, the interaction Lagrangian with the muon pair which has the CP-even and CP-odd components

$$L_{\Phi\mu\bar{\mu}} = \frac{m_\mu}{\eta}\bar{\mu}(a_\mu + b_\mu\gamma_5)\mu\cdot\Phi(p)\,. \qquad (3)$$

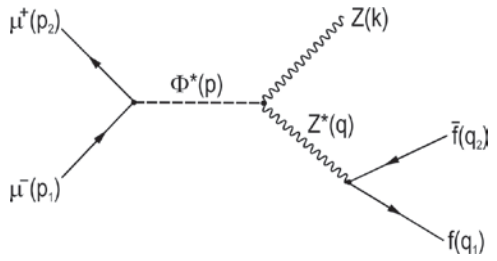

Fig. 1. *Feynman diagram of the reaction* $\mu^-\mu^+ \to \Phi^* \to Zf\bar{f}$

Here $\Phi(p)$ the Φ-boson wave function normalized to unity, η the vacuum expectation value of the scalar field, a_μ and b_μ some constants, where when $a_\mu = 1$, $b_\mu = 0$ we obtain the standard Higgs boson and when $a_\mu = 0$, $b_\mu = 1$ we obtain the CP-odd A-boson.

The transition amplitude of the process (1) is given by:

$$M(\mu^-\mu^+ \to \Phi^* \to Zf\bar{f}) = \frac{m_\mu}{\eta}[\bar{\upsilon}(p_2)(a_\mu + b_\mu\gamma_5)u(p_1)]D_\Phi(s)\times$$
$$\times\frac{2M_Z^2}{\eta}U_\mu^*(k)D_Z(s_1)\frac{e}{2\sin\theta_W\cos\theta_W}\{\bar{u}(q_1)\gamma_\mu\times$$
$$\times[g_L(f)(1+\gamma_5) + g_R(f)(1-\gamma_5)]\upsilon(q_2)\}. \qquad (4)$$

Here $U_\mu^*(k)-$ is the polarization 4-vector of the Z-boson, $D_\Phi(s) = (s - M_\Phi^2 + iM_\Phi\Gamma_\Phi)^{-1}$, M_Φ and Γ_Φ is the mass and total width of the Φ-boson, $\sqrt{s}$ – is the total energy of the $\mu^-\mu^+$-pair in the center-of-mass system, $D_Z(s_1) = (s_1 - M_Z^2)^{-1}$, $s_1 = (q_1 + q_2)^2$, M_Z – mass of the Z-boson, $g_L(f)$ and $g_R(f)$ – the left and right coupling constants of the fermions with the Z-boson

$$g_L(f) = I_3^f - Q_f\sin^2\theta_W,\ g_R(f) = -Q_f\sin^2\theta_W, \qquad (5)$$

θ_W – Weinberg's angle, I_3^f and Q_f the third projection of the weak isospin and the electric charge of the fermion.

By integration with respect to phase volume in the center-of-mass frame we obtain the following expression for the total cross section of the reaction (1):

$$\sigma(\mu^-\mu^+ \to \Phi^* \to Zf\bar{f}) = \frac{\alpha N_C}{768\pi^2}\left(\frac{m_\mu M_Z}{\eta^2}\right)^2\frac{|D_\Phi(s)|^2}{x_W(1-x_W)}\times$$
$$\times\{|a_\mu|^2[1 + (\vec{\xi}_1\vec{\xi}_2) - 2(\vec{n}\vec{\xi}_1)(\vec{n}\vec{\xi}_2)] + |b_\mu|^2[1 - (\vec{\xi}_1\vec{\xi}_2)] - 2\,\mathrm{Re}(a_\mu b_\mu^*)\times$$
$$[(\vec{n}\vec{\xi}_1) - (\vec{n}\vec{\xi}_2)] + 2\,\mathrm{Im}(a_\mu b_\mu^*)(\vec{n}[\vec{\xi}_1\vec{\xi}_2])\}\times$$
$$\times[g_L^2(f)(1-h_1)(1+h_2) + g_R^2(f)(1+h_1)(1-h_2)]R(x)\,. \qquad (6)$$

Here N_C is the color factor ($N_C = 1$ for leptons and $N_C = 3$ for quarks), $\vec{\xi}_1$ and $\vec{\xi}_2$ are the unit vectors directed along the muon and antimuon spins in their rest systems, $\vec{n}-$ the unit vector along the muon momentum, $x_W = \sin^2\theta_W -$ the Weinberg's parameter, h_1 and h_2 the helicities of the fermion and antifermion, through x the

indicated ratio M_Z^2/s, and the function $R(x)$ is

$$R(x)=\frac{3(20x^2-8x+1)}{\sqrt{4x-1}}\arccos\left(\frac{3x-1}{2x\sqrt{x}}\right)-$$
$$-\frac{3}{2}(4x^2-6x+1)\ln x-\frac{1-x}{2x}(47x^2-13x+2). \qquad (7)$$

Let us consider the case when the $\mu^-\mu^+$-pair is polarized transversely, and the summation is made over the polarizations of the fermions:

$$\sigma(\mu^-\mu^+\to\Phi^*\to Z\bar{f}f)=\frac{\alpha N_C}{192\pi^2}\left(\frac{m_\mu M_Z}{\eta^2}\right)^2\frac{|D_\Phi(s)|^2}{x_W(1-x_W)}\times$$
$$\times[g_L^2(f)+g_R^2(f)]\{|a_\mu|^2+|b_\mu|^2+(|a_\mu|^2-|b_\mu|^2)$$
$$\times\eta_1\eta_2\cos\varphi-2\,\mathrm{Im}(a_\mu b_\mu^*)\eta_1\eta_2\sin\varphi]R(x), \qquad (8)$$

where η_1 and η_2 are the modules of the transverse components of the muon polarizations, $\varphi-$ the angle between the vectors $\vec{\eta}_1$ and $\vec{\eta}_2$.

It follows from this formula that if the transverse polarizations of the muon and the antimuon are parallel ($\varphi=0$), then the production of the Φ-boson can occur only as a result of the CP-even interaction (for complete transverse polarization of the muons $\eta_1=\eta_2=1$):

$$\sigma(\varphi=0)\sim|a_\mu|^2[g_L^2(f)+g_R^2(f)].$$

The production of a Φ-boson due to the CP-odd interaction occurs only for antiparallel transverse polarizations of the muon pair ($\varphi=\pi$):

$$\sigma(\varphi=\pi)\sim|b_\mu|^2[g_L^2(f)+g_R^2(f)].$$

If the Φ-boson is indeed a mixture of the CP-even and CP-odd states, then transverse spin asymmetries appear in the process $\mu^-+\mu^+\to\Phi^*\to Z+f+\bar{f}$:

$$A_1=-\eta_1\eta_2\frac{2\,\mathrm{Im}(a_\mu b_\mu^*)}{|a_\mu|^2+|b_\mu|^2},\quad A_2=\eta_1\eta_2\frac{|a_\mu|^2-|b_\mu|^2}{|a_\mu|^2+|b_\mu|^2}. \qquad (9)$$

If the quantities a_μ and b_μ are of the same order, then the asymmetry A_1 can reach values of the order of 1 for a complete transverse polarization of muons. As for the transverse spin asymmetry A_2, it should be noted that for a pure CP-state one of the coefficients a_μ and b_μ is equal to zero and this asymmetry will either +1, or –1 depending on whether the Φ-boson is a CP-even or CP-odd state.

In the case of longitudinally polarized particles, the cross section of process (1) takes the form:

$$\sigma(\mu^-\mu^+\to\Phi^*\to Z\bar{f}f)=\frac{N_C}{768\pi^2}\left(\frac{m_\mu M_Z}{\eta^2}\right)^2\frac{|D_\Phi(s)|^2}{x_W(1-x_W)}\times$$
$$\times\{[|a_\mu|^2+|b_\mu|^2](1+\lambda_1\lambda_2)-2\,\mathrm{Re}(a_\mu b_\mu^*)(\lambda_1+\lambda_2)\}\times$$
$$\times[g_L^2(f)(1-h_1)(1+h_2)+g_R^2(f)(1+h_1)(1-h_2)]R(x). \qquad (10)$$

It follows that the muon and the antimuon (fermion and antifermion) should have the same (opposite) helicities $\lambda_1=\lambda_2=\pm1$ ($h_1=-h_2=\pm1$). This is due to the conservation of the total angular momentum of the particles in the transitions $\mu^-+\mu^+\to\Phi^*$ and $Z^*\to f+\bar{f}$. Consequently, the process (1) corresponds to four spiral sections:

$$\begin{aligned}
&1)\ \sigma(\mu_R^-\mu_R^+\to\Phi^*\to Zf_L\bar{f}_R)\sim|a_\mu-b_\mu|^2g_L^2(f),\\
&2)\ \sigma(\mu_R^-\mu_R^+\to\Phi^*\to Zf_R\bar{f}_L)\sim|a_\mu-b_\mu|^2g_R^2(f),\\
&3)\ \sigma(\mu_L^-\mu_L^+\to\Phi^*\to Zf_Rf_L)\sim|a_\mu+b_\mu|^2g_R^2(f),\\
&4)\ \sigma(\mu_L^-\mu_L^+\to\Phi^*\to Zf_Lf_R)\sim|a_\mu+b_\mu|^2g_L^2(f).
\end{aligned} \qquad (11)$$

Fundamental fermions are $f=\nu_e,\nu_\mu,\nu_\tau,e^-,\mu^-,\tau^-,u,d,s,c$ and b (because $M_H<m_t$ of t-quark is not production). To find the overall cross section of the process $\mu^-+\mu^+\to H^*\to Z+Z^*$, it is necessary to find the sum $N_C\sum_f[g_L^2(f)+g_R^2(f)]$ over the fundamental fermions.

After this summation for the cross section for the resonance production of the Higgs boson ($a_\mu=1$, $b_\mu=0$) by the channel $\mu^-+\mu^+\to H^*\to Z+Z^*$, we obtain:

$$\sigma(\mu^-\mu^+\to H^*\to ZZ^*)=$$
$$=\frac{4\pi}{(s-M_H^2)^2+\Gamma_H^2M_H^2}\Gamma(H\to\mu^-\mu^+)\Gamma(H\to ZZ^*). \qquad (12)$$

Here $\Gamma(H\to\mu^-\mu^+)$ und $\Gamma(H\to ZZ^*)$ – are the partial decay widths determined by expressions

$$\Gamma(H\to\mu^-\mu^+)=\frac{M_H}{8\pi}\left(\frac{m_\mu}{\eta}\right)^2,$$
$$\Gamma(H\to ZZ^*)=$$
$$=\frac{\alpha}{32\pi^2}\frac{M_H}{x_W(1-x_W)}\left(\frac{M_Z}{\eta}\right)^2\left(\frac{7}{4}-\frac{10}{3}x_W+\frac{40}{9}x_W^2\right)R(x). \qquad (13)$$

The cross section of the reaction $\mu^-\mu^+\to H^*\to WW^*$. The resonance production and decay of the Higgs boson according to the channels $\mu^-+\mu^+\to H^*\to W^-+f+\bar{f}'$, $\mu^-+\mu^+\to H^*\to W^++f'+\bar{f}$, where $f=\nu_e,\nu_\mu,\nu_\tau,u,c$, a $f'=e^+,\mu^+,\tau^+,\bar{d},\bar{s}$ also are studied. The Feynman diagram of the process $\mu^-+\mu^+\to H^*\to W^-+f+\bar{f}'$ is shown in Fig. 2. Calculations show that the squares of the amplitudes of the decay channels $\mu^-+\mu^+\to H^*\to W^-+f+\bar{f}'$ and $\mu^-+\mu^+\to H^*\to W^++f'+\bar{f}$ are the same, therefore

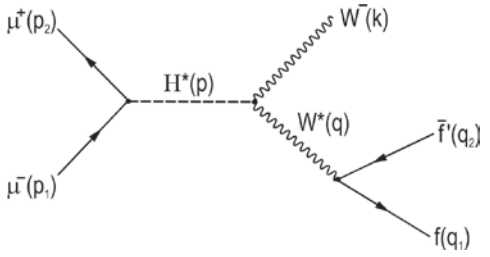

Fig. 2. *Feynman diagram of the reaction* $\mu^-\mu^+\to H^*\to W^-f\bar{f}'$.

for the cross section of the process $\mu^- + \mu^+ \to H^* \to$ $\to W + W^*$ we have the expression (for all possible fermions f and f' are summed):

$$\sigma(\mu^-\mu^+ \to H^* \to WW^*) = \frac{4\pi}{(s - M_H^2)^2 + \Gamma_H^2 M_H^2} \times$$
$$\times \Gamma(H \to \mu^-\mu^+)\Gamma(H \to WW^*), \qquad (14)$$

where $\Gamma(H \to WW^*)$ is the partial width of the decay $H \to W + W^*$ (with $R(x)$ being the same as before, x defining as $x = M_W^2/s$):

$$\Gamma(H \to WW^*) = \frac{3\alpha}{32\pi^2} \frac{M_H}{x_W} \left(\frac{M_W}{\eta}\right)^2 R(x). \qquad (15)$$

3. Results

In Fig. 3 shows the dependence of the cross section (12) on the energy $\sqrt{s}$ at $M_H = 125$ GeV, $\Gamma_H = 4$ MeV, $m_\mu = 0.1056$ GeV, $M_Z = 91.1875$ GeV and $x_W = 0.232$.

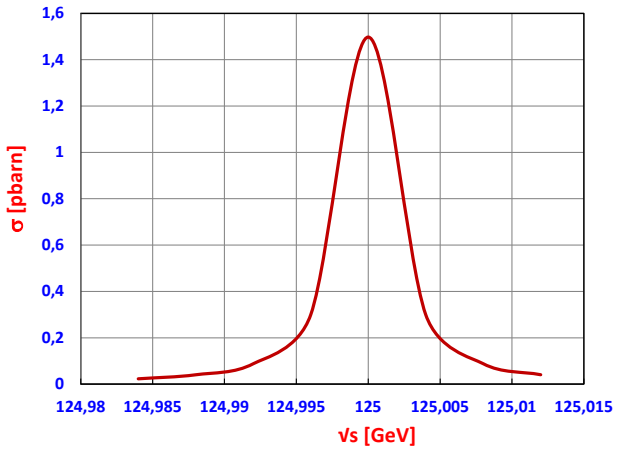

Fig. 2. *Energy dependence of the cross section of the process* $\mu^-\mu^+ \to H^* \to ZZ^*$.

Fig. 4 illustrates the dependence of the cross section (14) on the energy $\sqrt{s}$ at $M_H = 125$ GeV, $\Gamma_H = 4$ MeV, $M_W = 80.425$ GeV and $x_W = 0.232$.

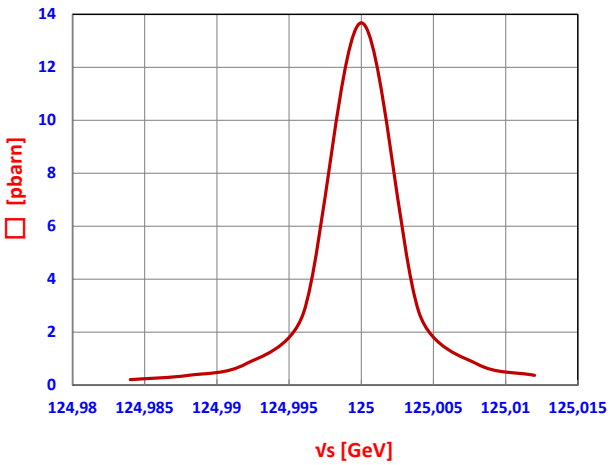

Fig. 4. *Energy dependence of the cross section of the process* $\mu^-\mu^+ \to H^* \to WW^*$.

As can be seen, the cross section of the reaction $\mu^- + \mu^+ \to H^* \to W + W^*$ is an order of magnitude larger than the cross section of the resonance reaction $\mu^- + \mu^+ \to H^* \to Z + Z^*$.

4. References

1. ATLAS Collaboration. Observation of a new particle in the search for the Standard Model Higgs boson with the ATLAS detector at the LHC // Phys. Letters, 2012, B176, p. 1-29.
2. CMS Collaboration. Observation of a new boson at mass of 125 GeV with the CMS experiment at the LHC // Phys. Letters, 2012, B716, p.30-60.
3. Djouadi A. The Anatomy of Electro-Weak Symmetry Breaking. Tome I: The Higgs boson in the Standard Model. arXiv: hep-ph/0503172v2, 2005.
4. Djouadi A. The Anatomy of Electro-Weak Symmetry Breaking. Tome II: The Higgs bosons in the Minimal Supersymmetric Model, arXiv: hep-ph/0503173v2, 2005.

Direct inclusive gluon production in pion-proton collision

[1,2,*)]A. I. AHMADOV, [3)]H. M. NAGIYEV, [3)]V. A. TARVERDIYEVA, [4)]E. A. DADASHOV

[1]*Department of Theoretical Physics, Baku State University, Z. Khalilov st.* 23, *AZ* 1148, *Baku, Azerbaijan,*
[2]*Institute for Physical Problems, Baku State University, Z. Khalilov st.* 23, *AZ* 1148, *Baku, Azerbaijan,*
[3]*Institute of Physics, Azerbaijan National Academy of Sciences, H.Javid ave.* 131, *AZ* 1143, *Baku, Azerbaijan,*
[4]*Lankaran State University, H. Aslanov ave.* 50, *AZ* 4200, *Lankaran, Azerbaijan*
[*]*ahmadovazar@yahoo.com*

Abstract

In this article we calculate the contribution of the higher-twist Feynman diagrams to the large- p_T inclusive gluon production cross-section in πp collisions for the case of the frozen coupling constant approach within perturbative and holographic QCD. The contributions of the higher-twist effects to the cross section has extracted for the different pion distributions amplitudes. It is shown that higher-twist cross sections and ratio higher-twist cross section on the leading twist one is very sensitive on the choice of the pion distributions amplitudes, as predicted by holographic and perturbative QCD. Analysis of our calculations shows that the contribution of the higher-twist effects to the magnitude of the cross section is decreasing by the increasing of beam energy.

Keywords: *Nanoparticles, layered crystals, 2-D materials, gallium sulfide, absorption spectra, characterization, semiconductors, carrier confinement, laser ablation, optical band gap.*

1. Introduction

It is well known that Quantum Chromodynamics (QCD) is the fundamental theory of the strong interactions. Therefore in order to describe the structure and dynamical properties of hadrons at the amplitude level many researchers have been studying QCD. The hadronic distribution amplitude in terms of internal structure degrees of freedoms plays a crucial role in QCD process predictions.

One of the basic problems in QCD is choosing the renormalization scale in running coupling constant $\alpha_s(Q^2)$. In principle, in perturbative QCD (pQCD) calculations, the argument of the running coupling constant in both the renormalization and factorization scale Q^2 should be taken as equal to the square of the momentum transfer of a hard gluon in a corresponding Feynman diagram [1]. In the pQCD, the physical information of the inclusive gluon production is obtained efficiently; therefore, it can be directly compared to the experimental data.

It should be noted that problem the existence of the higher-twist contribution is not yet settled. Also it is necessary to study the difference in the leading-twist results for the frozen coupling constant approach and compare it with that of the higher-twist.

The aim of this study is calculation and analysis the higher-twist cross section of the inclusive gluon production in the pion-proton collisions using the frozen coupling constant approach. Using this approach, the higher twist effects have been already calculated by many authors [2-8].

The calculation and analysis of the higher-twist effects on the dependence of the pion distribution amplitude in inclusive gluon production at πp collision within holhographic and pQCD in the frozen coupling constant approach is the interesting research problems. In this study, we compute the contribution of the higher-twist effects to an inclusive gluon production cross-section by using various pion distribution amplitudes from holographic and pQCD, and applying the frozen coupling constant approach. The higher-twist cross section numerically carried out for the energy of the ALICE experiment. We also estimate and perform comparisons of the leading and the higher-twist contributions.

The contents of the paper is as follows. The related formulas for the calculation of the contributions of the higher-twist and leading-twist diagrams are provided in the next section. The numerical results for the cross-section and discussion of the dependence of the cross-section on the pion distribution amplitudes also our conclusions of the study are presented in Section III.

2. HIGHER-TWIST AND LEADING TWIST CONTRIBUTIONS TO INCLUSIVE GLUON PRODUCTION

The higher-twist Feynman diagrams for the inclusive gluon production in the pion-proton collision $\pi p \to gX$ are shown in Fig.1. For the process $\pi p \to gX$, the amplitude is found by means of the Brodsky-Lepage formula [9]

$$M(\hat{s},\hat{t}) = \int_0^1 dx_1 \int_0^1 dx_2 \delta(1-x_1-x_2) \times$$

$$\Phi_M(x_1,x_2,Q^2)\, T_H(x_1,x_2;Q^2,\mu_R^2,\mu_F^2), \qquad (2.1)$$

where T_H is the sum of the graphs contributing to the hard-scattering part of the subprocess. For the higher-twist, the subprocess is taken as $\pi q_p \to gq$, which contributes to $\pi p \to gX$, where q_p is a constituent of the initial proton target. As seen from Fig. 1, the processes $\pi^+ p \to gX$ and $\pi^- p \to gX$, arise from subprocesses as $\pi^+ d_p \to gu$ and $\pi^- u_p \to gd$, respectively.

The production of the hadronic gluon in the large transverse momentum is available at the high energy, especially at the Large Hadron Collider. Finally, hadronic gluon is a product of the hard-scattering processes, before

hadronization. In the final state, this hadronic gluon is fragmented to hadron. The main dynamical properties of the gluon, which carried one part of the four momentum, are close to the parent parton. In order to understand the parton kinematics one should consider the gluon production process [10]. The higher-twist cross-section for as $\pi p \to gX$ process has the form:

$$E\frac{d\sigma}{d^3p}(\pi p \to gX) =$$

$$= \int_0^1 dx\delta(\hat{s}+\hat{t}+\hat{u})\,\hat{s}G_{q/p}(x,Q^2)\frac{1}{\pi}\frac{d\sigma}{d\hat{t}}(\pi q_p \to gq) \quad (2.2)$$

where $G_{q/p}(x,Q^2)$ is the quark distribution function inside a proton.

The cross section for higher-twist subprocess $\pi\, q_p \to gq$ is parameterized in terms of the following Mandelstam invariant variables in the form:

$$\hat{s} = (p_1 + p_g)^2 = (p_2 + p_\pi)^2,\ \hat{t} = (p_g - p_\pi)^2,$$
$$\hat{u} = (p_1 - p_\pi)^2. \quad (2.3)$$

Then the parton-level cross-section within running coupling constant method becomes [11]

$$\frac{d\sigma}{d\hat{t}}(\pi q_p \to gq) = \frac{256\pi^2}{81\hat{s}^2}[D(\hat{s},\hat{u})]^2\left(-\frac{\hat{t}}{\hat{s}^2}-\frac{\hat{t}}{\hat{u}^2}\right), \quad (2.4)$$

where

$$D(\hat{s},\hat{u}) = \int_0^1 dx\alpha_s^{3/2}(Q_1^2)\left[\frac{\Phi_\pi(x,Q_1^2)}{x(1-x)}\right] +$$
$$+\int_0^1 dx\alpha_s^{3/2}(Q_2^2)\left[\frac{\Phi_\pi(x,Q_2^2)}{x(1-x)}\right] \quad (2.5)$$

By the way, it must be denoted that as a special case we can directly get the result [12] from Eq(2.4) by the applying the frozen coupling constant approximation. It should be noted according to Ref. [1] that in pQCD calculations, the argument of the running coupling constant in both the renormalization and factorization scale Q^2 should be taken equal to the square of the momentum transfer of a hard gluon in a corresponding Feynman diagram:

$$Q_1^2 = (1-x)\hat{s} \text{ and } Q_2^2 = -x\hat{u}, \quad (2.6)$$

respectively.

In the soft regions $x \to 0$ and $x \to 1$ (for u and s channels), integrals (2.5) diverge, therefore in these regions for their calculations some regularization methods of $\alpha_s(Q^2)$ are needed. One of the simple method is called frozen coupling constant approximation for the regularization these singularity.

Although the frozen QCD coupling constant was introduced a long time ago, it is also interesting and important in these days [13-21]. The origin of it comes from the divergent infrared behavior of the well-known renormalization group expression for α_s. For this reason, it is used as a constant in the infrared domain. Another reason for introducing the frozen coupling is the pQCD coupling. Also, the effects of running α_s should be taken into account in all calculations. However, it makes some QCD calculations very difficult. If we want to estimate it approximately, it can be very convenient to use some effective coupling which minimizes the running of α_s in the perturbative region. For getting an agreement with experimental data, the values of the frozen coupling are usually fixed from purely phenomenological considerations. The frozen coupling is frequently used in combination with other phenomenological parameters to describe hadronic processes. We can come across fixed α_s very often in various calculations done in the framework of the leading logarithmic approximation where most important logarithmic contributions are totally resummed while α_s considered as fixed parameter and its argument is set off a posteriori from physical considerations. The solution of the Schwinger-Dyson equations can be also another method for investigating the infrared behavior of the gluon and ghost propagators and for the running coupling constant at low energies [22]. Although early studies of the Schwinger-Dyson equations for the gluon propagator are very singular in the infrared [23-25], other studies found infrared finite propagators. For example, in Ref. [26] the gluon acquires a dynamical mass m_g^2, and the other is extensively discussed in Refs. [27, 28] when the gluon propagator goes to zero when the momentum $Q^2 \to 0$. In both cases, the freezing of coupling constant appears in the infrared. In the case where squared momentum of a hard gluon gets the form $Q^2 \to Q^2 + m_g^2$, for running coupling constant leads to $\alpha_s(Q^2) \to \alpha_s(Q^2 + m_g^2)$. Here m_g^2 is interpreted as an effective dynamical gluon mass or fictitious mass of gluon. By frozen coupling constant approach for squared of transfer momentum of the hard gluon in single meson photoproduction, $\gamma p \to MX$ is taken as $Q_1^2 = \hat{s}/2$ and $Q_2^2 = -\hat{u}/2$ [5, 6].

There are different forms of the pion distribution amplitude available in the literature. In the present numerical calculations, we use several choices, such as the asymptotic distribution amplitude derived in pQCD evalution [29], distribution amplitudes predicted by AdS/CFT [30, 31], the Chernyak-Zhitnitsky (CZ) [32], the Bakulev-Mikhailov-Stefanis (BMS) [33, 34] and and pion distribution amplitudes in which Gegenbauer coefficients $C_2^{3/2}$ and $C_4^{3/2}$ are extracted from BELLE experiment [35]:

$$\Phi_{asy}(x,Q^2 \to \infty) = \sqrt{3}f_\pi x(1-x), \quad (2.7)$$

$$\Phi^{hol}(x,\mu_0^2) = \frac{4}{\sqrt{3}\pi}f_\pi\sqrt{x(1-x)}, \quad (2.8)$$

$$\Phi_{CZ}(x,\mu_0^2) = \Phi_{asy}(x)\left[C_0^{3/2}(2x-1)+\frac{2}{3}C_2^{3/2}(2x-1)\right], \quad (2.9)$$

$$\Phi_{BMS}(x,\mu_0^2) = \Phi_{asy}(x)[C_0^{3/2}(2x-1)+$$
$$+0.20C_2^{3/2}(2x-1)-0.14C_4^{3/2}(2x-1), \quad (2.10)$$

$$\Phi_{BELLE}(x,\mu_0^2) = \Phi_{asy}(x)[C_0^{3/2}(2x-1)+$$
$$+0.12C_2^{3/2}(2x-1)+0.08C_4^{3/2}(2x-1)] \quad (2.11)$$

here $C_n^{3/2}(2x-1)$, are Gegenbauer polynomials.

Substituting Eq.(2.4) into Eq.(2.2), then the differential cross-section for the process $\pi p \to gX$ takes the form [29]

$$E\frac{d\sigma}{d^3p}(\pi p\to gX)=\frac{s}{s+u}xG_{q/p}(x,Q^2)\cdot \frac{256\pi}{81\hat{s}^2}[D(\hat{s},\hat{u})]^2\left(-\frac{\hat{t}}{\hat{s}^2}-\frac{\hat{t}}{\hat{u}^2}\right) \quad (2.12)$$

It should be noted that, as seen from Eqs.(2.4) and (2.12), the higher-twist cross-section is linear with respect to $\hat{t}$, so the cross-section vanishes, if the scattering angle between the final gluon and incident pion is approximately equal to zero. From Eq.(2.12), we see that the higher-twist cross-section proportional to $\hat{s}^{-3}$, which is equivalent to the higher-twist contributions to the $\pi p\to gX$ cross-section have the form of $p_T^{-6}f(x_F,x_T)$.

In the expression Eq.(2.6), we fixed the variable x by taking it as mean value. So, average values for x we take $\bar{x}=1/2$. Thus, for the calculations higher-twist cross-sections within frozen coupling constant approach we substitute $\overline{Q}^2=\hat{s}/2$ and $\overline{Q}^2=-\hat{u}/2$ in Eq. (2.12) for the transfer momentum of the hard gluon, respectively.

The extracting of higher-twist contribution from the inclusive gluon production cross-section is also complicated. One can also consider the comparison of higher-twist corrections with leading-twist contributions. For the leading-twist subprocess in the inclusive gluon production, we take $q\overline{q}\to g\gamma$ as a subprocess of the quark-antiquark annihilation. The differential cross-section for subprocess $q\overline{q}\to g\gamma$ is

$$\frac{d\sigma}{d\hat{t}}(q\overline{q}\to g\gamma)=\frac{8}{9}\pi\alpha_E\frac{e_q^2}{\hat{s}^2}\left(\alpha_s(-\hat{u})\frac{\hat{t}}{\hat{u}}+\alpha_s(-\hat{t})\frac{\hat{u}}{\hat{t}}\right). \quad (2.13)$$

As is seen from Eq.(2.13), leading-twist cross-section strongly depends of the running coupling constant where the running coupling constant depends on the transfer momentum. However, running coupling constant depends on the channels of the process. Here running coupling have been evaluated in the momentum subtraction scheme, for momentum scales u and t, which define the off-shell momenta carried by the quark propagators.

The leading-twist cross-section for production of inclusive gluon is

$$\sum\nolimits_M^{LT}\equiv E\frac{d\sigma}{d^3p}(\pi p\to gX)=$$
$$=\int_0^1 dx_1\int_0^1 dx_2\delta(\hat{s}+\hat{t}+\hat{u})G_{\overline{q}/M}(x_1,Q_1^2)G_{q/p}(x_2,Q_2^2)\times$$
$$\times\frac{\hat{s}}{\pi}\frac{d\sigma}{d\hat{t}}(q\overline{q}\to g\gamma), \quad (2.14)$$

where $\hat{s}=x_1x_2s$, $\hat{t}=x_1t$, $\hat{u}=x_2u$.

Finally, leading-twist contribution to the large-p_T gluon production cross-section in the process $\pi p\to gX$ is

$$\sum\nolimits_M^{LT}\equiv E\frac{d\sigma}{d^3p}(\pi p\to gX)=$$
$$=\int_0^1 dx_1\frac{1}{x_1s+u}G_{\overline{q}/M}(x_1,Q_1^2)G_{q/p}(1-x_1,Q_2^2)\times$$
$$\times\frac{\hat{s}}{\pi}\frac{d\sigma}{d\hat{t}}(q\overline{q}\to g\gamma). \quad (2.15)$$

3. NUMERICAL RESULT AND CONCLUSION

In this study, the inclusive single gluon production is calculated via higher twist mechanism within perturbative and holographic QCD. Concerning the study of the higher-twist contribution, it is primarily important to analyse its relative magnitude of contribution compared to the leading-twist contribution, since only leading-twist diagrams are commonly considered in usual studies of the hadron-hadron collision. However, in our studies the difference of the higher-twist results for the frozen and running coupling constant approaches have been studied with importance. The following results can be concluded from the experiments: the higher-twist contributions to single gluon production cross-section in the pion-proton collisions have important phenomenological consequences.

In the numerical treatment, for the quark distribution functions inside the pion and proton we use the [37,38], respectively. We present our result for $\sqrt{s}=2.76TeV$. The results of our numerical calculations are displayed in Fig. 2-4. In Fig. 2 we show higher-twist cross section $(\Sigma_g^{HT})^0$ calculated in the context of the frozen (frozen cross section) coupling constant approach as a function of the gluon transverse momentum p_T for the pion distribution amplitudes presented in Eqs.(2.7)-(2.11) at $y=0$. In the region $2GeV/c<p_T<30GeV/c$ the cross sections of the process $\pi^+p\to gX$ decreases in the range between $1.801\cdot10^{-9}mbarn/GeV^2$ to $1.464\cdot10^{-15}mbarn/GeV^2$.

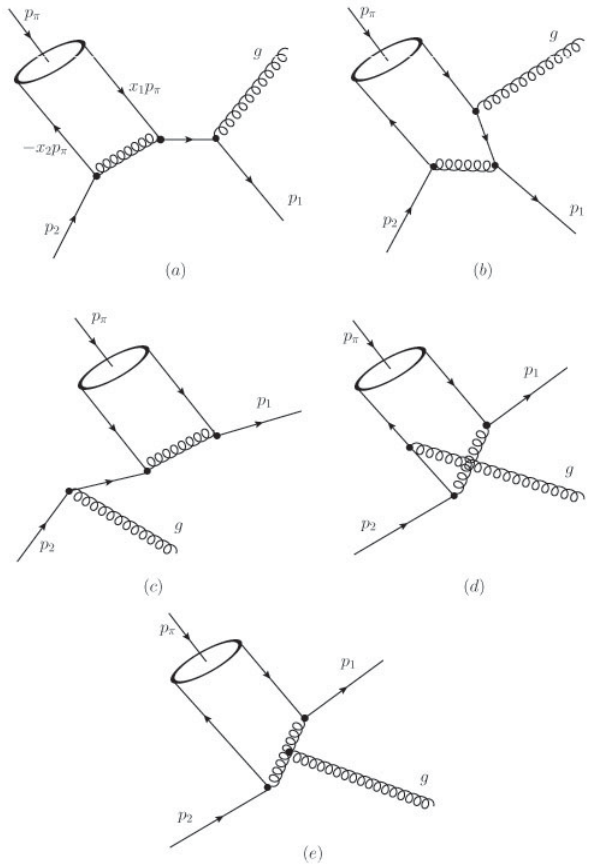

Fig. 1. QCD Feynman diagrams for higher-twist subprocess $\pi q\to gq$ ..

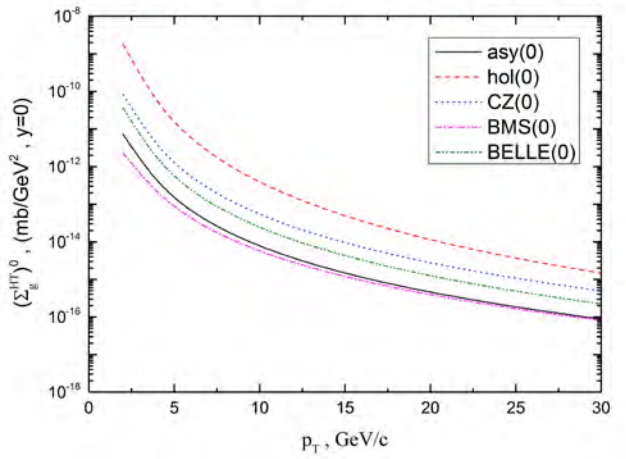

Fig. 2. Higher-twist $\pi^+ p \to gX$ inclusive gluon production cross-section $(\Sigma_g^{HT})^0$ as a function of the transverse momentum of the gluon p_T at the c.m. energy $\sqrt{s} = 2.76TeV$.

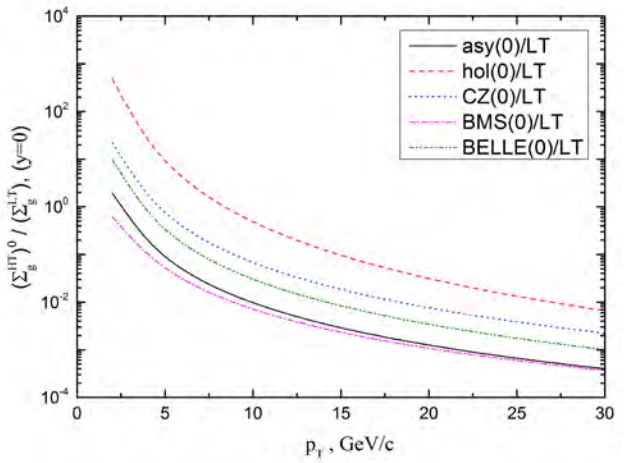

Fig. 3. Ratios $(\Sigma_g^{HT})^0 / \Sigma_g^{LT}$ in the process $\pi^+ p \to gX$, as a function of the transverse momentum of the gluon p_T at the c.m. energy $\sqrt{s} = 2.76TeV$.

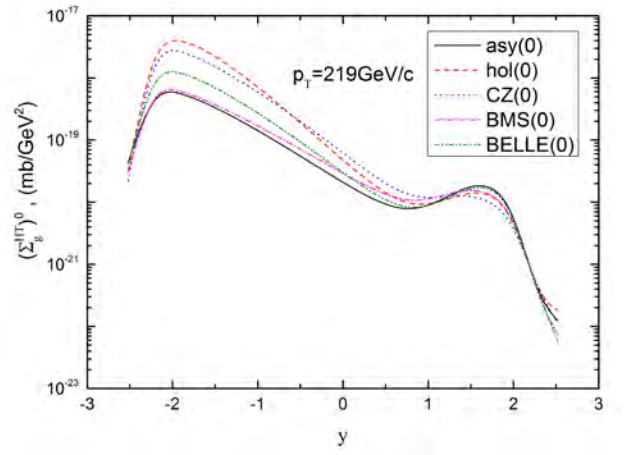

Fig. 4. Higher-twist $\pi^+ p \to gX$ inclusive gluon production cross-section $(\Sigma_g^{HT})^0$ as a function of the rapidity of the gluon y at the transverse momentum of the gluon $p_T = 219GeV/c$, at the c.m. energy $\sqrt{s} = 2.76TeV$.

In Fig. 3, we present the ratio $(\Sigma_g^{HT})^0 / \Sigma_g^{LT}$ the higher-twist cross section to leading-twist cross section as a function of the transverse momentum of the gluon p_T for the pion distribution amplitudes presented in Eqs.(2.7)-(2.11) at $y = 0$. In Fig. 4, we present higher-twist cross section $(\Sigma_g^{HT})^0$ as a function of the rapidity of the gluon y at the transverse momentum of the gluon $p_T = 219GeV/c$. It is seen from Fig. 4, that frozen cross section for all distribution amplitudes of pion have two maxima, where the first maximum is approximately at the point $y = -2$ and second maximum is approximately at the point $y = 1.7$. But, the leading-twist cross section only has one maximum at $y = 1.7$.

Therefore, they will be helpful for detailed investigation of the dynamical properties of the nucleon. The higher-twist gluon production cross-section in the pion-proton collisions depends on the form of the pion distribution amplitudes and may be used for future study. Moreover, the contributions of higher-twist effects within holographic QCD in these process are essential and may help to analyze experimental results. Note that the direct gluon production spectrum can be measured with large precision, so results obtained in this study will be helpful further tests of the hadron dynamics at large p_T . As is seen from Eq.(2.4) higher-twist cross-section is proportional to the third power of $\alpha_s(Q^2)$, but the leading-twist is linearly proportional to $\alpha_s(Q^2)$. Therefore, their ratios strongly depend on the $\alpha_s(Q^2)$.

Our investigation enables us to conclude that the higher-twist direct inclusive gluon production cross section in the pion-proton collisions strongly by depends on the choice of the pion distribution amplitudes and may be used for their study. Analysis of our calculations shows that the magnitude of cross sections calculated in the frozen constant coupling approach in some regions is larger than the leading-twist cross sections in 1-2 order. Further investigations are needed in order to clarify the role of high twist effects in this process. The pion-proton collisions provide us with a new opportunity to probe a proton's internal structure.

Further investigations are needed in order to clarify the role of higher-twist effects in QCD. In hadron-hadron collisions, real gluons at high transverse momentum can serve as a short distance probe of the incident hadrons. Especially, the future experimental measurements will provide further tests of the dynamics of large- p_T gluon production beyond the leading twist.

4. REFERENCES

1. S. J. Brodsky, G. L. Lepage, and P. B. Mackenize, Phys. Rev. D **28**, pp. 228 (1983).
2. F. S. Sadykhov and A. I. Akhmedov, Russ. Phys. J. **38**, pp. 513 (1995).
3. A. I. Ahmadov, I. Boztosun, R. Kh. Muradov, A. Soylu, and E. A. Dadashov, Int. J. Mod. Phys. E**15**, pp. 1209 (2006).
4. A. I. Ahmadov, I. Boztosun, A. Soylu, and E. A. Dadashov, Int. J. Mod. Phys. E**17**, pp.1041 (2008).

5. J. A. Bagger and J. F. Gunion, Phys. Rev. D **29**, pp. 40 (1984).
6. J. A. Bagger and J. F. Gunion, Phys. Rev. D **25**, pp.2287 (1982).
7. V. N. Baier and A. Grozin, Phys. Lett. B**96**, pp.181 (1980).
8. S. Gupta, Phys. Rev. D**24**, pp.1169 (1981).
9. 9. G. L. Lepage and S. J.Brodsky, Phys. Rev. D **22,** pp. 2157 (1980).
10. J. F. Owens, Rev. Mod. Phys. **59**, pp. 465 (1987).
11. A. I. Ahmadov, C. Aydin, R. Myrzakulov, and O. Uzun, Int. J. Mod. Phys. A**30**, 1550219 (2015).
12. E. L. Berger and S. J. Brodsky, Phys. Rev. D**24**, pp. 2428 (1981).
13. G. Curci, M. Greco, Y. Srivastava, Phys. Rev. Lett. **43**, pp. 834 (1979).
14. G. Curci, M. Greco, Y. Srivastava, Nucl. Phys. B**159**, pp.451 (1979).
15. M. Greco, Phys. Lett. B**100**, pp. 351 (1981).
16. M. Greco, G. Penso, Y. Srivastava, Phys. Rev. D**21**, pp. 2520 (1980).
17. Y. I. Dokshitzer, B. R. Webber, Phys. Lett. **404**, pp.321 (1997).
18. Y. I. Dokshitzer, G. Marchesini and B. R. Webber, Nucl. Phys. B **469,** pp.93 (1996).
19. B. Badelek, J. Kwiecinski and A. Stasto, Z. Phys. C **74**, pp.297 (1997).
20. M. Ciafaloni, D. Colferai, G. P. Salam, A. M. Stasto, Phys. Rev. D **66**, pp. 054014 (2002).
21. A. V. Kotikov, A. V. Lipatov, N. P. Zotov,JETP **101,** pp.811 (2005).
22. C. D. Roberts and A. G. Williams, Prog. Part. Nucl. Phys. **33**, pp. 477 (1994).
23. S. Mandelstam, Phys. Rev. D **20**, pp.3223 (1979).
24. N. Brown and M. R. Pennington, Phys. Rev. D **38**, pp.2266 (1988).
25. N. Brown and M. R. Pennington, Phys. Rev. D **39**, pp.2723 (1989).
26. J. M. Cornwall, Phys. Rev. D **26**, 1453 (1982).
27. R. Alkofer and L. von Smekal, Phys. Rep. **353**, pp. 281 (2001).
28. L. von Smekal, A. Hauck, and R. Alkofer, Ann. Phys. (N.Y.) **267**, pp.1 (1998).
29. G. Parisi and R. Petronzio, Phys. Lett. B **95**, pp.51 (1980).
30. J. Schwinger, Phys. Rev. **127**, pp. 324 (1962).
31. G. P. Lepage and S. J. Brodsky, Phys. Lett.B **87**, pp. 359 (1979).
32. S. J. Brodsky and G. F. de Teramond, Phys. Rev. D **77**, 056007 (2008).
33. S. J. Brodsky, Proc. Sci., LHC07 (2007) 002.
34. V. L. Chernyak and A. R. Zhitnitsky, Phys. Rep. **112**, pp.173 (1984).
35. A. P. Bakulev, S. V. Mikhailov and N. G. Stefanis, Phys. Lett. B **578**, pp. 91 (2004).
36. A. P. Bakulev, S. V. Mikhailov, A. V. Pimikov, and N. G. Stefanis, Phys. Rev. D**86**, pp.031501 (2012).
37. S. Uehara et al. [Belle Collaboration], Phys. Rev. D**86**, pp.092007 (2012).
38. E. L. Berger, Phys. Rev. D **26**, pp.105 (1982).
39. S.-I Nam, Phys. Rev. D **86**, pp.074005 (2012).
40. A. D. Martin, W. J. Stirling, R. S. Thorne, G. Watt, Eur. Phys. J. C **63**, pp. 189 (2009).

Analysis of Typical Economic Risks in the Development of Alternative Energy Sources

AMIL M. MAHARRAMOV[1], AND RUSTAM SH. SHAFAGATOV[2],

[1]*Baku State University, Faculty of International Relations and Economy, Department of Economy and Management. Akademik Zahid Khalilov Street 23, Az1148, Baku, Azerbaijan*
[2] *Academy of Public Administration under the President of Azerbaijan Republic, Department of Public Administration. Lermontov Street 74, Az1001, Baku, Azerbaijan*

Abstract

Hereby in this article, the problems of developing and maintaining main alternative energy sources were researched by the means of economic risks. As of the basic goal to get profit for any entrepreneurship, economic risks and their solution possibilities are main borders in the development of alternative energy resources, and for any government existence of risk issues are the factors in the decision making. At the end of current article as a conclusion there are given common risks solution suggestions.

Keywords: *alternative energy, renewable energy, risks, wind, solar, biomass, geothermal*

1. Introduction

Sustainable development is characterized by the application of advanced technologies and innovations, the growth of industrial production and the real sector nearby the environmental protection standards. All these are carried out in parallel with the growth in the production and consumption of electricity sometimes directly, sometimes indirectly. Therefore, the quantity of energy consumption per capita can be used as an indicator to determine the level of socio-economic development of the country or region. Energy production has a direct impact on the growth of living standards of the members of society, and any setback leads to the deterioration of the social welfare. Therefore, the diversification of energy sources can be considered as the main facing task. Transition from the use of traditional energy sources to alternative energy is seen as the first step on this path. Progressive expansion of the use of alternative and renewable energy sources leads to the achievement of environmentally friendly energy also becomes one of knowledge-intensive high-tech industries.

2. Methodology

Total energy production share of the energy gathered from alternative energy sources in Costa Rica - 99% (2015), Nicaragua - 54% (2015), in the US, 13% (2014), in Germany, 78% (2015) and whereas Finland, Scotland and in Sweden, the consumer use is fulfilled by 100% [1]. Along with the steady development of alternative energy technologies, with higher efficiency and less maintenance, makes more public confidence in this area. All this leads to positive psychological changes, and creates favourable conditions for attracting potential investors.

It is no coincidence that BP, the multinational company as a major hydrocarbon producer and processor, now thinks of the development of alternative energy sources as a prospective area and declares as priority investing in the amount of £ 4.6 billion [2]. In addition, the developed countries has quite a large amount of budget expenditures for the development and adoption of alternative energy sources each year, also to conduct research in this field, separately. Great attention can be seen if we add to the total the investments made by individual companies in the world to the sphere of alternative and renewable energy production and related subfields [3].

Figure 1 Global renewable electricity production by region

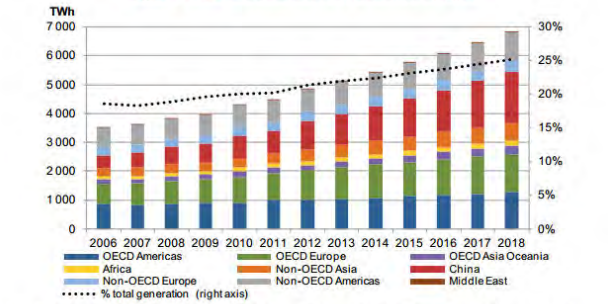

Notes: TWh = terawatt hours. Unless otherwise indicated, all materials in figures and tables in this chapter derive from International Energy Agency (IEA) data and analysis.

But, in all cases, the use of alternative energy technologies is accompanied by specific risks. It is clear that, these risks are different for each alternative source of energy, and formed under the influence of different factors such as anticipated production capacity, the required investment, the expected investment yield, profitability rate, the market long and short-term demand-supply balance, production costs, competition and other economic indicators, as well as the natural environment impact. An MIT spinout, EverVest, has built a data-analytics platform whose goal is to give investors rapid, accurate cash-flow models and financial risk analyses for renewable-energy projects. Recently acquired by asset-management firm Ultra Capital, EverVest's platform could help boost investments in sustainable-infrastructure projects, including wind and solar power [6]. Such projects help to calculate investment plans, but no risk may be overseen.

3. Results

In 2010 global investment in new renewable energy projects exceeded investment in new fossil fuel fired

plants for the first time, largely driven by a mix of renewable energy incentives and political pressure to invest in less emission-intensive energy production. Yet although investments in renewable energy plants are growing, so are the risks [7]. Alternative and renewable energy production is a government's policy component by the means of energy, environmental, innovative and safety aspects as well as being economical in terms of the effectiveness and based on the business logic. So, the area's economic risk assessment must be based on the risk assessment of the common methods of business organization and management. Such an approach allows determining the assessment of economic interests of business entities in this. Taking into account the above mentioned various economic risks of each alternative energy source can be classified as follows:

1. On Solar energy (helio energy):

- Revenue vary or rise and becoming higher the price of the obtained energy in comparison to the consumption energy price – this can be happen by the reduction in overall energy prices in the country. In this case, the energy gathered by means of solar energy generators can be sold to the appropriate business spheres where a higher price of energy is acceptable. Thus, the price of electricity sold to business entities usually is higher than the price of electricity sold to the population. In addition, in order to preserve the ecological balance and to meet the requirements of people and to provide the energy to the living areas where electrical wiring is not possible or very difficult in many cases the difference between the prices can be paid by the state subsidy.
- The sharp rise in the price of imported solar cells – this risk may occur in the atmosphere of hyper-inflation or the currency devaluation. In this case, the reduction or elimination of customs duties on government stimulus can be carried through. Ideally, it would be more appropriate to carry out preventive measures against such economic fluctuations creating local production, educating relevant personnel. It will also reduce dependence by using local resources and will lead to realization of the potential in this area. In addition to the creation of new jobs and technology that will make an increase in commodity production capacity. A developing country's local currency may fluctuate greatly, and if their currency inflates the project's revenue stream loses its value in international markets. To protect against currency risk, developers should either negotiate their PPAs to receive payment in a predictable currency or hedge this risk. Although, financial institutions offer exchange rate hedging instruments, such as currency swaps or currency futures options, the upkeep on these agreements may be expensive if the developer negotiates a good position on a volatile currency [5].
- The increase in the production cost in accordance with local requirements – this risk may take place when the rental cost of the land where solar panels are located increase, due to natural factors solar generators influence quality changes incur and efficiency decreases, as a result maintenance prices increase, as well as in the field of human labor price rise and so on. At such time, depending on the case the implementation of softening economic activity can be made to reduce costs with. Management reform, the transfer of production to new areas, the new acquisition of the means of production and so on.

2. On Wind energy:

- Rise and becoming higher the price of the obtained energy in comparison to the consumption energy price - the risk can also be applied to wind energy. Risk mitigation options and solutions are likely to be nearly identical;
- Wind speed maximum and minimum level fluctuations with changes in acute and long-term energy efficiency and lower the acquisition of a small quantity - the risk is related to the optimum altitude air masses flow changes and the structure and design of wind turbines. It is known that depending on the preparation material, the wind generators type, structure type, dimensions and indicators of sustainability to tremble support column and the main blade, any wind turbine has a maximum wind speed limit. And in any excess above maximal turnover the generators stopped working. In such cases, to ensure sustainable energy reduction it may be appropriate to use mobile devices and the development of coastal areas in cases of natural circumstances allow.

3. On Geothermal energy:

- Thermal source undergo temperature changes - the risk usually may take place under the influence of tectonic changes in the movement of rocks in the bottom of the water heat exchanger change in the riverbed. Such cases where as a result, decline in productivity is accompanied, is studied by a German scientist Burkhard Sanner and a technology to provide heat continuously is developed and tested in practice [4]. Solve of this problem as the main issue in the development of geothermal energy allows obtaining geothermal energy at any point of the planet.

4. on the acquisition of energy by means of waste processing:

- Decrement in the quantity of waste or reduction of efficiency as a result of the depreciation of the technology applied - this risk is very rear and not typical for Azerbaijan, but is in the list of possible circumstances that should be considered during the construction of waste processing facility.

5. on the acquisition of energy via small hydroelectric stations:

- The water flow rate or quantity decrease - the risk has been observed in recent years in Azerbaijan. To solve the problem of change the course of rivers because of natural influences can be caused to additional costs. In addition, the drying up of rivers in many cases can be considered as a typical problem. İn such cases the mobilization possibility of the installed equipment

may be the most appropriate solution to solve the problem.

6. on the acquisition of biofuel and biomass:

- a decline in production of the product because of the reduction in crop productivity under the influence of climatic conditions or changes in the needs of the local population - it is the most common problem in this area as well as being at risk would have easy solution methods. Technologies calculated for several plant species processing may be considered as typical way to solve the problem.
- İncrement in the price of imported contributed enzymes – this happens as a result of various risk factors, but can be eliminated by application of regulative and mitigation policies by the state. For entrepreneurial activity subjects this problem can be eliminated by applying a local production based business model.

4. Conclusions

As a conclusion, for economic risk assessment and to minimize costs in the sphere of implementation of alternative energy the followings may be offered:

- It is necessary for government to make great attention to this area as one of the main objectives of sustainable development;
- Tax and customs policy, stimulated widespread to use the alternative energy;
- increased attention to alternative energy management training and preparation sector,;
- For business entities, in the preparation of business projects make NOT only diversified, but also as single or combined type of alternative energy production;
- the risk assessment of hybrid power plants based NOT on the efficiency but, on sustainable energy supplement;
- If natural conditions allow, application of adaptive technologies.

References

[1] https://www.climaterealityproject.org/blog/follow-leader-how-11-countries-are-shifting-renewable-energy

[2] http://polit.ru/news/2013/04/04/ekologia_BP/

[3] http://www.investopedia.com/investing/top-alternative-energy-companies/

[4] *Burkhard Sanner* - Integrated use of geothermal and other renewable energy sources - heat pumps, solar thermal, combined heat and power. Institute of Applied Geosciences, Giessen, Germany, 2003

[5] *Jeffrey Karp, Morgan M. Gerard.* Managing the Risks of Renewable Energy Projects in Developing Countries (http://blog.sandw.com/energyfinancereport/2015/05/managing-the-risks-of-renewable-energy-projects-in-developing-countries/)

[6] *Rob Matheson* | MIT News Office , Calculating the financial risks of renewable energy, September 15, 2016 **(**http://news.mit.edu/2016/startup-evervest-calculating-financial-risks-renewable-energy-0915 **)**

[7] Economist Intelligence Unit (EIU) report, Managing the Risk in Renewable Energy, 2011 (http://digitalresearch.eiu.com/risksandrenewables/report

amagerramov@gmail.com,
rustemshefagatov@gmail.com

Phase transition by treating $TlInS_2$ amorphous films doped by Sn

E.Sh. ALEKPEROV, E.S. GARAYEV, S.A. SADRADDINOV, S.S. FARZALIYEV

Faculty of Physics, Department of Physical Electronics, Baku State University, Az1148, Z.Khalilov str., 23, Baku, Azerbaijan, e-mail: alekperoveldar@mail.ru

Abstract

By method of kinematic electron diffraction there has been investigated the crystallization of $TlInS_2$ amorphous films doped by Sn impurities in three crystal systems. It is shown that the crystallization of amorphous films 30nm in thickness obtained in vacuum by thermal method is described by Avraami-Kolmogorov analytical expression $V_t = V_o\ [1 - exp\ (-kt^m)]$. According to kinematical electron diffraction patterns the influence of Sn impurity on the measure of growth, values of crystallization activation energy for three crystal systems of amorphous films and unit cell lattice parameters of crystallizing samples have been determined.

Keywords: *electron diffraction, doping, structure, amorphous phase, kinetics, crystallization.*

1. Introduction

At present, $A^{III}B^{III}C_2^{VI}$ typed compounds have been admitted to be perspective materials in optoelectronics. Great interest in nanothick semiconductive films has motivated the study of structural characteristics of given materials. Semi-conductors comprising this group of compounds with band gap are mostly wide-band. Instrument making demands encourage the work on changing band gaps by the familiar methods: one of them is doping by suitably injected impurity having effects on the quality and physical properties of crystals. By changing technological process of film production as well as the doping one can modify their structure [4-7].

Experimental data of atom interactions in solid states, valence electrons in atoms can be obtained by electron diffraction methods[8-10]. One of the appropriate method for this investigation is the electron diffraction method. By using the given method there has been investigated the influence of Sn chemical element doping on the kinetics of $TlInS_2$ amorphous films crystallization process.

We investigate polystructural properties of $TlInS_2$ polymorphous thin films obtained by vacuum deposition[11]. As it is known it is one of the most complex ternary compounds having five structural modifications [12-14]. In present work the data on kinetic parameters of $TlInS_2$ amorphous film crystallization doped by Sn impurity have been quoted. The difficulty of the study is the unknown mechanism of film growth. The investigation of temperature and time dependence of film crystallization has an influence on making clear the mechanism of their growth.

We consider the influence of Sn atom doping in mentioned concentration range on thermal stability and kinetic parameters of $TlIn_{1-x}Sn_xS_2$ film crystallization (x=0.02÷0.09).

2. Experiment

In given work the vacuum assembly VD-5 of $TlIn_{1-x}Sn_xS_2$ (x=0.02÷0.09) film production of nanodimensional thickness to investigate them on the electron diffractometer EDM-102 has been used. Amorphous films under investigation~30 nm in thickness are obtained in vacuum $3x10^{-5}$ Pa by thermal method of simultaneous deposition of $TlInS_2$ and Sn from two molybdenum furnaces on the substrates of NaCl and KCl cleavages at T 230÷323K and preliminarily covered by carbon film. Deposition time is 5÷20 sec. To prevent volatile component evaporation and oxidation processes as a result of subsequent film thermal treatment a newly carbon film is applied on the obtained films. While dissolving the substrate the film under study is transported on the tungsten furnace-substrate where it undergoes thermal treatment.

Kinetics of $TlIn_{1-x}Sn_xS_2$ amorphous film crystallization has been investigated by method of kinematic electron diffraction method on electron diffractometer. EDM-102 model with electric registration of diffraction intensities being as a result of amorphous phase crystallization. By electric registration of chosen line intensity of crystal phase the slit size of intensity electron detector is determined from the ratio 2 / 3d = l, where d is the width of the slit, l is the halfwidth of the registered line.

By signal gain control one can achieve the maximum level of recording the chosen line intensity. At this recording level the film under investigation is heated at constant temperature within phase transition while the crystallization begins. Crystallization temperature of $TlIn_{1-x}Sn_xS_2$ (x=0.02÷0.09) amorphous films obtained under different conditions is 403K,388K and 393K. That is agreement with monoclinic, tetragonal and rhombic crystal systems. Given films being in off-beat carbon capsules are fully insulated from oxidation and reevaporation transferring them into the electron diffractometer

column and further thermal treatment. It might be well to point out the high quality of electron diffraction patterns obtained from the films deposited on KCl substrate.

On kinematic electron diffraction patterns there has been traced the phase transition, i.e. the change of number and line intensities of $TlIn_{1-x}Sn_xS_2$ amorphous films crystallized by nanoclinic (1), tetragonal (2), and rhombic (3) unit cell there have been taken electron diffraction patterns being distinguished by the duration of phase transition with the crystal system within the temperature range:1.403-478K, 2.388-453K, 3. 393-468K.

3. Results and discussions

To study crystallization kinetics of $TlIn_{1-x}Sn_xS_2$ (x=0.02÷0.09) the isothermal kinematic electron diffraction patterns at T 403 K, 458 K and 478 K have been obtained. Thereshold temperature for monoclinic phase of $TlIn_{092}Sn_{0.08}S_2$ films deposited on KCl is 503K. In this case there has been taken place the instantaneous crystallization of amorphous film preventing to follow the dynamics of phase transition process, i.e. to take the kinematic electron diffraction pattern. For electron diffraction pattern interpretation the measurements of intensity, reflex radia and others have been carried out. As it known [1] line intensity I_{nkl} is related to the irradiated volume of crystalline substance by the ratio:

$$I_{hkl} = I_o \lambda \left| \frac{\Phi_{hkl}}{\Omega} \right|^2 V \frac{d_{hkl}^2 \Delta}{4\pi L \lambda} P. \qquad (1)$$

Here I_0 is the intensity of primary beam, λ is the electron wavelength, Φ is the structure amplitude of diffraction reflection that is calculated from atomic scattering coefficients in kinematical approximation, Ω is the unit cell volume, V is the irradiated volume of polycrystalline specimen. Parameters of d_{nkl} and Δ show the interplanar distance and small section of Debye ring, P is the multiplicity factor of diffraction reflection amplification, L λ is the constant of the device which is defined due to the applied voltage that accelerating the electrons. Diffraction line measurements on the electron diffraction pattern show that the crystallization process of amorphous film comes about in a regular way, i.e. $I_{nkl} \sim V$.

By microphotometer the width and intensity of lines from various section of kinematical electron diffraction patterns are defined (Fig.1). The change from intensity values to the number of crystallized films is made out by normalization, i.e. maximum value of intensity is compared with fully crystallized volume of films and the volume falling at per unit of intensity is established. It offers to find values of volume of substance crystallized part due to annealing time. Thus there have been constructed crystallization isothermic lines given in Fig.2.

Referring to the data of kinematical electron diffraction patterns obtained after amorphous film treatment there have been determined unit cell periods of polycrystalline specimen having the values appropriate to the monoclinic crystal system: a=0.813; b=0.776; c=2.473 nm, PLO $P2_1/m$.

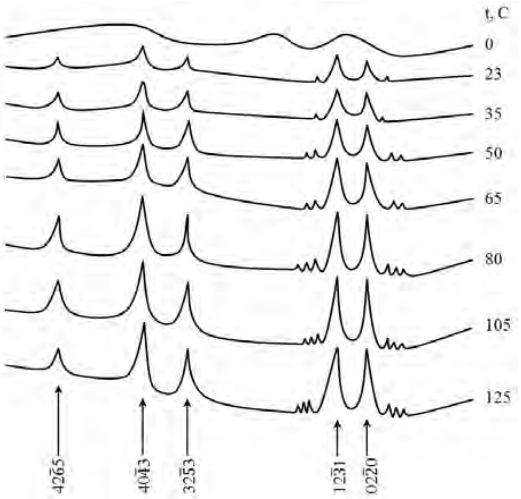

Fig.1. Microphotograms from various photometric sections of the isothermal kinematic electron diffraction pattern showing the crystallization of $TlIn_{0.92}Sn_{0.08}S_2$ - I at 458 K.

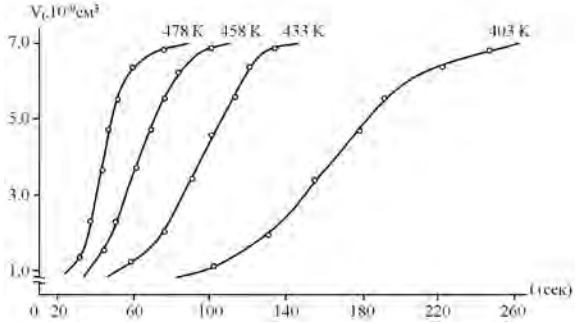

Fig.2. Kinetic curves of crystallization of amorphous $TlIn_{0.92}Sn_{0.08}S_2$ - I: 1) Tcr = 403 K; 2) Tcr = 433 K; 3) Tcr = 458 K; 4) Tcr = 478 K.

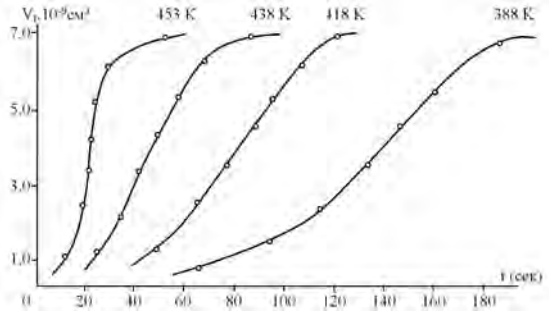

Fig.3. Kinetic curves of crystallization of amorphous $TlIn_{0.92}Sn_{0.08}S_2$ - II. 1) Tcr = 388 K; 2) Tcr = 418 K; 3) Tcr = 438 K; 4) Tcr = 453 K.

To construct crystallization isothermic lines (Fig.3) with subsequent determination of phase transition kinetic parameters there have been obtained isothermic kinematical electron diffraction patterns from $TlIn_{0.92}Sn_{0.08}S_2$ amorphous films at T 388K, 418K, 438K and 453K where amorphous phase transition into polycrystalline one has been investigated (Fig.4). Electron diffraction patterns from polycrystalline films are indexed on the base of tetragonal lattice with periods =0.804; c=3.062 nm, PLO I/4 mcm.

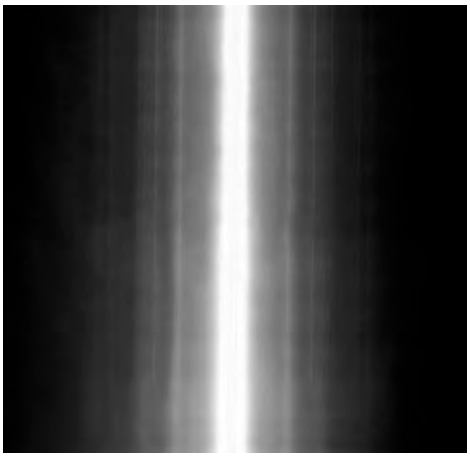

Fig.4. Isothermal kinematic electron diffraction pattern from amorphous $TlIn_{0.92}Sn_{0.08}S_2$ - II, undergoing a phase transformation at 438 K.

With the aim of constructing isothermic curves $TlIn_{0.92}Sn_{0.08}S_2$ (Fig.5) rhombic phase amorphous film crystallization there have been obtained kinematical electron diffraction patterns at T 393K, 423K, 448 and 468K (Fig.6). In this case electon diffraction patterns taken from crystallized films are indexed on the base of rhombic unit cell with periods a=0.687; b=0.399; c=1.567 nm; PLO D_{6h}^2. For all 3 phases of $TlIn_{0.92}Sn_{0.08}S_2$ compound dependences ln ln V_0/ V_0-V_t on lnt where experimentally obtained points for different temperatures are fallen on straight likes (Fig.7, a, b, c). By comparing these isothermic likes (Fig.2, 3, 5) with the analytical expression of kinetical curves of phase transitions

$$V_t = V_o [1 - \exp(-kt^m)] \qquad (2)$$

there has been determined the exponent at t, which appeared to be equal to approximately four. Here V_0 is he volume of amorphous phase at the beginning of the process, $K=1/3\ \pi\omega c^3$ here ω is the nucleation rate of the new phase in per growth, m is the parameter characterizing the measure of small crystal growth. Value $m\approx4$ obtained for each Tl $In_{1-x}Sn_xS_2$ phase individually shows that in the case of amorphous ranges under investigation the three-dimensional growth of small crystals has been taken place.

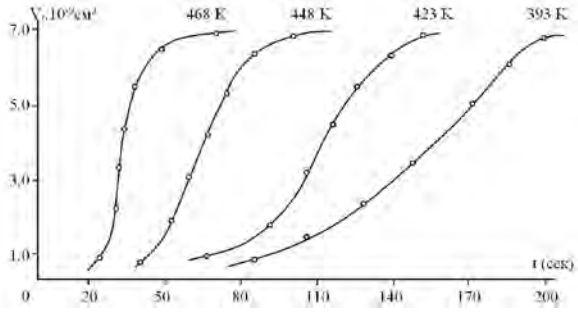

Fig.5. Kinetic curves of crystallization of amorphous $TlIn_{0.92}Sn_{0.08}S_2$ - III. 1) Tcr = 393 K; 2) Tcr = 423 K; 3) Tcr = 448 K; 4) Tcr = 468 K.

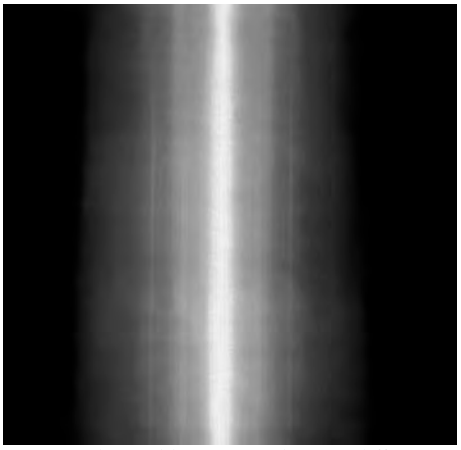

Fig.6. Isothermal kinematic electron diffraction pattern from amorphous $TlIn_{0.92}Sn_{0.08}S_2$ - III, undergoing a phase transformation at 448 K.

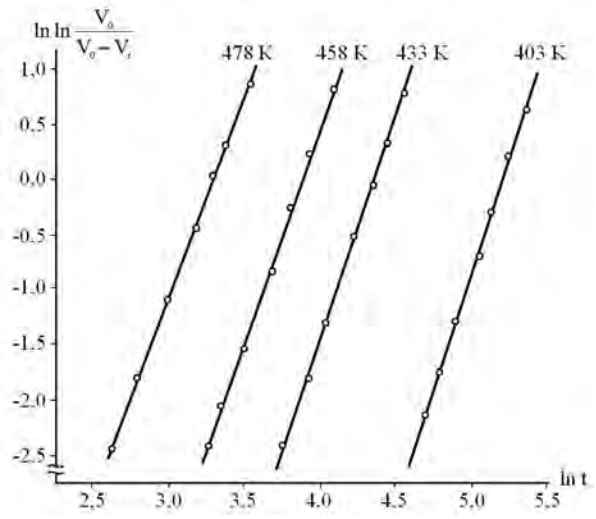

Fig.7, a. Dependence on lnt for crystallization of amorphous $TlIn_{0.92}Sn_{0.08}S_2$ - I.

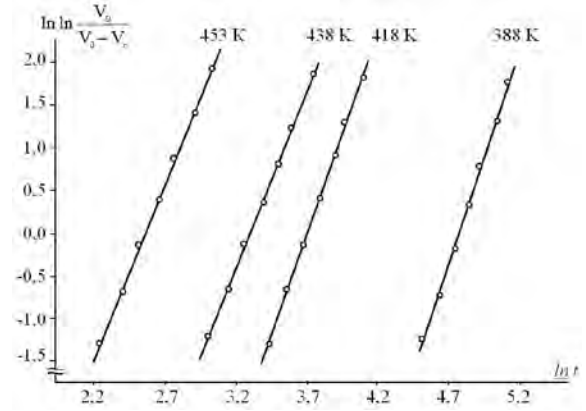

Fig.7, b. Dependence on lnt for crystallization of amorphous $TlIn_{0.92}Sn_{0.08}S_2$ - II.

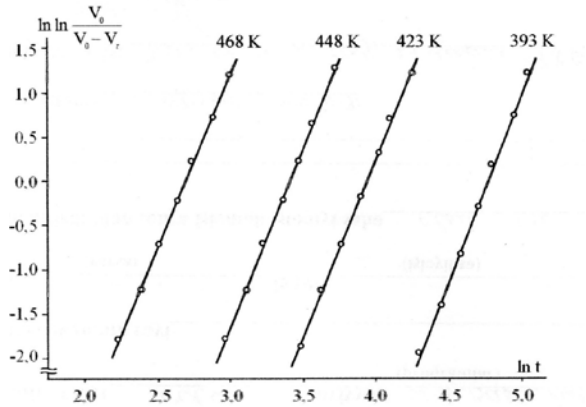

Fig.7, c. Dependence on lnt for crystallization of amorphous $TlIn_{0.92}Sn_{0.08}S_2$ - III.

By the slope of kinetical curves there has been determined total activation energy of crystallization $E_{tot} = E_e + 3E_g$ equal to 50.2; 52.3; 53.4 kcal/mol for monoclinic, tetragonal and rhombic $TlIn_{0.92}Sn_{0.08}S_2$, respectively. Nucleation activation energies E_e calculated by the slope of straight line of dependence $1/\tau$ on lnt (here τ is the incubation time, i.e. experimentally observed initial time of crystallization) are found to be equal to 18.1, 19.3, 20.1 kcal/mol, but growth activation energies of small crystals E_g determined for various modifications of Tl $In_{0.92}Sn_{0.08}S_2$ in above-mentioned sequence by the ratio $E_g=(E_t- E_e)/3$ are equal to 10.7, 11.0 and 11.1 kcal/mol.

Close values of crystallization activation energies established for Tl $In_{1-x}Sn_xS_2$ various modifications have been claimed attention. In view of amorphous film formation criteria it can be explained by the vicinity of Tl $In_{1-x}Sn_xS_2$ film amorphous phase structures. i.e. similarity of closest atom environment in given structures.

4. Conclusion

In present work there have been presented investigation results of $TlIn_{1-x}Sn_xS_2$ (x= 0.02÷0.09) thin amorphous film crystallization kinetics electron diffraction methods. It is established that for these compounds the effective activation energy of crystallization increases by 4÷5%, for three crystal systems, i.e. the temperature of amorphous film crystallization with impurity occurs at a higher temperature than without it. There has been also observed the increase of temperature ranges of amorphous film crystallization up to 80^0C. It is found out that three-dimensional growth of small crystals has been taken place in phase transition in the temperature range under study. In crystal films obtained after phase transition the lattice parameters of unite cells increase in agreement with crystal system in mentioned composition (at x=0.08) by 5÷6 %, respectively. Change of lattice parameters due to the composition is not rectilinear. By deping $TlInS_2$ with Sn impurity the detected rise of activation energy and lattice parameters at unchangedable space group of symmetry including Sn impurity should be regarded as regular.

5. References

1. Yu.I. Ukhanov, "Optical properties of semiconductors" Nauka, Moscow, 366 (1977).
2. J.S. Sanghera, I.D. Aggarwal, L.B. Shaw and C.M. Florea, J. Optoelektroniks and Advanced materials, **8**, 2148 (2006).
3. Ah.U. Malsagov "A review of the literature on semiconductor compounds such as $A^{I}B^{III}C_2^{IV}$, $TlB^{III}C_2^{VI}$," EL-FA, Nalchik, 692, (2007).
4. V. Kovanda, M. Vicek, and H.Jain, J. Non-Cryst. Solids, **326**, 88 (2003).
5. T.S. Kavetskyy, O. I. Shpotyuk and V.T. Boyko, J. Phys. and Chem. of solids., **68**, 712, (2007).
6. S. Mader, "Technology of thin films", Ed. L. Maissella, R.M. Glenga, Sov. Radio, Moscow, **2**, 57 (1977).
7. A.M. Filachev, I.I. Taubkin and M.A. Trishenkov, "Solid-state photoelectronics", Fizmatkniga, Moscow, 363 (2012).
8. B.K. Weinstein, "Modern crystallography", Nauka, **1**, Moscow, 383 (1979).
9. R.M. Imamov, A.S. Avilov and S.A. Semiletov, "Modern electronic microscopy in the study of substance", Nauka, Moscow, 73 (1982).
10. A.S. Avilov, "Precision electronography", Dis. Doc. Fiz.-mat. Sciences, Moscow, 274 (1999).
11. D.I. Ismailov, M.F. Aliyeva, E.Sh. Alekperov and F.I. Aliyev, Semiconductors., **37**, 744 (2003).
12. T.I. Isaacs, Z. Krustallogr., **B.141**, 104 (1975).
13. W. Henkel, H.D. Hochheimer and C. Carlone, Phys. Rev. **B.26**, 3211 (1982).
14. A.I. Najafov, O.Z. Alekperov and G.G. Guseinov Inorgan. materials., **41**, 138 (2005).

Polarization Effects in Processes With Knocking Out Bineutrons Clusters

I. G. AFANDIYEVA
Azerbaijan State University of Oil and Industry

Abstract
Based on the theory of association discussed the polarization effects in two-nucleon reactions. The anggular momentum of the internal states of the incident t, departing p are assumed symmetric S-states, so that the corresponding sequential interaction transmission is diagonal in the spin states of nuclei. The transition is happening from the initial to the final state transfer bineutron association without changing the internal states. The degree of polarization is proportional to the probability that bineutrons "aimed" at the nucleus of A with the corresponding values of angular momentum are captured with the formation of the state of the nucleus B.
Key words: nucleon clusters, scattering, matrix element, two-nucleon transfers, cross section, polarization.
.

1. Introduction

Some papers on the *(t, p)* and *(p, t)* reactions have already been published using both the plane wave Born approximation (PWBA) and the DWBA, but most investigations have been concerned with the angular distribution rather than the magnitude of the polarization. As a result of the spin dependence of the interaction the cross section of the scattering may depend on the polarization of the incident particle and the polarization of the target [1, 2]. The polarization of particles - a characteristic of the state of the particles associated with the presence of their own angular momentum - spin. microparticle system is called polarized if the spatial distribution of the orientations of the spins of the particles different from isotropic.The information obtained from *(t,* p) and *(p, t)* reaction experiments is concerned with the correlation of two like-nucleons. It is known that certain levels are strongly excited and the ground state of a even nucleus is most strongly excited in many cases, while, usually, higher zero spin states are not excited strongly, although there are some remarkable exceptions. The magnitude of the cross section gives us information about the detailed structure of the levels.

The idea of nucleons clustering has a history back to the early thirties of the last century. By observing alpha decay from nucleus, people speculated that nuclei are made up of alpha particles. Bethe in his paper [3] predicted that nuclei are made of alpha particles and gave also a geometrical arrangement of alpha particles inside nuclei. He predicted that, for each new addition of alpha particles, the number of bonds increased is three. At that time, this was too a big challenge for the clustering models and eventually these models disappeared from the nuclear structure theories. Clustering is a recurrent feature in light nuclei, from beryllium to nickel. In light nuclei, the nucleons have been observed to cluster together forming sub-structures within the atomic nucleus, for states where the nucleons are only just bound together. Cluster structures are typically observed as excited states close to the corresponding decay threshold; the origin of this phenomenon lies in the effective nuclear interaction, but the detailed mechanism of clustering in nuclei has not yet been fully understood. If we are taking into account the interaction between nucleons (as it is in reality) in the model approach, we can expect the formation of clusters. Calculations show that, the associations occur on the surface of the nucleus, where the density of nuclear matter less than in the downtown nucleus [4].

The information obtainable from bineutron cluster stripping reactions is different from that obtained from single-nucleon transfer reactions; from the latter only the single particle character of the levels is obtained. The sets of data obtained from the single and two nucleon transfer reactions are both valuable, and they are mutually complementary. The analysis of the former kinds of reactions has already reached a satisfactory enough stage to furnish quantitative information about nuclear structure. Now we are just trying to improve the theory of the two nucleon transfer reactions to the same stage of usefulness.

2. A formal description of polarization effects

A particle with nonzero rest mass (the electron, the atomic nucleus, and others.) and with spin J (in units of Planck's constant) has $2J + 1$ quantum state is corresponding to different spin orientations (different values of the spin projection onto a certain direction). State of a particle is a superposition of these states. If the superposition coefficients fully defined (pure state), then we say that the particle is completely polarized. If superposition factors are not fully defined and specified only some statistical characteristics (mixed state), we speak of partial polarization. In particular, the particle can be completely unpolarized; this means that its properties are the same in all directions, like a spinless (with $J = 0$) of the particle. In general, the polarization of the particles determines their degree of symmetry (or asymmetry) in the space.

Consider the $t + A \to B + p$ reaction in the laboratory system and we will study the knocking out bineutrons clusters. Let $\vec{r}_p$, $\vec{r}_{n_1}$ and $\vec{r}_{n_2}$ coordinates of the proton and neutron in the triton, $\vec{k}_p$ - free proton wave vector, $\vec{k}_t$ - wave vector of triton. In (*t, p*) reactions occur dissipative phenomena, i.e. the dissipation in the orbital

angular momentum of a reaction in which part of the relative angular momentum of $\mathbf{L_i}$,, characterizing the initial trajectory, transform into spin of fragments in accordance with the expression $\Delta\mathbf{L}= \mathbf{L_A} - \mathbf{L_t} \equiv \mathbf{L_B} + \mathbf{L_p}$.

We will neglect the internal structure of the associations and effects of the Pauli principle between the nucleons in the clusters are taken into account by introducing short range repulsion between the associations. The orthogonality condition model and excluded state model treat the clusters as elementary particles, but include effects of the Pauli principle in a more microscopic way. Wheeler's resonating group method is a fully microscopic theory for calculating properties of cluster systems. It makes simplifying assumptions about the internal structure of the clusters but takes the Pauli principle explicitly [5].

Scattering may be accompanied by transitions between different states of the LJ, compatible the conservation the total angular momentum. However, the orbital angular momentum and spin are not good quantum numbers and the partial wave corresponding to a certain L and S, may cause scattered wave with $L' \neq L, S' \neq S$. If we take into account that the good quantum numbers are the total angular momentum and parity, the amplitude of the scattered waves form a matrix, the elements of which depend on the following indices: J, L and S.

In the scheme of connection $\mathbf{I_t} + \mathbf{L} = \mathbf{j}, \mathbf{I_A} + \mathbf{j} = \mathbf{J}$, due to the statistical nature of the dissipation of angular momentum transmitted $\Delta\mathbf{L}$ not completely polarized, and the back can be decomposed into alignment $\boldsymbol{J}$ and fluctuation $\boldsymbol{J}'$ components, ie, from $\langle J_x \rangle = \langle J_y \rangle = 0,\ \langle J_z \rangle = J_0$.

The transmitted $\Delta\mathbf{L}$ orbital angular momentum is basically alignments and increases with the loss of kinetic energy. This transfer of angular momentum takes place in two ways: as the inelastic excitation of core as certain multipole and nucleons occupying certain orbital in the initial and the residual nucleus. Thus it is possible to put the physical problems of the dissipation of energy and angular momentum on the distribution $\Delta\mathbf{L}$ between fragments and the orientation of each fragment, characterized by the ratio J/J' depending on such typical reaction parameters such as energy, deflection angle.

This is an illustration of the fact that the a association of the nucleons is compatible with the Young scheme of the orbital part of the wave function if this scheme contains the maximal number of fourgroups.

The wave function of the initial state can be written as:

$$\Phi_i = \Psi_A(\xi) F_t(\vec{r}_t) f^S(\vec{r}, \vec{\rho}) \chi_{1/2,m_t}, \qquad (1)$$

where $\Psi_A(\xi)$ the wave function of the nucleus A, $F_t(\vec{r}_t)$ - distorted wave function of the triton, $\vec{r}_t$ the radius vector in the centre of inertia of triton, $f^s(\vec{r}, \vec{\rho})$ - the wave function of the internal motion of triton, $r = \left|\vec{r}_{n_1} - \vec{r}_{n_2}\right|$, $\vec{\rho}$ - distance from the proton to the centre of gravity bineutrons association, S indicates the spin state of the captured neutrons, $\chi_{1/2,m_t}$ - spin function of the triton.

The final state function describes the state of the nucleus B consisting of A and bineutrons cluster and the free movement of a proton. It can be represented as:

$$\Phi_f = \Psi_B(\xi, \vec{R}) f(\vec{r}_p) \chi_{1/2,m_p}, \qquad (2)$$

where $f(\vec{r}_p)$ - distorted function of the proton, $\vec{R}$ - the radius vector bineutrons cluster, $\chi_{1/2,m_p}$ - the spin function of the proton.

In approaching zero radius [6] a proton is emitted at the same point, which is captured bineutrons cluster. Mathematically, it comes down to the choice of potential as follows:

$$Vf^s(\vec{r}, \vec{\rho}) = W(\vec{r})\delta(\vec{\rho}). \qquad (3)$$

For this case, the analytical expression for the polarization of the emitted proton was derived in [3] on the basis of quasi-classical model with a Gaussian distribution:

$$P(J_p) = \exp\left(-(J_t - J_p)^2\right)/2(d\sigma/d\Omega)^2 \qquad (4)$$

For J_t =1/2 protons orientation is completely characterized by the polarization vector. If the spin J_t distributed symmetrically around the z axis, which is perpendicular to the plane of the reaction, the average value P_z can be expressed in terms of the scattering amplitude:

$$\langle P(J_p) \rangle = \frac{1}{J_p} \frac{\lambda\left(m_B^2 + m_t^2 + m_A^2\right)^2}{8E_t^2 E_A^2} \sum_{J_t LM_l} (2J_t + 1) \left\langle LM_L; k_p \middle| M_{i\to f} \middle| k_t \right\rangle^2 \qquad (5)$$

where $\vec{R}' = \frac{A}{A+2}\vec{R}$ and

$$M_{i\to f}^{S=0} = \delta_{m_l m_p} \sum_L 4\pi \sqrt{((2L+1)} i^L \int \Psi_B^{*S=0}(\xi, \vec{R}) \Psi_A(\xi)\, x$$
$$W(\vec{r}) j_l(k_p \vec{R}') j_L(k_t \vec{R}) d\xi d\vec{r} d\vec{R}' d\vec{R} \qquad (6)$$

Distance between R_a fragments associative decay is chosen in such a way that when $R > R_a$ overlapping fragments nucleon densities would be already so small that we can neglect the influence of the effects on the internal antisymmetriza - wave functions fragments. The transition occurs directly from the initial to the final state of the transmission binucleon cluster, without changing the internal states of the nucleons. It is assumed that the association is bound S - state.

The value of the transition matrix of the polarization dependent on the orbital angular momentum of cluster, which directly determines the parity of the final state (if known to the parity of the original nucleus) and provides essential information for determining the spin of this state.

In addition, the degree of polarization (the absolute value of the polarization vector is called the degree of polarization) should be proportional to the likelihood that cluster, "aimed" at the nucleus of *A* with the corresponding values of the momentum and angular momentum will be seized with the formation of the state of the nucleus *B*. This probability obviously depends on the extent of the nucleus in the final state is similar to the system consisting of the core a to the ground state, plus cluster with full orbital momentum *L*. For the case in which the nucleus *B* in a very small of the time in the configuration "a nucleus *A* in a ground state plus cluster" the degree of polarization is low. On the other hand, the formation of the final state, is in a configuration referred most of the time, will lead to a large polarization value.

A study of the polarization of the nucleons in scattering on nuclei is often done by double scattering. A bunch of nucleons, scattered on one of the cores of the first target, partially polarized. The degree of polarization is defined as the difference between the intensity of the beams, scattered second target nuclei at the same angle to the right and to the left. The polarization vector of the scattered particles in the nuclei of the zero spin is always directed perpendicular to the scattering plane.

3. Conclusion

In this paper, all the calculations were based on non-relativistic quantum mechanics. But at sufficiently high energies become significant inelastic processes associated with the formation of mesons. The problem, in the solution of such problems is the separation of variables, since it affects the possibility of analytic computation of integrals over the angles, as well as for those variables that are not related to the interaction of particles. Therefore, the ability to describe the interaction between nucleons via potential is limited by high energy. Such a restriction on energy means that the unambiguous definition of the potential at small distances impossible.

The paper was used approaching zero radiuses with the assumption that there is not take into account the exchange of nucleons between the two nuclei, and that the target nucleus is not excited. Then, we were limited by the fact that the internal states incident t, emitted p, and any intermediate state associations are fully balanced *S*-states, so that the corresponding sequential interaction of transmission are diagonal in the spin states of nuclei. With this reasoning radial wave functions two neutrons which form association close to one another, particularly in the peripheral region of the nucleus where there is a "cross-linking" of the wave functions of nucleons - target (*A*) and in the nucleus *B*.

The scattering nucleon by nuclei, possess spin, also comes down to the problem of scattering particles by potential field. However, in this case, due to the fact that the spin space of the system has a large number of degrees of freedom, the expression for the amplitude or polarization is more complicated.

For an explanation of two-nucleon transmission there are different approaches, each of which is treated properly, some but not all aspects of these transitions. Among these aspects: the use of the exact wave functions of Triton and the corresponding exact interaction; accurate interpretation of the limited domain of interactions in the amplitude of both the first and second order; explanation of non-orthogonality of the amendment to the term of the second order, which seeks to eliminate the amplitude of the first order. In addition, all the results are very sensitive to optical potentials and the wave functions of the kernel used for the transition matrix. The parameters in the spin-flip amplitude determined from one reaction allow us to obtain a wide circle of results for the polarization effects meson-nucleon scattering and charge-exchange reactions at high energies.

In conclusion it is of interest to anticipate the appearance of those effects of the peculiarities of the clusters which are due to the correlations between the nucleons which are not taken account of in the shell model.

References

[1] V.I Alfimenko, V.I Pikelner, E.B Sharapov. JINR, **11**, 411, (1980)
[2] S.V Goloskakov, S.V Kulishov, O.V Selyugin. N.Ph., **50**, 779, (1989)
[3] M. Freer, Scholarpedia, **5**, 965, (2010).
[4] D. Jenkins, S. Courtin J. Phys. G: Nucl. Part. Phys. **, 42**, 034010, (2010)
[5] D. M. Brink. J. Phys.: Conf. Ser. 111, 012001, (2008)
[6] S. G. Abdulvahabova, I.G.Afandiyeva. Jornal of Qafgaz University. Physics. **3**, 57, (2015)

irada.e@mail.ru

The electrical and physical properties of the system system alloys $Ga_{1-x}Mn_xSb\left(x\le 0{,}25\right)$

[1]I.Sh. DADASHOV, [1]A.N. QULIYEV, [1]Y.H.HUSEYNALIYEV, [1]A.A. NABIYEV, [2]A.X. MAMMADOV, [1]N.A. HASANLI

[1]*Azerbaijan State Pedagogical University*

[2]*Ministry of Defence Industry of Azerbaijan Republic*

Abstract

In a wide temperature range $\left(100\div 600\right)K$ the electrical and physical properties $\left(\sigma,\ \alpha,\ R_x\right)$ and carrier scattering prevailing mechanisms of the system system alloys $Ga_{1-x}Mn_xSb\left(X\le 0{,}25\right)$ has been studied.

Keywords: solid solution, Nernst-Ettinqshauzen effect, electrical conductivity

1. Introduction

For a long time it was believed that the structure of outer electron layers of the 3-d and 4-d transition elements is the same for the common elements of a group and they should not significantly affect to the physical properties of the crystal.

The researches of the last few decades showed that due to the presence of the unfilled with electron inner levels in these elements and by interaction with the matrix material of those inner electrons a partial eclipse occurs by electrons in specific circumstances and that have an impact on physical properties. So it is of great interest the crystals with the effect of the transition elements in scientific literature.

The switch elements arranged on the basis of the spike in phase are applied to various fields of electronics $A^{III}B^{V}$ crystalline compounds [1, 2].

The admixtures added of this or that element of the matrix as a solution to a greater or lesser extent in such materials radically change the physical properties of the material. Therefore, the study of the impact of the transition elements on $A^{III}B^{V}$ additive compounds is of interest with the effect of theoretical and practical aspects. Displaying the different valence of the transition elements is related with appearance of interesting anomalies in physical properties.

The impact of the elements of Fe and Ni to InSb alloy studied by Emeliyenko and his colleagues. Here are considered Fe's impact and created by them acceptor level in dependence of temperature was studied and it was determined that with increasing the temperature the level is shifting to the valence zone by 0,52 eV.

The impact of 3d transition elements (Fe, Co, Cr, Cu, etc.) to the $A^{III}B^{V}$ combinations, most of all, to GaAs alloys is studied. When the impact of iron to electrical properties of GaAs studied, it has been identified that in the temperature range of 200-400 K untill 0,1 am % the n-type GaAs crystall is formed, and larger than 0,1 am% - the p-type one. According to the results of Fe, GaAs energy level was found to be 0.37 eV. It is shown that increasing the amount of iron increases the activation energy of 0.1 eV. Later, as a matrix material, GaSb taken for $A^{III}B^{V}$ semiconductor compounds.

Among the semiconductor compounds, the combination of GaSb is an easily obtained compound. GaSb, sphalerite-type structure of the crystallized Tetraedr. Some papers [3,4] shows that getting the GaSb monocrystalls the Bridjeman method is more useful. In some cases the zone melting and the slow cooling methods are used too. Regardless on technology the concentration of the holes no less than 1 sm^{-3} and according to this concentration the special electric conductivity for GaSb is around ~14 Om^{-1} sm^{-1}.

It is known [5] that, made on the basis of GaSb in the condition diagram of system $Ga_{1-x}Mn_xSb$ the solid solutions is received at values x≤0,3. In that paper, the values of a number of x's been a few examples of $Ga_{1-x}Mn_xSb$ system, electro properties of some of them (100-600) K temperature range, as well as to explore the mechanism of these examples is to investigate the scattering of carriers that prevails.

The purpose of this article is to take a few examples of $Ga_{1-x}Mn_xSb$ system for some values of x, to explore electro properties of some of them in (100-600) K temperature range, as well as to explore the mechanisms of these examples to investigate the scattering of carriers that prevails.

Here are the examples of the proposed research to the following composition synthesized by us:

1. GaSb
2. $Ga_{0,95}Mn_{0,05}Sb$
3. $Ga_{0,85}Mn_{0,15}Sb$
4. $Ga_{0,75}Mn_{0,25}Sb$

The results of the measurement of the kinetic properties at room temperature are shown in the table below.

As can be seen from the table, all proposals have p-type conductivity. Depending on content (σ), increasing the concentration of carriers, thermoelectric power decreases in the natural way. Such a natural change in the physical quantity is related to the increase in the amount of Mn.

In Figure 1 a special electrical conductivity in dependence of inverse temperature is given. As can be seen to some extent in all samples at relatively low temperatures, σ increases with increasing temperature, in a wide temperature region, all except the main ingredient composition GaSb, remains stable. In the electrical conductance at temperatures greater than about 300K the reduction is observed. Most likely, this reduction is due to the approach of intrinsic conductivity-temperature region (transition from p type to n type). More precisely, the temperature measuring conductivity regions cover all of the samples.

Table 1: *The results of the measurement of the kinetic properties at room temperature*

Content	Type	σ, $Om^{-1} cm^{-1}$	α, mcV/K	Concentration of carriers, cm^{-3}
GaSb	p	14	497	$1,4 \cdot 10^{17}$
$Ga_{0,95}Mn_{0,05}Sb$	p	715	146	$1,2 \cdot 10^{19}$
$Ga_{0,85}Mn_{0,15}Sb$	p	841	91	$5,8 \cdot 10^{19}$
$Ga_{0,75}Mn_{0,25}Sb$	p	1250	62	$8,2 \cdot 10^{20}$

Email: yashartur@yahoo.com

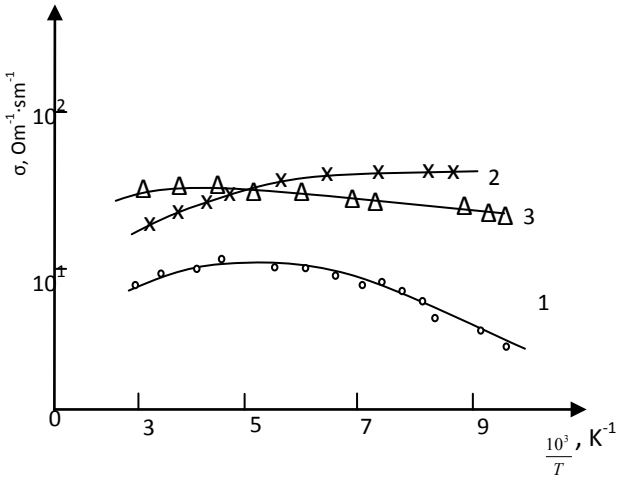

Fig. 1. Special electrical conductivity in dependence on inverse temperature

Here are the carriers (holes) to the study of scattering mechanisms considered. To determine the mechanism of carrier scattering effects usually are widely used thermomagnetic effects. Transverse Nernst-Ettinqshauzen effect (N-E) is more sensitive to the carrier scattering mechanism.

To determine the mechanism of carrier scattering, the transverse Nernst-Ettinqshauzen effect in all samples has been measured, and was constructed transverse Nernst-Ettinqshauzen ratio $Q^{\perp}_{N-E}$ (T) in dependence of temperature (Figure 2).

As one can see from $Q^{\perp}_{N-E}$ (T) dependence in temperatures lower than 250K, the prevailed mechanism is the scattering of the holes on impurity ions, but in temperatures higher than 250K, the prevailed mechanism is the acoustic phonons scattering.

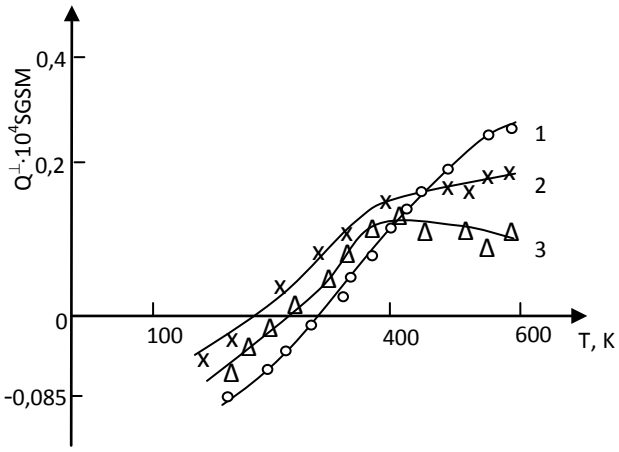

Fig. 2. Transverse Nernst-Ettinqshauzen ratio $Q^{\perp}_{N-E}$ *(T) in dependence of temperature*

References

1. K. Rouz Xilsum. $A^{III}B^{V}$ Poluprovodniki stopper. M. 1963

2. R.W. Haisti Appl. Phys. Letters, **8** 208 (1965)

3. I.Sh. Dadashov, K.A. Azimov, A.N. Quliev. News of Azerbaijan State Pedagogical University, **5**, 9 (2009)

4. I.Sh. Dadashov, A.A. Aliyev, A.N. Quliev. Azerbaijan Architecture and Construction University. Modern problems of physics. Baku, the Second Scientific Conference, 60 (2009)

5. I.Sh. Dadashov. Autoreferat, Chisinau, 1976

Laser based fusion reaction for peaceful purpose

S J IQBAL

City University of Science and Technology Menara City-U Petaling Jaya Selangor, Malaysia, Email: syedjav@yahoo.com

Abstract

In February 2016 Wedberstein 7-X in Germany has demonstrated a fusion reaction which lasted for less than a second. Fusion reactor is very difficult to build and it is expensive. Here we have discussed the possibility for using divergent fusion reaction with the help of high power pulse laser. Fusion reaction happened at very high temperature and pressure. This was unattainable with normal heating and compression process. High pressure and high temperature must be maintained for certain duration to initiate and sustain fusion reaction. Now all above condition can be achieve using available high chemical explosive and high power laser beams.

Keywords Fusion reaction, Laser based direct fusion, Peaceful nuclear energy, Induced fusion reaction

Introduction

Einstein's equation $E = mc^2$ proved that mass is form of energy. Usually this can happened in nuclear reaction. A nuclear reaction is a process in which nucleus disintegrates to smaller more stable nuclei or two or more light nuclei combined to form more stable nucleus. Difference of mass appears in form of energy which is given by Einstein equation. Reverse process is also possible. We are using nuclear energy since Second World War. America tested Trinity a first nuclear bomb in 16 July 1945 in New Mexico. We do use nuclear reactor for generating electricity. But these fission nuclear reactors are not safe. It can explode like in 1986 in Chernobyl in Russia or Fukushima Daiichi nuclear disaster in March 2012 in Japan.

Fuel: The most suitable reaction for an earth-bound fusion is between two isotopes of hydrogen, deuterium and tritium. When these two nuclei combine, a neutron gets shoot out at high speed and heaver nucleus is formed with the release of large amount of energy.

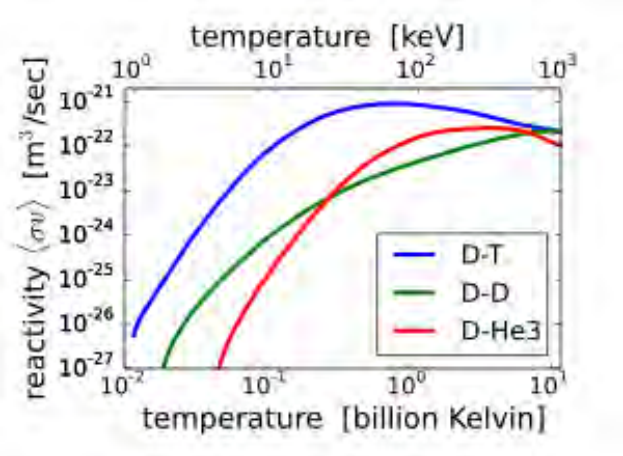

Fig. 1 Reactivity and temperature

We can see in Fig. 1. Deuterium-Tritium (D-T) reaction is optimum at lowest temperature.

It is difficult to initiate this reaction but still most promising reaction. The fusion reaction rate increases rapidly with temperature until it maximizes and then gradually drops off.

Table 1 Conditions for fusion

Lawson's criterion for fusion	**nt** $\geq 10^{14}$ s/cm^3	Deuterium – tritium fusion
	nt $\geq 10^{16}$ s/cm^3	Deuterium – deuterium fusion

Where **n** is the deuterium / tritium density and **t** is temperature in kelvin

The deuterium-tritium fusion rate peaks at a lower temperature (about 70 keV, or 800 million kelvin degree) and at a higher value than other reactions commonly considered for fusion energy. Reaction can only start when above condition remains for few microseconds. Usually plasma physicists combine these three parameters – temperature, density and time by multiplying then together to form what is called fusion product (or triple product).

At a certain value of the fusion product, called ignition, the reaction become self-sustaining: the heat generated by the reaction enough to keep the plasma hot so the external heating system is not needed. Normally eighty percent of the fusion energy is carried away by the neutrons which are produced during fusion reaction. Remaining twenty percent energy is carried by the helium nuclei remains in plasma. The newly formed helium collides with unburnt fuel nuclei, heating them up, thereby reducing the need of external heating. However it usually takes time which depends on the density and temperature of the plasma.

Density limitation: If the plasma is too dense then collisions of the different kind, like between nuclei and

electrons begin to generate large amount of bremsstrahlung radiation. This radiation prevents fusion from occurring. Optimum density is around one million times the atmosphere pressure.

Methods

Direct laser driven with initial confinement is the most promising method

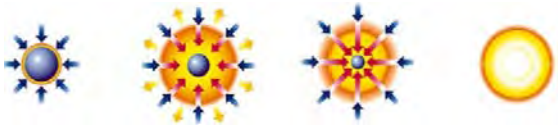

Fig. 2 Direct Fusion reaction

In this process deuterium and tritium are confined in thin metal sheet which is surrounded by high explosive as shown in Fig. 2. In case of thermonuclear device this explosive is Uranium or plutonium. Now this can partially be achieved by high explosive DDF (4,4'Dinitro-3,3'dinitroamine) or ONC (Octanitrocubane). Many of similar explosive does not exist in early sixties. Both have more than 10km/s detonation velocity. Even this detonation velocity does not enough compression which is needed for fusion reaction. To satisfy the Lawson's criterion for fusion we have to use very powerful pulse laser. Laser pulse can increase the plasma temperature for hundreds of million degree kelvin. Once fusion reaction is initiated for certain duration it is self-sustaining. In case a very high power laser is not available then it can be complemented by simultaneous neutrons injection. Many countries, like Germany, France, Japan and America are in process of developing nuclear fusion reaction. All of these countries know how to initiate fusion reaction and they have already demonstrated in the laboratories in their countries.

There are four main challenges for fusion reaction. Which are i) High density of plasma ii) Very high temperature. iii) Ignition time iv) Suitable material.

High density of fuel

Fusion gases like deuterium and tritium must be compressed to very high pressure so nuclei are close enough to interact with one another. This pressure is usually around 10,000 atmospheres pressure. This pressure cannot be achieved by chemical processes for sufficient period of time. NTN has detonation velocity 6.9 km/s. Now we do have few new explosive like DDF (4,4'-Dinitro-3,3'-diazenifuroxen) and ONC (Octanitrocubane) which have detonation velocity above 10 km/s. This can produce pressure many time the minimum required pressure.

Since Pressure created by explosive is directly proportion to square of the velocity so we can create around three time more pressure than the pressure created by the detonation of TNT. In 1960's it was almost impossible to ignite compressed fuel which lasted for less than a microsecond. Now technology do exist which can trigger high power laser with in nanosecond using optical feedback system. More high power pulse laser even this condition is relaxed.

Temperature

Second most important factor is temperature. Now we can increase the temperature by laser. Temperature can go as high as few hundred million degree kelvin. This can be achieved by multiple laser pulse fired simultaneously. This has been demonstrated in may research laboratories around the world. In February 2016 Wenderstein 7-X has demonstrated ignition of plasma for fusion reactor.

Ignition

Steady ignition can be achieved if following conditions are met, which are

i) Providing condition in which fusion reaction can proceed at high rate.
ii) These conditions must be maintained for certain period of time, such that:
iii) The rate of production of energy exceeds the external rate of energy supplied.

For fast ignition, the target is first compressed to high density with high implosion than ignited by high-intensity laser pulse or particle mean or ions. The reaction rate is highly dependent on temperature.

Energy of nuclear material exceeds that of a conventional explosive is one to one million. In Teller-Ulam's design, the fissile material provide both compression and ignition temperature. The drawback of this design is lot of left over radiation because of radioactive fission material which is used for compression and temperature.

Teller design also use tamper of opaque pusher because the thermal radiation arrives well ahead the shock was which is used to compressed deuterium-tritium mixture and this mixture gases should not be heated before the compression to the required density.

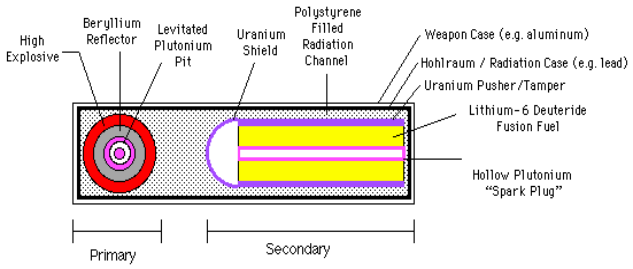

Fig. 3 Teller-Ulmer's design in which fission reaction is used to create necessary pressure and temperature

Laser direct drive

In our proposed design compress is done by highly explosive chemical material, RDX, DDF or ONC. Once the compression is done only then high power laser beam arrive to ignite the compressed material using optical feedback system. This is also called laser direct drive system.

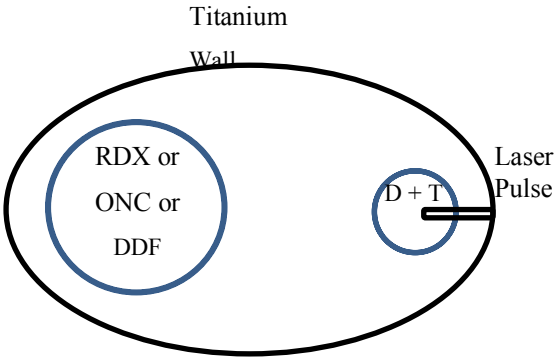

Fig. 4 Proposed Thermonuclear design

In the above propose design compression will be done high chemical explosive as shown in Fig. 4. When the deuterium and tritium (D + T) are compressed to the minimum size the high energy laser pulse[1] will ignite the D + T mixture. Duration for the pulse should be long enough to create sustainable fusion reaction. There will be an optical feedback system to synchronize laser pulse and the optimum compression. Shock wave takes longer time to reach target than laser pulse. Proper synchronization is required. This can easily be achieved by Q-switching.

Main purpose of compressing the fusion fuel is to allow the reaction to occur fast enough to cover large part of the fuel to burn before whole thing is disassembled by its own expansion. Compression helps the fusion in many ways. Suppose fusion fuel is compressed 16 times then reaction rate will simply increase 16 times due to density increase alone. Temperature will also increase which is proportional to fourth root of the energy density. So $(16)^{1/4} = 2$. In case of D – D reaction[2] it would be 6.7 fold which would decrease as the temperature rises.

Another advantage is the neutrons released by fusion reaction will undergo more collisions with the fuel nuclei before they can escape.

Initially combustion of pure deuterium fuel 66.3% of all the energy produced is in form of neutron kinetic energy. In each collision on the average a neutron will lose 51.6% of its energy. After many collisions almost all the energy given by neutron will be transferred to heating the fusion fuel.

For example mean free path (MFP) of neutrons produced by the D+T reaction is 22cm.

One kg of sphere of liquid deuterium would be 22.4 cm. Which means most of the neutrons produced with in this mass will escape without single collision. If this spherical deuterium massed is compressed to 125 times, then it will shrink to 4.49 cm but now MFP would be 0.18 cm. Only few neutrons would be escape without depositing most of their kinetic energy in the fuel mass. This is even more important if fuel is Li-6 D[3] .

Temperature and fuel burnup time

In simple D – D fusion effective ignition temperature is around 30 million degree K. At this temperature the reaction rate and fuel temperature starts rising rapidly. 80% reaction is completed in just 20 nanoseconds if the fuel density is 100g/cm^3.

Lower temperature creates slow start before suddenly climbing to 30 million degree K. Initial temperature could be 12 million degree K. Slow period is 60 nanoseconds after that rest of fuel burn in the same 20 nanoseconds. Other fuel densities will take slightly different time to complete the reaction.

There is another way of doing fusion explosions at laboratory scale is first allowing the compression shock to converge in the center of the fuel and place a tritium-deuterium spark plug. Since this reaction ignites at much lower temperatures. Lithium[4] tritide has been used by USA for initial ignition. D – T reaction is 100 times faster than D-D combustion. Tritium is not found in nature and it is very expensive[5] . On the other hand deuterium is an inexpensive fusion fuel, which is on the order of USD 100/kg to manufacture. Lithium deuteride[2] can also be use with some variation.

USA has used natural lithium successfully as a fusion fuel in the tests in the 11Mrt Castle Romeo.

Advantages

There are number of advantages for direct laser base fusion reaction.

i) I does not produce high radiation

ii) Size of such fusion reaction can vary greatly. It can be as small as 0.1kilo ton to mega ton TNT.
iii) Fusion fuel especially deuterium is cheap and raw material is almost limitless.
iv) It can be used for mining, oil drilling, major earth work, and etc.
v) There are lesser safety issue with fusion reaction than fission reactions[5]

Note: Exact shape of thermonuclear device depends on simulation because fuel must be compressed uniformly.

Conclusion

Fusion divergent reaction is possible with the present available technology. D – T fuel can be compressed by new chemical explosive. At the same time high energy pulse laser can be used to ignite the gas mixture. Lithium deuterium liquid can also be used as basic fusion fuel. **Note:** Exact shape of thermonuclear device depends on simulation because fuel must be compressed uniformly.

Reference

1) S. Atzeni and J. Meyer-ter-Vehn, "Beam Plasma Interaction, Hydrogynmics, Hot Dense Matter" Oxford University Press, 2004.
2) S.E. Sharapov[1], T. Hellsten[2], V.G. Kiptily[1], T. Craciunescu, J. Eriksson, M. Fitzgerald, J.-B. Girardo, V. Goloborod'ko, C. Hellesen, A. Hjalmarsson, Fusion product studies via fast ion D–D and D–^{3}He fusion on JET' Nuclear Fusion, Volume **56**, 11 , 24th August (2016)
3) Mohan Chen, T. Abrams, M.A. Jaworski and Emily , A.Rock-salt structure lithium deuteride formation in liquid lithium with high-concentrations of deuterium: a first-principles molecular dynamics study in Carter Nuclear Fusion, Volume **56**, 11, December 17 , (2015)
4) F.L. Tabares, Y. Hirooka, R. Maingi, G. Mazzitelli, V. Mirnov, R. Nygren, M. Ono[3]and D.N. Ruzic ,4rd International Symposium on Lithium Applications by in Nuclear Fusion, Volume **56**, 12 September (2016)
5) Iole Palermo, David Rapisarda, Iván Fernández-Berceruelo and Angel Ibarra, Tritium production assessment for the DCLL EUROfusion DEMO, in Nuclear Fusion, Volume **56**, 10, August 9 , (2016)

The role of microscopes in biology and medicine

A.B. ISMAILOVA

Baku State University, Baku, Azerbaijan

Abstract
The different kind of microscopes are a main tool for microbiologists, cell biologists, histologists, embryologists.The main stages of cytological and histological analysis are the choice of the object of study, its preparation for study under a microscope, the qualitative and quantitative analysis of images. The objects of the study are living and fixed tissues and cells, their constituent macromolecules (for example, molecules of deoxyribonucleic acid-DNA), images obtained with the use of light and electron microscopes or on the display screen. Basically, a biological microscope is used in various research centers and hospitals to make more clear in-time diagnosis for patients.
Keywords: the history and structure of the microscope, the modern types of microscopes, the modern biomedical methods

Today modern technology is actively used in many areas of science and industry. The resolving power of the human eye is about 100 micrometers (0.1 mm), which is roughly corresponds to the thickness of the hair. To see smaller objects the special devices are required. The microscope invented at the end of the 17th century opened up new world of a living cell. The history of the microscope is extremely diverse and interesting. People wanted to see, make bigger and study the small particles. So there were polished glasses - loops, which can already be called the ancestor of a modern microscope. People learned to look far above the earth and into heaven, when they wanted to look inside. So first there appeared the simplest light microscopes of the two-lens system, when it became necessary to study what is even deeper – **the electronic microscopes** appeared. The first electron microscopes appeared in the mid-1930s. In England and Germany shortly after the discover of E. Ruska, for which he received the Nobel Prize in 1986, and by the mid of 1950s., they have already been widely used in natural sciences. Even the first observations carried out with the help of the simplest and most imperfect electron microscope according to modern concepts, opened the "whole world in a drop of water". Due to the use of fluorescent reporters, optical microscopes have been developed that have overcome the "magic barrier" of the Abbe principle, postulated that the resolution that can be achieved with optical microscopy can not be less than 0.2 μm. In 2014, the Nobel Prize in Chemistry was awarded to Eric Betzig, Stefan Hell and William Moerner for the development of the ultra-high resolution (nanoscopic) method of fluorescence microscopy ("nanoscopy").

The light microscope is the main device of biology, and optical system consisting of a capacitor, lens and eyepiece, which are used to view the object. A beam of light from the light source is collected in the condenser and sent to the object. The main optical part of the microscope, which determines its main capabilities is the lens. In modern microscopes, objective lenses are replaceable, which allows one to study cells at different magnifications. The main characteristic of a microscope as an optical system is the resolving power. The images given by the lens can be magnified many times, using a powerful eyepiece or, for example, by projecting on a screen (up to 105 times). The image quality, its clarity, is determined by the resolving power of the microscopes. The resolution limit - the minimum distance at which these points are still seen separately-depends on the wavelength of the light, the object which is illuminated and the numerical aperture of the lens.

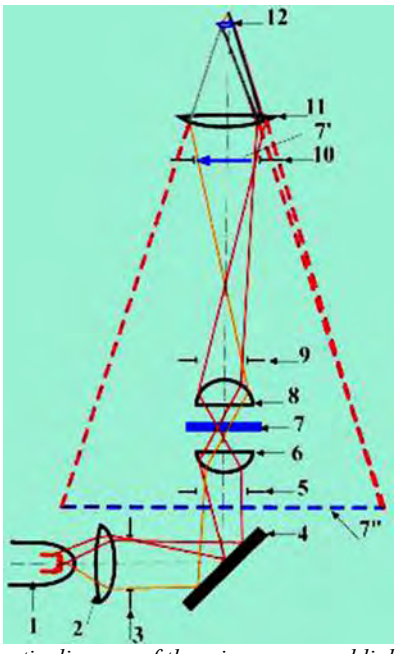

Pic.1. Schematic diagram of the microscope and lighting system: 1. Light source; 2. Collector; 3. Iris field diaphragm; 4. Mirror; 5. Iris aperture diaphragm;6. Condenser; 7. A preparation; 7.1 Increased actual intermediate image of the drug formed; Lens; 7.2 Increased imaginary final image of the drug, observed in the eyepiece; 8. The lens; 9. The output icon of the lens; 10. Field diaphragm of the eyepiece; 11. The eyepiece; 12. The eye.

The larger the aperture and the closer the refractive index of the medium between the lens and the preparation to the refractive index of glass, the higher the resolving power of the lens. If we assume that the aperture of the condenser is equal to the objective aperture, then the resolution formula has the following form:

$R = \frac{\lambda}{2NA}$, where **R** is the resolution limit; **λ**-wavelength; **NA** is the numerical aperture. Distinguish useful and useless increase. A useful increase is usually equal to the numerical aperture of the lens, increased by

500-1000 times. A higher eyepiece magnification does not reveal new details and is useless.

Usually light microscopes use sources of illumination in the visible region of the spectrum (400-700 nm), therefore the maximum resolution of the microscope in this case can not be more than 200-350 nm (0.2-0.35 μm). If we use ultraviolet light (260-280 nm), you can increase the resolution to 130-140 nm (0.13-0.14 microns). This will be the limit of the theoretical resolution of the light microscope, determined by the wave nature of light. Thus, all that a light microscope can give as an auxiliary device to our eye is to increase its resolution by about 1000 times (the unarmed human eye has a resolving power of about 0.1 mm, which is 100 μm). This is the "useful" increase in the microscope, above which we will only increase the contours of the image without opening new details in it. Therefore, when using the visible light range, the value 0.2-0.3 μm is the final resolution limit of the light microscope.

Modern microscopy devices are incomparably more complex devices than microscopes of the recent past. In addition to conventional light microscopy, there are methods of microscopy that allow studying unpolluted microorganisms: **phase-contrast, dark-field and fluorescence microscopy**.

To study microorganisms and their structures, the size of which is smaller than the resolution of a light microscope, electron microscopy is used. In recent years, with the skillful use of an electron microscope, it has been surprisingly easy to see the largest biological molecules, such as antibody molecules, and using the high-resolution microscope, the structure of one of the adenovirus viruses has been almost completely studied. For microanatomy purposes, the most powerful electron microscope with the highest resolving power will not necessarily prove to be the best. An electron microscope with an average resolution is sufficient for the most detailed microanatomy, whereas a microscope with a very large magnification can give nothing in these case.

By means of a light microscope, particles smaller than 0.2 μm can be seen. This is the "dark field" method or as it was called earlier, the "**ultra microscopy**" method. Its essence is that, like dust particles in a ray of light (the Tyndall effect), in the cell with side illumination the smallest particles (less than 0.2 μm) glow, the reflected light from which gets into the objective of the microscope. The method is successfully used in the study of living cells. If the untreated live or dead cells are viewed in transmitted light, then only large parts are distinguished in them, since they have a different coefficient of refraction and absorption of light rays than the surrounding medium. The greater part of the cellular components differ little in these properties from both the medium (water or tissue solutions) and from each other and is therefore not very noticeable or contrast. To study them, we have to change the illumination (losing at the same time in the clarity of the image) or apply special methods and devices. One such technique is the method of **phase-contrast microscopy,** which is widely used to observe living cells. It is based on the fact that individual sections of a transparent cell in general are at least small, but still differ from each other in density, but also in terms of refraction. Passing through them, the light changes its phase, however, our eye does not detect such a change in the phase of the light wave, since it is sensitive only to a change in the intensity of light. The latter depends on the magnitude of the amplitude of the light wave. A special plate is inserted into the lens of the phase-contrast microscope, passing through which the light beam experiences an additional phase shift of the oscillations. In the construction of the image, beams interacting in one phase or in anti-phase, but having different amplitudes and thereby creating a light-dark contrast image of the object.

A similar technique is used in an **interference microscope**. It is designed so that a beam of parallel light rays from the illuminator is divided into two streams. One of them passes through the object and acquires changes in the oscillation phase, the other goes bypassing the object. In the prism of the lens, both streams reconnect and interfere with each other. As a result of interference, an image will be constructed in which sections of cells of different thicknesses or different densities will differ from one another in the degree of contrast. By measuring the phase shifts, it is possible to determine the concentration and mass of dry matter in the object.

Objects with isotropy are studied using **a polarization microscope**. Ordered orientation of submicroscopic particles (for example in myofibrils, etc.). In such microscope a polarizer is placed in front of the condenser, which transmits light waves with a definite plane of polarization. After the preparation and the objective lens, an analyzer is placed that can transmit light with the same polarization plane. The polarizer and analyzer are prisms made from Iceland spar (Nicolas prism). If the second prism (analyzer) is rotated then 90 ° relative to the first, then the light will not pass. In the case when between such crossed prisms there will be an object having double refraction, i.e. the ability to polarize light, it will be seen as glowing in a dark field. Using a polarization microscope, one can we see, for example, in the oriented arrangement of micelles in the cell wall of plants.

Basically, a biological microscope is used in various research centers, scientific institutions or hospitals. In medicine there are many devices that help to make more clear in-time diagnosis for patients. One such tool is a biological research microscope, which is actively used both in clinical practice and in a microbiological laboratory, for example, in microbiological examination or analysis of blood cells. **The method of phase contrast** serves to obtain images of transparent and colorless objects that are invisible when viewed by the bright field method. Such objects include, for example, living unpainted animal tissues. The method is based on the fact that even with very small differences in the refractive indices of different elements of the preparation, a light wave passing through them undergoes different phase changes (acquires the so-called phase relief). These phase changes, not directly perceived by the eye or by a photographic plate, are transformed by means of a special optical device into changes in the amplitude of the light wave, i.e. changes in brightness ("amplitude relief") that

are already discernible by the eye or fixed on the photosensitive layer.

The principle of **the luminescent microscope** (series LUMAM ™) is based on the use of luminescence of biological objects arising under the action of ultraviolet radiation. By observing or photographing the preparations in reflected light, one can judge the structure of the test sample, which is used in microbiology and immunological studies. Direct staining with luminescent dyes makes it possible to identify such cell structures that are difficult to consider in a light microscope.

The **operating microscope** (series MIKO ™, MX ™) is used for microsurgical operations in ophthalmology, neurosurgery and other fields of microsurgery. The microscope has a fiber optic illumination system for the operating field, a demonstration visual device, a photographic device. It is possible to connect to it cine-equipment for shooting operations and television surveillance.

Pic. 2. The microscope Axio Scope

This is Carl Zeiss's unique C-DIC (circularly polarized) method for obtaining additional information about the facility; • New light sources based on LEDs for transmitted and reflected light (LED) and fluorescence analysis (FL-LED and Colibri). The operating time (15000-30000 h), convenient to configure, allowing to obtain images without light distortion; • The overall increase is 12.5-2500x; • Nozzles: binocular, binocular nozzle with photo / video output; Angle of inclination of the ocular tubes -30º, 20º, 15º (ergonomic nozzles). In this microscope are available : bright field, dark field, phase contrast, differential interference (DIC), polarization, circular polarization, luminescence made of environmentally friendly materials that do not contain lead.

The **Fluorescence recovery after photobleaching (FRAP)** - a technique in a light microscopy using a pulse from a focused laser micro beam to deplete the fluorescence in a local region in a living cell. The subsequent recovery of fluorescence in the irradiated region is measured to establish the mobility of the molecules that carry the fluorescent tag. In up to date life a **binocular microscope** is simply indispensable in hospitals or scientific laboratories.

The next stage of achievements is **digital microscope**, in which the lens was replaced by a digital camera. Actually, the main difference between a digital microscope and **a conventional microscope** is the absence of an eyepiece, through which is observed by the human eye. Instead, a digital camera is installed, firstly, it does not give distortion (reduces the number of lenses), and secondly, color reproduction improves, and as well as images are obtained in digital form, which allows for an additional post- processing, as well as store huge arrays of photos on just one hard drive. For example the microscope ***Axio Scope***. It is equipped with a converter of visual information into digital, providing the transfer to the computer in real time of the image of the micro object and micro process and also their storage, including in form of digital video recording. The microscope has a simple structure, USB-interface, two-level illumination; included with software with a simple and intuitive interface. Export results for use in other programs: Graphic files - in the formats * .jpg or * .bmp, and video files - in the format *.avi. Collect from the received results of photo and video shooting demonstration selections - "filmstrips" (program memory can store simultaneously 4 sequences, including up to 50 objects each). Subsequently, a selection of frames, temporarily unused, can be easily disassembled, since the graphic files remain on the hard disk of the computer.

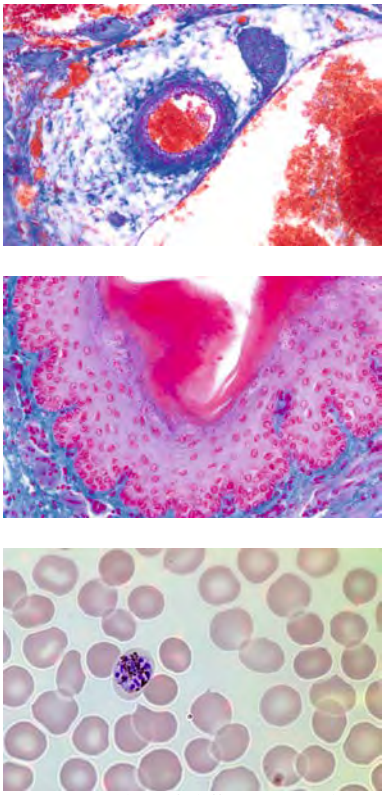

*Pic. 3. These are examples of different samples, studied by the microscope **Axio Scope** in histology, cell biology, hematology*

Summarizing, these microscopes will be a good acquisition for students of higher education institutions, who simply need to practice in different studies to gain experience. The parameters thus obtained represent a multidimensional "portrait" of the cell and have a specific numerical expression. They can be subjected to various methods of statistical processing, they allow to precisely

classify micro objects, to reveal the features of their structure that are not detectable visually. Thus, the application of new research methods in genetics, microbiology, cell biology, histology and embryology makes it possible to elucidate the general patterns of organization of tissues and cells, the structural basis of biochemical processes that determine the function of specific structural components of the cell.

REFERENCES

[1] A. Bonnell Dawn “Scanning probe microscopy and spectroscopy : Theory, techniques, applications”, Wiley-VCH, New York (2001)

[2] P.C.Cheng et al. “Multidimensional microscopy”, Springer, New York (1994)

[3] Y.I. Afanasiev, N.A.Yurina, E.F.Kotovskiy at al., “Gistologiya, embriologiya, tsitologiya”, Moscow, 800 (2012)

[4] K. Mihel, “Osnovi teorii mikroscopa”, Moscow (1955)

[5] T.V. Utkin, O. S. Bugorkova, N.A. Kuznetsov at al., Sovremennie vozmojnosti izucheniya ultrastrukturi kletok, Izvestiya Saratovskoqo Universiteta , Seriya Fizika **12**, 36 (2012)

[6] http://nsau.edu.ru/images/vetfac/images/ebooks/microbiology/stu/bacter/microscop.htm

science4@mail.ru

Light nuclei production in proton-Carbon and nucleus-Carbon interactions at 4.2 AGeV/c

KAMAL HUSSAIN KHAN[1], M.K SULEYMANOV[2,3], M. AJAZ[4], ALI ZAMAN[2], H. YOUNIS[2] , YA. H. HUSEYNALIYEV[5]

[1]*Department of Physics, Women University of Azad Jammu & Kashmir, Bagh, Pakistan*
[2]*Department of Physics, COMSATS Institute of Information Technology, Islamabad, Pakistan*
[3]*Joint Institute for Nuclear Research (JINR) Dubna, Russia*
[4]*Department of Physics, Abdul Wali Khan University Mardan, Pakistan*
[5]*Science and Innovation Department, Azerbaijan State Pedagogical University Baku, Azerbaijan*

Abstract

Average multiplicity of light nuclei, produced in different interactions at 4.2A GeV/c is studied as a function of centrality. A change in multiplicity is observed with increase in the mass of projectile. In ^{12}CC-interactions an unexpected increase in the multiplicity is seen in the most central events. These measurements are compared with the predictions of Cascade and Fritiof models, which fail to account for the experimentally observed effects. In case of ^{12}CC, it is suggested that the inclusion of nuclear coalescence effect can be an explanatory reason for the deviation of experimental measurements from the models' predictions.

1. Introduction

In heavy ion collisions, light nuclei are produced mainly from the disintegration of projectile and target nuclei. However, nuclei are believed to be formed in final state interactions between nucleons as a result of coalescence, when they are in same phase space [1]. Considering the momentum space, the probability density of nuclei formation of mass number (A) is proportional to the A^{th} power of proton density [2-4]. A quantitative description of this process is typically based on the proportionality parameter B_A known as coalescence parameter, which depends upon the transverse mass of cluster and does not depend upon the centrality of the collisions [5]. The fragments of the projectile and target decrease with the centrality of the collisions [6]. In the most central events the production of Deuterons and Tritons from target spectator area is suppressed [7]. At maximum centrality, the nuclei from either mechanism (fragmentation or coalescence) decrease exponentially with the mass number (A) of producing nuclei [8]. So the study of the centrality dependent properties of light nuclei production can give essential information about the initial and final states of collisions and the production mechanisms. In this paper the average multiplicity of light nuclei produced in Proton-Carbon (pC), Deutron-Carbon (dC), Helium-Carbon (HeC) and Carbon-Carbon (^{12}CC)-interactions at 4.2 A GeV/c is studied as a function of centrality. The centrality is defined by the number of identifying protons (N_p) in an event [9-11].This study provides significant information about the behavior and production mechanisms of light nuclei.

2. Experiment and Method

The data were recorded with the 2m Propane Bubble Chamber [13], installed at the Laboratory of High Energy of the Joint Institute for Nuclear Research (JINR), Dubna, Russia. The chamber was placed in a 1.5 T magnetic field, and irradiated with the beams of relativistic Protons (p), Deutron (d), Helium (He) and Carbon nuclei (^{12}C) with Propane (C_3H_8) as target. Almost all charged particles emitted at 4π, provided they exceed the threshold value of the energy required for visible track formation were detected well in the chamber.

In total, we analyzed 12757 (twelve thousands seven hundred and fifty-seven) events

of pC_3H_8, 9016 (nine thousands and sixteen) of $d\ C_3H_8$, 22975 (twenty-two thousands nine hundred and seventy-five) of HeC_3H_8 and 39543 (thirty-nine thousands five hundred and forty-three) of $^{12}C\ C_3H_8$.The interactions with Carbon nuclei were selected from all interactions of beams with Propane (C_3H_8), using criteria based on the determination of total charge of secondaries, presence of slow Protons (with momentum P < 0.75 GeV/c) , Protons in backward hemisphere and negatively charged particles etc. as described in Refs. [14,15]. This criterion is not used for *pC* interaction because light nuclei cannot be produced in *pp (Proton-Hydrogen)* interaction.

Particles were identified by their tracks, which they left in the chamber and their momentum was calculated by the curvature of these tracks and the magnetic field of the chamber. The uncertainty in the measurement of momentum was about 11% and in measurement of emission angle θ, was about 0.8% [16,17].

Every particle required a least amount of momentum to produce a visible track particular to its mass. The average momentum for Pion registration was set to about 70 MeV/c, below this momentum Pion cannot produce visible tracks. All negative particles, except for those identified as electron were considered as π^- mesons. The contamination from the misidentified electrons and negative strange particles were about 5% and 1% respectively. The π^+ mesons were identified and differentiated well from Protons by the ionization produced in the chamber in momentum region less than 0.5 GeV/c. Above this momentum π^+ mesons were mixed with Protons except a few which were recognized as π^+- mesons. The lowest momentum required for the track formation of Proton, singly charged nuclei and multi charged nuclei was about 0.15 GeV/c, 0.75 GeV/c and 0.185 GeV/c respectively. The corrections to account for losses of particles were introduced by the weights defined by the Collaboration of 2m propane bubble chamber [13] for each particle. The protons were identified finely within the momentum interval 0.15-0.5 GeV/c beyond this momentum Protons were contaminated with π^+ mesons. The nuclei were detected in two groups singly charged and multi-charged nuclei. The singly charged nuclei Deuteron (*d*) and Triton (*t*) were identified as a mixture and differentiated well from other singly charged positive particles in the momentum interval 1-3GeV/c, for the momentum greater than this value and emission angle θ less than 4^o Deuteron and Triton could not be separated from striping Protons. The multi-charged nuclei with charge $Z \geq 2$ were identified together. There was no possibility to identify the nuclei species separately because they produce about similar ionization in the bubble chamber. In this manuscript, all identified nuclei (singly or multi-charged) in an event were considered as light nuclei. The centrality of the collisions was defined by the number of identified Protons (N_p) in an event, and identified Protons (N_p) was calculated as;

N_p= Protons (with any momentum) + π^+ mesons (with momentum >0.5 GeV/c) - π^- mesons (with momentum >0.5 GeV/c) - Protons (with momentum >3 GeV/c and emission angle θ less than 4^o).

As mentioned above that several π^+ mesons with momentum greater than 0.5 GeV/c were identified as Protons, whereas π^- mesons were identified very well. To address the contamination of π^+ mesons with Protons, it was assumed that an equal number of π^- and π^+ mesons were produced because the projectile (except proton) and target nuclei are Isospin singlet, that is why the π^- mesons (with momentum > 0.5 GeV/c) were subtracted from Protons. To deal with the contamination of *d* and *t* , the Protons with momentum greater than 3Gev/c and emission angle θ less than 4^o were excluded (subtracted from Protons) also in defining N_p.

To observe the coalescence mechanism we used the simple idea of baryon number conservation and centrality. As the number of identified Protons in an event was used to fix the centrality of the collision, therefore an increase in the number of Protons (Increasing centrality) in an event will result in a decrease in the number of nuclei (multiplicity of nuclei) to conserve the baryon numbers. So the study of multiplicity of light nuclei as a function of

centrality can give some direct information about the production mechanism of nuclei in these collisions.

The experimental results were compared with the predictions of two theoretical models, Cascade [18 Sec.3.1] and Fritiof [18 Sec.3.2]. These codes are available on the website: http:/hepweb.jinr.ru (created by V.V. Uzhinskii). Cascade model is used to describe the general features of relativistic nucleus-nucleus collisions. This model does not include any medium or collective properties and each of the colliding nuclei is treated as a gas of nucleons bound in a potential well. The Pauli principle and the energy momentum conservation are obeyed in each inter-nuclear interaction. The remaining excited nuclei, after the cascade stage, are described by the statistical theory in the evaporation approximation. Fritiof is a famous Monte-Carlo code which assumes all Hadron-Hadron interactions as binary reactions ($h_1+h_2 \rightarrow h'_1+ h'_2$), where $h'_1+ h'_2$ are excited states of hadrons with discrete or continues mass spectra. The excited hadrons are treated as QCD strings, and the corresponding Lund-string fragmentation model is applied in order to simulate their decays. The evaporation of residue nucleus is taken into account also. A similar approach is applied to simulate nucleus- nucleus collision, where successive interactions of projectile hadrons with target are considered. Unlike Cascade model, Fritof code uses the approach, which gives zero excitation energy to residual nucleus when all spectator nucleon are ejected. The Cascade results can be reproduced by Fritiof model by changing limits of energy and distance between the nucleons. The Fritiof code has been modified [19] for lower energies and we used the modified version of this code. Both Models include nuclear fragments from projectile and target, but do not include the possibility of nuclei formation as a result of coalescence of nucleons. In both, the Cascade and the Fritiof codes 40,000 (forty thousands) events of each interaction (*pC dC, HeC* and ^{12}CC) were analyzed, using the same criteria of event selection and particle identification as used for experimental data.

3. Results and Discussions

The average multiplicity of the light nuclei ($<N>_{nuclei}$) in *p*C-interactions at 4.2A GeV/c as a function of centrality is presented in Figure 1, which includes statistical uncertainties only. The measurements are compared with the predictions of two models, Cascade and Fritiof. Experimental results for average multiplicity are almost constant in *p*C -interactions. In these interactions the observed light nuclei are Deuterons (*d*) and Tritons (*t*) only, which are the fragments of target nuclei (Carbon). More nuclei are identified in events with $N_p \geq 4$ and can be concluded that the target fragments evaporated in these events are recorded relatively well. The Fritiof model describes the qualitative behavior of experimental data very well but overestimates the average multiplicity. The Cascade model is incapable to illustrate the qualitative or quantitative behavior of the experimental data.

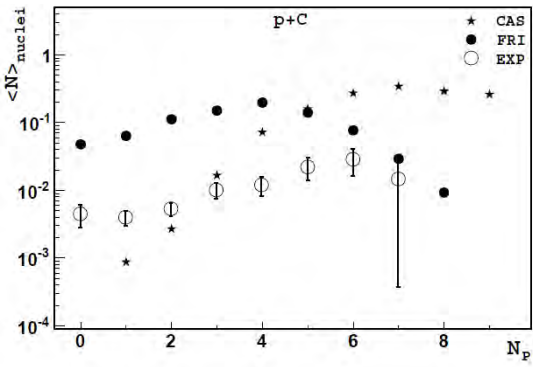

Figure 1. Average multiplicity of light nuclei as function of centrality (N_p) in pC - interactions. Stars, solid circles and open circles represent Cascade (CAS),Fritiof (FRI) and data (EXP) respectively.

The average multiplicity of the light nuclei ($<N>_{nuclei}$) produced in *d*C-interactions at 4.2A GeV/c as a function of centrality is presented in Figure 2. Only statistical errors are included in the Figure 2. Now the projectile is itself a nucleus (Deuteron) and the total energy of the collision is double of the above interaction (*pC*-interactions), which increases the average multiplicity of light nuclei about 10 times greater than the multiplicity in *pC*- interactions. Like *pC*-interactions, the observed light nuclei in *d*C-interactions are Deuterons and Tritons only. The experimental results are almost constant except at the first point (N_p=0), where the average multiplicity is maximized, which shows the contribution from the projectile. The Fritiof

model predictions are still deviating from the experimental results but lower as compared to the *pC*- interactions and the Cascade code is again unable to describe the experimental results.

The average multiplicity of the light nuclei ($<N>_{nuclei}$) produced in *He*C-interactions at 4.2A GeV/c as a function of centrality is shown in Figure 3. Only statistical errors are considered in Figure 3. Unlike the above-mentioned interactions, the experimental data (*He*C-interactions) contains both singly charged (*d, t*) and multi charged (z≥2) nuclei. The Average multiplicity decreases sharply in the region ($0 \le N_p \le 4$) as compared to the region (Np>4). Both models reproduce the data, which diverge from the experimental results in the region

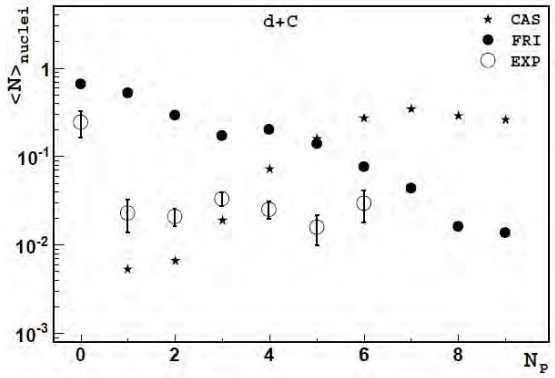

Figure 2. Average multiplicity of light nuclei as function of centrality (N_p) in dC -interactions. Stars, solid circles and open circles represent Cascade (CAS), Fritiof (FRI) and data (EXP) respectively.

($2 \le N_p \le 7$), however the divergence is small as compared to the interactions discussed above. In *HeC*-interactions the mass and energy of the projectile is double of the *dC*-interaction, which increases the average multiplicity about 10 times to *dC*-interactions. Keeping in view the above Figures 1and 2, the first region ($N_p < 4$) of Figure 3 can be considered as a projectile fragmenting region, whereas the second one ($N_p > 4$) is as target fragmenting region. The projectile fragmenting region is more sensitive for centrality than the target fragmenting region , which has almost constant behavior as can be seen from Figures (1-3).

The average multiplicity of the light nuclei ($<N>_{nuclei}$) in ^{12}CC-interactions at 4.2A GeV/c as a function of centrality is presented in Figure 4, statistical uncertainties are incorporated only. Now the projectile mass and energy is much greater than the above interactions, which results in an increase in multiplicity and better identification of light nuclei. These light nuclei contain both the singly charged *(d, t)* and multi charged (z≥2) nuclei. Experimental results are described qualitatively by dividing them into different regions as shown in Figure 4. The measurements are compared with the models' predictions also. Both the models underestimate the average multiplicity in the region ($N_p \le 2$) by a small amount. In experimental data maximum number of light nuclei is found in peripheral collisions ($N_p \le 2$) where the impact parameter is large. In this region the experimental data measures the average multiplicity about 1.17 times to Cascade and about 1.45 times to Fritiof

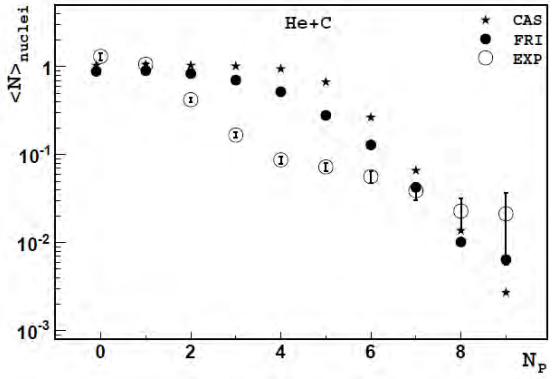

Figure 3. Average multiplicity of light nuclei as function of centrality (N_p) in HeC –interactions. Stars, solid circles and open circles represent Cascade (CAS), Fritiof (FRI) and data (EXP) respectively.

model. As the impact parameter decreases and collisions become more central ($N_p \le 7$) the projectile starts to fragment into hadrons rather than light nuclei so the average multiplicity of light nuclei decreases linearly with a slope of -0.305±0.009. This region is considered as semi-central region. In this area both models underestimate the average multiplicity but both have the behavior similar to that of the experimental data. The deviation of models from experimental data becomes greater than in the peripheral region. Furthermore, when the interactions are more central ($8 \le N_p \le 12$) the $<N>_{nuclei}$ decreases more slowly with a slope of -0.175±0.008. It can be expected that the light nuclei are more contributing in this region than

the above region, which changes the slope of decrease. This central region can be considered as some mixture of projectile and target fragmentation. In this region models' measurements are low as compared to the experimental results. The different behaviors of multiplicity of light nuclei as a function of centrality emitting from projectile and target are also discussed in Ref. 6 and the yields of Deuteron and Triton from the target spectator area are discussed in Ref. 7. So the studies of light nuclei production in other experiments also give some clues to distinguish projectile and target regions. In the most central collisions (N_p>12), in contrast to models, a minor increase in the average multiplicity of light nuclei is observed. This increase in average multiplicity and the decrease in the slope of central region indicate a new source of light nuclei production other than the fragmentation of projectile and target. It is suggested that the new source can be the coalescence mechanism, because in the most central events the collisions are head on, and more possibly the projectile and the target disintegrate into hadrons rather than nuclei. A dense medium is expected in the most central events due to the maximum number of participants, in which the nucleons within the same phase space can coalesce to make nuclei. Light nuclei production via coalescence mechanisms is predicted in experiment E864 [2] for 10% most central events in Au+Pt (Pb) (for heavy ion collisions) interactions at 10.6 A GeV/c. In our study we find some direct and sharp signatures of nuclear coalescence effect in ^{12}CC (light ion collisions) interactions at 4.2A Gev/c. This information is necessary for theoretical models to describe the dynamics of the coalescence effect at high energy hadron-nuclear and nuclear-nuclear interaction.

4. Summary

In summary, analyses of experimental data for the average multiplicity of light nuclei as a function of centrality in *pC*, *dC*, *HeC* and ^{12}*CC* - interaction and their comparison with models are presented. With the increase in the mass of projectile average multiplicity of nuclei increases and diversity between models and experiment decreases. A systematic change in

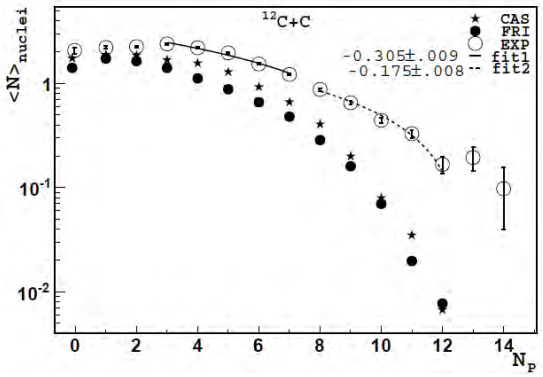

Figure 4. Average multiplicity of light nuclei as function of centrality (N_p) in ^{12}CC – interactions. Stars, solid circles and open circles represent Cascade (CAS), Fritiof (FRI) and data (EXP) respectively.

behavior of the projectile can be seen clearly from Figures (1-4) (*pC* to ^{12}*CC)*. In ^{12}*CC* interactions as shown in Figure 4, we identified four regions (N_p≥2, 2<N_p≤7, 8≤Np≥11 and N_p>12), in regions (N_p>7) the slope of average multiplicity is reduced. In the region (N_p≥ 12) a minor increase in multiplicity is seen which, indicates a mechanism of light nuclei formation other than the fragmentation of the colliding nuclei, which could possibly be the nuclear coalescence effect.

References

[1] J. L Nagle et al. Phys. Rev. C **53** 367- 376 (1996).
[2] M. J. Bennett et al., Phys. Rev. C **58** 1155-1164(1998).
[3] J. Barrette et al., Phys. Rev. C **50** 1077- 1084 (1994).
[4] S. Albergo et al., Phys. Rev. C **65** 034907(2002).
[5] I. G. Bearden et al. Eur. Phys. J. C **23**, 237–247(2002).
[6] Dabrowska et al. Nuclear Physics A**693,** 777–786 (2001).
[7] L. Ahle et al., Phys. Rev. C **57** 1416- 1427(1998).
[8] T. A. Armstrong et al., Phys. Rev.Lett. **83**, 5431-5434(1999).
[9] M. Ajaz et al. J. Phys. G: Nucl. Part.Phys. **40** 055101(2013)
[10] M. Ajaz et al., Modern Physics Letters A, **28** 1350175(2013).
[11] M. Ajaz et al. International Journal of Modern Physics E **21** 1250095(2012).
[12] M. Ajaz et al. International Journal of Modern Physics E **25** 1650019 (2016).
[13] A. I. Bondarenko et al., JINR communications PI -98-292, Dubna,(1998), A. I. Bondarenko et al., Physics of Atomic Nuclei, **65** 90–101 (2002).
[14] Agakishiyev, H.N et al,:JINR Commun.1-83-662,Dubna (1983).

[15] D. Armutlisky et al. Z. physics A **328** 455-461(1987).
[16] N. Akhababian et al., JINR Preprint 1-12114(1979).
[17] Armutlisky et al., Yad. Fiz **49** 182-190(1989).
[18] M. I. Adamovich, et al., Z. Phys, A **358** (1997).
[19] V.V. Uzhinskii, Modified code FRITIOF. User's Guied.

E-mail address: mais_suleymanov@comsats.edu.pk

Strong Magnetic Fields in Compact Stars as a Macroscopic Parity Violation Phenomenon

M. DVORNIKOV[a,b]

[a] Pushkov Institute of Terrestrial Magnetism, Ionosphere and Radiowave Propagation (IZMIRAN), 108840 Moscow, Troitsk, Russia

[b] Physics Faculty, National Research Tomsk State University, 36 Lenin Avenue, 634050 Tomsk, Russia

Abstract

We review the results in our recent works on the generation of strong magnetic fields in compact stars driven by the parity violating electroweak interactions between background fermions. The cases of a neutron star, a hybrid star, and a quark star are considered. We formulate the system of kinetic equations for the description of the spectra of the magnetic energy and the magnetic helicity, as well as for the chiral imbalances. Turbulence effects, which can be important for the evolution of small-scale magnetic field, are also taken into account. We find the numerical solution of these equations in case of large- and small-scale magnetic fields in quark matter. The applications of the obtained results for the generation of large-scale magnetic fields in magnetars and for the explanation of magnetar bursts are discussed.

Keywords: *magnetar, chiral magnetic effect, quark matter, electroweak interaction, compact star, turbulence.*

In the wake of the discovery of anomalous X-ray pulsars (AXP) and soft gamma ray repeaters (SGR), it was commonly accepted that strong magnetic fields are important for the energy radiation by compact stars. From the point of view of modern astrophysics [1] AXP and SGR are assumed to be strongly magnetized, with $B>10^{15}G$, compact stars, or magnetars. Since the discovery of magnetars, the origin of their strong magnetic fields is still a puzzle for modern physics and astrophysics [1]. Indeed one should explain the enhancement of the magnetic field of a pulsar $B_0=10^{12}G$ by at least three orders of magnitude to achieve the values observed in magnetars $B>10^{15}G$.

There are numerous models for the generation of strong magnetic fields in magnetars. Many of these models are reviewed in Ref. [1]. Recently there were several attempts to explain the generation of magnetic fields in magnetars using the elementary particle physics methods based on the chiral magnetic effect (CME) [2]. Among them one should mention Refs. [3-5]. Another approach for the generation of magnetic fields in compact stars, which is based on the field instability, driven by the parity violating interaction between background fermions, was proposed in Ref. [6].

In Refs. [7-11], we used the idea of Ref. [6] to elaborate the model for the generation of strong large-scale magnetic fields in magnetars driven by the electroweak electron-nucleon interaction in the neutron star matter. Then, in Ref. [12], we applied this approach to study the generation of magnetic fields in a hybrid star (HS) and in a quark star (QS). Moreover, in Ref. [13], we studied the generation of small-scale magnetic field in quark matter accounting for the electroweak interaction between quarks and the turbulent motion of matter as well as applied the results to describe magnetar bursts. In this work, we summarize the results in Refs. [7-13].

Let us consider degenerate fermions, which the background matter of a compact star is composed of. We shall assume that the matter density is high enough for the chiral symmetry to be restored. In this case CME can happen in this system. We showed in Ref. [14] that CME for electrons cannot take place inside a neutron star since the background matter is not sufficiently dense. Nevertheless, the chiral symmetry can be restored in HS/QS [15]. In Ref. [12], accounting for the electroweak interaction between quarks, we showed that the anomalous electric current $\mathbf{J}_5$ along the external magnetic field $\mathbf{B}$ is induced in this matter,

$$\vec{J}_5=\Pi\vec{B},\quad \Pi=\frac{1}{2\pi^2}\sum_q e_q^2\left(\mu_{5q}+V_{5q}\right), \tag{1}$$

where e_q is the electric charge of a quarks, $\mu_{5q}=\left(\mu_{qR}-\mu_{qL}\right)/2$ is the chiral imbalance, $\mu_{qR,L}$ are the chemical potentials of right and left quarks, $V_{5q}=\left(V_{qL}-V_{qR}\right)/2$, and $V_{qL,R}$ are the effective potentials of the electroweak interaction of left and right quarks with background fermions [12, 13].

The evolution of the magnetic field is described by the spectra of the magnetic helicity density $h(k,t)$ and the magnetic energy density $\rho_B(k,t)$. The total system of kinetic equations has the form [12, 13],

$$\frac{\partial h(k,t)}{\partial t}=-2k^2\left[\frac{F_Q^{5/6}}{\sigma_{cond}}+\frac{4}{3}\frac{r_D}{\rho_E+p}\int dk'\rho_B(k',t)\right]h(k,t)$$
$$+4\left[\frac{2\alpha_{em}F_Q^{5/6}}{\pi\sigma_{cond}}\left\{\frac{4}{9}\left[\mu_{5u}(t)+V_{5u}\right]+\frac{1}{9}\left[\mu_{5d}(t)+V_{5d}\right]\right\}\right.$$
$$\left.+\frac{2}{3}\frac{r_D}{\rho_E+p}\int dk'k'^2\,h(k',t)\right]\rho_B(k,t)$$
$$\frac{\partial\rho_B(k,t)}{\partial t}$$
$$=-2k^2\left[\frac{F_Q^{5/6}}{\sigma_{cond}}+\frac{4}{3}\frac{r_D}{\rho_E+p}\int dk'\rho_B(k',t)\right]\rho_B(k,t)$$

$$+\left[\frac{2\alpha_{em}F_Q^{5/6}}{\pi\sigma_{cond}}\left\{\frac{4}{9}\left[\mu_{5u}(t)+V_{5u}\right]+\frac{1}{9}\left[\mu_{5d}(t)+V_{5d}\right]\right\}\right.$$

$$\left.-\frac{2}{3}\frac{r_D}{\rho_E+p}\int dk'k'^2\,h(k',t)\right]k^2h(k,t)$$

$$\frac{d\mu_{5q}(t)}{dt}=\frac{e_q^2F_Q^{5/6}}{4\mu_q^2\sigma_{cond}}\int dk\left[k^2h(k,t)\right.$$

$$-\frac{4\alpha_{em}}{\pi}\left\{\frac{4}{9}\left[\mu_{5u}(t)+V_{5u}\right]\right.$$

$$\left.\left.+\frac{1}{9}\left[\mu_{5d}(t)+V_{5d}\right]\rho_B(k,t)\right\}\right]-\Gamma_q\mu_{5q}(t) \quad (2)$$

where σ_{cond} is the conductivity of quark matter, F_Q is the quenching factor [9-12] accounting for the anticorrelation of the magnetic field and the matter temperature, ρ_E is the energy density of the background matter, p is the matter pressure, and Γ_q is the helicity flip rate of quarks in their mutual collisions.

To account for the evolution of small-scale magnetic fields, in Eq. (2), we take into account the effects of turbulence governed by the phenomenological drag time parameter τ_D [14]. We shall suppose that the initial spectrum of the magnetic energy density has the Kolmogorov form, $\rho_B(k,t_0)\sim k^{-5/3}$. The initial values of the chiral imbalances are taken as $\mu_{5q}(t_0)=1MeV$.

We present below the numerical solution of Eq. (2) in the case of large-scale magnetic field, i.e. we set $\tau_D=0$. In this case, the wave number k in Eq. (2) changes in the range: $R^{-1}<k<\Lambda_{\min}^{-1}$, where $R=10km$ is the compact star radius and $\Lambda_{\min}$ is a free parameter. In Fig. (1), one can see the time evolution of magnetic fields for different initial temperatures, initial helicities, and various $\Lambda_{\min}$.

As one can see in Fig. 1, the seed magnetic field $B_0=10^{12}G$, which is typical in a young pulsar, is amplified in quark matter up to $B\sim(10^{14}-10^{15})G$, depending on the initial temperature. It should be noted that we predict the generation of large-scale magnetic field with $10^2m<\Lambda<10km$. Such magnetic fields can be found in magnetars [1]. Therefore one can conclude that HS/QS can potentially become a magnetar.

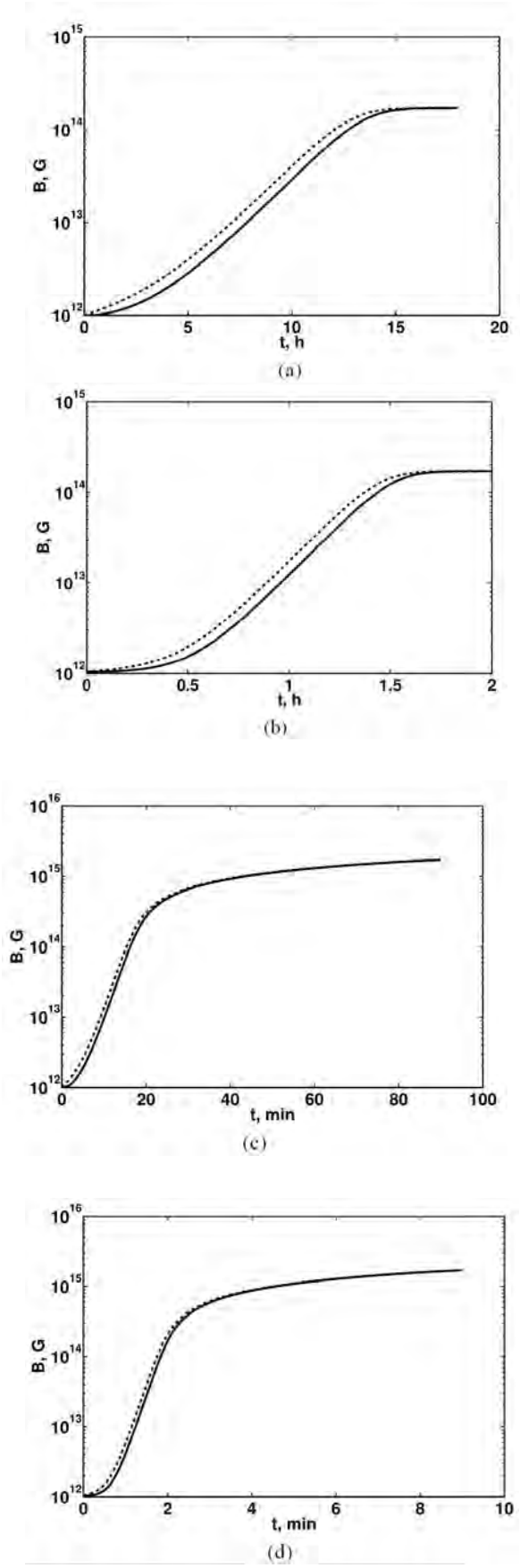

Figure 1: The magnetic field versus time for different initial temperatures T_0 and $\Lambda_{\min}$ in quark matter

consisting of u and d quarks. The solid lines correspond to initially nonhelical fields and dashed ones to the fields having maximal initial helicity. (a) $T_0 = 10^8 K$ and $\Lambda_{\min} = 1 km$. (b) $T_0 = 10^8 K$ and $\Lambda_{\min} = 100 m$. (c) $T_0 = 10^9 K$ and $\Lambda_{\min} = 1 km$. (d) $T_0 = 10^9 K$ and $\Lambda_{\min} = 100 m$.

Now let us turn to the evolution of small-scale magnetic fields. In this situation, we shall take that $\Lambda_{\min} = \Lambda_{\max}/10$ and suppose that the initial magnetic field is maximally helical. The time evolution of magnetic fields in turbulent quark matter is shown in Fig. 2. One can see that the matter turbulence becomes important as soon as the small-scale magnetic field reaches certain strength. Then the magnetic field starts to decrease compared to the case of non-turbulent matter, shown as dashed line in Fig. 2.

The time evolution of small-scale magnetic fields driven by the electroweak interaction of quarks in turbulent quark matter resembles the profiles of electromagnetic flashes of magnetars known as short bursts and giant flashes of AXP and SGR [1]. These flashes are believed to originate from the twists of magnetic field lines in the magnetar magnetosphere. Such a twist should be related to the plastic deformation of the stellar crust, which can be driven by a thermoplastic wave [16]. Despite the plausibility of the thermoplastic wave model, the origin of an effect, which triggers the propagation of this wave from the core to the stellar surface, is unclear. We suggest that a fluctuation of a magnetic field near the magnetar core, where the chiral symmetry can be restored, can initiate the propagation of a thermoplastic wave.

In conclusion we mention that, in Refs. [7-11], we developed the model for the generation of strong large-scale magnetic fields in dense matter of a compact star driven by the electroweak interaction between background fermions. Then, in Ref. [12], this model was applied to generate magnetic fields in dense quark matter in HS/QS. The electromagnetic flashes of magnetars were explained in frames of our model in Ref. [13].

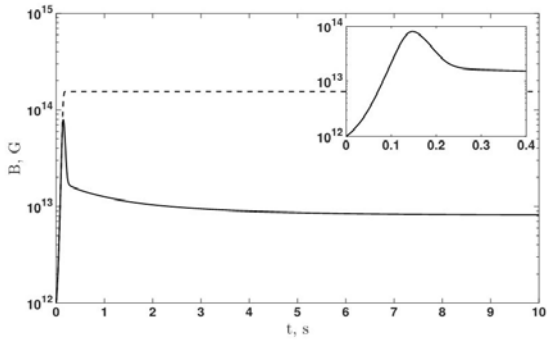

(a)

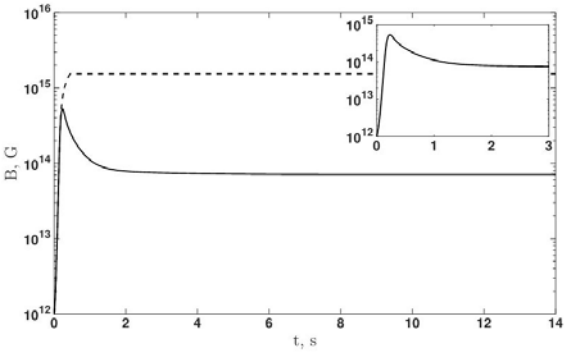

(b)

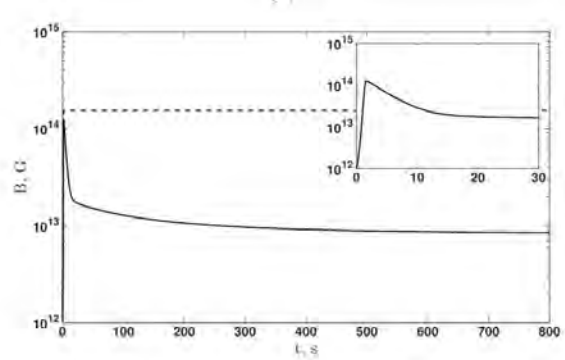

(c)

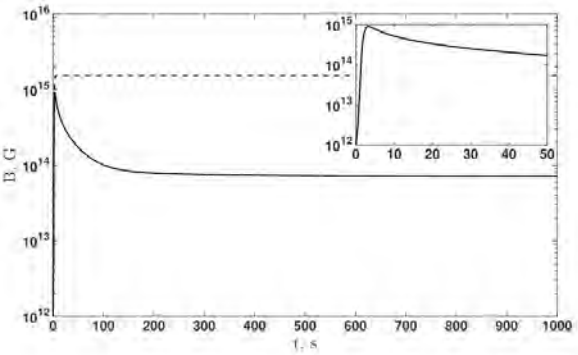

(d)

Figure 2: The evolution of the magnetic field for different T_0 and $\Lambda_{\min}$ in case when u and d quarks are present in a compact star. The panels (a) and (c) correspond to $T_0 = 10^8 K$, whereas the panels (b) and (d) to $T_0 = 10^9 K$. The panels (a) and (b) show the evolution of the field with $1cm < \Lambda < 10cm$, whereas the panels (c) and (d) with $10cm < \Lambda < 10^2 cm$. The insets demonstrate the magnetic field behavior at small evolution times. Dashed lines represent the magnetic field evolution with the corresponding initial conditions at the absence of the turbulence.

Acknowledgements I am thankful to the organizers of the "Modern Trends in Physics" for the invitation and a financial support, as well as to the Tomsk State University

Competitiveness Improvement Program and RFBR (research project No. 15-02-00293).

References

[1] Turolla R., Zane S., Watts A.L. Rep. Prog. Phys. **78**, 116901 (2015).
[2] Miransky V.A., Shovkovy I.A. Phys. Rept. **576**, 1 (2015).
[3] Charbonneau J., Zhitnitsky A. J. Cosmol. Astropart. Phys. **10**, 010 (2010).
[4] Sigl G., Leite N. J. Cosmol. Astropart. Phys. **01**, 025 (2016).
[5] Yamamoto N. Phys. Rev. D **93**, 065017 (2016).
[6] Boyarsky A., Ruchayskiy O., Shaposhnikov M. Phys. Rev. Lett. **109**, 111602 (2012).
[7] Dvornikov M., Semikoz V.B. Phys. Rev. D **91**, 061301 (2015).
[8] Dvornikov M., Semikoz V.B. J. Cosmol. Astropart. Phys. **05**, 032 (2015).
[9] Dvornikov M., Semikoz V.B. Phys. Rev. D **92**, 083007 (2015).
[10] Dvornikov M. J. Exp. Theor. Phys. **123**, 976 (2016).
[11] Dvornikov M. Russ. Phys. J. **59**, 1881 (2017).
[12] Dvornikov M. Nucl. Phys. B **913**, 79 (2016).
[13] Dvornikov M. "Magnetic fields in turbulent quark matter and magnetar bursts". ArXiv:1612.06540.
[14] Dvornikov M. Phys. Lett. B **760**, 406 (2016).
[15] Buballa M., Carignano S. Eur. Phys. J. A. **52**, 57 (2016).
[16] Beloborodov A.M., Levin Yu. Astrophys. J. Lett. **794**, L24 (2014).

maxdvo@izmiran.ru

Long-lived Natural Plasma Structures as an Alternative Energy Source

M. S. DVORNIKOV[a,b], G. SH. MEHDIYEVA[c]

[a] *Pushkov Institute of Terrestrial Magnetism, Ionosphere and Radiowave Propagation (IZMIRAN), 108840 Moscow, Troitsk, Russia*

[b] *Physics Faculty, National Research Tomsk State University, 36 Lenin Avenue, 634050 Tomsk, Russia*

[c] *Baku State University, 23 Z. Khalilov Street, AZ1148 Baku, Azerbaijan*

Abstract

We discuss the model of a stable plasmoid based on radial quantum oscillations of charged particles in plasma. This plasma structure is described on the basis of the nonlinear Schrödinger equation. In frames of the present model, we consider the new phenomenon of the effective attraction between oscillating charged particles. The possibility of the existence of a composite plasmoid is also considered. Finally, we discuss the applications of our results to the description of a natural long-lived plasma structure, which can be an alternative energy source.

Keywords: *spherically symmetric plasma structure, quantum plasma, effective attraction, acoustic wave, exchange interaction.*

1. Introduction

The model of a plasma structure based on spherically or axially symmetric quantum oscillations of electrons in plasma is developed. In Sec. 2, on the basis of the nonlinear Schrödinger equation describing the radial motion of electrons we obtain the dispersion relation for these oscillations and the typical length scale of a plasmoid, which turns out to be in the nano-range [1]. Then, in Sec. 3, we study the effective interaction between oscillating charged particles inside such a plasma structure due to the exchange of a virtual acoustic wave [2]. It was found that, in case of a dense plasma, this kind of interaction can be attractive and result in the formation of bound states of oscillating particles [3]. In frames of our model, we discuss the possibility of the existence of a composite plasma structure, consisting of multiple kernels, each of them being a nano-sized plasma oscillation (see Sec. 4). The cohesion between separate plasmoids is owing to the quantum exchange interaction between ions [4]. Finally, in Sec. 5, we discuss the application of our results to the theoretical description of long-lived natural plasma structures.

2. Quantum radial oscillations of electrons

In this section we describe a model of a quantum plasma structure on the basis of the nonlinear Schrödinger equation. This result is published in Ref. [1].

The motion of an electron gas in plasma obeys the following nonlinear Schrödinger equation [5]:

$$i\hbar\frac{\partial\psi}{\partial t}=\hat{H}\psi,\qquad \hat{H}=-\frac{\hbar^2}{2m}\vec{\nabla}^2+e\varphi(\vec{r},t)+e^2\int d^3\vec{r}'\frac{|\psi(\vec{r}',t)|^2}{|\vec{r}-\vec{r}'|}, \quad (1)$$

where $\psi(\vec{r},t)$ is the wave function related to the number density of an electron gas as $n_e=|\psi(\vec{r},t)|^2$, $\psi(\vec{r},t)$ is the potential of electrostatic interaction between ions and electrons, m is the electron mass, e is the proton charge.

The approximate solution of Eq. (1) corresponding to the spherically symmetric plasma oscillations was found in Ref. [1] as $\psi(r,t)=\psi_0+\chi(r)e^{-i\omega t}$, where $|\psi_0|^2=n_0$ is the unperturbed density and $\chi\sim\sin\gamma r/r$ is the small perturbation of the wave function. The frequency of quantum oscillations ω depends on the parameter γ as

$$\gamma^2=\frac{\omega m}{\hbar}\left[1\pm\left(1-4\frac{\omega_e^2}{\omega}\right)^{1/2}\right], \quad (2)$$

where $\omega_e=\sqrt{4\pi n_0e^2/m}$ is the Langmuir frequency for electrons.

The typical radius of a plasma structure described by Eq. (1), corresponding to $\omega=2\omega_e$, can be found using Eq. (2) as $R=\pi\hbar/2m\omega$. Supposing that we deal with a singly ionized plasma with $n_0=2.7\times10^{19}cm^{-3}$, the radius of a plasmoid turns out to be in the nano-range: $R=1.4\times10^{-7}cm$.

3. Effective attraction between charged particles in a quantum plasmoid

In this section we show that charged particles inside a quantum plasmoid can form bound states. This result is published in Refs. [2,3].

In Sec. 1, we show that one can excite a spherically symmetric plasma structure based on quantum radial oscillations of electrons. Taking into account the nano-scaled radius of such a plasmoid, one can expect that other quantum phenomena would take place inside this object.

Let us consider the case of relatively low temperature plasma, where one can find a neutral component along with electrons and ions. Then, rapid oscillations of a charged particle will excite acoustic waves in the neutral component. If this acoustic wave is coherently absorbed by another charged particle, it will result in the non-Coulomb effective interaction between charged particles. We shall demonstrate that this effective interaction takes place in

dense plasmas. Moreover, in some situations it can be attractive.

Note that for the first time the exchange by virtual acoustic waves between ions in dense plasma was studied in Ref. [6], where it was shown that this kind of effective interaction is important for the stability of a plasmoid. This effective interaction was recently studied in Ref. [2]. Using qualitative analysis, it was demonstrated in Ref. [2] that the exchange of a virtual acoustic wave can result in the formation of a bound state between two charged particles inside a nano-sized plasmoid.

Note that the idea that charged particles in plasma can form bound states due to various quantum effects was previously considered in a number of works (see, e.g., Ref. [7]). It should be noted that the quantum attraction is different from the well-known effective attractive interaction between charged particulates with the same polarity in dusty plasmas [8].

To discuss the quantum effective interaction between charged particles inside a plasmoid we should construct the ground state of the system. The ground state based on particles wave functions corresponding to a plane wave is inappropriate since it does not fully reflect the spherical symmetry of the system. In Ref. [3], it was suggested to use the ground state wave functions corresponding to a $3D$ harmonic oscillator with frequency ω, where ω is the frequency of an ion-acoustic wave. In this case, the wave function in the momentum representation has the form,

$$\psi_{n\sigma}(p)=2\pi\left[\frac{n!}{\Gamma(l'+n+3/2)}\right]\times\left(\frac{\hbar}{m_i\omega_i}\right)^{3/4}\left(\frac{p^2}{m_i\omega_i\hbar}\right)\times\exp\left[-\frac{p^2}{2m_i\omega_i\hbar}\right]L_n^{l'+1/2}\left(\frac{p^2}{m_i\omega_i\hbar}\right)\chi_\sigma, \quad (3)$$

where n and σ are the radial and spin quantum numbers, m_i is the ion mass, ω_i is the Langmuir frequency for ions, $L_n^{\alpha}(z)$ is the associated Laguerre polynomial, l' is the effective orbital quantum number, and χ_σ is the spin wave function.

The following secondly quantized Hamiltonian describes the interaction between charged particles and the field of the acoustic waves:

$$\hat{H}_{\text{int}}=K_0\int d^3\vec{r}\,\hat{\psi}^{\dagger}(\vec{r})\hat{\psi}(\vec{r})\hat{n}_1(\vec{r}), \quad (4)$$

where $\hat{\psi}(\vec{r})$ is the secondly quantized wave function of charged particles, based on Eq. (3), $\hat{n}_1(\vec{r})$ is the perturbation of the acoustic field, and K_0 is the phenomenological constant of the interaction.

After the elimination of the acoustic degrees of freedom, the total Hamiltonian of the system can be represented in the form,

$$\hat{H}=\sum_{n\sigma}e_n\hat{a}^{\dagger}_{n\sigma}\hat{a}_{n\sigma}-\sum_{nn'\sigma}F_{nn'}\hat{a}^{\dagger}_{n\sigma}\hat{a}^{\dagger}_{n',-\sigma}\hat{a}_{n',-\sigma}\hat{a}_{n\sigma}, \quad (5)$$

where $\hat{a}^{\dagger}_{n\sigma}$ and $\hat{a}_{n\sigma}$ are the creation and annihilation operators for charged particles, $e_n=E_n-\mu$, E_n is the energy of an oscillating charged particle, μ is the chemical potential of the system, and

$$F_{nn'}=\frac{4K_0^2n_n^{(0)}m_i}{3\pi^2\hbar\omega_i m_n}\left(\frac{m_i\omega_i}{\hbar}\right)^{3/2}\times\frac{\tilde{n}^{3/2}}{\sqrt{nn'}}\left(1+\frac{3\hbar\omega_i}{16m_ic_s^2\tilde{n}}\right)^{3/2}. \quad (6)$$

Here $n_n^{(0)}$ is the unperturbed number density of neutral atoms, m_n is the mass of a neutral atom, c_s is the sound velocity, and $\tilde{n}=\min(n,n')$.

As was shown in Ref. [3], the Hamiltonian in Eqs. (5) and (6) describes the effective attraction between charged particles in plasma, which, in its turn, results in the formation of bound states of oscillating particles. Using Eq. (6) one can obtain the typical radius of a plasmoid, where this pairing takes place,

$$R_{cr}=\frac{4\hbar n_n^{(0)}\sigma_s}{3\pi m_n\omega_i}, \quad (7)$$

where σ_s is the total cross section of scattering of ions off neutral atoms. If we suppose that a spherical plasma structure is based on the oscillations of protons in the matter neutron with the density $n_n^{(0)}=10^{38}cm^{-3}$, which corresponds to a matter in a compact star, we get from Eq. (7) that the radius of a plasmoid should be $R_{cr}=4.47\times10^{-10}cm$.

Note that to get the above estimate we supposed that only ions (protons) rather than electrons form pairs. It is because of the fact that the Langmuir frequency of ions is much smaller than that for electrons. Moreover, the cross section of proton scattering off neutral atoms (neutrons) is much larger than that for electrons.

Despite the matter density and the plasmoid radius derived are beyond the values, which can be expected in terrestrial conditions, in Ref. [3], we put forward the assumption that, under certain conditions, the pairing of charged particles, owing to the exchange of a virtual acoustic wave, can be implemented in a spherically symmetric atmospheric plasma structure.

4. Composite plasma structures

In this section we describe the formation of a composite plasma structure in frames of our model. This result is published in Ref. [4].

Let us discuss the possibility of the formation of a composite plasma object consisting of separate kernels, each of them being a spherically symmetric plasma oscillation. The cohesion between plasmoids is due to the quantum exchange interaction between ions, which can be present inside the nano-sized plasma structure. Note that the importance of the exchange interaction for the description of the stability of a spherically symmetric plasma structures was previously considered in Ref. [9].

We assume that ions are $1/2$ -spin particles. The Hamiltonian corresponding to the exchange interaction between such ions has the form,

$$H_{eX} = -\sum_{i \neq j} J_{ij} \left(\hat{S}_i \cdot \hat{S}_j \right), \qquad (8)$$

Where J_{ij} is the exchange integral and $\hat{S}_i$ is the spin operator of an ion. The sum in Eq. (8) is taken over the pairs of ions belonging to different plasmoids.

Using Eq. (8) we can get the total exchange energy of the interaction between two oscillating plasma structures, V_{eX} . It is convenient to normalize it to the energy of electromagnetic field of a plasmoid, V_{eX} . The final expression reads

$$\frac{V_{eX}}{W_{em}} = -6.0 \times 10^{-3} \times J_0 \sigma^3 \cos \Delta\varphi \left(\frac{p_0 n_0}{T} \right)^2 F(a,b),$$

$$F(a,b) = b \exp\left(-\frac{a^2}{4} \right)$$

$$\times \left\{ \frac{1+4b^2}{a} \left[erfcx\left(2b - \frac{a}{2} \right) - erfcx\left(2b + \frac{a}{2} \right) \right] \right.$$

$$\left. - b \left[erfcx\left(2b - \frac{a}{2} \right) - erfcx\left(2b + \frac{a}{2} \right) \right] \right\} . \qquad (9)$$

where J_0 is a positive constant characterizing the magnitude of the exchange interaction, σ is the effective plasmoid radius, $\Delta\varphi$ is the phase difference in oscillations of two plasmoids, p_0 is the electric dipole moment of an ion, n_0 is the ion density, T is the ion temperature, $erfcx(z)$ is the scaled complementary error function, $a = R/\sigma$, $b = \kappa\sigma$, R is the distance between plasmoids centers, $\kappa = \sqrt{2ME_i}/\hbar$, M is the ion mass, and E_i is the mean ion energy in a plasmoid.

For a numerical estimate we consider a couple of plasmoids excited in dense water plasma with $n_0 \sim 10^{23} cm^{-3}$ and $T \sim 300\text{K}$. Using Eq. (9), one gets that the quantum exchange interaction between plasmoids can be attractive for a nano-sized plasma structure with $\sigma \sim 10^{-7} cm$. In some cases the ratio in Eq. (9) can reach several percent. The radius of a plasmoid found here is in agreement with the results of Sec. 2. Thus we have demonstrated that nano-sized plasmoids, described in frames of our model, can form a composite object owing to the quantum exchange interaction between ions.

5. Application

We put forward a hypothesis that quantum nonlinear oscillations of plasma can be a theoretical model of stable spherically symmetric natural plasma objects [10]. These glowing objects appear mainly during a thunderstorm and have the lifetime up to several minutes. There are numerous models of this natural phenomenon summarized in Ref. [10]. However, none of these theoretical approaches can convincingly reproduce the observed properties of the plasmoids. Thus, the existence of these objects is still a riddle for modern physics.

These natural plasma structures are likely to be of electromagnetic origin. However, as argued in Ref. [6], one faces formidable difficulties while applying classical electrodynamics for the description of this kind of plasma objects.

In a series of our works [1-4] we developed a quantum approach for the description of stable spherically plasma structures. The effect of the formation of bound states of charged particles inside a plasmoid as well as the possibility of the creation of a composite plasma structure are described in these works. We also predicted some of the observed properties of natural plasma objects in frames of our model.

The implications of our theoretical results for the analysis of the experiments, in which luminous plasma structures were generated in electric discharges in water (see, e.g. Ref. [11]), are studied in Refs. [1-4]. We also discussed the application of our model for the description of nano-sized plasmoids recently generated in a laboratory [12].

It is interesting to mention that the observation of an atmospheric plasmoid was recently analyzed in Ref. [13]. It was reported that a plasmoid, having the core with a sub-millimeter size, melted the window glass. This observation is in agreement with the predictions of our model. Moreover, a high temperature of the plasmoid core, necessary to melt glass, is the indication that this object can be powered by an energy source different from that based on chemical reactions.

The models of the natural plasma structures powered by microdose nuclear reactions were proposed in Ref. [14]. Besides the case mentioned in Ref. [13], these models can explain some observations of very high energy atmospheric plasma structures described in Ref. [15]. In this situation, such atmospheric plasmoids could become an alternative energy source, provided there will be a successful implementation of these phenomena in a laboratory.

Acknowledgements One of the authors (M.D.) is thankful to the organizers of the "Modern Trends in Physics" for the invitation and a financial support, as well as to the Tomsk State University Competitiveness Improvement Program and RFBR (research project No. 15-02-00293).

References

[1] M. Dvornikov and S. Dvornikov, in 'Advances in Plasma Physics Research, Vol. 5, ed. by F. Gerard (New York, Nova Science Publishers,) , pp. 197 – 212 (2006).

[2] M. Dvornikov, Proc. R. Soc. A **468**, 415(2012).

[3] M. Dvornikov, J. Plasma Phys. **81**, 905810327(2015); J. Phys. A: Math. Theor. **46**, 045501(2013).

[4] M. Dvornikov, J. Atm. Sol.-Terr. Phys. **89**, 62(2012).

[5] L. S. Kuz'menkov and S. G. Maksimov, Theor. Math. Phys. **118**, 227(1999); G. Manfredi and F. Haas, Phys. Rev. B **64**, 075316(2001).

[6] A. A. Vlasov and M. A. Yakovlev, Theor. Math. Phys. **34**, 124(1978).
[7] T. Neugebauer, Z. Phys.**58**, 474(1937); G. C. Dijkhuis, Nature **284**, 150(1980); B. A. Veklenko, Plasma Phys. Rep. **38**, 513(2012).
[8] P. K. Shukla, and A. A. Mamun, *Introduction to Dusty Plasma Physics* (Bristol, IOP Publishing, 2002).
[9] A. V. Kulakov and A. A. Rumyantsev, Dokl. Akad. Nauk SSSR **320** (1991) 1103.
[10] R. K. Doe, in *Forces of Nature and Cultural Responses*, ed. by K. Pfeifer and N. Pfeifer (Berlin, Springer, 2013), pp. 7 – 26.
[11] G. D. Shabanov, Tech. Phys. Lett. **28** (2002) 164; A. Versteeg, *et al.*, Plasma Sources Sci. Tech. **17** (2008) 024014.
[12] J. B. A. Mitchell, *et al.*, Phys. Rev. Lett. **100** (2008) 065001; T. Ito and M. A. Cappelli, AIP Advances **2** (2012) 012126.
[13] V. L. Bychkov, *et al.*, J. Atm. Sol.-Terr. Phys. **150** (2016) 69.
[14] M. D. Altschuler, *et al.*, Nature **228** (1970) 545; Yu. L. Ratis, Phys. Part. Nucl. Lett. **2** (2005) 374.
[15] V. L. Bychkov, *et al.*, in *The Atmosphere and Ionosphere: Dynamics, Processing and Monitoring*, ed. by V. L. Bychkov, *et al.* (Dordrecht, Springer, 2010), pp. 201 – 373.

maxdvo@izmiran.ru, m.gulnara@hotmail.com

Design of the radiation detector modules for security systems

M.S.NAZAROV[a*], F.I.AHMADOV[a,b], S.S.SULEYMANOV[a,b], N.N.HEYDAROV[a], R.V.VALIYEV[A], I.I.ABBASOV[c].

a- National Academy of Science of Azerbaijan -AD and IRP
b- National Nuclear Research Center
c-Azerbaijan State Oil and Industrial University

maqsudnazarov90@gmail.com

ABSTRACT

In this work presented the results of research of the newest silicon photodiodes manufactured by Zecotek company. The new photodiode has the following parameters sensitive area- 3.7mm 3.7 mm, density of pixels - 10000 pixels / mm^2, photon detection efficiency - 35-40% (at wavelength of 450-550 nm) and operation voltage -91V. The gamma ray detector modules demonstrated a perfect linear behavior of detected signal amplitudes as a function of the gamma ray energy (from 26.3 keV up to 1.33 MeV). Energy resolution for 662 keV gamma rays was 11.2% and the minimum detectable energy was 26.3 keV.

Keywords
Micropixel Avalanche Photodiode, inverter, converter, amplifier, gamma rays

1. Introduction

The micropixel avalanche photodiodes (MAPDs) are produced by different Companies during the last ten years. A new type of MAPD with deeply buried pixels developed by Zecotek Photonics. This type of photodiodes allowed to improve their main parameters such as photon detection efficiency (PDE), pixels density and radiation hardness [1–5].

2. Experiment

The new detector module includes the following electronic parts: DC-DC converter, voltage inverter, amplifier and MAPD-3NK+scintillator. DC-DC converter is designed on the basis of MC34063 monolithic switching regulator subsystem (figure 1).This type of DC-DC converter allowed to convert +5V to +91.3V. The output voltage accuracy of the DC-DC converter was 0:02V. Voltage inverter is designed on the basis of MAX1044 for LMH-6657 (figure 2).

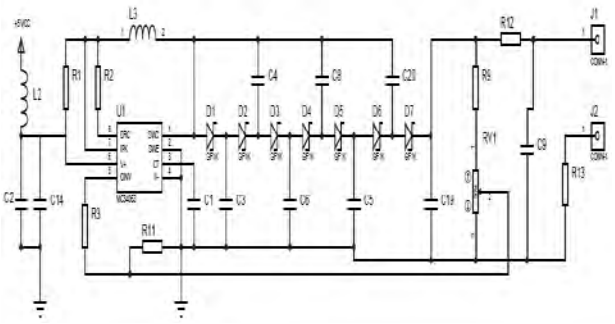

Figure 1. DC-DC converter circuit diagram.

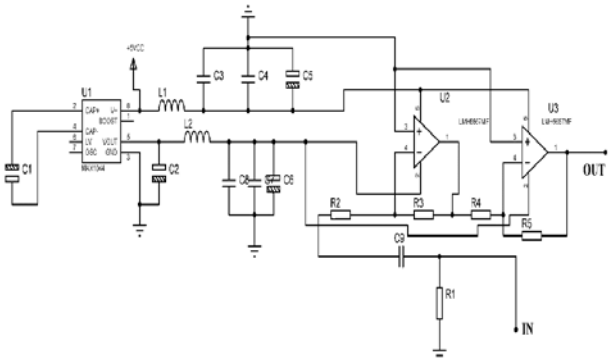

Figure 2. Voltage inverter and amplifier circuit diagram.

The amplifier consists of two operational amplifiers of LMH-6657 type, which are used to amplify the detector output signal. It is noticed that the unity-gain bandwidth of LMH-6657 is a 270 MHz. There are used two stages of amplification to keep the bandwidths of the amplifiers as high as possible, due to inverse proportionality between gain and bandwidth of operational amplifiers. The obtained gain of the amplifier is 36 at the bandwidth about 45 MHs. The maximum amplitude of the output signal is 4.5V.

The MAPD-3NK photodiode contains a silicon substrate of n-type conductivity on which two silicon epitaxial layers of p-type conductivity were grown. The device also contains a dense matrix of independent n^+ - type pixels buried between the epitaxial layers mentioned above. The diameter of n^+ - type pixels and spacing between them were 7 μm and 3 μm, respectively. This design of the device provides super-wide linearity range of photo response due to high pixel density within the sensitive area. The MAPD-3NK consists of 1.37*105 pixels in 3.7*3.7mm2 a sensitive area. The MAPD-3NK photodiode characterizes by the following working parameters: operating voltage - 91.3V, gain - 1*105, device capacitance- 160 pF, PDE at 450–550 nm light wavelengths- 35–40%.

Gamma ray detection performance of "MAPD-3NK+NaI" detector module is investigated using a calibration point gamma sources in this work. The pulse-height spectra of 22Na (511keV and 1.27 MeV) is presented in figure 3. Obtained energy resolution for 511 keV gamma rays is worth in comparison with "MAPD-

3N1P+LFS" and equals to ~23%. It was obtained that amplitudes of detected signals were linearly proportional to the energy of gamma rays (511 keV and 1.27MeV).

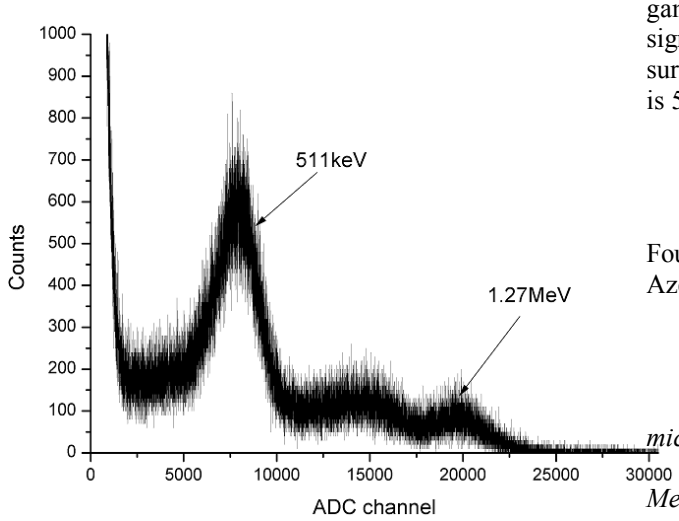

Figure 3. Pulse-height spectrum of gamma rays from 22Na gamma ray sources is measured with NaI scintillator coupled to MAPD-3NK.

Significant mismatch of the scintillator size and MAPD-3NK a sensitive area did not allow to detect the low energy gamma rays from 241Am source. The minimum detected energy of gamma rays was 59.6 keV and it's about tens of photoelectrons.

3. Results

As result the gamma ray detection performance of MAPD with large size NaI(Tl) detector module is investigated, too. Energy resolution of the 511 keV gamma ray is ~23% for this scintillation detector. Due to significant mismatch of the scintillator size and MAPD surface area the minimum detected energy of gamma rays is 59.6 keV and it was about tens photoelectrons.

Acknowledgments

This work was supported by the Science Development Foundation under the President of the Republic of Azerbaijan Grant No.**EIF-KETPL-2-2015-1(25)-56/04/1**.

Reference

[1] Z. Sadygov et al., *Three advanced designs of micro-pixel avalanche photodiodes: their present status, maximum possibilities and limitations*, *Nucl. Instrum. Meth.* **A 567** (2006) 70.

[2] Z.Ya. Sadygov, Russian Patent #2316848, priority from 01.06.2006.

[3] Z. Sadygov and A. Sadigov, Russian patent #2528107, published 10 September 2014.

[4] Z. Sadygov et al., *Development of scintillation detectors based on micro-pixels avalanche photodiodes*, PoS(PhotoDet 2012)037.

[5] D. Renker and E. Lorenz, *Advances in solid state photon detectors*, 2009 *JINST* **4** P04004.

Search for the Associated Production of a Higgs Boson and a Top Quark Pair in Multilepton Final States with the Atlas Detector

N.A. HUSEYNOV
Joint Institute of Nuclear Research, Dubna, 141980, Russia and *Azerbaijan National Academy of Sciences, Institute of Physics, 33 H. Javid str., Baku, Azerbaijan 1143*

The Yukawa coupling of the Higgs boson to the top quark is a key parameter of the Standard Model, and can be constrained using the associated production process $pp \to ttH+X$. A search for this process using final states with multiple leptons, primarily targeting the decays $H \to WW^*$ and $H \to \tau\tau$, has been performed using 13.2 fb^{-1} of data recorded by the ATLAS detector in 2015 and 2016 at a center of mass energy $\sqrt{s}$ = 13TeV. The best-fit value of the ratio of observed and Standard Model cross sections is $2.5 \pm 0.7(stat)^{+1.1}_{-0.9}(syst)$, and an upper limit on this ratio of 4.9 (2.3 expected) is found at 95% confidence level.

Keywords: *the Standard Model, the Higgs mechanism*

The Yukawa coupling of the Higgs boson to the top quark is a key parameter of the Standard Model(SM). It can be determined from the ratio of the top quark mass and Higgs field vacuum expectation value, from the cross section of $gg \to H$ production through a top quark loop, or from the cross section of the process $gg/qq \to ttH$, which is a tree-level process at lowest order in perturbation theory. Comparison of these measurements has the potential to identify and disambiguate new physics effects that can modify the ttH production cross section relative to the SM expectation.

The ATLAS and CMS collaborations have searched for production of *ttH* in pp collisions at the Large Hadron Collider (LHC) using data collected during LHC Run 1 at a centre of mass energy $\sqrt{s}$ of 7 and 8TeV, with analyses sensitive to $H \to WW^*$, $\tau\tau$, bb, and $\gamma\gamma$ decays. The combination of ATLAS and CMS Run 1 results yields a best fit of the ratio of observed and SM cross sections, $\mu_{ttH}=\sigma/\sigma_{SM}$, of The excess over the SM expectation $\mu_{ttH}=1$ is driven primarily by multileptonic final states sensitive to $H \to WW^*$ and $\tau\tau$. Improvement on this measurement requires the addition of more data. The cross section for *ttH* production in the SM rises by a factor of 3.9 as the centre of mass energy is changed from 8 to 13 TeV. The first ATLAS *ttH* multilepton search results at $\sqrt{s}$ =13TeV were released for the ICHEP 2016 conference, using 13.2fb^{-1} of data collected with the ATLAS detector during 2015 and 2016. The best-fit result of the ratio μ_{ttH} of the *ttH* production rate to the Standard Model expectation was found to be which is consistent with the Standard Model expectation. This note reports the results of a search for *ttH* production using 36.5fb^{-1} of data collected with the ATLAS detector at $\sqrt{s}$=13TeV during 2015 and 2016. The search uses eight final states distinguished by the number and flavour of leptons: two same-charge light leptons (e or μ) and no hadronically-decaying τ lepton candidates (*2lSS*); two same-charge light leptons and one hadronically-decaying τ lepton candidate (*2lSS*+1τ_{had}); three light leptons (*3l*); four light leptons (*4l*); two opposite-charge light leptons and one hadronically-decaying τ lepton candidate (*2lOS*+1τ_{had}); three light leptons and one hadronically-decaying τ lepton candidate (3l+1τ_{had}); one light lepton and two hadronically-decaying τ lepton candidates (1l+2τ_{had}). These signatures are primarily sensitive to $H \to WW^*$ (with subsequent decay to *lvlv* or *lvjj*) and H→ττ decays, and are effective in suppressing *tt* backgrounds. Back-grounds are estimated with a combination of simulation and data-driven techniques, and a global fit in all final states is used to extract the best estimate for the *ttH* production rate.

The expected backgrounds, *ttH* signal, and observed data yields in each category are in Table 1. The best-fit value of the *ttH* signal strength μ_{ttH} is obtained using a maximum likelihood fit to the data yields of the six categories, which are treated as distinct Poisson terms in the likelihood function. The fit uses the profile-likelihood approach, in which systematic uncertainties are implemented as nuisance parameters with prior uncertainties which the fit is allowed to further constrain. In practice the changes in the central values and uncertainties of the nuisance parameters after the fit are small. The likelihood function is also used to obtain 95% confidence level (CL) upper limits on μ_{ttH} using the Cls method, where the test statistic (the profile likelihood ratio) is computed against the $\mu_{ttH}=0$ hypothesis. For the 4 channel the limits are obtained with the use of pseudo-Monte Carlo events, while for other channels and the combination the limits are obtained using asymptotic approximations for the CLs value. Production of *ttH* is assumed to be SM-like in kinematic distributions. Single top-Higgs boson associated production is fixed to the SM rate.

The best-fit value of μ_{ttH}, combining all channels, is $2.5 \pm 0.7(stat)^{+1.1}_{-0.9}(syst)$. The best-fit value of and 95% CL upper limit on μ_{ttH} for each individual channel and the combination of all channels are shown in Figures 1 and 2 and Table 2. For the 4 channel, the

observation of zero events makes it difficult to quote a best-fit result with meaningful uncertainties, and a 68% confidence level CLs upper limit is shown instead. In the presence of the SM *ttH* signal, the fit is expected to return

$\mu_{ttH}=$ The p-value associated with the no-*ttH* hypothesis is 0.015 (2.2σ), and the *p*-value associated with the SM expectation $\mu_{ttH}=1$ is 0.09 (1.3σ).

1. Conclusions

A search for *ttH* production in multilepton final states has been performed using 13.2 fb of proton-proton collision data at $\sqrt{s}$ = 13 TeV recorded by the ATLAS experiment at the LHC. The best-fit result of the ratio μ_{ttH} of the *ttH* production rate to the Standard Model expectation is $2.5 \pm 0.7(stat)^{+1.1}_{-0.9}(syst)$ which is consistent with the Standard Model expectation. At 95% confidence level, μ_{ttH} is found to be less than 4.9 (2.3 expected).

References

[1] ATLAS Collaboration, Search for the associated production of the Higgs boson with a top quark pair in multilepton final states with the ATLAS detector, Phys. Lett. B 749 (2015) 519.

[2] ATLAS Collaboration, Search for the Standard Model Higgs boson produced in association with top quarks and decaying into bb in pp collisions at $\sqrt{s}$ = 8 TeV with the ATLAS detector, Eur. Phys. J. C 75 (2015) 349.

[3] ATLAS Collaboration, Search for $H\rightarrow\gamma\gamma$ produced in association with top quarks and constraints on the Yukawa coupling between the top quark and the Higgs boson using data taken at 7 TeV and 8 TeV with the ATLAS detector, Phys. Lett. B 740 (2015) 222.

[4] W. Beenakker et al., Higgs radiation off top quarks at the Tevatron and the LHC, Phys. Rev. Lett. 87 (2001) 201805.

[5] W. Beenakker et al., NLO QCD corrections to *t anti-t H* production in hadron collisions, Nucl. Phys.B 653 (2003) 151.

[6] S. Dawson et al., Associated top quark Higgs boson production at the LHC, Phys. Rev. D 67 (2003) 071503.

[7] S. Dawson et al., Associated Higgs production with top quarks at the large hadron collider: NLOQCD corrections, Phys. Rev. D 68 (2003) 034022.

[8] Y. Zhang et al., QCD NLO and EW NLO corrections to *ttH* production with top quark decays at hadron collider, Phys. Lett. B 738 (2014) 1.

[9] S. Frixione et al., Weak corrections to Higgs hadroproduction in association with a top-quark pair, JHEP 09 (2014) 065.

nazim.huseynov@cern.ch
nguseynov@jinr.ru

Table 1: Expected and observed yields in the six signal region categories in 13.2fb^{-1} of data at $\sqrt{s}$=13 TeV. Uncertainties in the background expectations due to systematic effects and MC statistics are shown. "Other" backgrounds include tZ, tWZ, tHqb, tHW, tttt, ttWW, and triboson production. Values are obtained pre-fit, i.e., using the initial values of background systematic uncertainty nuisance parameters.

	$2\ell 0\tau_{had}$ ee	$2\ell 0\tau_{had}$ $e\mu$	$2\ell 0\tau_{had}$ $\mu\mu$	$2\ell 1\tau_{had}$	3ℓ	4ℓ
$t\bar{t}W$	2.9 ± 0.7	9.1 ± 2.5	6.6 ± 1.6	0.8 ± 0.4	6.1 ± 1.3	—
$t\bar{t}(Z/\gamma^*)$	1.55 ± 0.29	4.3 ± 0.9	2.6 ± 0.6	1.6 ± 0.4	11.5 ± 2.0	1.12 ± 0.20
Diboson	0.38 ± 0.25	2.5 ± 1.4	0.8 ± 0.5	0.20 ± 0.15	1.8 ± 1.0	0.04 ± 0.04
Non-prompt leptons	12 ± 6	12 ± 5	8.7 ± 3.4	1.3 ± 1.2	20 ± 6	0.18 ± 0.10
Charge misreconstruction	6.9 ± 1.3	7.1 ± 1.7	—	0.24 ± 0.03	—	—
Other	0.81 ± 0.22	2.2 ± 0.6	1.4 ± 0.4	0.63 ± 0.15	3.3 ± 0.8	0.12 ± 0.05
Total background	25 ± 6	38 ± 6	20 ± 4	4.8 ± 1.4	43 ± 7	1.46 ± 0.25
$t\bar{t}H$ (SM)	2.0 ± 0.5	4.8 ± 1.0	2.9 ± 0.6	1.43 ± 0.31	6.2 ± 1.1	0.59 ± 0.10
Data	26	59	31	14	40	0

Table 2: Best-fit values of the signal strength μ_{ttH} and 95% CL upper limits obtained using the CLs method. For the best-fit values, the first uncertainty is statistical and the second systematic. For the expected upper limits, the median is reported, and the uncertainties give the 68% expected range. The signal-injected upper limit is the median expected upper limit that is set by this procedure, testing against the μ_{ttH}=0 hypothesis, in the presence of a SM ttH signal. For the 4 category, as zero events are observed, a 68% CLs upper limit is shown in place of the best-fit value.

Category	Best fit μ_{ttH}	Observed (expected) 95% CL upper limit	Signal-injected 95% CL upper limit
$2\ell 0\tau_{had}$	$4.0^{+1.2}_{-1.1}{}^{+1.7}_{-1.3}$	$7.8\ (3.5^{+1.7}_{-1.0})$	4.2
$2\ell 1\tau_{had}$	$6.2^{+2.8}_{-2.3}{}^{+2.3}_{-1.4}$	$12.9\ (5.9^{+2.9}_{-1.6})$	6.3
3ℓ	$0.5^{+1.2}_{-1.0}{}^{+1.2}_{-1.3}$	$3.9\ (3.5^{+1.5}_{-1.0})$	4.3
4ℓ	< 2.2 (68% CL)	$5.2\ (6.6^{+2.9}_{-1.4})$	7.4
Combined	$2.5^{+0.7}_{-0.7}{}^{+1.1}_{-0.9}$	$4.9\ (2.3^{+1.1}_{-0.6})$	3.1

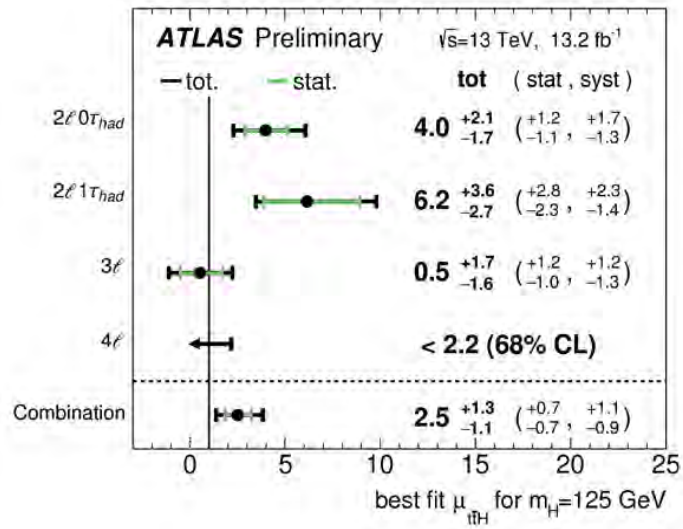

Figure 1. Best fit values of the ttH signal strength μ_{ttH} by final state category and combined. The SM prediction is μ_{ttH}=1. For the 4 category, as zero events are observed, a 68% CL s upper limit is shown instead.

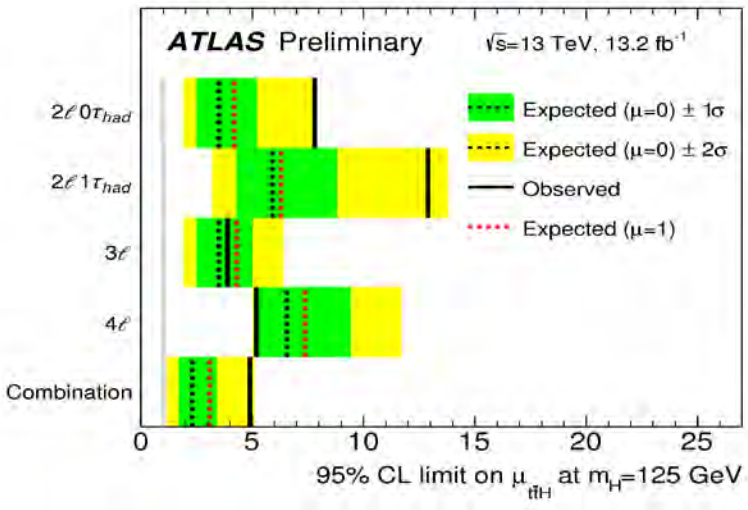

Figure 2. Upper limits on the *ttH* signal strength μ_{ttH} at 95% CL by final state category and combined. The SM prediction is $\mu_{ttH}=1$. The median upper limit that would be set in the presence of a SM *ttH* signal ($\mu = 1$) is also shown.

Features of Electrical Conductivity of Composites Based on Polyvinyl Alcohol and Copper Sulfide Nanoparticles

O.O.BALAYEVA, N.F.DADASHOVA, M.B.MURADOV, G.M.EYVAZOVA, E.H.GULIYEV
Nano Research Laboratory, Baku State University, Z. Khalilov 23, Baku, AZ 1148, Azerbaijan

The nanocomposites on the base of copper sulfide nanoparticles and polyvinyl alcohol (PVA) were obtained from electrolyte solutions of ethylene glycol by using successive ion layer adsorption and reaction (SILAR) technique. Analysis of diffraction patterns shows that the samples are CuS. From X-ray diffraction pattern, the average size of particles for 15 growth cycles was estimated - 4.6 nm. The average size of particles determinate from Transmission Electron Microscopy is 5.3 nm. With increase in the quantity of cycles because of electrostatic interactions on the near-surface region of substrate and electrolyte solution the concentration of nanoparticles on volume of polymeric matrix redistributed. Surface area enriched by nanoparticles of semiconductor. The resistance of the surface layer due to the large contribution of the semiconductor part of composite decreasing by quantity of growth cycles. Volume resistivity of samples decreasing by increasing quantity of growth cycles. This process is connected with changing of distribution of concentration of semiconductor nanoparticles on thickness on growth process. This leads to a significant difference in surface and in volume of resistivity of the sample PVA- semiconductor (CuS) nanocomposites.
Keywords: nanocomposites, copper sulfide nanoparticles, volume resistivity, surface resistivity

1. Introduction

For application in optoelectronics and electronics there is a huge scientific and technical interest of polymeric nanocomposite materials, in which dielectric polymer matrix contains nanoparticles of metal, oxides of metals and semiconductors [1-8]. It is well known fact that, sensory properties of nanomaterials substantially are determined by the change in resistance depending on exposure factors (ambient factors)[9,10] and thereupon investigation of electrical properties of nanocomposites has a particular interest [11-15]. In these materials interfacial interaction of nanoparticle - polymer matrix is large enough and interfacial electron-ion processes define conductivity of polymer nanocomposites [11].

The purpose of this paper is obtaining of nanocomposites on base of PVA and copper sulfide nanoparticles and comparative analysis of changes in the specific surface and bulk resistances depending on temperature for composites from polyvinyl alcohols (PVA) with various concentrations of copper sulfide (CuS) nanoparticles.

2. Experimental

CuS chalcogenide semiconductor nanoparticles are formed by the method described in the previous papers [16 - 18]. In order to generate PVA - CuS nanocomposites, ethylene glycol solutions $CuSO_4 \cdot 5H_2O$ and $Na_2S \cdot 9H_2O$ with 0,2 M concentration have been used. Firstly, during the formation process, we produced sorption of metal ions (Cu^{2+}) and after intermediate washing in ethylene glycol solvents, the sorption of sulfur ions (S^{2-}) has been conducted. By this process one cycle of the formation nanoparticles has been completed. To increase the size and concentration of nanoparticles we increased the number of formation cycles. Transmission Electron Microscopy (TEM) images were taken on a FEI TECNAI G220 X–TWIN at 200 kV. TEM specimens were prepared by dripping the droplets of sample solutions onto carbon coated copper grids. Powder XRD patterns were recorded on a RigakuMiniFlex Desktop X–ray diffractometer using CuKα radiation (1.5418 Å).

In order to measure the surface resistance on the one surface of the films we applied two parallel conductive strips with a silver paste.To measure the volume resistivity of the pressure applied electrodes. The temperature of samples was changed with constant velocity –2 ° C / min.

3. Results and discussion

The structure of the received samples was investigated by X-ray diffractometer Rigaku MiniFlex Desktop X–ray diffractometer. Figure 1 shows the diffraction pattern obtained from the samples of 15 growth cycles. Analysis of diffraction patterns shows that the samples are CuS with hexagonal structure. From X-ray diffraction pattern, the average size of particles was calculated based on Debye-Scherrer formula:

$$L = 0{,}9\lambda/\beta CoS\theta$$

Where β - half-width of the diffraction line intensity, measured in radians, λ=1,5406A^0 – is the wavelength, θ – is the angle of diffraction. The calculation shows that the average size of the nanoparticles is about 4,6 nm. The received samples also were investigated with a transmission electron microscope FEI TECNAI G220 X–TWIN. The results of electron microscopy shown in Figure 2(a,b). As can be seen from the figure the average size of particles is 5.3 nm, which agrees with the results of X-ray diffractometer. We should also mention that particles with the size of about 5,3 nm make up the bulk. As can be seen from the figure, in addition to these units there are in the composite particles also particles with smaller sizes. This feature is associated with the specific growth mechanism of the nanoparticles. The main absorption centers in the system are filled in the first half-cycle and in the further number increase of cycles increase occurs primarily at these sites. At the same time,

with further increase in the number of cycles, the formation of new growth centers

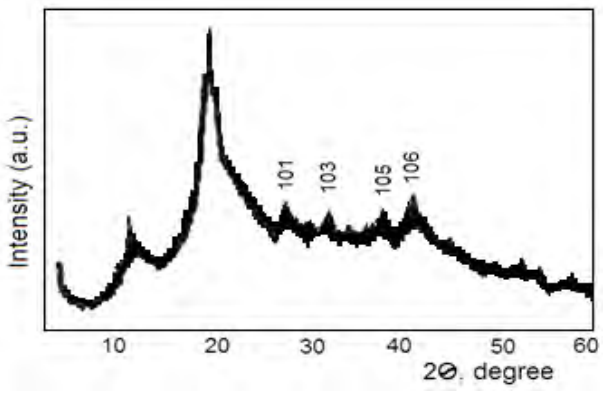

Fig. 1. The diffraction pattern from the samples CuS/ PVA with 15 growth cycles.

takes place. As a result of this, new particles are forming. It should be noted that on the particle size distribution will also affect coalescence processes which occur in the system. This process is mainly determined by the temperature of environment of the medium and the concentration of the solutions. Because of the fact that the average distance between the particles are determined by the concentration of the solution, increasing the concentration of the solutions must lead to an increase in the probability of coalescence processes occurrence in such systems.

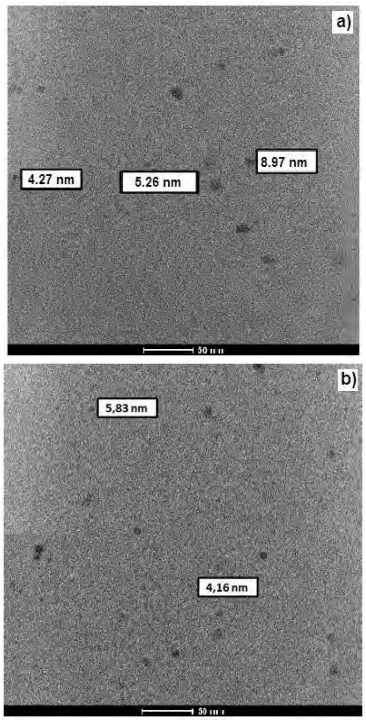

Fig. 2. Microphotography the surface samples of CuS/ PVA with 15 growth cycles.

To measure the volume resistivity and surface resistivity used samples with 1 and 5 growth cycles. This choice is based on the fact that the nanoparticles obtained from electrolyte solution by SILAR in the volume PVA polymer matrix are mainly formed in the initial cycle of growth. After 2-3 growth cycles, changes in the inorganic portion of the composite are not essential [16]. The figure 3.a. shows dependence of the volume resistivity for samples PVA / CuS with one (curve 1) and five cycles of forming (curve 2) of nanoparticles. It is clear, that, the behavior of both samples is identical. The difference observed in the resistance values, the sample with the high-cycle formation has a relatively high resistance. We measured in the same samples the temperature dependence of the surface resistivity (Fig.3b). Here, in contrast to the relative volume of resistivity is certain regularity observed, the sample with one cycle forming (curve 1) has a relatively higher resistance than the sample with five forming cycles (curve 2).

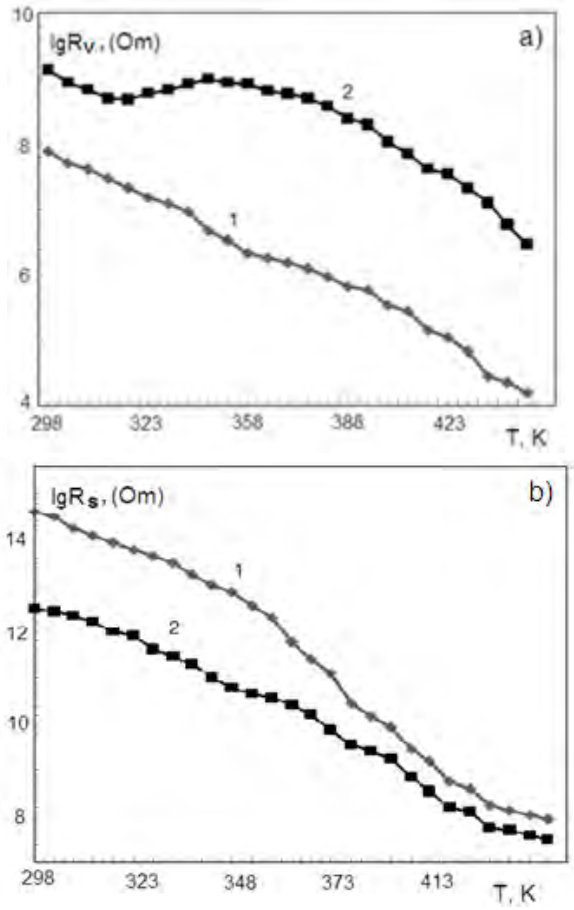

Fig. 3. The dependence of relative the volume resistivity (a) and surface resistivity (b) on temperature for samples PVA /CuS: 1- one growth cycle; 2 – five growth cycles

It is known that diffusion processes play an important role for the formation of nanoparticles. The diffusion of the metal ions in the depth of film does not depend on the thickness of the sample. The increase of cycles of formation must lead to an increase in the size and concentration of nanoparticles in compositions. It is known that the rate of diffusion is defined as the diffusion coefficient and as the gradient of concentration in the

solution and a film [17]. At the beginning of process the flow rate of diffusion of ions S^{2-} has a maximum value across the boundary of polymer-solution. Rate of S^{2-} ions decrease as ions approaching to the depth of the sample due to the formation of nanoparticles. In this region, the velocity of the ions $Cu^{2+}$is almost unchanged, remains constant. This phenomena is due to the fact that the process of formation of nanoparticles occurs in the diffusion area and after some time the speed of Cu^{2+} and S^{2-} becomes the same. Weakly bound to the polymer matrix (PVA) metal ions are more mobile and as a result, as shown by experiments with increasing cycles of formation the dispersed phase is redistributed unevenly and is formed closer to the surface (Kirkendall effect) [18], in other words forming enriched near-surface layer with a high concentration of nanoparticles [16]. The forgoing is confirmed by experiments, the sample with five growth cycles have a higher volume resistivity and relatively low sheet resistance resulting from the displacement of the concentrated rich layer to the surface.

4. Conclusion

Thus, it can be stated that feature of conductivity of nanocomposites based on copper sulfide, which were obtained by the mechanism of SILAR, is determined by the mechanism of tunneling at low values of the cycles of formation. With further increase in the quantity of cycles because of electrostatic interactions on the near-surface region a layer , the layer is formed ,which enriched by nanoparticles of semiconductor. The resistance of the subsurface layer due to the large contribution of the semiconductor part of composite decreases. This leads to a significant difference in surface and in volume of resistivity of the sample PVA- semiconductor (CuS).

References

[1] A. D. Pomogaylo, Ros, J. Ximicheskiy, **46** (5), 64-73 (2002).
[2] S. A. Zavyalov, E. I. Grigoryev, A. N. Pivkonas, J. Fizicheskoy Ximii, **80** (23), 560-563 (2006).
[3] F. Zuo, M. Angelopoulos, A. G. MacDiarmid, A.J. Epstain, Phys. Rev. B **36**, 3475 (1987).
[4] Q. Wu, Z. Xuc, Z. Qi, F. Wavg, Polymer, **41**, 2029 (2000).
[5] A.V. Volkov, M. A. Moskvina, A. L. Volinckiy, N. F. Bakeyev, Polymer Science, **40** (9), 1441-1450 (1998).
[6] V. V. Petrov, Sensor **1**, 48-50 **(**2003).
[7] A. H. Babkin, M. I. Fedorov. Sensor , **21**, 54-55 (2003).
[8] E. I. Grigoryev, P. S. Vorontsov, S. A. Zavyalov, S. N. Chvalun, Pis'ma v Zhurnal Tekhnicheskoi Fiziki, **28** (20), 215-218 (2000).
[9] B. Raquet, M. Goiran, N. Negre, Phys. Rev. B 62 (24), 17144 (2000).
[10] S. Bhattacharya, S. Malik, A. K. Nandi, A. Ghosh, J. Chem. Phys., **125**, 174717 (2006).
[11] R. Chandrakanthi, Thin Solid Films, **417** (1-2), 51-56 (2002).
[12] J. Y. Kim, I. J. Chunq, J. K. Kim, J. W. Yu, Current Applied Physics, **6** (5), 969-978 (2006).
[13] A. M. Kutepov, V. I. Maslov, I. S. Pervov, M. B. Muradov, Dokladi AN SSSR, Fizicheskaya Ximiya, **304** (1), 900-903 (1989).
[14] V.V. Klechkovskaya, V. I. Maslov, M. B. Muradov, Kristallografiya, **34** (1), 182-186 (1989).
[15] Y. A. Kalandaragh, M. B. Muradov, R. K. Mammedov, A. Khodayari, J. of Crystal Growth, **305** (1), 175-180 (2007).
[16] M. B. Muradov, K. A. Yusifova, G. M. Eyvazova, R. K.Mammadov, A. Z.Salahova, World J. of Condensed Matter Physics, **3** (1), 82-86 (2013).
[17] A. V. Volkov, M. A. Moskvina, I. V. Karachensev, O.V. Lebedeva, A. JI. Volinskiy, N. F. Bakeyev, Visokomolekulyarniye Soyedineniya, A **40** (6), 970-976 (1998).
[18] V. V. Klechkovskaya, V. N. Maslov, M. B. Muradov, Izvestiya AN SSSR, ser. Fizika, **52** (7), 1324-1326 (1988).

dadasova.nermine@rambler.ru

Polarization Effects in Neutron -Nucleus Collisions

R.A. AHMEDOV

Azerbaijan State University of Oil and Industry

Abstract: The high energy neutron -nucleus collisions in the crystals is discussed by means of the multiple - diffraction theory. The nucleon densities found are closely comparable in dimensions to the known charge densities. It is shown that passage of high energy neutron through a crystal gives rise to polarization. The analysis shows that when the preasymptotic corrections are absent, we have the zero polarisations. It is important to emphasise that the case of the nucleon-nuclei scattering the leading asymptotic terms of the spiral amplitudes is also determined by the contribution of the quark cluster with the evident replacement of by the pion-nucleon scattering amplitudes.

Key words: scattering, matrix element, cross section, polarization.

.

1. Introduction

An increasing number of experiments have been undertaken in recent years to study the scattering or production of high- energy particles in nuclei. The polarization phenomena take place when neutron pass through crystals. The interaction of the crystal with particles of sufficiently high energy moving in directions close to parallel to some family of axes is described by the potential of the axes which is averaged in the direction of these axes. The analysis shows that when the preasymptotic corrections are absent, we have the zero polarizations. The parameters in the spin-flip amplitude determined from one reaction, for example nucleon-nuclei scattering, allow us to obtain a wide circle of results for the polarization effects of elastic, nucleon-nuclei, *pp* or meson-nucleon scattering at high energies. If neutron interactions with nucleons of the crystal depend on the spin, the average cross-section of interaction with nucleons polarized target for hadrons, polarized parallel and antiparallel to the direction of polarization of the target will be different from each other. This means that the filtration of unpolarized beam through a polarized beam of the target will be relatively enriched hadrons with the polarization direction for which the interaction cross section of the smaller; there will be a polarization of the beam in this direction.

In the work [1] assumed that the hypothesis of self-similarity of proton structure, constituent interactions and hadronization process confirmed in unpolarized $p + p$ collisions over a wide kinematic range is extended for processes with polarized particles. The established properties of data z-presentation, like energy, angular and flavour independence from the scaling function give us basis to study the spin structure of proton in the framework of z-scaling theory.

2. The polarization parameter

The polarization of particles - a characteristic of the state of the particles associated with the presence of their own angular momentum - spin. microparticle system is called polarized if the spatial distribution of spin orientations of the particles in the system is non-isotropic.

A particle with a nonzero rest mass and spin J (in units of the Planck constant) has $2J + 1$ quantum states corresponding to different spin orientations. The state of a particle is a superposition of these states. If the superposition coefficients are completely determined (pure state), then the particle is said to be completely polarized. If the superposition coefficients are not completely determined, but are specified only by certain statistical characteristics (mixed state), then we speak of partial polarization. In particular, the particle can be completely unpolarized; This means that its properties are the same in all directions, as in a spinless (with $J = 0$) particle. In the general case, particle polarization determines the degree of their symmetry (or asymmetry) in space.

Let us analyze in conclusion the production of transversely polarized neutrons in a crystal. The application of the multiple diffraction theory to data on unstable particle production, for example, makes it possible to evaluate the unstable particle- nucleon cross section. But such applications of the theory require knowledge of the nucleon density distributions in nuclei, and present uncertainties regarding those distributions lead to large uncertain- tie s in the inferred cross sections. It would be of great helping to various areas of elementary particle physics, therefore, if these densities could be established more accurately.

To understand the effect of the passage of the neutron through the matter it is necessary to develop a theory with the help of wave mechanics, assuming a possible potential neutron interaction (neutron field) with other particles in accordance with the experimental results.

The Schrodinger equation for this system is:

$$\left[-\frac{\hbar^2}{2m_n}\Delta_p - \frac{\hbar^2}{2m_N}\Delta_N + V_{12}(r_{n,N})\right]\Psi(r_n r_N) = E\Psi(r_n, r_N) \qquad (1)$$

Let φ_N and E_N, respectively, the wave function and energy of the target particle. They satisfy the equation:

$$\left[-\frac{\hbar^2}{2m_N}\Delta_N + V_0(r_N)\right]\varphi_N = E_N\varphi_N . \qquad (2)$$

If (φ_i, k_i) initial and $(\varphi_f, k_f$ final state of the system, then

$$\frac{1}{2m_N}\hbar^2 k_i^2 + E_i = \frac{1}{2m_N}\hbar^2 k_f^2 + E_f = E . \qquad (3)$$

We seek a solution $\Psi(r_n r_N)$ containing the incident plane wave and the scattered wave. The impulse approximation exact wave function $\Psi(r_n r_N)$ is replaced by

$$\Psi(r_n, r_N) \to \frac{1}{(2\pi)^3}\iint dKdre^{-iKr}\varphi_i(r)\psi_{k_iK}(r_n r_N), \quad (4)$$

In the case of a spherically symmetric central field we have the following expression for the scattering matrix elements

$$f = \frac{1}{(2\pi)^6}\int e^{i(k_i - k_f + K)r_p} e^{-iKr}\psi_f^*(r_p)\psi_i(r_p)x, \quad (5)$$
$$(k_f K'|V|k_i K)drdKdK'$$

where

$$(k_f K'|V|k_i K) = (2\pi)^3\delta(k_f + K' - k_i - K)x \quad (6)$$
$$\int e^{\left[i(K - k_i)r/2\right]}V(r)\varphi_{k_i - K}(r)dr$$

Here k_f momenta of neutron and K' after scattering. This expression is valid in the entire range of scattering angles and can be seen as a generalization of the eikonal approximation for the scattering amplitude [2].

This polarization will on the average be parallel to the atomic planes and perpendicular to the quantum momentum. The mechanism that produces the polarization can be explained in the following manner.

The scattering amplitudes $f_{m_{si}, m_{sj}}$ are elements of the 2 x 2 matrix, which can be expressed in terms of the Pauli matrices σ and the unit matrix ***n***

$$f = g\mathrm{E} + (h\sigma). \quad (7)$$

In (7), the factor g corresponds to an interaction independent of spin, and the vector h to the interaction causing the spin reorientation.

If the y-axis is chosen along the direction of the vector **n** (ie. φ = 0), then the wave function of the scattered particle initially located in the spin state χ_S can be written in the form:

$$\begin{pmatrix} c \\ d \end{pmatrix} e^{ikr} + \begin{pmatrix} f^+(\theta) \\ f^-(\theta) \end{pmatrix}\frac{e^{ikr}}{r}, \quad (8)$$

where f+ and f- are the complex functions of the scattering angle θ,

$$f^+(\theta) = cg - idh, \qquad f^-(\theta) = cg + idh \quad (9)$$

In order to obtain the scattering amplitude of a particle in an arbitrary state of polarization

$$\begin{pmatrix} c \\ d \end{pmatrix} = c\alpha + d\beta, \quad (10)$$

it is sufficient to know the amplitudes for the states α and β. However, if we select the spin-quantizing axis along the direction of the primary beam, the amplitudes of these two states turn out to be connected because of the invariance with respect to reflection.

The amplitude of the diverging spherical wave formed as a result of the action of a unit–amplitude plane wave on the scattered is called the scattering amplitude. In scattering of scalar waves described, in particular, by the Schrödinger equation, the amplitude *f* is a scalar. Due to the spin dependence of the interaction, the scattering cross section can depend on the polarization of the incident particle and on the polarization of the target [3]. Using the definition of the differential scattering cross section we obtain that

$$\sigma(\theta,\phi) = \left|f^+(\theta)\right|^2 + \left|f^-(\theta)\right|^2 = |g(\theta)|^2 + |h(\theta)|^2 + 2\,\mathrm{Re}(g^*h), \quad (11)$$

or

$$\sigma(\theta,\varphi) = \{1 + P(\theta)\cos\phi\}I(\theta), \quad (12)$$

where

$$I(\theta) = |g(\theta)|^2 + |h(\theta)|^2, \quad (13)$$

and

$$P(\theta) = 2\frac{Re(g^*h)}{I(\theta)}. \quad (14)$$

The function is called the polarization function. Thus, the scattering cross section $\sigma(\theta,\phi)$ depends on the angle θ between the vectors **k** and **k′** and on the angle between the polarization vector **e** of the incident particle and the vector **n**. The polarization vector of particles scattered on nuclei with zero spin is always directed perpendicular to the scattering plane. It should be noted that the polarization parameter decreases with increasing energy at small momentum transfers, since with increasing energy the region of small momentum transfers increasingly corresponds to the collinear configuration of the scattered particles, and the polarization must zero.

Assume that the particle beam with the wave vector **k** is scattered by the nucleus *A* in the direction and the angle between the direction of the vector **k** and **k′** equal to θ_1. The scattered beam is polarized in the direction of $\mathbf{n}_1$, which is perpendicular to the plane **k** and **k′**. Broken particle falls on the second core *B* in and dispersed in the direction $\mathrm{k}''(\theta_2,\varphi_{1,2})$, where θ_2- the angle between the vectors **k′** and **k″**, and $\varphi_{1,2}$ - the angle between the vectors n1 and n2, and perpendicular to the planes, respectively. Because after scattering on the target *A* the average spin of the particles is equal $\langle\sigma\rangle_1 = P_1\mathrm{n}_1$, then the target of the incident polarized beam of particles with $\langle\sigma\rangle_1$ spin. Therefore, the double scattering cross section can be expressed as:

$$\sigma(\theta_1,\theta_2,\varphi_{12}) = \left(1 + P_2\mathbf{n}_2\langle\sigma\rangle_1\right)I_2(\theta_2)I_1(\theta_1) = \quad (15)$$
$$= \{1 + P_2(\theta_2)P_1(\theta_1)\cos\varphi_{12}\}I_1(\theta_1)I_2(\theta_2)$$

In the scattering of unpolarized neutrons on nuclei, polarization of elastically scattered neutrons arises. Since the scattering amplitude contains a term that depends on the orientation of the spin, and a term that does not depend on the spin orientation, the polarization is due to interference between these two scattering parts. Large values of the degree of polarization (the absolute value of the polarization vector is called the degree of polarization) are possible in the case when the interference value is comparable with the scattering cross section.

At high energies, only one experiment to measure the cross section at any angle makes it possible to determine all the characteristics of neutron scattering. For neutron scattering, two numbers are usually found: the phase shifts of the states $^1S_0$ and $^3S_1$. The measurement of the correlation coefficient of these states makes it possible to determine directly the weights of singlet and triplet scattering.

3. Conclusion

Experiments on the study of polarization effects are carried out in all accelerators. After the experimental discovery of a number of important spin effects, taking into account the spin degrees of freedom became a necessary part of the theoretical analysis. The spin dependence of forces between nucleons is the need for a large number of experiments to determine the interaction. If this dependence is absent, the scattering experiments could identify only a single value for each scattering angle and energy - the differential cross section.

Using different hypotheses about the property of the nucleon interaction at large distances a number of model approaches lead to the nondisappearing polarization in high -energy processes at small transfer moment.

Spin effects are important from the point of view of studying the structure of particles, in particular, the problem of the relationship between the spin of a particle and the spin of its components and the interaction mechanism of the components. A qualitative description of the polarization of hyperons is explained by the spin-orbit interaction in a scalar field that connects quarks within the hadron [4].

We assumed that one of the basic properties of spin as a quantum characteristic of particles is fractality.

In view of the finite length of the crystal and the smaller difference of the probability of emission with spin flip by particles having oppositely directed polarizations, it is impossible for the beam to acquire the high degree of polarization attainable in storage rings.

The requirement of a universal description of the hadron spectra in collisions at different energies gives restrictions on the values of spin-dependent parameters of the z-scaling and their dependences on proton polarization.

We assume that the considered scaling property for polarization processes rejects selfsimilarity of the spin structure of the colliding objects, interaction mechanism of their constituents, and process of fragmentation of the polarized constituents in the final state

The study of spin phenomena gives more rich information than the study of spin-averaged quantities, and the quantities measured in the corresponding experiments are more fundamental, which allows for a detailed analysis of various theoretical concepts and approaches.

References

[1] M.V.Tokarev, I.I.Zborovsky, A.A. Aparin. Письма в ЭЧАЯ, **12**, (1), 81(2015)
[2] F.G,Sitenko. PEPAN,, **4**, (2) 546, (1973)
[3] V.I.Alfimenko et al. PEPAN,, **11**, (2), 411, (1980)
[4] K.I. Kubo, K. Suzuki. Proceedings of the 10th Intern. Conf. Nucl. Reaction Mechanisms (Varenna), 559, (2003).

rasim.a15@mail.ru

Magnetic Nanoparticles in Plants

R.I. KHALILOV[1,2], A.N. NASIBOVA[2], I.Y. FRIDUNBAYOV[1], N.N. NABIYEV[2], U.M. QASUMOV[2]
[1]Baku State University, Baku, Azerbaijan;
[2]Azerbaijan National Academy of Sciences, Institute of Radiation Problems, Baku, Azerbaijan

The effect of different doses of radiation on the generation of magnetic nanoparticles in plants has been studied by method electron paramagnetic resonance (EPR). The objects of research were wheat seeds (Triticumvulgare) and peas (Pisum L.). Studies were conducted with control and irradiated in various doses of gamma radiation in plants. The results of EPR experiments showed that in these plants, compared to the control plants, when the low radiation doses (100, 200 Gy) are influence, the signal amplitude, which characterizes the magnetic nanoparticles of iron oxides, increases significantly. When the dose of radiation increased to 300 Gy, a significant decrease in the amplitude of the wide EPR signal was observed. It is assumed that the process of photosynthesis plays a certain role in the formation of magnetic nanoparticles in plants.

Key words: magnetic nanoparticles, irradiation, gamma radiation, wide EPR signal.

In the last three decades, nanotechnology as one of the world's top research areas has been developing very intensively. Therefore, studies devoted to the study of nanomaterials, nanoobjects, nanoparticles are attracting increasing attention. Widespread in nature and used in various studies - magnetic nanoparticles of iron oxides (magnetite Fe3O4 and maghemite γ-Fe2O3). Metal nanoparticles based on iron are a promising material for use as information carriers, drug delivery systems, etc. [1]. They occur in many biological objects and are widely used in biomedicine. At present, there is a growing need to obtain non-toxic magnetically controlled drugs for use in medicine. In a word, magnetic nanoparticles are very important and necessary for modern medicine.

Materials and Methods. The objects of our research were wheat seeds (Triticumvulgare) and peas (Pisum L.). Artificial gamma irradiation of the samples was carried out on the K-25 equipment (power 33.31 rad / sec). The sources of irradiation were the isotopes Co60 and Co57. Seeds of wheat were irradiated in doses of 100, 200 and 300 Gy, and pea seeds in doses of 30, 60 and 100 Gy. Irradiated and control seeds were germinated at room temperature in Petri dishesfor 10 days.

Further, the grown seedlings were dried at room temperature and ground to a powder. EPR studies were carried out with prepared samples of plants.

EPR spectra of plant objects were recorded at room temperature (297 K) on an ECS-106 EPR spectrometer from Bruker (Germany) X-band under the conditions indicated in the caption to the corresponding figures.

In the following experiments, we again irradiated wheat seeds in doses of 100, 200 and 300 Gy on equipment "K-25". This time the seeds were germinated under special conditions: at a stable temperature of 25 ° C, 16 hours in the light, 8 hours in the dark. Two types of experiments were carried out: 1 - the seeds were watered with distilled water, 2-with a solution of FeCl3 (10-5 mol concentration).

Seeds were germinated for 10 days. The seedlings were then dried at room temperature and ground to a powder.

Results and discussion

In Fig. Figures 1, 2 and 3 show the EPR spectra of seedlings of wheat seeds (control and irradiated with various doses of gamma radiation) recorded at room temperature (297 K).

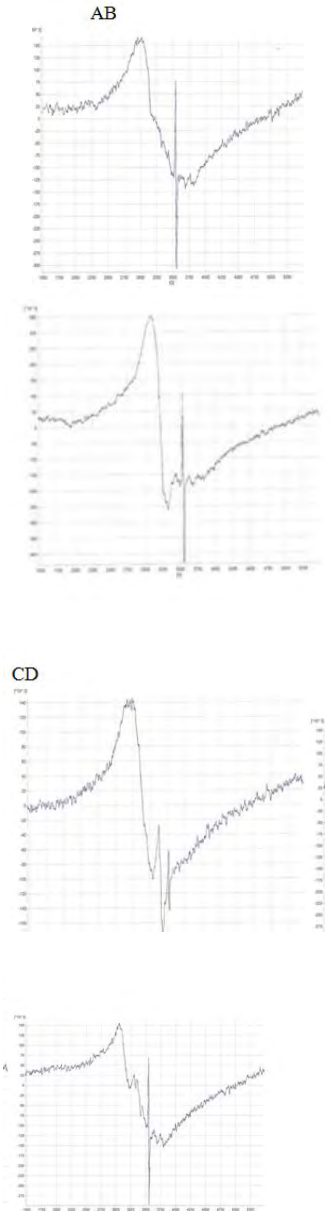

Fig.1. EPR signals seedling wheat seeds. Control (A), irradiated with 100 Gy (B), 200 Gy (C), 300Gy (D). Registration conditions: amplitude of HF-modulation of the

magnetic field 10.00 G, microwave frequency - power 2.105 mW, field center 3480 G, temperature 297 K.

As can be seen from fig. 1 at room temperature, a characteristic wide EPR signal characterizing the magnetic nanoparticles of iron oxides (g = 2.38, ΔH = 320 Gs) [2] in dried seedlings of wheat seeds was detected. With the influence of low radiation doses (100, 200 Gy), the amplitude of the wide EPR signal has significantly increased (Fig. 1 B, C). But, when the radiation dose increased to 300 Gy, a decrease in the signal amplitude was observed (Fig. 1D).

A wide EPR signal was recorded in dried pea seed sprouts. Under the influence of different doses of radiation, the results of EPR studies conducted with pea seedlings were identical to the results of experiments conducted with seedlings of wheat seeds.

In previous studies, we showed that the parameters of this wide EPR signal recorded by us in plant leaves at room temperature and its variation with a decrease in the recording temperature to 80 K were identical to those of wide EPR signals in synthesized magnetite nanoparticles [2, 3, 4].

This gives us grounds to say that the wide EPR signal obtained is a broad EPR signal in synthesized magnetite nanoparticles.

The results of our studies have shown that the paramagnetic centers characterizing a wide EPR signal depend on the intensity of the irradiation dose of wheat seeds. This dependence is associated with various biological processes (cell division, respiration, photosynthesis, genetic changes, etc.) occurring during the germination of wheat seeds. Depending on the dose of gamma radiation in connection with the development of seeds, some processes are stimulated or slowed down. According to our assumptions, the influence of biological processes on iron ions leads to the appearance of magnetic nanoparticles of iron oxide (magnetite Fe3O4 and maghemite γ-Fe2O3). Primary experiments show that this is the process of photosynthesis [5]. Because the dried wheat seeds themselves did not show a signal that was observed in green seedlings. As a result of the action of the electron transport chain (ETC) of photosynthesis during the destruction, the participation of iron ions in the oxidation-reduction process ultimately leads to the synthesis of magnetic nanoparticles. To verify this, we conducted the following experiments.

Sprouted seeds under special conditions: at a stable temperature of 25 ° C, 16 hours in the light, 8 hours in the dark. Two types of experiments were carried out: 1- seeds were watered with distilled water, 2- with a solution of added FeCl3 (10-5 mol concentration).

Figure 2 shows the results of the EPR studies of wheat seed objects that were watered with distilled water.

As can be seen from fig. 1 at room temperature, a characteristic wide EPR signal characterizing the magnetic nanoparticles of iron oxides (g = 2.38, ΔH = 320 Gs) [2] in dried seedlings of wheat seeds was detected. With the influence of low radiation doses (100, 200 Gy), the amplitude of the wide EPR signal has significantly increased (Fig. 1 B, C). But, when the radiation dose increased to 300 Gy, a decrease in the signal amplitude was observed (Fig. 1D).

A wide EPR signal was recorded in dried pea seed sprouts. Under the influence of different doses of radiation, the results of EPR studies conducted with pea seedlings were identical to the results of experiments conducted with seedlings of wheat seeds.

In previous studies, we showed that the parameters of this wide EPR signal recorded by us in plant leaves at room temperature and its variation with a decrease in the recording temperature to 80 K were identical to those of wide EPR signals in synthesized magnetite nanoparticles [2, 3, 4].

This gives us grounds to say that the wide EPR signal obtained is a broad EPR signal in synthesized magnetite nanoparticles.

The results of our studies have shown that the paramagnetic centers characterizing a wide EPR signal depend on the intensity of the irradiation dose of wheat seeds. This dependence is associated with various biological processes (cell division, respiration, photosynthesis, genetic changes, etc.) occurring during the germination of wheat seeds. Depending on the dose of gamma radiation in connection with the development of seeds, some processes are stimulated or slowed down. According to our assumptions, the influence of biological processes on iron ions leads to the appearance of magnetic nanoparticles of iron oxide (magnetite Fe3O4 and maghemite γ-Fe2O3). Primary experiments show that this is the process of photosynthesis [5]. Because the dried wheat seeds themselves did not show a signal that was observed in green seedlings. As a result of the action of the electron transport chain (ETC) of photosynthesis during the destruction, the participation of iron ions in the oxidation-reduction process ultimately leads to the synthesis of magnetic nanoparticles. To verify this, we conducted the following experiments.

Sprouted seeds under special conditions: at a stable temperature of 25 ° C, 16 hours in the light, 8 hours in the dark. Two types of experiments were carried out: 1- seeds were watered with distilled water, 2- with a solution of added FeCl3 (10-5 mol concentration).

Figure 2 shows the results of the EPR studies of wheat seed objects that were watered with distilled water.

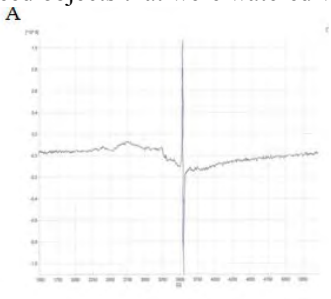

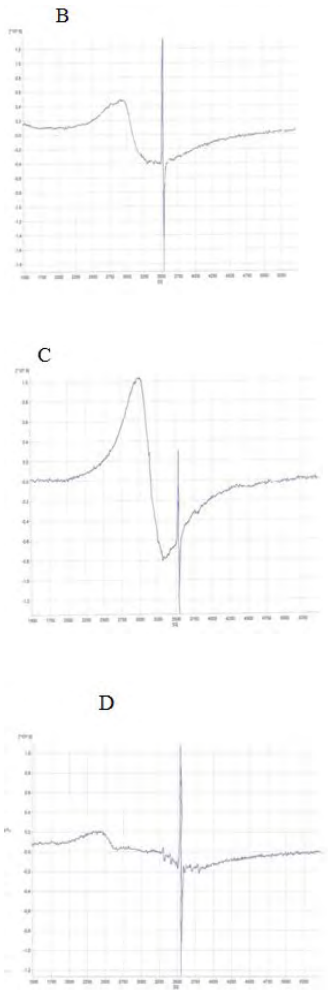

Fig.2. EPR signals seedlings of wheat seeds, which were watered with distilled water. Control (A), irradiated with 100 Gy (B), 200 Gy (C), 300Gy (D). Registration conditions: amplitude of HF - magnetic field modulation 10.00 G, microwave - power 2.105 mW, field center 3480 G, temperature 293 K.

Figure 3 shows the results of the EPR studies of wheat seed samples that were watered with a solution of added FeCl3 (10-5 mol concentration).As can be seen from fig. 2 and 3, the intensity of the EPR signals in the irradiated seed sprouts is significantly different. This means that in experiments of the second type, as a result of the reduction of iron ions, paramagnetic centers appear that characterize a broad EPR signal (Fig. 3A). In experiments of the first type, this signal is not observed, which is due to the absence of iron ions (Fig. 2A). The result of the experiments carried out with irradiated seedlings is significantly different. In the experiments of the first type, an increase in the amplitude of a wide EPR signal was observed with the influence of a small radiation dose (100, 200 Gy) and a decrease in the signal amplitude under the influence of a relatively large radiation dose (300 Gy). In experiments of the second type, on the contrary, a decrease in the amplitude of the wide EPR signal was observed with the influence of a small dose of gamma radiation. This shows that, as indicated in the literature [6], the acceleration of the appearance of active oxygen species (ROS) (the Fenton reaction) affects the process of the appearance of paramagnetic centers.

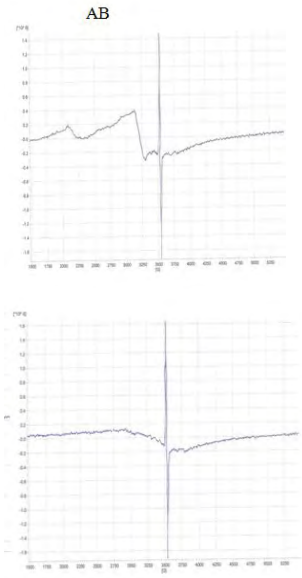

Fig.3. EPR signals of seedlings of wheat seeds, which were watered with a solution of added FeCl3. Control (A), irradiated with 100 Gy (B). Registration conditions: amplitude of HF-modulation of magnetic field 10.00 G, microwave - power 2.105 mW, field center 3480 G, temperature 293 K.

It is assumed that a large amount of ROS leads to damage to cells in the leaves. Therefore, as a response, cells tend to reduce the effect of damage. As a result of the appearance of magnetic nanoparticles of iron oxides (magnetite and maghemite) due to iron ions (Fe2 +, Fe3 +), the intensity of the Fenton reaction decreases. This process, that is, the reduction of iron ions of magnetic nanoparticles, occurs via the electron-transport chain of photosynthesis (in light).

In other words, the formation of magnetic nanoparticles of iron oxides as a result of photosynthesis (biomineralization) occurs as a phenomenon that protects the cell from damage.

References

[1] P. A. R. Ade et al. [Planck Collaboration], Astron. Astrophys. **594**, A20 (2016).
[2] P. Channuie, Nucl. Phys. B **892**, 429 (2015).
[3] T. Inagaki, S. D. Odintsov, H. Sakamoto, Astrophys. Space Sci. **360**, 67 (2015).
[4] T. Inagaki, S. D. Odintsov, H. Sakamoto, Nucl. Phys. B **919**, 297 (2017).
[5] P. Channuie and C. Xiong, Phys. Rev. D **94**, 043521 (2017).
[6] Y. Nambu and G. Jona-Lasinio, Phys. Rev. **122**, 345 (1961); Phys. Rev. **124**, 246 (1961).
[7] V. A. Miransky, "Dynamical Symmetry Breaking in Quantum Field Theories", World Scientic (1993).
[8] M. Harada and K. Yamawaki, Phys. Rept. **381**, 1 (2003).
[9] K. i. Kondo, S. Shuto and K. Yamawaki, Mod. Phys. Lett. A **6**, 3385 (1991).

[10] K. i. Kondo, M. Tanabashi and K. Yamawaki, Prog. Theor. Phys. **89**, 1249 (1993).
[11] K. Kondo, M. Tanabashi and K. Yamawaki, Mod. Phys. Lett. A **8**, 2859 (1993).
[12] C. N. Leung, S. T. Love and W. A. Bardeen, Nucl. Phys. B **273**, 649 (1986).
[13] C. N. Leung, S. T. Love and W. A. Bardeen, Nucl. Phys. B **323**, 493 (1989).
[14] M. Harada, Y. Kikukawa, T. Kugo and H. Nakano, Prog. Theor. Phys. **92**, 1161 (1994).
[15] W. A. Bardeen, C. T. Hill and M. Lindner, Phys. Rev. D **41**, 1647 (1990).
[16] C. T. Hill and D. S. Salopek, Annals Phys. **213**, 21 (1992).
[17] B. Geyer and S. D. Odintsov, Phys. Rev. D **53**, 7321 (1996).
[18] B. Geyer and S. D. Odintsov, Phys. Lett. B **376**, 260 (1996).
[19] T. Inagaki, S. D. Odintsov, H. Sakamoto, in writing.
[20] S. Weinberg, Phys. Rev. Lett. **37**, 657 (1976).
[21] E. Eichten, K. D. Lane, J. Preskill, Phys. Rev. Lett. **45**, 225 (1980).
[22] W. Goldstein, Nucl. Phys. B **213**, 477 (1983); B **229**, 157 (1983).
[23] S. Hashimoto, T. Inagaki and T. Muta, Phys. Rev. D **48**, 1301 (1993).
[24] T. Inagaki, Nucl. Phys. Proc. Suppl. **37A**, 197 (1994).
[25] K. j. Hamada and M. Matsuda, Phys. Rev. D **93**, 064051 (2016).

hrovshan@hotmail.com
f.ismayil@mail.ru

Scattering of Neutrons on Nuclei at High Energies

S.G. ABDULVAHABOVA, N.SH. BARKHALOVA, T.O. BAYRAMOVA

Baku State University

Abstract: The cross section for elastic nN scattering is investigated at high energies and in the region of small momentum transfers |t| from the point of view of s and t channel unitarity. Much attention is paid to the analysis of the analytic properties of the amplitude of elastic processes as a function of angular variables and the possibility of expanding the corresponding domains of analyticity. In eikonal approximation formulas for the scattering amplitude and cross section are obtained. It is shown that at high energies the cross section remains exponentially dependent on the momentum transferred.

Key words: scattering, matrix element, eikonal approximation, cross section.

1. Introduction

One of the most important criteria for comparison with the experience of modern theories of strong interaction is the dependence on the energy of the total cross sections for collisions of neutrons on nuclei.

The problems of the theory of nucleon-nucleon collisions at very high energies are the observation of a large number of secondary particles. This number is too large on the one hand to develop a simple theory that takes into account the exchange of only well-known mesons, on the other hand, it is too small to be able to apply the methods of probability theory.

The experimental data reveal the following main features [1]:

1. The differential effective cross section for elastic proton-nuclear scattering decreases exponentially with increasing t, and this shows that collisions with a large transmitted perpendicular component of the momentum is rare.

2. The number of particles produced in such collisions falls very rapidly with increasing momentum in a direction perpendicular to the incident beam of particles;

3. Most secondary particles are pions, and in the center of mass system of colliding neutrons almost all pions have small momenta.

The behavior of the partial cross sections at high energy can serve as a test of the hypothesis of the Yang collision mechanism, according to which hadrons are excited and emit particles during a collision.

Theoretical models describe some regularities of spectra, however, the insufficient accuracy and systematic character of the experimental data do not allow one to uniquely choose the best interaction model. In this paper we consider the interaction of neutrons with the nucleus at high energies and small momentum transfers.

2. The amplitude of elastic scattering

The applicability of the Glauber-Sitenko diffraction scattering is determined [2] by the conditions of adiabaticity and eikonality. Adiabaticity is the neglect of the nucleus internuclear nucleus motion during the passage of a falling particle through it. The eikonal approximation (high-energy approximation) is widely and successfully used to describe the scattering of particles in complex nuclei as scattering in a certain continuous optical medium. In this approximation, instead of the law of conservation of energy, the law of conservation of the momentum projection holds. This means that the movement in the transverse directions is completely neglected. The eikonal approximation in its sense is very close to the semiclassical approximation, and the condition for the applicability of the high-energy approximation coincides with the usual quasiclassical condition. In high-energy scattering, the wavelength of a particle is much smaller than the dimensions of the potential. In addition, in the eikonal approximation, no restrictions are imposed on the masses and coordinates of the particles, both the final radius and the recoil are considered exactly, and the effect of distortion is taken into account only in the phase of the plane wave. Therefore, the eikonal approximation can be used to calculate the angular distributions of scattered particles. In the case of elastic scattering in this approximation, the scattering amplitude is calculated by the eikonal wave functions.

Under the assumption that the kinetic energy of the incident neutron is large in comparison with the binding energies of the individual particles, the interaction of the incident particle with the particles of the nucleus can be treated independently. The maximum collision frequency is A. With each scattering center, the incident particle interacts only once. It can not dissipate at one of the potential centers, then on some other and again at the first. This is due to the fact that in the diffraction approximation the particle propagates only along a straight line and can not be scattered backward.

Elastic scattering is due to the unitarity condition with all inelastic processes. The scattering matrix F is generally complex:

$$F = D + i\,A, \tag{1}$$

where D is real; A is the imaginary part of the amplitude.

In the representation of invariant variables (Mandelstam variables), the standard relation between the scattering amplitude F and the differential cross section for elastic scattering

$$\frac{d\sigma(s,t)}{dt} = \left|F(s,t)\right|^2, s = 4(k^2 + m^2) = 4E^2,$$
$$t = -(\mathbf{p} - \mathbf{k})^2. \tag{2}$$

For the hadron scattering amplitude at high energies, it is very convenient to pass from expansion in partial waves to the representation of the impact parameter *b*

$$F(s,t) = i\int bdb(1 - exp[i\chi(s,b)])J_0(b\sqrt{-t}), \qquad (3)$$

where J_0 is the Bessel function, and the eikonal has the following form [3]

$$\chi(s,b) = i\left(exp(-\mu\sqrt{b^2+a^2}) - exp(-2\mu\sqrt{b^2+a^2})\right). \qquad (4)$$

Eikonal with a high degree of accuracy is proportional to the effective quasipotential interaction of hadrons. Therefore, the high-energy approximation can also be used to calculate the angular distributions of scattered particles [4]. Here the parameters μ_0 and a_0 has the meaning of the reduced mass and the interaction radius:

$$\mu = \mu_0 / \sqrt{1 + ln\, s - i\pi/2}\,;$$
$$a = a_0 / \sqrt{1 - ln\, s - i\pi/2}\,. \qquad (5)$$

The unambiguous kinematic relation (3) in elastic scattering facilitates comparison with experiment, which at the present time, with the help of the new technique, practically covers the entire range of variation of *t*. Further, the eikonal (4) can be expanded in a series containing only even powers of the regularity condition for the Fourier-Bessel transform of the function (3) for $t = 0$:

$$F(s,t) = is\sum_{n=1}^{\infty} \frac{\exp(a|t|n)}{n!\cdot n}\left(-\frac{4\pi^2\mu}{a}\right)^{n-1} \qquad (6)$$

Neglecting the spin effects and assuming that the dependences of the real and imaginary parts of the nuclear scattering amplitude F_N are the same, one can parameterize the amplitudes (3) for small | t | as

$$F_N = (\sigma_{total}/4\pi)(i + \rho)\, exp(bt/2), \qquad (7)$$

where

$$\rho = \mathrm{Re}\, F_N(0) / \mathrm{Im}\, F_N(0). \qquad (8)$$

As a concrete example, we choose a nucleon-nucleon interaction in the form of a Gaussian potential:

$$V(s,r) = is\left(\frac{\pi}{a}\right)^{3/2} \exp\left(-r^2/4a\right) \qquad (9)$$

Corresponding to a purely imaginary amplitude of diffraction scattering. In this connection, it is important to emphasize that there are some general considerations in favour of expression (9) and that it allows one to explain the most important features of the diffraction part of the scattering.

Taking all this into account, as a concrete example, we choose the interaction potential in the following form:

$$\delta(b) = -\int_{-\infty}^{\infty} V\left(\sqrt{b^2+z^2}\right)dz \qquad (10)$$

Taking into account (6) in (3), after exponential expansion in a series and parametrize in accordance with the experimental data [4] the slope of the exponential in the region t = 2-8(ГэВ/с)^2 is conserved. In such a picture, diffraction is generated by the absorption of proton waves by the scatterer, whose geometric structure determines the structure of the differential cross section with respect to t. Theoretical models for elastic pp scattering give very close predictions concerning the positions of the minima of the differential cross section, that is, they are based at all on the analogy with optical diffraction.

If the scattering amplitude as a function of the variable $z = \cos\theta = 1 + 2t/s$, the cosine of the scattering angle in the channel, is analytic inside the ellipse with foci at the points $z_0 = \pm 1$, then the total scattering cross-section satisfies condition

$$\sigma_{tot} \le 4\pi R^2(s)\,. \qquad (11)$$

The analytic property of the scattering amplitude of elastic or inelastic processes as a function of the scattering angle makes it possible to extend the corresponding regions of analyticity when the unitarity condition is taken into account. In the language of the analytic properties of the scattering amplitude, the possibility of preserving in quantum field theory a representation of the effective region of interaction depends on how slowly the ellipse of analyticity is expressed with increasing energy in the segment $-1 \le z \le 1$.

At high energies, too many waves are involved in the scattering and the differential cross section has a clearly pronounced peak in the forward direction, i.e dσ/dt~exp(*bt*), which is observed in the experiment. Because of intense meson formation, all phases become complex and the nuclear amplitude *nN* of forward scattering is almost completely imaginary. However, scattering in the region immediately adjacent to these angles can be represented as due to the action of the one-pion exchange potential. In addition, the scattering cross section is only slightly larger than the square of the imaginary part. This difference can not be attributed to the real part $A(0)$. Its appearance should be attributed to the spin-dependent part of the scattering matrix.

3. Conclusion

In explaining the energy dependence of the *pN* scattering cross section, the t-channel exchange picture is more adequate, which for high energies was formulated in the form of the Regge model [5]. In the framework of the Regge model, the inelastic states are taken into account on the basis of a quasi-eikonal approximation. However, here we do not take into account the contribution of inelastic diffraction states of a perpherical nature, which does not

allow us to obtain a correct description of scattering for large | t |. It should be noted that the practical utility of the Regge-eikonal approach lies in the possibility of reducing the functional arbitrariness by reducing the unknown function of two variables to several functions of one variable, such as Regge trajectories and Regge's deductions.

Scattering in this energy range and transmitted pulses has features of both diffraction scattering, determined by the geometry of the scattered hadrons, and self-similar, connected with the interaction of point-like constituents. We can assume that the value found for large | t | The behavior of the elastic scattering cross section is a reflection of some peculiarities of the internal structure of hadrons.

The differential cross sections of binary processes (in particular, the elastic *nN* scattering reactions), according to the formula (11), are concentrated in a narrow region of transmitted pulses |t|, whose width decreases logarithmically with increasing energy [6]. This phenomenon in elastic processes is usually called the reduction of the diffraction cone.

The eikonal was conceived as a direct generalization of the potential theory of two-particle interaction to the relativistic case, and the existence of inelastic processes. The range of application of the eikonal approximation for the nonrelativistic case shows that it is not only a good method for taking into account the kinematical features of high-energy scattering, but also allows us to introduce dynamics of interaction in the theoretical approach.

At high hadron energies (E> 4 GeV), the diffraction mechanism is the main mechanism for the formation of a neutral vector meson [7], which can be found within the framework of a peripheral quark model. Near the threshold, the model of central quark collisions is usually applied.

All calculations were performed on the basis of nonrelativistic quantum mechanics. As noted, at sufficiently high energies, the inelastic processes associated with the production of mesons become significant. Therefore, the possibility of describing the interaction between nucleons by means of a potential is limited on the part of high energies. Such an energy limitation means that a single-valued determination of the potential at short distances is impossible at all. However, since in the nuclei the maximum permissible values of the nucleon momenta correspond to energies less than 150 MeV, it can be hoped that, when considering the structure of the nuclei, relativistic effects can be neglected.

Thus, the method of continued unitarity gives a simple possibility of taking into account the analytical properties of the scattering amplitude in the plane of the angular momentum of the direct channel and obtaining explicit expressions for it in various kinematic regions.

References

[1] J.Benecke, C.Yang, Phys. Rev., **188**, 2159, (1979).
[2] R.J. Glauber. Proc. Conf. on High Energy Physics and Nuclear Structure . Amsterdam, 311, (1967)
[3] S.G Abdulvahabova. E.A. Rasulov. International workshop “Quantum particles, fields and strings” Fizika, **3**, 83, (2002).
[4] M.A.Jusupov, E.T. Ibraeva. PEPAN, **21**, (6), 1427, (2000).
[5] A.A.Godizev, V.A.Perov. PEPAN, **39**, (1), 243, (2008).
[6] S.G Abdulvahabova. Journal of Qafqaz University, **30**, 19, (2010).
[7] J.L. Hartmann, Phys.Rev.Lett, **39**, 975, (2007).

sajida.gafar@gmail.com

Dependence of thermoelectric power of quantum well with complex profile on Fermi level

S.R. FIGAROVA, M.M. MAHMUDOV

Baku State University, Department of Physics, Solid States Physics Chair, Azerbaijan, AZ1148, Baku, 23 Z.Khalilov st.

Abstract: Using energy spectrum of an electron gas in a quantum well with complex shape, the thermoelectric power of a degenerate two-dimensional electron gas has been determined for scattering by acoustic phonons. Dependence of the thermoelectric power on the Fermi level is investigated. It has been shown that the thermoelectric power of a degenerate two-dimensional electron gas depends nonmonotonically on the Fermi level and, depending on quantum well parameters; the thermoelectric power can take both positive and negative values.

Keywords: thermoelectric power, two-dimensional electron gas, quantum well with complex shape, acoustic phonons scattering.

1. Introduction. Interest in study of thermoelectric properties of low-dimensional structures has been increased after appearance of papers [1-5], in which possibility of increasing the thermoelectric figure of merit due to an increase in the density of states in systems with reduced dimensionality was theoretically and experimentally demonstrated. Various approaches to this problem and various structures were considered. Those papers, in particular, consider the basic physical ideas and methods used to improve the quality of modern thermoelectric materials and increase the efficiency of thermoelectric conversion, and special attention was paid to the effect of nanostructure of materials on their thermoelectric characteristics. Changes in the density of states can lead to a substantial increase in the thermoelectric power with an appropriate choice of the Fermi level position. When studying these structures, the simple form of the quantum well has been basically considered. However, it is obvious that the quantum well shape must significantly influence the thermoelectric power and effects associated with it. The present paper is devoted to a study of thermoelectric properties of a two-dimensional electron gas in a quantum well with complex profile. Dependence of the thermoelectric power of a degenerate two-dimensional electron gas on the Fermi level is investigated for charge carriers scattering by acoustic phonons. It has been shown that the thermoelectric power of a degenerate two-dimensional electron gas, depending on the parameters of the quantum well, can be either positive or negative.

2. Theory of the thermopower. For the problem in hand, we can use the well-known Mott formula [6]:

$$\alpha = \frac{\pi^2}{3}\frac{k_0 T}{e}\frac{\partial \ln \sigma(\varepsilon)}{\partial \varepsilon}\bigg|_{\varepsilon=\varepsilon_F}, \qquad (1)$$

here $\sigma(\varepsilon)$ is the charge carrier electrical conductivity, e the elemental charge, T the absolute temperature, k_0 the Boltzmann constant, ε_F the Fermi energy. It should be noted that the Mott formula is well satisfied at high concentrations ($n = 5\cdot10^{11}\ cm^{-2}$), while at low concentrations ($n = 5\cdot10^{11}\ cm^{-2}$) it is valid only at low temperatures. As can be seen from (1), in order to calculate the thermoelectric power of a degenerate two-dimensional electron gas, it is necessary to know the general expression for the electrical conductivity $\sigma(\varepsilon)$, and also to take into account the problem geometry. In our case, the temperature gradient is directed along the axis x. To calculate the electrical conductivity, it is necessary to start from a specific type of the quantum well. In this paper, we consider a quantum well with potential energy of the form [7]:

$$U = \frac{U_0}{\cos^2(z/a)}. \qquad (2)$$

Proceeding from the solution of the Schrodinger equation, where the potential energy is determined by formula (2) for the energy spectrum we obtain [8]:

$$\varepsilon_n = \varepsilon_0\left(1 + 2n + \sqrt{1 + \frac{U_0}{\varepsilon_0}}\right)^2, \qquad (3)$$

here $\varepsilon_0 = \hbar^2\pi^2/(8ma^2)$ at $n = 0$ and $U_0 = 0$, a is the quantum well half-width, U_0 the potential energy minimum, $n = 0,1,2,...$ the quantum number.

Calculating for the given energy spectrum the diagonal component of the electrical conductivity, we obtain [9]:

$$\sigma_{xx}(\varepsilon) = \frac{e^2}{\pi\hbar^2 a}\sum_n \int_{\varepsilon_n}^{\infty} \Theta(\varepsilon-\varepsilon_n)(\varepsilon-\varepsilon_n)\tau(\varepsilon)\left(-\frac{\partial f_0(\varepsilon)}{\partial\varepsilon}\right)d\varepsilon, \qquad (4)$$

where $\Theta(\varepsilon-\varepsilon_n)$ is the Heaviside step function, $\tau(\varepsilon)$ is the relaxation time, $f_0(\varepsilon)$ is the Fermi distribution function. It follows from formula (4) that the electrical conductivity, as well as the thermoelectric power, depend on the mechanism of current carriers scattering. Here we consider the scattering of electrons by acoustic phonons. Taking into account the dependence of the relaxation time on the density of states and the results of papers [10, 11] for the case of electron-phonon scattering, we have:

$$\tau(\varepsilon) = \frac{1}{g_{2D}(\varepsilon)}\left(\frac{\varepsilon_\perp}{k_0 T}\right)^r\left(\frac{2mk_0 T}{\hbar^2}\right)^r\frac{1}{A_r}, \qquad (5)$$

here $g_{2D}(\varepsilon)$ is the density of states of a two-dimensional electron gas in the quantum well [9], $\varepsilon_\perp = \hbar^2 k_\perp^2/2m$, r the scattering parameter, which for acoustic phonon scattering $r = 0$, $A_0 = \pi E_1^2 k_0 T/\hbar\rho\upsilon_0^2$, E_1 the deformation potential constant, ρ the crystal density, υ_0 the speed of sound in the

crystal (see [10]). It follows from (5) that for scattering by acoustic phonons the relaxation time does not depend on the energy.

With allowance for (4) and (5) from formula (1) for the thermoelectric power of a degenerate two-dimensional electron gas in a quantum well with complex shape for acoustic phonon scattering, we obtain:

$$\alpha = -\frac{\pi^2}{3}\frac{k_0^2 T}{n_{el} e}\frac{m}{\pi\hbar^2 a}\sum_{n=0}^{n_0}\Theta(\varepsilon_F - \varepsilon_n), \qquad (6)$$

here n_{el} is the surface concentration of electrons. Using (6), it can be shown that the thermoelectric power of a degenerate two-dimensional electron gas for acoustic phonon scattering is expressed in terms of the state density:

$$\alpha = -\frac{\pi^2}{3}\frac{1}{n_{el} e}k_0^2 T\, g_{2D}(\varepsilon_F), \qquad (7)$$

where

$$g(\varepsilon_F) = \frac{m}{\pi\hbar^2 a}\sum_{n=0}^{n_0}\Theta(\varepsilon_F - \varepsilon_n), \qquad (8)$$

is the density of quantum states at the Fermi level. Since the density of states is an oscillating function, accordingly, the thermoelectric power also oscillates.

From (6) in the limiting cases it is possible to obtain an expression for the thermoelectric power of thin films in infinitely deep rectangular and parabolic potential wells.

Infinitely deep rectangular potential well. From (6) for the thermoelectric power of a degenerate electron gas in infinitely deep rectangular potential well, we obtain:

$$\alpha = \alpha_m\left(\frac{\pi}{3n_{el}}\right)^{1/3}\frac{n_0}{d}, \qquad (9)$$

where α_m is the bulk specimen thermoelectric power, n_0 the number of subbands situated below the Fermi level, d the film width. It can be shown that the thermoelectric power in a size-quantized thin film is 20% larger in comparison with bulk samples. If the width of the subbands is smaller than the distance between them, then for the thermoelectric power of a degenerate two-dimensional electron gas, expression (7) is obtained. In this case it can also be shown that the maximum value of the thermoelectric power is equal to:

$$\alpha_{\max} = -\frac{k_0}{e\,n}\ln 2, \qquad (10)$$

where n is the number of completely filled subbands.

Parabolic potential well. In the quantum limit, from (6) for the thermoelectric power of a degenerate two-dimensional electron gas in a parabolic quantum well, we find:

$$\alpha = -\frac{k_0}{e}\frac{\pi^2}{3}\frac{k_0 T}{\varepsilon_F - \varepsilon_n}. \qquad (11)$$

3. Discussions. On the basis of formula (6), the dependence of the thermoelectric power of a degenerate two-dimensional electron gas in a quantum well with complex shape on the Fermi level for acoustic phonon scattering was investigated (Fig. 1). When constructing the graph, the following data were used: $m = 0.067 m_0$, $\varepsilon_0 = 60\,meV$, $a = 5\,nm$, $n_{el} = 10^{17} m^{-2}$.

It can be seen from Fig. 1 that the thermoelectric power of a degenerate two-dimensional electron gas oscillates, therewith depending on the quantum well shape, it can be either positive or negative. According to the classical theory, since the direction of $E(x)$ depends on the charge carrier sign, it is clear that the sign of the thermoelectric power is connected with the sign of the charge carriers (according to the formula (6)). This is the thermoelectric field is directed opposite to the temperature gradient, when electrons are charge carriers, and thus the thermoelectric power is always negative. But in the quantum transport the thermoelectric power can be both positive and negative for electrons.

The fact that the thermoelectric power changes its sign depending on the Fermi level position can be explained as follows. When the temperature on the left side of the conductor is greater than on the right, then $\Delta f = f(\varepsilon, \mu + eU, T + \Delta T) - f(\varepsilon, \mu, T)$ is positive for $\varepsilon > \mu$ and negative for $\varepsilon < \mu$, that is, the density of current carriers on the left-hand side with an energy ε greater than that on the right side, when $\varepsilon > \mu$ and it is less, when $\varepsilon < \mu$, μ is the chemical potential. Consequently, when integrating with respect to energy from $-\infty$ to μ, the current density j_1 is negative, and when integrating from μ to $+\infty$, the current density j_2 is positive. Consequently, the sign of the total current density $j = j_1 + j_2$ is the result of a competition between j_1 and j_2, and is completely determined by the transmission coefficient or electrical conductivity. It can be said that when the transmission ratio increases with ε, we have a positive electron current and a negative thermoelectric power, and vice versa. It follows from Fig. 1 that with an increase in the Fermi level (carrier current concentration), the oscillations weaken. The largest value of the thermoelectric power corresponds to a peak near $\mu_F = 1eV$ (see Fig. 1).

The change in the sign of the thermoelectric power in quantum films was noted also in [12, 13], where this fact was explained by the correlation effects in two-dimensional systems. In the present work, this fact is explained by the profile of the quantum well. In [13], a change in the sign of the thermoelectric power at high concentrations $n_{el} = 10^{16}$ ì $^{-2}$ for film thicknesses $d = 6\,nm$ was observed experimentally. It can be seen from Fig. 1 that the thermoelectric power is reduced to zero, which occurs when the Fermi level is located in a localized region. All states below the Fermi level are localized, and heat is activated at the edges.

In films, there is a substantial increase in the thermoelectric power in comparison with a massive sample. The physical reason for the increase lies in the fact that in the considered temperature range the thermal energy is less in comparison with the distance from μ_F to the nearest of the boundaries $\varepsilon_{n-1}, \varepsilon_{n+1}$. Narrow energy subbands are equivalent to degenerate energy levels, which leads to practically temperature-independent entropy.

4. Conclusions. Physical properties of a two-dimensional electron gas depend strongly on the region of the film thicknesses, where the electron motion is confined. We have investigated dependence of the thermoelectric power on the thickness and obtained that for a given Fermi level the thermoelectric power oscillates with the thickness of the quantum well. When the Fermi level becomes larger, the period of oscillations of the thermoelectric power decreases. The intersections of the size-quantized energy levels with the fixed Fermi levels are the cause of the thermoelectric power oscillations. At large values of ε_F, more energy levels cross it, which leads to stronger oscillations. Consequently, by analyzing the thermoelectric power, it is possible to obtain additional information on the energy levels of the quantized structure. Experimentally, the presence of oscillations with a thickness for *n-PbTe* films was observed in [14]. The presence of sharp peaks in the dependence of the thermoelectric power on the film thickness is due to the manifestation of significant quantum effects.

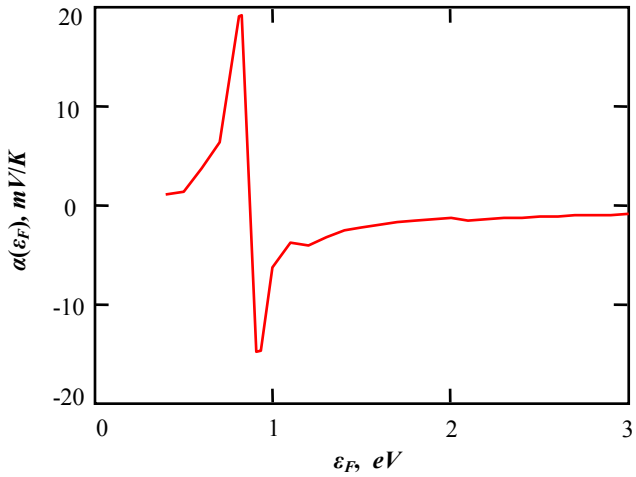

Fig.1. *Thermoelectric power of degenerate two-dimensional electron gas vs. Fermi level.*

References

[1] A.V. Dmitriev, I.P. Zvyagin, Physics-Uspekhi, 2010. **53**(8), 789 (2010).
[2] A. Balandin, Phys. Low-Dim. Structures, **1**, 1 (2000).
[3] T.C. Harman, D.L. Spears, M.J. Manfra, Journal of Electronic Materials, **25**(7), 1121 (1996).
[4] L.D. Hicks, T.C. Harman, X. Sun, M.S. Dresselhaus, Phys. Rev. B., **53**, 10493 (1996).
[5] I.V. Sur, Semiconductors, **43**(5), 624 (2009).
[6] M. Cutler, N.F. Mott, Phys. Rev., **181**, 1336 (1969).
[7] A.B. Shvartsburg, Physics-Uspekhi, **43**(12), 1201 (2000).
[8] S.R. Figarova, G.N. Hasiyeva, V.R. Figarov, Physica E: Low-dimensional Systems and Nanostructures, **69**, 24 (2015).
[9] S.R. Figarova, G.N. Hasiyeva, V.R. Figarov, Physica E: Low-dimensional Systems and Nanostructures, **78**, 10 (2016).
[10] B.M. Askerov "Electron Transport Phenomena in Semiconductors. World Scientific, Singapore, p.412, 1994.
[11] B.K. Ridley, Rep. Prog. Phys., **54**(2), 169 (1991).
[12] V.V. Tai, N.Q. Khanh, Superlattices and Microstructures, **88**, 474 (2015).
[13] Wang Jianming, Modern Physics Letters B, **20**(5), 215 (2006).
[14] S.S. Patil, P.H. Pawar, Chalcogenide Letters. **9**(4), 133 (2012).

Gauge model with exotic particles

SEVDA RZAYEVA

Sumqayit State University, Baku Street, Sumqayit AZ5008 and Institute of Physics of Azerbaijan National Academy of Sciences, AZ143, Baku, G. Javid av.33

Abstract

The possibility of construction of the electroweak model based on spontaneously broken gauge SU(3)C × SU(3)L × U(1) group
symmetry has been investigated. In case of arbitrary values of hypercharges of Higgs and fermions fields, the expressions for charges of leptons and the quarks, testifying to the natural solving of the electric charge quantization problems in the considering model are obtained. Influence of Higgs fields on particles charges "formation" and on electric charge quantization are shown.

Keywords: *Gauge Models, Electroweak, Higgs fields*

Introduction

Evidence strengthens more and more that the new particle discovered by ATLAS [1] and CMS [2] at the LHC at CERN is the last missing state required by the Standard Model (SM) of particle physics [3,4], the Higgs boson [5]. Standard Model (SM) of strong and electroweak interaction well describing existing experimental data involves several unanswered questions. Within SM have not been solved such problems as existence of three families [6,7], mass hierarchy problem [6,7], electric charge quantization etc. This work is devoted to investigation of electric charge quantization in $\mathrm{SU(3)_C \times SU(3)_L \times U(1)_X}$ model with exotic particles independent of parameters α and β.

The particle content in this model which is anomaly free, is given as follows:

$$\hat{\psi}_L = \begin{cases} \hat{q}_L : \left(3,3,X_q^L\right) == \left(3,2,X_q^L\right) \oplus \left(3,1,X_q^L\right), \\ \hat{l}_L : \left(1,3,X_l^L\right) == \left(1,2,X\right) \oplus \left(1,1,X_l^L\right), \end{cases}$$

$$\hat{\psi}^*{}_L = \begin{cases} \hat{q}^*_L : \left(3,3^*,-X_q^L\right) = \left(3,2^*,-X_q^L\right) \oplus \left(3,1,-X_q^L\right), \\ \hat{l}^*_L : \left(1,3^*,-X_l^L\right) = \left(1,2^*,-X_l^L\right) \oplus \left(1,1,-X_l^L\right), \end{cases}$$

$$\hat{\psi}_R = \begin{cases} \hat{q}_R : \left(3,1,X_q^R\right), \\ \hat{l}_R : \left(1,1,X_l^R\right), \end{cases}$$

Here, the values in the parentheses denote quantum numbers based on the symmetry. In this case, the electric charge operator takes a form

$$\hat{Q} = \alpha \hat{T}3 + \beta \hat{T}8 + X\hat{I}, \qquad (1)$$

with $T_3 = diag(1,-1,0)/2$ and $T_8 = diag(1,1,-2)/2\sqrt{3}$, where the normalization chosen is $Tr(T_\alpha T_\beta) = \delta_{\alpha\beta}/2$ and $I = diag(1,1,1)$ is the identity matrix. The value of the parameters α and β determines the fermion assignment and it is customary to use this number to classify the different models.

Let's consider the case when symmetry is broken by the Higgs fields

$$SU(3)_c \otimes SU(3)_L \otimes U(1)_X$$
$$\downarrow$$
$$SU(3)_c \otimes SU(2)_L \otimes U(1)_Y$$
$$\downarrow$$
$$SU(3)_c \otimes U(1)_Q$$

The covariant derivative D_μ is given by

$$D_\mu = \partial_\mu - igT_aW_{a\mu} - ig'T_9XB_\mu, \qquad (2)$$

where $T_a\ (a = 1,...,8)$ are the $SU(3)_L$ generators, and $T_9 = diag(1,1,1)/\sqrt{6}$ are defined as $Tr(T_aT_b) = \delta_{ab}/2$, $(a,b = 1,2,...,9)$; g and g' – coupling constants.

To keep consistency with the effective theory, the VEVs in the model satisfy the constraint: $V >> \upsilon >> u$.

For lepton and quark fields we choose the flowing representations (we will consider one family of leptons and quarks without mixing):

$$\psi_{lL} = \begin{pmatrix} \nu_e \\ e^- \\ N \end{pmatrix}_L \sim(1,3,y_{lL}), \quad \psi_{eR} = e_R \sim(1,1,y_{eR}),$$
$$\psi_{NR} = N_R \sim(1,1,y_{NR}),$$
$$\psi_{QL} = \begin{pmatrix} u \\ d \\ U \end{pmatrix}_L \sim(3,3,y_{QL}), \quad \psi_{uR} = u_R \sim(3,1,y_{uR}),$$
$$\psi_{dR} = d_R \sim(3,1,y_{dR}), \quad \psi_{UR} = U_R \sim(3,1,y_{UR}). \qquad (3)$$

Transformation of neutral fields $W_{3\mu}, W_{8\mu}, B_\mu$ to the physical photon field, can be written in the form

$$A_\mu = -\frac{g'}{\sqrt{2g}}\left(X_\rho - X_\eta\right)W_{3\mu} + \frac{3g'}{\sqrt{6g}} \times \\ \times\left(X_\rho + X_\eta\right)W_{8\mu} - \frac{\sqrt{3}g}{\bar{g}}B_\mu \quad , \tag{4}$$

where

$$\bar{g} = g\left[3 + 2t^2\left(X_\eta^2 + X_\rho^2 + X_\eta X_\rho\right)\right]^{1/2}. \tag{5}$$

From the expressions (4), and (5) one can see that, the photon eigenstate is independent on VEVs structure. This is a natural consequence of the $U(1)$ invariance [17-19]. However photon eigenstate depends from the Higgs fields hypercharges. Moreover, to be consistent with the QED based on the unbroken $U(1)$ gauge group, the photon field has to keep the general properties of the electromagnetic interaction in the framework of the 3-3-1 model, such as the parity invariant nature [18]. These would help us to obtain some consequences related to quantities which are independent on VEVs structure.

At first let us consider interaction of leptons with the electromagnetic field. In the considered model it looks like

$$L_{l\gamma} = Q_\nu \bar{\nu} e\gamma_\mu(1+\gamma_5)\nu_e A_\mu + \bar{e}\gamma_\mu(Q_{0e} + \\ + Q'_{0e}\gamma_5)eA_\mu + \bar{N}\gamma_\mu(Q_N + Q'_N\gamma_5)NA_\mu, \tag{6}$$

Taking into account the parity invariance of the electromagnetic interaction from (24), we have

$$Q_\nu = 0, \quad Q'_{0e} = 0, \quad Q'_N = 0.$$

In the considered case when neutrino has not the right component, the requirement parity invariance of electromagnetic interaction and the condition of neutrino charge equality to zero are equivalent. Besides, from the condition of parity invariance of electromagnetic interaction we have the relations between hypercharges of Higgs and lepton fields

$$y_{lL} = X_\eta, y_{eR} = X_\eta - X_\rho, y_{NR} = X_\eta - X_\chi \tag{7}$$

Consequently for the electric charges of leptons we have

$$Q_\nu = 0, \quad Q_{0e} = -Q_e, \quad Q_N = -Q_e\frac{2X_\eta + X_\rho}{X_\eta - X_\rho}, \tag{8}$$

where

$$Q_e = \frac{gg'}{\sqrt{2}g}\left(X_\eta - X_\rho\right). \tag{9}$$

In the considered model the Yukawa interactions which induce masses for the leptons can be written as

$$L_Y^l = f_e\bar{\psi}_{lL}\rho\psi_{eR} + f_N\bar{\psi}_{lL}\chi\psi_{NR} + h.c. \tag{10}$$

From (10) under the U (1) invariance we also have conditions (7). As a result we can conclude that conditions following from the P-invariance of electromagnetic interaction are equivalent to the conditions following from the Yukawa interactions which induce masses for the leptons. The equations (7) are the fixing condition for the hypercharges of the leptons fields by the Higgs fields and further it will be shown that they are also the conditions of electric charge quantization of leptons.

Let's consider interaction of quarks with electromagnetic field. In the considered model it looks like

$$L_{q\gamma} = \bar{u}\gamma_\mu(Q_u + Q'_u\gamma_5)uA_\mu + \bar{d}\gamma_\mu(Q_d + \\ + Q'_d\gamma_5)dA_\mu + \bar{U}\gamma_\mu(Q_U + Q'_U\gamma_5)UA_\mu, \tag{11}$$

Similarly to the of leptons case taking into account P-invariance of electromagnetic interaction from (11) we have conditions

$$Q'_u = 0, \quad Q'_d = 0, \quad Q'_U = 0. \tag{12}$$

These conditions lead to the following relations between hypercharges of Higgs and quarks fields

$$y_{QL} - y_{uR} = X_\eta, \quad y_{QL} - y_{dR} = X_\rho \\ y_{QL} - y_{UR} = X_\chi. \tag{13}$$

The expressions (13) fix the left and right hypercharges difference of quarks fields are also the conditions of quarks electric charge quantization. Equations (13) also follow from the Yukawa interactions which induce masses for the quarks

$$L_Y^q = f_u\bar{\psi}_{QL}\eta\psi_{uR} + f_d\bar{\psi}_{QL}\rho\psi_{dR} + \\ + f_U\bar{\psi}_{QL}\chi\psi_{UR} + h.c, \tag{14}$$

Similarly to the leptons case we can conclude that conditions following from the P-invariance of electromagnetic interaction are equivalent to the conditions following from the Yukawa interactions which induce masses for the quarks. The quarks electric charges we have

$$Q_u = Q_e\frac{X_\eta - y_{QL}}{X_\eta - X_\rho} \qquad Q_d = Q_e\frac{X_\rho - y_{QL}}{X_\eta - X_\rho} \\ Q_U = Q_e\frac{X_\chi - y_{QL}}{X_\eta - X_\rho} \tag{15}$$

The obtained expressions (8) and (7) can be considered as the evidence of electric charge quantization of leptons and quarks. However these expressions do not define numerical values of electric charges of leptons and quarks. For obtaining of the numerical values for the leptons and quarks electric charges, it is necessary to have the additional relations

between fermions field hypercharges. Such of relations can be obtained from the conditions of cancellations of gauge [8] and mixed gauge-gravitational anomalies [19]. In the considered model we have

$$y_{QL} = -\frac{1}{3}X_\eta, \quad y_{uR} = -\frac{4}{3}X_\eta$$
$$y_{dR} = -\frac{1}{3}X_\eta - X_\rho, \quad y_{UR} = -\frac{1}{3}X_\eta - X_\chi. \qquad (16)$$

This leads to the electric charge quantization

$$Q_\nu = 0, \quad Q_e = \frac{\sqrt{2}gg'X_\eta}{\left(3 + 2X_\eta^2 t^2\right)^{1/2}}, \quad Q_N = -\frac{1}{2}Q_e,$$

$$Q_u = \frac{2}{3}Q_e, \quad Q_d = -\frac{1}{3}Q_e, \quad Q_U = \frac{1}{6}Q_e, \qquad (42)$$

Similar expressions can be written for other fermions. Conditions (7) and (13) fix the hypercharges of fermions fields. The conditions following from the anomalies cancellations, fix hypercharges of all remained fields. Thus, if there are no conditions (7) and (13) it is obvious that to solve the equations following from the anomalies cancellations is impossible and consequently there are not electric charge quantizations, hence, these conditions are electric charge quantization ones. However these conditions depend from the hypercharges of Higgs fields, so these facts can be interpreted as a presence of influence of Higgs fields on the electric charge quantization.

Results

As a result we can conclude that photon eigenstate does not contain vacuum average of Higgs fields. The fixation of hypercharges of fermions fields by the Higgs fields and the dependence of the electric charges quantization conditions from the hypercharges of Higgs fields can be interpreted as influence of Higgs fields on the electric charge quantization. Unlike results of [17] it is shown that in the considered model the classical constraints following from the Yukawa interactions are equivalent to the conditions following from the P – invariance of electromagnetic interaction. This fact may be useful for the explanation of the P – invariance of electromagnetic interaction.

Conclusions

Taking into account the arbitrary values of fermions and Higgs fields hypercharges the possibility of construction of electroweak interactions model, based on spontaneously broken symmetry group by three Higgs fields have been investigated.

Expressions for fermions charges, testifying the electric charge quantization are obtained. Dependence of the particles charges from the hypercharges of Higgs fields can be interpreted as new property of Higgs fields. Higgs fields influence on particles charges "formation", and on particles electric charge quantization.

References

[1] G. Aad et al. [ATLAS Collaboration], Phys. Lett. B 716,1, (2012).

[2] S. Chatrchyan et al. [CMS Collaboration], Phys. Lett. B 716, 30, (2012).

[3] S. L. Glashow, Nucl. Phys. B22 (1961) 579;

[4] H. Fritzsch, M. Gell-Mann, H. Leutwyler, Phys. Lett. 47,365, (1973).

[5] P. W. Higgs, Phys. Lett. 12 132, (1964); Phys. Rev. Lett. 13, 508, (1964).

[6] P. Laugacker, Phys. Rev., 72,185, (1981).

[7] P. Fayet, hep-ph/9812300, (1998), hep-ph/9709356.

[8] C. Bouchiat, J. Iliopoulos and Ph. Meyer. Phys. Lett., B 38, 519, (1972).

[9] F. Pisano and V. Pleitez, Phys. Rev., D46, 410, (1992).

[10] M. Singer, J. W. F. Valle and J. Schechter, Phys. Rev., D22,.738, (1980).

[11] H. N. Long, Phys. Rev.,D53, 437,(1996).

[12] W. A. Ponce, D. A. Gutierrez and L. A. Sanchez. Phys. Rev. D 69, 055007, (2004).

[13] W. A. Ponce, D. A. Gutierrez and L. A. Sanchez. hep – ph/031243v3, (2004).

[14] W. A. Ponce, J. B. Flores and L. A. Sanchez. hep – ph/0103100v2, (2001).

[15] H. N. Long. hep – ph /9603258v1, (1996).

[16] P. V. Dong, H. N. Long and D. T. Nhung. hep – ph /0604199v2, (2006).

[17] P. V. Dong and H. N. Long. hep – ph/0507155v1, (2005).

[18] T. D. Lee and C. N. Yang. Phys.Rev.,104, 254, (1956).

[19] S. L. Adler. Phys.Rev, 177, 2426, 1968,

[20] R. Delbourgo and A. Salam. Phys. Lett., B40, 381, (1972).

E – mail: nurelmar@gmail.com

Modern Trends in Physics

The axial vector meson-Δ-baryon coupling constant from the hard-wall model of AdS/QCD

SH.A. MAMEDOV[1+], N.J. HUSEYNOVA[1,2*],

[1]*Institute for Physical Problems of BSU, Z.Khalilov 23, Baku, Azerbaijan 1148*

[2]*Theoretical Physics Department of Baku State University, Z.Khalilov 23, Baku, Azerbaijan 1148* *nerminh236@gmail.com; +sh.mamedov62@gmail.com

We consider a_1-meson-Δ-baryon coupling constant in the framework of the hard-wall model of AdS/QCD. The axial vector field is determined by means of gauge fields with left and right chiral symmetry in the bulk of Anti-de Sitter (AdS) space. The profile functions were found from the solution of equations of motion for a_1-meson and Δ-baryons in the bulk of AdS space. According to AdS/CFT correspondence using bulk interaction Lagrangian we derive an integral for the a_1-meson-Δ-baryon $g_{a_1\Delta\Delta}$ coupling constant in the framework of hard-wall AdS/QCD model.

Keywords: axial vector, meson, baryon, coupling constant, hard-wall, AdS/QCD

1. INTRODUCTION

According to Holographic duality there is a correspondence between a string theory in Anti-de-Sitter (AdS) space and the conformal field theory (CFT) in its boundary. AdS/QCD has two models, which are called soft-wall model and hard-wall models of AdS/QCD. Within the framework of the AdS/QCD models, by modifying the theory in the bulk one may try to explain experimental results in different sectors of QCD. So that, the AdS/QCD models are an effective tool for calculation physical effects and quantities, such as coupling constants, decay constants, form-factors, mass spectrum for mesons and baryon and etc.

In the present paper, we will be interested in the hard-wall AdS/QCD model, where the confinement is modeled by the cut off space at the infrared boundary (IR) of AdS space. In the framework of hard-wall models, it is possible to find wave functions, form-factors, coupling constants and etc. for mesons and baryons. We have calculated the a_1-axial-vector meson-Δ-baryon coupling constant within this hard-wall AdS/QCD model.

The paper is organized in the following way. We start with recalling, in Section II, the basics of the hard-wall AdS/QCD model and some results obtained in Ref. [1,2] , we define the bulk geometry of the model, then we briefly present the equations of motion for the axial vector and Rarita-Schwinger fields in the bulk and write profile function for these fields. In Section III, we write a Lagrangian for the axial vector-Δ-baryon interaction in this geometry and according to AdS/CFT correspondence using from the bulk interaction Lagrangian we derive an integral over an extra dimension for the a_1-meson-Δ-baryon $g_{a_1\Delta\Delta}$ coupling constant. At the end, we give numerical results for the a_1-meson-Δ-baryon $g_{a_1\Delta\Delta}$ coupling constant.

2. THE HARD-WALL MODEL

The metric of d+1 dimensional AdS space is given by

$$ds^2 = g_{MN}dx^M dx^N = e^{2A(z)}\left(dz^2 + \eta_{\mu\nu}dx^\mu dx^\nu\right) =$$

$$= \frac{1}{z^2}\left(-dz^2 + \eta_{\mu\nu}dx^\mu dx^\nu\right) \quad \mu,\nu = 0,1,2,\dots,d-1, \tag{1}$$

where $\eta_{\mu\nu} = diag(1,-1,-1,-1)$ is a 4-dimensional Minkowski metric. The mesons are described by 5D fields propagating with the action given by

$$S = \int d^5x \sqrt{g}\mathcal{L}, \tag{2}$$

where $\mathcal{L}$ is a Lagrangian density and $g = |det g_{MN}|$ (M,N=0,1,2,3,z) . The z variable extends from 0, which is called the ultraviolet boundary, to z_M, which is called the infrared boundary [1-6].

AXIAL VECTOR MESON

In the bulk of AdS space there are two gauge fields A_L^M and A_R^M , which transform as a left and right chiral fields under $SU(N_F)_L \times SU(N_F)_R$ chiral symmetry group of the model.

Besides gauge fields there is scalar field *X*, which transforms under bifundamental representation of gauge group $SU(N_F)_L \times SU(N_F)_R$. The chiral symmetry group is broken to the isospin group $SU(2)_V$ due to the interaction of the bulk gauge fields with the scalar field X. The gauge coupling g_5 is fixed by matching the UV asymptotics of current two point function between bulk and boundary theories. From the gauge fields A_L and A_R one can construct a bulk vector $V^M = \frac{1}{\sqrt{2}}(A_L{}^M + A_R{}^M)$ and the axial vector $A^M = \frac{1}{\sqrt{2}}(A_L{}^M - A_R{}^M)$ fields. According to AdS/CFT correspondence of vector field the UV boundary value of Kaluza-Klein (KK) modes of bulk vector field correspond to the vector meson series of the dual theory. In common with vector mesons, the axial vector mesons are the KK modes of the transverse part of the axial-vector gauge field. The axial-vector field consist of transverse $A_\perp^a$ and longitudinal $A_\parallel^a$ components and can be written $A = A_\perp^a + A_\parallel^a$. The longitudinal components have physical meaning and are related to the pion field as $A_{\parallel\mu}^a(x,z) = \partial_M \Psi^a(x,z)$. Action for these fields has a form:

$$S = \int d^5x \sqrt{g}\, Tr\left\{-|DX|^2 + 3|X|^2 - \frac{1}{4g_5^2}Tr(F_V^2 + F_A^2)\right\}. \tag{3}$$

Here 5-dimensional coupling constant is related to the number of colors Nc in the dual theory as: $g_5^2 = \frac{12\pi^2}{N_c} = 2\pi$. We choose the axial-like gauge, $A_5 = 0$, to fix the A_5 component. 4-dimensional components of axial vector field at UV boundary

$(A_\mu(x,z=0))$ correspond to the source of the axial vector current. Fluctuations of the bulk vector field correspond to the axial vector mesons at the boundary. $X(x,z)=v(z)\frac{U(x,z)}{2}$ is a bulk scalar field, $U(x,z)=exp(2it^a\pi^a(x,z))$ is a product of chiral field, $v(z)=\frac{1}{2}(m_q z+\sigma z^3)$, where the coefficient m_q is the mass of u and d quarks and the σ is the value of chiral condensate. The coefficients m_q and σ were established from the UV and IR boundary conditions on the solution for the field X. Expanding $U(x,z)$ in powers of π^a gives the appropriate part of the action:

$$S_{AdS}^{axial}=\int d^5x\sqrt{g}\,Tr\left\{-\frac{1}{4g_5^2 z}+\frac{v^2(z)}{2z^3}(A_M^a-\partial_M\pi^a)^2\right\}. \quad (4)$$

Thus, the S_{AdS}^{axial} Lagrangian is bringing a z-depending mass to break the axial-vector gauge symmetry like Higgs mechanism. It is useful to write the transverse part of bulk axial-vector gauge field $A_{1\mu}^a(x,z)$ in momentum space by help of Fourier transformation. Equation of motion for Fourier components $\tilde{A}_{1\mu}^a(p,z)$ is easily obtained from the action (4) and has the form:

$$\left[z^3\partial_z\left(\frac{1}{z}\partial_z\tilde{A}_\mu^a(p,z)\right)+m_n^2 z^2\tilde{A}_\mu^a(p,z)-g_5^2v^2\tilde{A}_\mu^a(p,z)\right]_\perp=0. \quad (5)$$

The $\tilde{A}_\mu^a(p,z)$ can be written as $\tilde{A}_\mu^a(p,z)=A_\mu^a(p)A(p,z)$ and at UV boundary $A(p,z)$ satisfies the condition $A(p,0)=1$. For the n-th mode $A_n(z)$ in the KK decomposition $A(p,z)=\sum_{n=0}^{\infty}A_n(z)f_n(p)$ with mass $m_n{}^2=p^2$.

$$\left[-\frac{m_n^2}{z}-\partial_z\left(\frac{1}{z}\right)\partial_z+\frac{2g_5^2v^2}{z^3}\right]A_n(z)=0, \quad (6)$$

for solving (6) equation of motion it was used boundary condition as down

$$0=\left(\partial_z+\frac{2g_5^2v^2}{z^2}\right)A_n(z)|_{z=z_m}. \quad (7)$$

Thus the profile function for axial-vector meson in the term of Bessel function is [6,8]

$$A_n(z)=\frac{z\,J_1(m_{a_1}z)}{\sqrt{\int_0^{z_m}dz\,z[J_1(m_{a_1}z)]^2}}. \quad (8)$$

SPIN 3/2 BARYONS IN THE HARD-WALL MODEL OF ADS/QCD

In the hard-wall model, description of Δ-baryons with spin 3/2 in the boundary theory is given by the Rarita-Schwinger fields Ψ_M in the bulk, which were introduced in [3]. For demonstrating profile function for the Δ-baryons field in the bulk of the AdS space, we need to write action for Δ-baryons field, where was not considered interaction with the gauge fields as follows [7,8]:

$$S_{F_1}=\int d^5x\,\sqrt{g}\left(\frac{i}{2}\bar{\Psi}_A\Gamma^{ABC}D_B\Psi_C-m_1\bar{\Psi}_A\Psi^A-m_2\bar{\Psi}_A\Gamma^{AB}\Psi_B\right), \quad (9)$$

where $\Psi_A=e_A^N\,\Psi_M$, $e_A^N=z\delta_A^N$ is the inverse vielbein and the covariant derivative is:

$D_N=\partial_N+\frac{1}{8}\omega_{N\,AB}[\Gamma^A,\Gamma^B]-iV_N$.

Non-zero components of spin connection are: $\omega_{\mu zv}=-\omega_{\mu vz}=\frac{1}{z}\eta_{\mu v}$. 5-dimensional matrices obey the anticommutation relation $\Gamma^{ABC}=\frac{1}{2}(\Gamma^B\Gamma^C\Gamma^A-\Gamma^A\Gamma^C\Gamma^B)$, $\Gamma^{AB}=\frac{1}{2i}[\Gamma^A,\Gamma^B]$ $\{\Gamma^A,\Gamma^B\}=2\eta^{AB}$ and are defined as $\Gamma^A=(\gamma^\mu,-i\gamma^5)$. From the action (9) the equation of motion was obtained as follow:

$$(iz\Gamma^A\partial_A+2i\Gamma^5-m_-))\Psi_\mu=0,\ (\mu=0,1,2,3). \quad (10)$$

After using expressions for the left and right-hand chiral fields $\Psi_{M(R)}=\frac{1}{2}(1+\gamma^5)\psi_m$, $\Psi_{M(L)}=\frac{1}{2}(1-\gamma^5)\psi_m$, the second order differential equations for the profile function was obtained from (10) as

$$\begin{aligned}\left(\partial_z^2-\frac{4}{z}\partial_z+\frac{(6+m-m^2)}{z^2}\right)f_{1L}&=-|P|^2f_{1L}\\ \left(\partial_z^2-\frac{4}{z}\partial_z+\frac{(6-m-m^2)}{z^2}\right)f_{1R}&=-|P|^2f_{1R}\end{aligned}. \quad (11)$$

The n-th normalized Kaluza-Klein mode $f_{L,R}^{(n)}(z)$ of the solutions $f_{L,R}$ with $p^2=m_n^2$ may be expressed in terms of Bessel functions:

$$f_{1L}^n=c_1^n z^{\frac{5}{2}}J_2(pz),\ f_{1R}^n=c_1^n z^{\frac{5}{2}}J_2(pz),$$
$$f_{2L}^n=-c_2^n z^{\frac{5}{2}}J_2(pz),$$
$$f_{2R}^n=c_2^n z^{\frac{5}{2}}J_2(pz), \quad (12)$$

and normalization constants n_{1L} and n_{1R} are found from normalization condition like this [8,9]

$$\int_0^\infty\frac{dz}{z^{2M}}f_{1L}^{(n)}(z)f_{1L}^{(m)}(z)=\delta_{nm},$$

and equal to following one:

$$|c_{1,2}^n|=\frac{\sqrt{2}}{z_m J_2(m_n z_m)}. \quad (13)$$

The profile functions of the first and second bulk fermion fields are related each other like follow:

$$f_{1L}=f_{2R}$$
$$f_{1R}=-f_{2L}. \quad (14)$$

3. CALCULATION OF AXIAL VECTOR MESON-Δ-BARYON COUPLING CONSTANT

A boundary axial vector meson-Δ-baryon coupling constant will be derived from the 5-dimensional action for the interaction in the bulk of the AdS space between axial vector field A_μ with the axial vector current of Δ-baryon $j^{\mu,\alpha}$.

$$S_{int}=\int d^5x\,\sqrt{g}\,\mathcal{L}_{int}. \quad (15)$$

According to the AdS/CFT correspondence classical bulk action S is the generating func-tion Z for the vacuum expectation value of the current in dual 4-dimensional theory at the UV boundary as follows:

$$Z_{AdS}=e^{iS_{int}},$$

$$J_\mu^{AdS}{}_{|z=0}=-i\frac{\delta Z_{AdS}}{\delta A_\mu^0}|_{A_\mu^0=0}=<J_\mu>, \quad (16)$$

where $\tilde{A}_\mu^0=\tilde{A}_\mu(q,z=0)=A_\mu(q)$ is the UV boundary value of the axial vector field (V(z=0)=1) and $J_\mu(p,p)=g_{a_1\Delta\Delta}\bar{u}(p)\gamma_\mu u(p)$.

The interaction Lagrangian $\mathcal{L}_{int}$ is constructed according gauge invariance of the model and consist of three kinds of interaction terms [3,10]

$$\mathcal{L}_{int} = \mathcal{L}^{(0)}_{a_1\Delta\Delta} + \mathcal{L}^{(1)}_{a_1\Delta\Delta} + \mathcal{L}^{(2)}_{a_1\Delta\Delta} . \quad (17)$$

A minimal gauge interaction consists of interaction between axial vector field with the current of vector spinors [3, 7]

$$\mathcal{L}^{(0)}_{a_1\Delta\Delta} = \frac{1}{2}(\bar{\Psi}^M_1 e^M_A \Gamma^M A_M \Psi_{1M} - \bar{\Psi}^M_2 e^M_A \Gamma^M A_M \Psi_{2M}). \quad (18)$$

The non-minimal coupling term between axial-vector field and vector spinors megnetic moment is follow [3] :

$$\mathcal{L}^{(1)}_{a_1\Delta\Delta} = \frac{i}{2} k_1 e^M_A e^N_B (\bar{\Psi}^M_1 \Gamma^{MN} F_{MN} \Psi_{1M} + \bar{\Psi}^M_2 \Gamma^{MN} F_{MN} \Psi_{2M}). \quad (19)$$

We introduce a new interaction term, which has requested invariance [10]

$$\mathcal{L}^{(2)}_{a_1\Delta\Delta} = g_Y e^M_A e^N_B (\bar{\Psi}^M_1 X \Gamma^M A_M \Psi_{2M} + \bar{\Psi}^M_2 X^+ \Gamma^M A_M \Psi_{1M}). \quad (20)$$

After performing the expressions for profile functions in momentum space and applying the holography principle this Lagrangian term gives the following contribution to the $g^{h_1VV}_{a_1\Delta\Delta}$ constant represented in terms of integral over z:

$$g^{(0)nm}_{a_1\Delta\Delta} = \int_0^\infty \frac{dz}{2z^4} A_n(z) \left(f^{(n)*}_{1R}(z) f^{(m)}_{1R}(z) - f^{(n)*}_{1L}(z) f^{(m)}_{1L}(z) \right) , \quad (21)$$

$$g^{(1)nm}_{a_1\Delta\Delta} = k_1 \int_0^\infty \frac{dz}{2z^3} \partial_z A_n(z) \left(f^{(n)*}_{1R}(z) f^{(m)}_{1R}(z) + f^{(n)*}_{1L}(z) f^{(m)}_{1L}(z) \right) , \quad (22)$$

$$g^{(2)nm}_{a_1\Delta\Delta} = 2 g_Y \int_0^\infty \frac{dz}{z^4} A_n(z) v(z) f^{(n)*}_{1L}(z) f^{(m)}_{1R}(z), \quad (23)$$

where $A_n(z) = \frac{z J_1(m_{a_1} z)}{\sqrt{\int_0^{z_m} dz\, z [J_1(m_{a_1} z)]^2}}$ is a profile function for the ground state of a_1-meson, $v(z) = \frac{1}{2} m_q z + \frac{1}{2} \sigma z^3$ and $X(z) = v(z)(1 + iP)$ is a scalar field. $k_1 = -0.98$ [3], $z_M = \frac{1}{0.32}$, $\sigma = (0.311)^2$, $m_q = 0.00234$, $g_Y = 9.182$ [5, 6].

So, in the hard-wall model we shall describe the a_1-meson- Δ-baryon $g^{h_1VV}_{a_1\Delta\Delta}$ coupling constant as the sum of three terms as follow:

$$g^{h_1VV}_{a_1\Delta\Delta} = g^{(0)nm}_{a_1\Delta\Delta} + g^{(1)nm}_{a_1\Delta\Delta} + g^{(2)nm}_{a_1\Delta\Delta}, \quad (24)$$

but we shall calculate numerical results of these terms separately to clear relative contri-butions of different terms of coupling lagrangian.

To calculate numerical value of the a_1-meson- Δ-baryon $g^{h_1VV}_{a_1\Delta\Delta}$ coupling constant within the hard-wall model of AdS/QCD, we must carry out the integral expressions for this coupling constant (21), (22), (23). For this aim,we use "MATEMATİCA 9" program. Then we generalize obtained results for $g^{h_1VV}_{a_1\Delta\Delta}$ in the table as follows down.

Table 1. *a_1-meson-Δ-baryon $g^{h_1VV}_{a_1\Delta\Delta}$ coupling constant within the hard-wall model of AdS/QCD*

n	m_Δ (GeV)	$g^{(0)}_{a_1\Delta\Delta}$	$g^{(1)}_{a_1\Delta\Delta}$	$g^{(2)nm}_{a_1\Delta\Delta}$	$g^{h_1VV}_{a_1\Delta\Delta}$
0	1.232	-0.983	8.197	10.102	17.316
1	1.700	0.263	4.231	6.658	11.153
2	1.920	0.473	2.232	2.684	5.389

4. CONCLUSIONS

1. a_1-meson-Δ-baryon $g^{h_1VV}_{a_1\Delta\Delta}$ coupling constant is calculated in the framework of the hard-wall model of AdS/QCD. Unfortunately, there is no experimental and theoretical data for $g^{h_1VV}_{a_1\Delta\Delta}$ coupling constant, in the both – ground and excited states of the Δ-bar-yons. So, we can not get compare for these results.

.

2. The contributions of $g^{(1)nm}_{a_1\Delta\Delta}$ and $g^{(2)nm}_{a_1\Delta\Delta}$ to $g^{h_1VV}_{a_1\Delta\Delta}$ coupling constant is more larger than the one coming from $g^{(0)nm}_{a_1\Delta\Delta}$, which are consistently coming from the (19), (20) and (18) interaction lagrangians. The value of $g^{h_1VV}_{a_1\Delta\Delta}$ decreases as a number of excitation n for Δ-baryons increases.

REFERENCES

1. A.Karch, E. Katz, D.T.Son and M.A. Stephanov, J. Phys. Rev.D, **74**, 015005 (2006)

2. D.K. Hong, T.Inami and H.U. Yee, J. Phys. Lett. B, **646**, pp.165-171 (2007)

3. H.C. Ahn. D.K. Hong, C.Park and S. Siwach, J. Phys. Rev.D **80**, 054001 (2009)

4. H.R. Grigoryan and A.V. Radyushkin, J. Phys. Rev.D, **76**, 095007 (2007)

5. J,Erlich, E.Katz, D.T.Son and M.A.Stephanov, J. Phys. Rev. Lett., **95**, 261602 (2005)

6. N. Maru and M. Tachibana , J. Eur. Phys. J. C, **63**, pp. 123-132 (2009)

7. N.Huseynova, Sh. Mamedov, J. Int. J.Th. Phys., **54**, pp. 3799-3810, (2015)

8. T. Gherghetta, J.I. Kapusta and T.M. Kelley, J. Phys. Rev. D, **79**, 076003(2009)

9. Z. Abidin and C.Carlson, J. Phys. Rev. D, **79**, 115003 (2009)

10. Sh. Mamedov, B. Sirvanli, I. Atayev and N. Huseynova, Int. J. Theor. Phys., **56** (6), pp. 1861-1874 (2017)

Inflationary Cosmology in the Gauged Nambu-Jona-Lasinio Model

T. INAGAKI
Information Media Center and Core of Research for the Energetic Universe, Hiroshima University, Higashi-Hiroshima, 739-8521, Japan

The inflationary cosmology is studied in the gauged Nambu-Jona-Lasinio model. Starting from the quasi de-Sitter stage, we evaluate the exit period from the inflation and calculate the thermal fluctuations of the cosmic microwave background. As a characteristic feature of the model, we show the weak gauge coupling limit of the produced CMB fluctuations. The dynamical mechanism of the CP violation is proposed at the inflation era.

Keywords: *Gauged Nambu-Jona-Lasinio model, Inflation, CBM fluctuations*

1. Introduction

Since the discovery of the expanding universe through measuring the red shift of the spectral lines from distant galaxies by E. Hubble in 1929, it is considered that the early universe is in extreme conditions, i.e. high density and high temperature state. When the universe had cooled to the recombination temperature, the protons capture the free electrons and the universe is filled with neutral atoms. After the charged particles are bound in neutral atoms, the universe becomes transparent to radiation. The released photon survives for the age of the universe. A. Penzias and R. W. Wilson discovered the relic photon as the cosmic microwave background (CMB) in 1965. Nowadays the fluctuations of the Cosmic Microwave Background (CMB) is precisely observed by Planck satellite [1].

There are well-known problems in a simple big-bung cosmology, horizon problem, flatness problem, monopole problem, singularity problem and so on. Primordial inflation, an exponential expansion of the early universe, gives a solution for such cosmological problems. A broad class of the particle physics models have been proposed as practical models of the inflation theory. For example, the potential energy of the Higgs like scalar can induce the inflationary expansion in early universe. However, there is not a small possibility where composite states constructed by fermion fields dominate the energy density of the early universe [2-5].

It is considered that the fluctuation of CMB is originally generated by the quantum fluctuation of the inflaton field which induces the inflation. There is a possibility to test the model of inflation from the thermal fluctuation of CMB. Thus, we have lunched a plan to find a fermionic model of inflation and test the model by observing the CMB fluctuations. In this paper, we consider the gauged Nambu-Jona-Lasinio (gNJL) model as a simple prototype model of composite scalar. Evaluating the CMB fluctuations, we show a characteristic feature of the model. A possibility of the CP violation and the domain wall problem are discussed.

2. gNJL model

Here we consider that the inflationary expansion induced by a meson like composite state constructed by the fermion and anti-fermion. Since the low energy phenomena of light mesons is well described by gNJL model, we start from a scale up model of the gNJL model [6-14],

$$\mathcal{L}_{\rm gNJL} = \mathcal{L}_{\rm gauge} + \bar{\psi} i \not{D} \psi + G_4 \left[(\bar{\psi}\psi)^2 + (\bar{\psi} i \gamma^5 \tau^a \psi)^2 \right], \quad (1)$$

where $\mathcal{L}_{\rm gauge}$ represents the Lagrangian for the $SU(N_c)$ gauge theory with the coupling, α, G_4 is the four-fermion coupling and τ^a denote the generators of the flavor symmetry, $SU(N_f)$.

The model can be rewritten by the composite scalar and the pseudo scalar fields with Yukawa interactions below the compositeness scale, Λ. We assume that the composite scalar field σ dominates the vacuum energy density and omit the parts with gauge fields, fermions and pseudo scalars. Solving the renormalization group equations, the composite scalar field σ is found to obey the action [15-18],

$$S = \int d^4x \sqrt{-g} \left[-\frac{1}{2} R + \frac{1}{2} g^{\mu\nu} \partial_\mu \sigma \partial_\nu \sigma - V(\sigma) \right], \quad (2)$$

where we employ the reduced Planck unit, $M_{\rm Planck} = 1$. Imposing the compositeness conditions at the scale, Λ, and neglecting the running of the gauge coupling, we obtain the explicit expression for the renormalization group improved effective potential. At the leading order, it is given by

$$V(\sigma) = \frac{B}{2}\sigma^2 + \frac{C_1}{4}\sigma^{\frac{4}{1+A\alpha}} - \frac{C_2}{4}\sigma^4 + \frac{RD_1}{12}\sigma^{\frac{2}{1+A\alpha}} - \frac{RD_2}{12}\sigma^2, \quad (3)$$

with the functions,

$$A \equiv \frac{3(N_C^2-1)}{4\pi N_C}, \quad (4)$$

$$B \equiv \frac{4\pi^2 A\alpha}{N_f N_C G_{4r}} \frac{(\mu^2/\Lambda^2)^{A\alpha}}{1-(\mu^2/\Lambda^2)^{A\alpha}}, \quad (5)$$

$$C_1 \equiv \frac{N_f N_C \mu^4}{8\pi^2}\left(3+\frac{1}{A\alpha}\right)\left[\frac{8\pi^2}{N_f N_C \mu^4}\frac{A\alpha}{1-(\mu^2/\Lambda^2)^{A\alpha}}\right]^{2/(1+A\alpha)}, \quad (6)$$

$$C_2 \equiv \frac{8\pi^2 A\alpha}{N_f N_C}\left[\frac{(\mu^2/\Lambda^2)^{A\alpha}}{1-(\mu^2/\Lambda^2)^{A\alpha}}\right]^2, \quad (7)$$

$$D_1 \equiv \frac{N_f N_C \mu^2}{8\pi^2}\left(1+\frac{1}{A\alpha}\right)\left[\frac{8\pi^2}{N_f N_C \mu^2}\frac{A\alpha}{1-(\mu^2/\Lambda^2)^{A\alpha}}\right]^{2/(1+A\alpha)}, \quad (8)$$

$$D_2 \equiv \frac{(\mu^2/\Lambda^2)^{A\alpha}}{1-(\mu^2/\Lambda^2)^{A\alpha}}, \quad (9)$$

where G_{4r} denotes the renormalized four-fermion coupling at the renormalization scale μ.

In practical calculations, it is more convenient to study the inflationary cosmology in the Einstein frame. We apply the Weyl transformation, $\tilde{g}^{\mu\nu} = \Omega^{-2}(x) g^{\mu\nu}$,with the Weyl factor,

$$\Omega^2(x) \equiv 1 + \frac{D_1}{6}\sigma^{\frac{2}{1+A\alpha}} - \frac{D_2}{6}\sigma^2. \quad (10)$$

Then the action reduces to [3]

$$S = \int d^4x \sqrt{-\tilde{g}} \left[-\frac{1}{2}\tilde{R} + \frac{1}{2}\tilde{g}^{\mu\nu}\partial_\mu\varphi\partial_\nu\varphi - V_E \right], \quad (11)$$

with the effective potential

$$V_E = \Omega^{-4}(x)\left(\frac{B}{2}\sigma^2 + \frac{C_1}{4}\sigma^{\frac{4}{1+A\alpha}} - \frac{C_2}{4}\sigma^4\right). \quad (12)$$

In order to have a canonical kinetic term we redefine the scalar field by

$$\frac{d\varphi}{d\sigma} = \left[\frac{1}{\Omega^2} + \frac{3}{2}\left(\frac{d\Omega^2/d\sigma}{\Omega^2}\right)^2\right]^{1/2}. \quad (13)$$

We evaluate the evolution of our universe from the effective action (11) in the Einstein frame.

3. gNJL inflation

Here we confine ourselves in a homogeneous and isotropic expanding universe described by Friedmann-Lemaitre-Robertson-Walker (FLRW) metric. In a locally flat FLRW universe the equation of motion for φ and the Friedmann equation are given by

$$\ddot{\varphi} + 3\frac{\dot{a}}{a}\dot{\varphi} = -\frac{\partial V_E}{\partial\varphi}, \quad (14)$$

$$3\left(\frac{\dot{a}}{a}\right)^2 = \frac{1}{2}\dot{\varphi}^2 + V_E, \quad (15)$$

with the scale factor a. Here we employ the slow roll chaotic inflation scenario. As is shown in Fig. 1, we assume that the composite scalar, φ, develops a large field variable and the variable is slowly varying at the beginning of the universe. Thus, we set $\dot{\varphi}^2 \ll V_E$ in the Friedmann equation (15) and obtain an exponentially expanding solution,

$$a(t+\Delta t) \sim a(t) e^{\sqrt{V_E/3}\Delta t}. \quad (16)$$

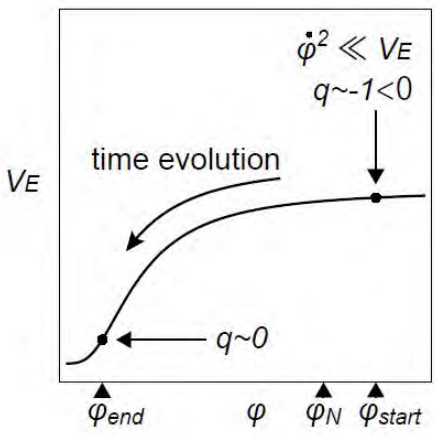

Fig. 1. Schematic image for the slow roll chaotic inflation scenario.

At $\varphi = \varphi_{start}$ the potential energy, V_E, plays a role of the cosmological constant and the inflation starts. We find that the deceleration parameter, $q \equiv -\frac{a\ddot{a}}{\dot{a}^2}$, is almost -1 at the very beginning, $\varphi = \varphi_{start}$. According to the equation of motion (14) the field variable φ rolls down on the slope of the potential. Then the deceleration parameter vanishes $q \sim 0$ and the universe exits from the quasi de-Sitter phase at $\varphi = \varphi_{end}$. We also denote the field variable at the horizon crossing as $\varphi = \varphi_N$ which can be fixed to generate a suitable e-folding, $a(\varphi_{end}) = a(\varphi_N)e^N$ with $N = 50 \sim 60$.

One of evidences of the primordial inflation is found in the thermal fluctuations of CMB. It is considered that the origin of the scalar type fluctuation is introduced by the quantum fluctuation of the field φ. The tensor type fluctuation can be generated from the quantum fluctuation of the space-time. Thus, the non-vanishing tensor type fluctuation shows an existence of the primordial gravitational wave. The fluctuations are approximately expressed by the power spectra,

$$P_R(k) \equiv A_R\left(\frac{k}{k_0}\right)^{n_s - 1}, \quad (17)$$

for a scalar mode and

$$P_t(k) \equiv A_t\left(\frac{k}{k_0}\right)^{n_t}, \quad (18)$$

for a tenser mode.

Since the CMB fluctuations depend on the details of the potential V_E, the model parameters in the effective potential, N_f, N_c, G_{4r}, α, μ and Λ are fixed to generate the observed values of CMB which are shown in Tab. 1.

Tab. 1. Observed fluctuations with $k_0 = 0.05\text{Mpc}^{-1}$ [1].

$\ln(10^{10}A_R)$	3.094 ± 0.034	(68%CL)
n_s	0.9645 ± 0.0049	(68%CL)
$r \equiv \frac{P_t(0.002Mpc^{-1})}{P_R(0.002Mpc^{-1})}$	≤ 0.01	(95%CL)

4. Weak gauge coupling limit

The CMB fluctuations in the gNJL model can be evaluated according to the following procedure. In the slow roll approximation, the end of the inflation can be estimated by calculating the deceleration parameter. The initial value of the field configuration is fixed to generate a suitable e-folding. Then we evaluate time evolution of the scalar and tensor fluctuations.

Systematic analysis of the model parameter dependence of the CMB fluctuations has been presented in Refs. [3] and [4]. Here we focus on the characteristic behaviour of the gNJL model. In Fig. 2 we illustrate the weak coupling

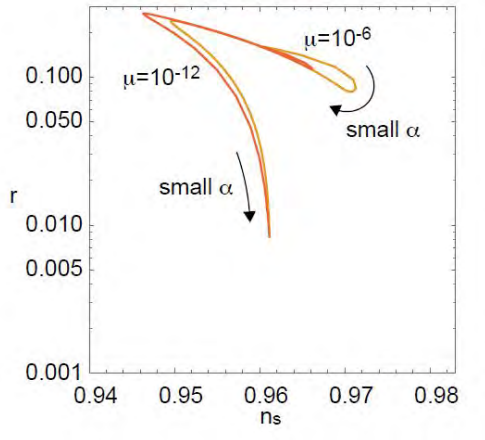

Fig. 2. Weak gauge coupling limit of the tensor-to-scalar ratio, r, as a function of the spectral index, n_s, for $N_f = 1$, $N_c = 2$, $G_{4r} = 10^{10}$, $\Lambda \gg 1$, $N = 50$ at $\mu = 10^{-6}$ and 10^{-12}.

limit of the CMB fluctuations on the tensor-to-scalar ratio, r, and the spectral index, n_s, plane. It is found that the values approach to a fixed point at the large compositeness scale, $\Lambda \gg 1$, and the weak coupling limits, $\alpha \ll 1$ [19],

$$r = \frac{24}{N^2} + O\left(\frac{1}{N^3}\right), \tag{19}$$

$$n_s = 1 - \frac{2}{N} + O\left(\frac{1}{N^2}\right). \tag{20}$$

At the large compositeness scale a consistent curvature perturbation A_R is obtained for a weak coupling, $\alpha \sim O(10^{-12})$. The results at the weak gauge coupling limit are consistent with the current observation of the CMB.

5. Origin of the CP violation

CP violation is observed in rare decay processes of K and B mesons. It is described by phases appearing in the Yukawa coupling in the standard model of the particle physics. The phases are introduced as free parameters in the standard model. On the other hand, there is no theoretical reason to prohibit the CP violating θ-term in QCD. The term can be generated from the phase in the Yukawa coupling and strongly constrains $\theta < 10^{-9}$ by the experimental upper bounds of the electric dipole moment. It is called the strong CP problem.

One of the origins of the CP violation is proposed by introducing complex expectation values for the Higgs filed [20]. The idea is applied to one of the composite Higgs models, the technicolor models [21-24]. CP symmetry is violated by the technicolor dynamics. In Ref. [23] we present a special solution to violate CP without introducing the strong CP problem. In these models, the CP symmetry is violated at the electroweak scale.

The violation of a discrete symmetry produces a stable domain wall. The cosmological domain wall has unacceptable contribution to the energy density of the universe. One of the known solution of the domain wall problem is given by the inflationary expansion. If the discrete symmetry is broken before the inflation, the produced domain wall can be removed away from the horizon after the inflation.

It is quite natural to push forward the idea of the dynamical CP violation from the electroweak scale to the inflation scale. Because of the flavor symmetry, $SU_L(N_f) \otimes SU_R(N_f)$ in the Lagrangian (1), all the fermions develop an equal vacuum expectation values at the minimum of the effective potential. The CP symmetry cannot be broken. Flavor symmetry breaking terms are necessary to introduce the mass hierarchy for the fermions. We assume a presence of a flavor symmetry breaking but the CP conserving term L'. According to the mechanism proposed in Refs. [23, 24], the term generates complex expectation values for the composite operators constructed by the fermion and the anti-fermion. The CP symmetry is broken near the minimum of the effective potential.

Here we employ the chaotic inflation scenario where the field variables of the composite operators are chaotic before the inflation. Thus, we assume that the variables have non-vanishing phases. The space dependent phases can construct a domain wall structure and fix the vacuum state interior of the domain wall. After the inflation, the domain wall is away from the horizon and the CP symmetry is broken by the complex vacuum expectation values.

Since we start form the CP conserving Lagrangian, there is no CP violating θ-term. The electric dipole moments produced by the dynamically generated CP violating interactions are suppressed by the inflation scale.

6. Discussions

The typical mass scale of the inflation is Planck scale. In the present analysis, we consider the compositeness scale larger than the Planck scale. There is a field theoretical problem above the Planck scale where we cannot neglect higher dimensional operators. For example, the operator $(\bar{\psi}\psi)^{2n}$ introduces σ^{2n} term in the effective potential. It can introduce an additional inflection point for the potential and enlarge the consistent parameter range of the model.

Above the Planck scale, the quantum gravity (QG) effect may have a unignorable contribution to the origin of the CMB fluctuations. It seems to produce the tensor type fluctuation. In Ref. [25] the QG effect is evaluated in the renormalizable conformal gravity. Though the result is obtained in a specific model of the modified gravity, a small tensor type fluctuation is predicted at high energy.

Finally, we shortly discuss the reheating process after the inflation. The inflationary expansion immediately cools down the Universe. We need a mechanism to heat up the Universe after inflation. The inflaton field roll down and the space-time exits from the inflation era. The potential energy of the inflaton is released through the decay process of the inflaton into light particles. The reheating temperature depends on the interaction between the inflaton field and the light particle. If we assume a Yukawa type coupling between the inflaton field and the light fermion, we obtain the reheating temperature proportional to the Yukawa coupling,

$$T_R = 0.2 y_h \sqrt{\frac{B}{8\pi}}, \tag{21}$$

To obtain GUT scale temperature for a perturbative Yukawa coupling $y_h < 1$, we obtain a constraint for the coupling constants in the gNJL model.

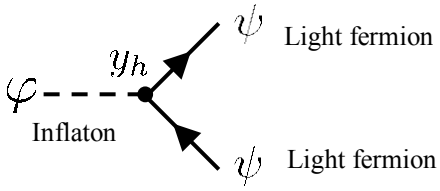

Fig. 3. Yukawa type interaction between the inflaton and the light fermion.

7. Conclusions

One of the possible environments where the high-energy physics near the Planck scale can be tested is found in the astrophysical observations of the early universe. There are several observations which cannot be explained in the standard model of the particle physics. Here I assume a fermionic model at early universe.

I have employed the gNJL model as one of a prototype model of the inflation theory and calculated the CMB fluctuations in the model. From the analysis of the CMB fluctuations, we have found that the model has an interesting weak gauge coupling limit. We also show explicit expression of the CMB fluctuations at the large compositeness scale and the weak coupling limit. It is one of characteristic feature of the gNJL model.

In this paper, we consider the four-fermion interaction, the gauge interaction and the Yukawa type interaction. Near the Planck scale we should consider the interactions described by the higher dimensional operators and the QG effect. The interaction with light fermion is expected to contribute not only the reheating temperature but also some process observed by high-energy experiments. Since the gNJL model can introduce the dynamical origin of the CP violation, CP violating rare processes are especially interesting. I continue the work further and hope to report on these problems.

Acknowledgements The work is supported in part by JSPS KAKENHI Grant Number JP26400250. The author would like to thank S. D. Odintsov and H. Sakamoto for fruitful discussions.

References

[1] P. A. R. Ade et al. [Planck Collaboration], Astron. Astrophys. **594**, A20 (2016).
[2] P. Channuie, Nucl. Phys. B **892**, 429 (2015).
[3] T. Inagaki, S. D. Odintsov, H. Sakamoto, Astrophys. Space Sci. **360**, 67 (2015).
[4] T. Inagaki, S. D. Odintsov, H. Sakamoto, Nucl. Phys. B **919**, 297 (2017).
[5] P. Channuie and C. Xiong, Phys. Rev. D **94**, 043521 (2017).
[6] Y. Nambu and G. Jona-Lasinio, Phys. Rev. **122**, 345 (1961); Phys. Rev. **124**, 246 (1961).
[7] V. A. Miransky, "Dynamical Symmetry Breaking in Quantum Field Theories", World Scientic (1993).
[8] M. Harada and K. Yamawaki, Phys. Rept. **381**, 1 (2003).
[9] K. i. Kondo, S. Shuto and K. Yamawaki, Mod. Phys. Lett. A **6**, 3385 (1991).
[10] K. i. Kondo, M. Tanabashi and K. Yamawaki, Prog. Theor. Phys. **89**, 1249 (1993).
[11] K. Kondo, M. Tanabashi and K. Yamawaki, Mod. Phys. Lett. A **8**, 2859 (1993).
[12] C. N. Leung, S. T. Love and W. A. Bardeen, Nucl. Phys. B **273**, 649 (1986).
[13] C. N. Leung, S. T. Love and W. A. Bardeen, Nucl. Phys. B **323**, 493 (1989).
[14] M. Harada, Y. Kikukawa, T. Kugo and H. Nakano, Prog. Theor. Phys. **92**, 1161 (1994).
[15] W. A. Bardeen, C. T. Hill and M. Lindner, Phys. Rev. D **41**, 1647 (1990).
[16] C. T. Hill and D. S. Salopek, Annals Phys. **213**, 21 (1992).
[17] B. Geyer and S. D. Odintsov, Phys. Rev. D **53**, 7321 (1996).
[18] B. Geyer and S. D. Odintsov, Phys. Lett. B **376**, 260 (1996).
[19] T. Inagaki, S. D. Odintsov, H. Sakamoto, in writing.
[20] S. Weinberg, Phys. Rev. Lett. **37**, 657 (1976).
[21] E. Eichten, K. D. Lane, J. Preskill, Phys. Rev. Lett. **45**, 225 (1980).
[22] W. Goldstein, Nucl. Phys. B **213**, 477 (1983); B **229**, 157 (1983).
[23] S. Hashimoto, T. Inagaki and T. Muta, Phys. Rev. D **48**, 1301 (1993).
[24] T. Inagaki, Nucl. Phys. Proc. Suppl. **37A**, 197 (1994).
[25] K. j. Hamada and M. Matsuda, Phys. Rev. D **93**, 064051 (2016).

inagaki@hiroshima-u.ac.jp

Formation and Evoltion of Sustainable Dynamic System in Mathematical Models of the Theory of Population of Families of Small Bodies

[1]G.T. ARAZOV, [2]T.G ALIYEVA
[1]Institute of Applied Mathematics of Baku State University
[2]Institute of Physical Problems of Baku State University

This paper shows that the formation and evolution of the dynamic system is the result of population of stable and unstable orbits of primary fragment -clots- oddments of relict substances and their families, with special initial conditions. Each fragment-clot-oddment of the relict substance has their original chemical composition and primary physical structures. They define their place in space, as well as the stability or in-stability of their orbits, which became the foundation and the building material of formation of the Sun and planets. The forces of attraction and bombardment by small bodies govern the laws of the evolution of increase of mass and internal energy processes. As a result, the fragments with stable orbits eventually become massive at the expense of fragments with unstable orbits. Areas of stable and unstable movements and formations, i.e. regional populations of celestial bodies, have been discovered in the solar system. As a result of this, the observed system appeared. This process continues today in the form of the bombardment by small bodies and their families of the Sun and the planets, including the Earth.

Keywords: *dynamic system; mathematical modeling; population of small bodies.*

1. Introduction

We know that the sun, moon and the whole universe is involved in the formation and evolution of both external shape and internal structure of the Earth and other bodies. These processes take place under the influence of two forces: 1) forces sum of which are greater than the sum of the errors of observed assessments (values). They always countable and can be expressed as: $\sum_{i=1}^{n} F_i(x,t)$, $\left(n<\infty,\ x\in(x_i,\ x_{i+1}),\ t\in(t_i,\ t_{i+1})\right)$. They are identifiable with the help of mathematical modeling. 2) forces, sum of which are less than the observational errors. These forces are hidden and are involved in all of abnormal phenomena. They are elusive. Their amount can be expressed as: $\sum_{j=1}^{\infty} R_j(x,t)$. For all dynamic systems the following equality is true:

$\min\left(\sum_{i=1}^{n} F_i(x,t)\right)=\max\left(\sum_{j=1}^{\infty} R_j(x,t)\right)$. In other words [1], $\sum_{j=1}^{\infty} R_j(x,t)\le O-C<\sum_{i=1}^{n} F_i(x,t)$, where O - the result of estimates found from observations, C - the result obtained from the calculation according to the formulas of mathematical modeling. The sum $\sum_{j=1}^{\infty} R_j(x,t)$ displays itself only when resonance phenomena formed between some of its components i.e. when the frequenciesof components phenomena become commensurable. Such phenomena are usually called abnormal phenomena of nature and expressed in the form of chaos or catastrophe. Everything that happens in the universe is under the influence of these two sums of forces.

In $F=\sum_{i=1}^{n} F_i(x,t)$, $(n<\infty)$ and F- is a limited sum. All of the observed processes, phenomena, formation and development of the patterns in the nature are a reflection of this function. $R=\sum_{j=1}^{\infty} R_j(x,t)$, is the sum of infinitesimal actions (disturbances). All abnormal phenomena, processes, formation and development of patterns of disasters is a reflection of actions of this sum. This happens when the frequency of components of the sum become commensurable. Under the influence of forces $K(x,t)=\sum_{i=1}^{n} F_i(x,t)+\sum_{j=1}^{\infty} R_j(x,t)$, all bodies in the universe are in a state of great tension. Characteristic indicators of space regions are also subject to such impacts. This is particularly often observed in abnormal natural phenomena such as earthquakes, volcanic eruptions, tsunamis, etc. if the Earth is considered as an example. In [2] it is shown that if we take for granted the principle observed in the nature that "variability of the process of cyclic formation, distribution and evolution of mass and energy is constant, then the absence of the beginning and the end of time, i.e.absence of birth of nature, can be proved. "This implies, that in the nature, observed objects, processes, phenomena, including chaos and catastrophe, exist as a flow of huge waterfall. Such compactness of bodies, processes and events in time, can only exist if they are connected and organize a unified automated system. It is managed by unified patterns of birth, existence, evolu-

tion, chaos and catastrophes. In this paper, as an example, the dynamic system is considered the basic properties of which coincide with the main characteristic parameters of the observed Solar System. They as follows [3]. 1) The orbits of all the planets are in the Solar equatorial plane; 2) The planets move around the Sun in orbits close to circular; 3) The direction of rotation around the Sun is the same for all the planets and coincides with the direction of rotation of the Sun and planets' own rotation (except Venus and Uranus) around the axes; 4) 99.8% of the mass of the Solar system falls on the Sun and 0.2% for the planets, while the planets have 98% of the angular momentum throughout the Solar system; 5) Planets are divided into two groups, sharply differing in the average density.

2. Boundary Values of the Formation and evolution of Stable Dynamic System in the Mathematical Models of the Theory of Families of Populations of Small Bodies

Comparative analysis of the results of observations of small Solar system bodies indicate that their orbits, depending on their initial conditions and the movement regions can be divided into two groups: stable and unstable. According to the theory of stability of motion [4], stable orbits under small perturbations, maintain their state, while the unstable orbit are subject to dissipation of energy and can become a cause of joining with other objects, chaos and catastrophes. It is assumed that, there was a large fragment in the center of "Solar system", and there were fragments with stable orbits in the orbits of the planets. Bodies with unstableorbits, eventually, joined the central fragment and the fragments with stable orbits. And eventually, this led to formation of the Solar planetary system we observe today. This process is still ongoing in the form of counter-bombardment or joining small bodies with the Sun and the planets.

Analysis of the set of observed facts shows that the space of the currently existing Solar system could be filled with some of the fragments and their families [5, 6]. Central configurations observed in the present, various phenomena and processes comply with the applicable patterns of development. Mathematical modeling of these processes is the only key to unlocking truths, clarifying the past and the future of configurations of bodies, phenomena and processes we observe today. Each particle of the Solar system is in motion under the influence of the sum of the forces of both the system itself and the Universe. Some of them are changing continuously, and others, as a result of a variety of chaos and catastrophes are of discrete nature. Various bodies of the solar system have different weights, sizes, locations, temperature, composition, internal structure and external forms, and they are in different aggregate states and energy. The observed state of the Solar system is a consequence of the patterns of development of the system, fragments and their evolution throughout its existence.

Thus, a space, i.e. the entire universe, divided into specific subspaces with stable and unstable properties. New objects are formed in them, with the special characteristic properties. This includes processes such as the birth of the Sun, the planets, including the planet Earth with all its features. For example, it took (4,6 ± 0,2) 10^9 *years* for the formation of today observed Earthfrom primary fragments-clot-oddment of relict substance. As for how these processes occur in various embodiments, these phenomena were studied in detail in [5; 7; …, 11], and in other sources of development of patterns, education and evolution of the Earth, Solar system and Universe.

Normal and chaotic motions (including abnormal phenomena) are always nearby. And the latter is subtly pursuing the former. They are usually subtle and manifest themselves only when the commensurability arise between the frequencies of components.

Dependencies between the mass and the temperature in its center, as well as the relationship between the amount of the central body mass and stability of orbits around the various bodies indicate the stability of a dynamic system. Therefore, the stable Solar dynamic system we observe today was being formed during 10^9 *years*. At the same time, its stability can be destroyed because to the resonance between its components or because of entrance into it of external perturbing forces.

As an example, the behavior of one embodiment of the process of the birth and evolution of a dynamical system is shown in Figures 1-3, [8]. They are in good agreement with the earlier results of various authors [5; 7; …, 11]. Detailed analysis of the choice of the initial conditions of the problem as well as the possible patterns of development of its various stages can be found in [9; 11].

From figures 1-3, [9] it follows that at the time of the formation and evolution of the observed Solar dynamic system it did not include the large disturbing objects. There were not large resonance phenomena between its components. Maybe there were, but they were minor and had only local character. They did not have an impact on the dynamics of the processes of formation and evolution of the Solar system.

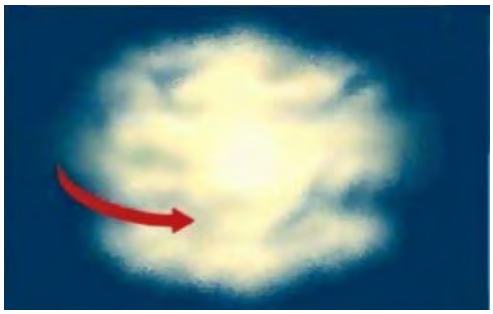

Figure 1. Formation of cluster sets of particles families.

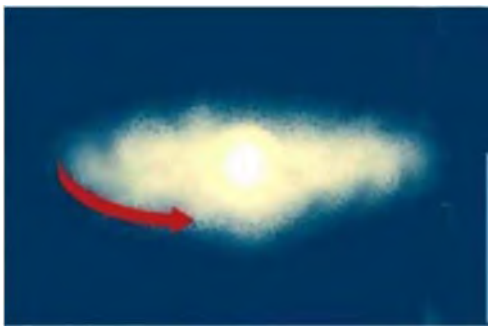

Figure2. Formation of cluster sets of small bodies families

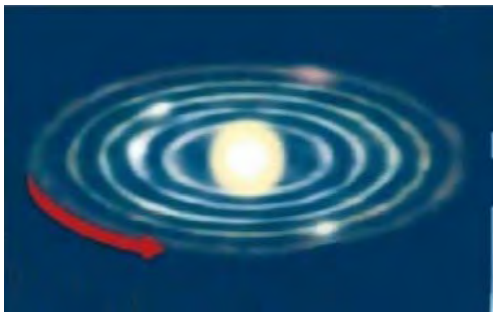

Figure3. Formation of stable dynamical system.

3. Conclusions

From figures 1-3, [9] it follows that at the time of the formation and evolution of the observed Solar dynamic system it did not include the large disturbing objects. There were not large resonance phenomena between its components. Maybe there were, but they were minor and had only local character. They did not have an impact on the dynamics of the processes of formation and evolution of the Solar system.

References

1. G.T. Arazov and T.H. Aliyeva "Advances in Research, Chaos and Boundary Values Problems of Mathematical Models of Nonautonomous Dynamical Systems", p. 230-234 (2015)
2. G.T. Arazov Time in mathematical modeling of dynamical systems. News of Baku University. Physico-Mathematical Sciences. p. 173-177(2013)
3. I.A. Klimishin "Astronomy today".Moscow, 560 p.(1986)
4. A.M. Lyapunov "The general problem of stability of motion". Moscow. Gostehzdat.471 p. (1959)
5. S.U. Carey "In search of the laws of development of the Earth and Vselennoy". Moskva. Peace. 447 p. (1991)
6. G.T.Arazov, S.A Ganiev., A.G. Novruzov "Evolution of the external form and internal structure of the Earth". Baku, Elm 193 p.(2006).
7. Abraham Loeb and R. Steven Furlanetto. "The first galaxies in the Universe". Prinston University Press. Prinston and Oxford. 540 p.(2013)
8. Oded Regev. Chaos and complexity in Astrophysics, Cambridge University Press. 455 p. (2006)
9. V.S.Safronov "The evolution of the protoplanetary cloud and Earth and planetary formation". Moscow. Science. 347 p.(1969)
10. Y.S.Sun, L.Y. Zhou "From ordered to chaotic motion in Celestial Mechanics". Nanjing University, China. World Scientific. 405 p.(2016)
11. Zeleniy L.M., Zakharov A.V., Ksanfomaliti L.V. 2009. Researches of the solar system, the state and prosnpects.Moscow. Science, Russian Academy of Sciences, Volume 179, №10, p. 1118-1140.

arazov_h@yahoo.com

General aspects on pair creation by peak electric field

T.C. ADORNO[1], C.P. GAVRILOV [3]and D.M. GITMAN[1,2,4]

[1] Department of Physics, Tomsk State University, Lenin Prospekt 36, 634050, Tomsk, Russia;

[2]Instituto de Fisica, Universidade de Sao Paulo, Caixa Postal 66318, CEP 05508-090, Sao Paulo, S.P.,Brazil;

[3] Department of General and Experimental Physics, Herzen State Pedagogical University of Russia, Moyka Embankment 48, 191186 St. Petersburg, Russia;

[4]P. N. Lebedev Physical Institute, 53 Leninskiy prospekt, 119991, Moscow, Russia.

Differential and total quantities underlying the vacuum instability by the so-called peak field are further explored, in particular, in the slowly varying field configuration.

Keywords: *QRD*

1. Introduction

In a series of works of the present authors [1] we discussed particle creation from the vacuum by time-dependent exponential electric fields in the framework of QED with external fields [3, 4]. In this article, prepared for the proceedings, we detail the main aspects of vacuum instability by peak electric field, characterized by a time-dependent electric field directed along a fixed direction[1] $E(t) = (E^i(t) = \delta^i_1 E(t). \quad i = 1,..., D$

$$E(t) = E\begin{cases} e^{k_{1i}t}, & t \in I, \\ e^{-k_2 t}, & t \in II, \end{cases} \tag{1}$$

provided by the vector potential

$$A_x(t) = E\begin{cases} k_1^{-1}\ (-e^{k_{1i}t} + 1), & t \in I, \\ k_2^{-1}\ (e^{-k_2 t} - 1), & t \in II, \end{cases} \tag{2}$$

where I = (-∞,0], II = (0, +∞) stands for time intervals where the peak electric field grows exponentially from the infinitely remote past (switching-on at t = -∞) and decreases exponentially to the infinitely remote future (switching-off at t =+∞), respectively. Here k_1, $k_2$are positive constants with k_1^{-1}, k_2^{-1} representing scales of time duration for the increasing and decreasing phases of the electric field.

The Dirac equation[1]

$$i\partial_t \psi(x) = H(t)\psi(x), \qquad H(t) = \gamma^0(\gamma P + m),$$
$$P_x = -i\partial_x - U(t), \quad P_\perp = -i\nabla_\perp, \quad U(t) = -eA_x(t), \tag{3}$$

where $\psi_n(x)$ is a $2^{[d/2]}$-component spinor ([d/2] stands for the integer part of the ratio (d/2), ⊥stands for spacial components perpendicular to the electric field, m=0 is the electron mass, γ^μ are the γ atrices in d dimensions and U (t) is the potential energy of one electron, can be integrated in terms of Confluent Hypergeometric Functions (CHFs) [5], whose spinors

$$\psi_n(x) = \exp(ipr)\psi_n(t), \quad n = (p, \vartheta)$$
$$\psi_n(t) = \left\{\gamma^0 i\partial_t - \gamma^1\left[p_x - U(t)\right] - \gamma p_\perp + m\right\}\varphi_n(t)\nu_{x(\vartheta)}, \tag{4}$$

are expressed in terms of CHFs Φ(a, c;η) as follows:

$$\varphi_n^j(t) = b_2^j y_1^j(\eta_j) + b_1^j y_1^j(\eta_j),$$
$$y_1^j(\eta_j) = e^{-\eta_j/2}\eta_j^{\nu_j}\Phi(a_j, c_j; \eta_j),$$
$$y_2^j(\eta_j) = e^{\eta_j/2}\eta_j^{-\nu_j}\Phi(1 - a_j, 2 - c_j; -\eta_j), \tag{5}$$

Here $\nu_{\chi,(\vartheta)}$ is a set of constant orthonormalized spinors $\nu^+_{x,\{\vartheta\}}\nu_{x'\cdot\{\sigma\}} = \delta_{x\cdot x'}\delta_{\{\vartheta\},\{\sigma\}}$ and the index j distinguishquantities associated to the first I (j = 1) from the second II (j = 2) interval, respectively, $b_1^j, b_2^j$are constants fixed by the initial conditions, vj, aj and cj constants and ηj time-dependent functions

[1]Greek indices refer to the Minkowski spacetime $\mu = 0,..., D$ while Latin indices refer to Euclidean space $i = 1,..., D$. Here $d = D + 1$ is the dimension of the spacetime. Bold letters represent Euclidean vectors such as $r = x^1, x^2, ..., x^D$. The Minkowski metric tensor is diagonal $\eta_{\mu\nu} = diag\ (+1, \underset{d}{-1,...,-1})$

$$
\begin{aligned}
&\nu_j = \frac{i\omega_j}{k_j}, \quad \omega_j = \sqrt{\pi_j^2 + \pi_\perp^2}, \\
&\pi_j = p_x - (-1)^j \frac{eE}{k_j}, \\
&a_j = \frac{1}{2}(1+x) + (-1)^j \frac{i\pi_j}{k_j} + \nu_j, \\
&c_j = 1 + 2\nu_j, \\
&\eta_1(t) = ih_1 e^{k_1 t}, \quad \eta_2(t) ih_2 e^{-k_2 t}, \\
&h_j = \frac{2eE}{k_j^2}
\end{aligned}
\tag{6}
$$

Selecting χ=0 in Eqs above (5), (6) allows one to discuss exact solutions for the Klein-Gordon (KG) equation. Introducing an additional quantum number $\xi = \pm$ to label particles (ξ = +) and antiparticle (ξ = -), the set of solutions (5) (and the corresponding Dirac spinors) are conveniently written as

$$
\begin{aligned}
&{}_{+}\varphi n(t) = {}_{+}N \exp(i\pi\nu_1)/2) y_2^1(\eta_1), \\
&{}_{-}\varphi n(t) = {}_{-}N \exp(-i\pi\nu_1)/2) y_1^1(\eta_1), \ t \in I \\
&{}^{+}\varphi n(t) = {}^{+}N \exp(-i\pi\nu_2)/2) y_1^2(\eta_2), \\
&{}^{-}\varphi n(t) = {}^{-}N \exp(-i\pi\nu_2)/2) y_2^2(\eta_2), \ t \in II
\end{aligned}
\tag{7}
$$

so that at $t \to -\infty(\xi\varphi_n(t))$ and $t \to +\infty(\xi\varphi_n(t))$ these solutions represents free-(anti)particle states. Here ${}_{\xi}^{N}$ and ${}^{\xi}N$ denotes normalization constants with respect to the inner product of Dirac spinors (or Klein-Gordon solutions, in the case of Bosons).

2. Differential and total quantities

To study particle creation by the field under consideration, it is necessary to compute decomposition coefficients between two pairs of complete and orthonormalized sets of exact solutions, for example, the out-set $\{{}^{\xi}\psi_n(x)\}$ interms of the in-set $\{{}_{\xi}\psi_n(x)\}$ of Dirac spinors,

$$
\{{}^{\xi}\psi_n(x)\} = {}_{-}\psi_n(x) g({}_{-}|^{\xi}) + {}_{+}\psi_n(x) g({}_{+}|^{\xi}) \tag{8}
$$

wherein the latters are identified by the coefficients $g({}^{\xi}|_{\xi})$, defined as inner products between both sets[2]

$$
({}_{\xi}\psi_{|}, {}^{\xi}\psi_n) = \delta_{|,n} g(x) g({}_{\xi}|^{\xi}), \quad g({}^{\xi}|_{\xi}) = g({}^{\xi}|_{\xi})^* \tag{9}
$$

and are diagonal matrix elements with respect to the quantum numbers n = **(p,σ).**These coefficients are important since they define linear canonical transformations between in- and out-sets of creation and annihilation operators
[3],

$$
\begin{aligned}
&a_n(in) = g({}_{+}|^{+}) a_n(out) + g({}_{+}|^{-}) b_n^{\div}(out), \\
&k_n^{\div}(in) = g({}_{-}|^{+}) a_n(out) + g({}_{-}|^{-}) b_n^{\div}(out),
\end{aligned}
\tag{10}
$$

from which one may compute basic elements concerning particle creation, for instance, the differential mean number of particles created from the initial vacuum[3]

$$
N_n^{cr} = \langle 0, in \mid a_n^{\div}(out) a_n(out) \mid 0, in \rangle = \mid g({}_{-}|^{+}) \mid^2 \tag{11}
$$

the total number

$$
\begin{aligned}
&N^{cr} = \sum_n N_n^{cr} = \sum_n \mid g({}_{-}|^{+}) \mid^2 = V_{(d-1)} n^{cr}, \\
&n^{cr} = \frac{J_{(d)}}{(2\pi)^{d-1}} \int dp N_n^{cr},
\end{aligned}
\tag{12}
$$

and the vacuum-to-vacuum transition probability

$$
P_\nu = \exp\left\{ k \sum_n in\left[1 - kN_n^{cr}\right] \right\} \tag{13}
$$

In Eqs. (10) and (13), κ= +1 and κ= -1 refers to Fermions and Bosons[4], respectively. Moreover in Eq. (12) n^{cr} denotes the density of pairs created and the number $J(d)$ denotes the spinning degrees of freedom, i. e., $J(d) = 2^{[d/2]-1}$ for Fermions and $J_{(d)} = 1$ for Bosons.
In Ref. [2] we derived the coefficient $g({}_{-}|^{+})$ for the peak electric field (2) which, for Fermions takes the form

$$
\begin{aligned}
&g({}_{-}|^{+}) = C\Delta, \\
&C = -\frac{1}{2}\sqrt{\frac{q_1^-}{\omega_1 q_2^+ \omega_2}} \exp\left[\frac{in}{2}(\nu_1 - \nu_2)\right], \\
&\Delta = \\
&\left[k_1 h_1 y_1^2(\eta_2) \frac{d}{d\eta_1} y_2^1(\eta_1) + k_2 h_2 y_2^1(\eta_1) \frac{d}{d\eta_2} y_1^2(\eta_2) \right]_{t=0},
\end{aligned}
\tag{14}
$$

---

[3]The relativistic system of units is used throughout in this paper ($h = c = 1$), except when indicated otherwise
[3]The notation ψ', ψ stands for inner products of Dirac spinors. For details see; e. g., Refs. [1]
[3]Which coincides with the mean number of antiparticles created from the vacuum.
[4]By "Bosons" we mean "Klein-Gordon particles".

while for Bosons reads

$$g(_{-}|^{+}) = C_{sc}\Delta|_{x=0},$$

$$C_{sc} = (4\omega_1\omega_2)^{-1/2}\exp[in(\nu_1-\nu_2)/2]. \quad (15)$$

The most favorable conditions for pair creation by time-dependent external fields are associated to its large time duration, i. e. in slowly varying field configurations. For a peak field (1), the time dependence is encoded in the parameters h_1 and h_2, since k_1^{-1}, k_2^{-2} represent scales of time duration for increasing and decreasing phases of theelectric field. Hence for k_1, k_2 sufficiently small, satisfying

$$\min(h_1,h_2) >> \max(1, m^2/eE). \quad (16)$$

the differential mean number of particles created N_n^{cr} (11) acquires the asymptotic form

$$N_n^{cr} \sim \begin{cases} \exp[-2\pi(\omega_1-\pi_1)/k_1], & p_x<0, \\ \exp[-2\pi(\omega_2+\pi_2)/k_2], & p_x>0, \end{cases} \quad (17)$$

as $k_1, k_2 \to 0$, valid both for Fermions and Bosons (see Ref. [2]). To illustrate the exact (11) and the asymptotic (17) results, we present below plots of the mean number of particles created from the vacuum N_n^{cr} as a function of $p_x$for different values of k_1 and k_2 (Fig. 1). For simplicity, we select $k_1 = k_2 = k$, set $p_\perp = 0$ and consider the reduced system of units, in which besides $h=c=1$, the particle mass is also set equal to the unity, $m = 1$[5]. In Fig 1 is presented plots of exact expressions of eq. (11) (red and blue solid lines) for Fermions and Bosons, respectively, and the asymptotic approximation (17) (green solid lines) for different values of k, namely, $k = 0.05$ (solid gray lines) and $k = 0.1$ (dashed gray lines). Both values fulfil the inequality (16), since $k = 0.05$ corresponds to $h1=h2=h=2/k^2 = 800$ and $k = 0.1$ corresponds to $h = 200$.

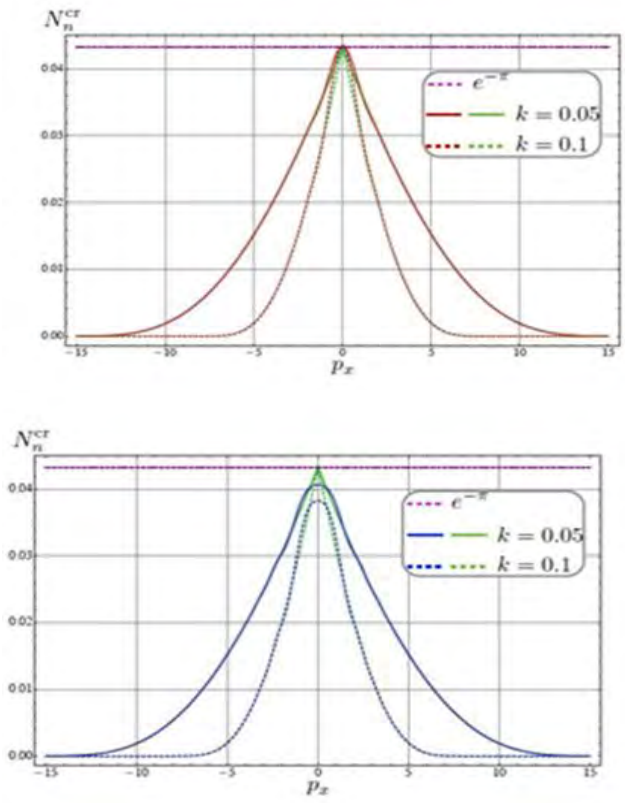

Figure 1: Mean number of Fermions (red solid lines) and Bosons (blue solid lines) created from the vacuum (black lines) by a symmetrical peak electric field with amplitude $E = E_c$. Here it is plotted exact results (red/blue) with asymptotic estimates (green lines), for two possible values of k, namely $k = 0.05$ (solid lines) and $k = 0.1$ (dashed lines). The horizontal dashed purple line corresponds to the uniform distribution $e^{-\pi}$.

The results in Fig. 1 reveal wider distributions (solid lines) corresponding to peak electric fields with small values of k in comparison to those with higher values to this phase (dashed lines); feature that is common both for Fermions and Bosons. The results are consistent with the fact that the larger the duration of an electric field, the longer it has to accelerate pairs. Consequently larger values to px are expected in plots corresponding to electric fields with larger duration. Besides the characteristics above, it should be noted in Fig. 1 that N_n^{cr} tends to the uniform distribution $e^{-\pi\lambda}$as k decreases (horizontal dashed lines). Moreover, in both plots, it is seen a better approximation between exact and asymptotic results as px increases, as expected.

To estimate the total number of pairs created N^{cr}, one has to sum the corresponding differential mean numbers N_n^{cr} over the momenta **p**and spins projections (for Fermions), as displayed in Eq. (12). In the large time durationregime (16), this can be accomplished through the asymptotic results (17), whose results are given by

[5]In this system, the Compton wavelength correspond to one unit of length $\lambda_e = h/mc = 1[ru] \cong 3.8614\times10^{-14}\,m$, one unit of time correspond to $\lambda_e/c = 1[ru] \cong 1.3\times10^{-21}\,s$ and one unit of energy correspond to the electron rest energy $mc^2 = 1[ru] \cong 0.511MeV$. In all plots below, the longitudinal momentum $p_x$is relative to electron's mass m, that is $p_x = p_x/m$ in the reduced system of units.

$$N_n^{cr} \sim \begin{cases} \exp\left[-2\pi(\omega_1 - \pi_1)/k_1\right], & p_x < 0, \\ \exp\left[-2\pi(\omega_2 + \pi_2)/k_2\right], & p_x > 0, \end{cases} \qquad (18)$$

where n^{cr} and r^{cr} are, the density and rate or pairs created, respectively (see Ref. [2]). From the latter result it follows the vacuum-to-vacuum transition probability P_v (13) is given by

$$P_v = \exp(-\mu N^{cr}),$$

$$\mu = \sum_{i=0}^{\infty} \frac{(-1)^{(1-k)l/2}}{(l+1)^{d/2}} \in_{l+1} e^{-i\pi m^2/eE},$$

$$\in_l = G\left(\frac{d}{2}, \frac{i\pi m^2}{eE}\right)\left[G\left(\frac{d}{2}, \frac{\pi m^2}{eE}\right)\right]^{-1} \qquad (19)$$

3. Final comments

In this proceedings contribution we summarized general aspects concerning vacuum instability by peak electric field in the framework of QED with f-electric potential steps and addressed to peculiarities of particle creation by such a field. To examine how the differential mean numbers N_n^{cr} depend on the longitudinal momentum p_x and on the phases k_1, k_2, we compare plots of exact (11) and asymptotic (17) results. The results show wider distributions for peak fields with small phases k, as expected since k^{-1} correspond to time scale for the peak electric field and, therefore, the field has a larger time to accelerate pairs. Moreover comparing the exact results with asymptotic results, it is seen a higher accuracy at regions of sufficiently large p_x, the latter increasing as k decreases. Conversely, in the range of small p_x and k satisfying (16), the well-known uniform distribution $e^{-\pi\lambda}$ provides a better approximation instead, whose accuracy also increases as k decreases. The results presented in this proceedings illustrate how a peak electric field create particles from the vacuum. These results are important to visualize how differential mean quantities depend on the quantum number p_x and withal to compare with another exactly and non-exactly solvable models. At last, but not least, comparing how the total number of particles created depend on time with another exactly-solvable external fields, namely the T-constant and Sauter type fields (see; e. g. Ref. [6]), we obtain the time dependence for the peak field is effectively represented by the combination $(k_1^{-1} + k_2^{-2})G(d/2,\ \pi m^2/eE)$. Thus, a peak electric field with the effective time dependence $T_{eff} = (k_1^{-1} + k_2^{-2})G(d/2,\ \pi m^2/eE)$ is equivalent, in particle creation, with a T-constant electric field with time duration $T = T_{eff}$.

Supported by Russian Science Foundation, Research Project No. 15-12-10009.

References

[1] T. C. Adorno, S. P. Gavrilov, and D. M. Gitman, Phys. Scr **90,** 074005 (2015); arXiv:1512.01288.

[2] T. C. Adorno, S. P. Gavrilov, and D. M. Gitman, Eur. Phys. J. C **76,**447 (2016).

[3] E.S. Fradkin, D.M. Gitman and S.M. Shvartsman, *Quantum Electrodynamics with Unstable Vacuum* (Springer, Berlim (1991)).

[4] W. Greiner, B. Muller and J. Rafelsky, "*Quantum Electrodynamics of Strong Fields"* (Springer, Berlim 1985); N.D. Birrell and P.C.W. Davies "*Quantum Fields in Curved Space"* (Cambridge University Press, Cambridge (1982)); A.A. Grib, S.G. Mamaev and V.M. Mostepanenko, "*Vacuum Quantum Effects in Strong Fields"* (Friedmann Laboratory Publishing, St. Petersburg, (1994)).

[5] NIST Digital Library of Mathematical Functions, http://dlmf.nist.gov/, 2015-08-07 DLMF Update; Version1.0.10.

[6] S.P. Gavrilov and D.M. Gitman, Phys. Rev. D **53,**7162 (1996).

Study of dielectric parameters of cyclopentanone and its concentrated binary solutions and analysis of measurement results

S.M.Useynova
Baku State University,Baku, Azerbaijan, moonsun8486@mail.ru

Measurment of dielectric parameters $\varepsilon_0, \varepsilon', \varepsilon''$ of cyclopentanone(C_5H_8O) and itsconcentrated binary solutions in low-frequency (LF) and ultrahigh frequencies (UHF) diapason(λ=3,21sm; λ=1,70sm; λ=7,10mm) in wide range of temperatures using the new variational method. Cole-Cole diagrams have been constructed,The ultrahigh frequencieslimitε_∞,the relaxation time τ and the distribution parameter of the relaxation times α have been calculated. The results were summarized and conclusions drawn.
Keyword: new variational method, cyclopentanone, polar liquid

1.Introduction

The mechanism responsible for the dipole relaxation phenomenon in pure liquids can be detected by analyzing the dielectric behavior of liquids when diluted by specially selected solvents whose properties have been fairly well studied [1-9]. When choosing a solventwe proceeded from the following considerations:

1.The molecules of the solvent and solute should little differ in size and geometric configuration;

2.Between molecules of dissolved substances there should be no specific interactions that could "veil" mechanism of the phenomenon found in the investigated pure polar liquids. In this case, it is more expedient to use inert non-polar solvents.

2. Discussion

The main object of research - an organic cyclic hydrocarbon cyclopentanone(C_5H_8O)which has a nonplanar form of a five-membered ring molecule.The most stable conformation corresponds to a ring in the "armchair" form. Cyclopentane (C_5H_{10}) chosen as a solvent is also a cyclic hydrocarbon with a nonplanar five-membered ring shape[10-11]. According to the data [11], cyclopentane molecules can be in two most probable configurations: in the form of a "semi-armachair" or "envelope".Cyclopentane is an inert substance, its molecule does not possessby dipole moment.

The frequency dependences of the permittivity ε' and dielectric losses ε'' of pure cyclopentanone solutions in the entire studied temperature range (-40^0C ÷ 40^0C) and concentrations (0 ÷ 1) obey to the Cole-Cole equation [12-14], taking into account the presence inthese solutions the distribution spectrum of the relaxation times (τ):

$$\dot{\varepsilon} = \varepsilon_\infty + \frac{\varepsilon_0 - \varepsilon_\infty}{1+(i\omega\tau)^{1-\alpha}} \qquad (1)$$

here $\dot{\varepsilon} = \varepsilon' - \varepsilon''$ - the complex permittivity of the substance,ε_0 – the static (or equilibrium) permittivity, ε_∞- the part of the permittivity that is due to the electronic and atomic polarization of the substance,ω- the circular frequency of the applied field;τ – the molecular or intrinsic time of dipole relaxation, α - an empirical parameter varying from 0 to 1 have determined from the generalized Cole-Cole equation (1) and characterizes the symmetrical spectrum of the relaxation times near the most probableτin a pure cyclopentanone.The calculation of the parameters τ.α and ε_∞ included in the generalized equation (1) was carried out by a graphical method using Cole-Cole arc diagrams [19]. The value $\varepsilon_\infty$was determined by extrapolating of the experimental data for$\omega \to \infty$, the value α have measured by the angle between the abscissa axis and the straight line connecting the center of the circle of the arc diagram and the point (ε_∞, 0).

Equation (1) was written in the next form for calculate the relaxation time

$$(\omega\tau_0)^{1-\alpha} = v/u \qquad (2)$$

here v and $u$are the chords sizes,respectively connecting the experimental point along the arc diagram with the extreme points of the diagrams (ε_0,0) and (ε_∞, 0) (Fig. 1)

Figure 1

Arc diagrams of cyclopentanone-cyclopentane solutions at t=20^0C.

Concentration of cyclopentanone in mole fractions.

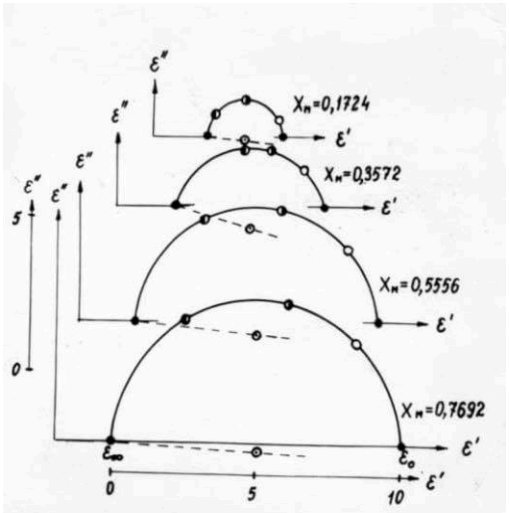

Cole-Cole arc diagrams and the measurements results and calculations carried out for concentrated solutions of cyclopentanone-cyclopentane in wide range of temperatures are given on Figure 1 and in Table 1.

Table 1

The relaxation time $\tau \cdot 10^{12}$secounds and the distribution parameter of relaxation time α of the cyclopentanone-cyclopentane solutions.

Tem-	The concentration of cyclopentanone in mole fractions

pera-ture, t^{0}C	0, 1724		0,3572		0,5556		0,7692		1,0	
	T	A	τ	α	τ	α	τ	α	τ	α
-40	7,82	0,11	9,55	0,11	11,7	0,09	14,5	0,05	20,30	0,14
-30	7,25	0,09	8,92	0,11	10,8	0,10	12,9	0,05	15,70	0,12
-20	6,60	0,08	8,12	0,11	9,57	0,11	11,4	0,04	12,50	0,10
-10	6,12	0,08	7,40	0,10	8,55	0,10	9,55	0,03	10,30	0,08
0	5,76	0,07	6,85	0,09	7,75	0,09	8,30	0,02	8,30	0,03
10	5,49	0,06	6,32	0,08	7,12	0,08	7,50	0,02	7,47	0
20	5,28	0,06	5,98	0,07	6,61	0,06	6,88	0,02	6,72	0
30	5,06	0,05	5,70	0,05	6,18	0,04	6,39	0,01	5,99	0
40	4,92	0,04	5,40	0,03	5,80	0,02	6,05	0,01	5,22	0

Frequency dependences of the permittivity $\varepsilon'$and the dielectric lossesε'' of the cyclopentanone-cyclopentane solutions in the entire studied range of temperatures and concentrations also obey to the Cole-Cole equation (1), which takes into account the presence of the time distribution spectrum in these solutions have been shown analysis of the obtained data [15-19]. Family of arc diagrams of the solutions studied at t=20^{0}C have been shown on figure 1.The values τ and α found by the graphical method for solvinghave shown in table 1 (1).
At 10-40^{0}Ctemperatures in the concentration dependence τis observed maximum which lies in 0.7-1.0 mole fractions.

At temperatures below 0^{0}Caddition topure cyclopentanone of a small percentage leads to a decrease of α. α increases with subsequent dilution and with an increase of the concentration of cyclopentane in solution the value α passes through a maximum lying at concentrations of cyclopentane 0,3-0,4 mole fractions. The existence of a spectrum of relaxation times at these concentrations is typical for solutions of polar liquids in nonpolar solvents [10, 11] and is associated with a decrease in the energy barrier of dipole relaxation of polar molecules withan increase in the concentration of the nonpolar solvent.

3.Conclution

The frequency dependences ε'andε''approach the Debye description with a further dilution of cyclopentanon by cyclopentane.

Dependences lgτ on $1/T$ are linear for all solution concentrations in the studied temperature range have been shown analysis of the temperature dependences τ.

References

[1]. Debye P. Polar molecules. M-L., 1931. pp. 90-210 (by russian)
[2]. Whiffen D.H., Thompson H.W. Trans. Farsoc. 42A, 122, `6.1946
[3].Skanavi G.I. Physics of dielectrics, Moscow, 1960 (by russian)
[4]. Frelech G. The theory of dielectrics, M., 1960 (by russian)
[5]. Brown I. Dielectrics, M., 1961(by russian)
[6]. Hippel A.R. Dielectrics and waves, M., 1961(by rusian)
[7]. Bogoroditsky N.N. and ets. The theory of dielectrics.M.-L., 1965.pp. 146-278 (by russian)
[8]. Shakhparonov M.I. Methods for studying of the thermal motion of molecules and the structure of liquids, M., 1963 (by russian)
[9]. Cole R.H., J. Chem. Phys. 23, 3, 1955; 23, 1767, 1955
[10]. Winstein S., Holness N.J., J.Am. Chem. Soc., 77, 5562, 1955
[11]. Reisse J., Celotte J.C., Zimmenrmann D., Chirodogli G., Tetrahedron Letters, 2145, 1964
[12]. Useynova S.M. Study of the processes of polarization in the ultrahigh frequencies of binary solutions. BSU.J. “Xeberler”. 2011, No. 4, pp. 156-161 (by russian)
[13]. Useynova S.M. Equilibrium dielectric properties of cyclopentanone. BSU, IFP. Proc. of the International Conference, Baku, 2015, pp.268-271 (by russian)
[14]. Useynova S.M. Study of dielectric properties of cyclopentanone and its concentrated binary solutions in ultrahigh frequencies(λ = 1,70sm), Baku, IFP, 2016, pp. 197-198 (by russian)
[15]. KasimovR.M., UseynovaS.M. Measuringtechnique, 2, 1975, pp. 76-82 (by russian)
[16]. Useynova S.M. About the variational method for studying the dielectric properties of liquids and solutions. BSU, Proc. of V Rep. Conf., Baku, 2011, pp. 200-202 (by russian)
[17].Useynova S.M. Development of a variational method for measuring the dielectric parameters of polar liquids in the ultrahigh frequenciesdiapason. 1.Theoretical principles of the variational measurement method. Bulletin of the Baku State University, Baku, 1,2015, pp.176-184 (by russian)
[18].Useynova S.M. Development of a variational method for measuring liquids in the ultrahigh frequencies diapason. 2.Graphical method for solving initial equations. Baku State University, Baku, 1,2015, p.177-188 (by russian)
[19].Useynova S.M. Study of dielectric parameters of cyclopentanone and graphical analysis of measurement results, BSU, IFP, "Actual problems of physics", Proceedings of IX Republican Conference, Baku, 2016, pp.198-202 (by russian)

Measurement of ultrahigh frequencies dielectric parameters of liquids (ε' и ε'') at length of wave λ = 7,10mm (uhf)

S.M.Useynova, Baku State University,Baku, Azerbaijan, moonsun8486@mail.ru

Measurements of the ultrahigh frequencies permittivity (dielectric constant) ε' and the dielectric losses ε'' of pure cyclopentanone (C_5H_8O) and its concentrated solutions in cyclopentane (C_5H_{10}) in wide temperature range (from -40°C to + 40 °C) have been conducted. The thickness of liquid layer lm was measured at the first extreme value $\eta_м$ have determined. Values ε' и ε'' were determined by variational method with the use of nomograms.

Keywords: polar liquids, cyclopentanone, cyclopentane, nomograms, new variational method.

1.Introduction

The permittivity (dielectric constant) ε' and the dielectrically loss ε'', $(\varepsilon = \varepsilon' - i\varepsilon'')$ of the investigated liquid cyclopentanone (C_5H_8O) and its concentrated solutions in cyclopentane (C_5H_{10}) have been measured in wide temperature range (from -40°C to + 40°C) in ultrahigh frequencies diapason at length of wave λ = 7,10mm by fundamentally new variational method [1-5] using the following equations for calculating ε' и ε'':

$$\varepsilon' = (\lambda/\lambda_0)^2 + \left(\lambda/\lambda_g\right)^2 (1 - tg^2 \Delta/2) \quad (1)$$

$$\varepsilon'' = 2(\lambda/\lambda_g) \cdot t_g \Delta/2 \quad (2)$$

here: λ - the length of the electromagnetic wave in free space in the absence of the medium, λ_o - the critical length of the electromagnetic wave determined by the dimensions of the waveguide (λ_o = 2a, a - the internal dimension of the waveguide), λ_b - the length of the electromagnetic wave in the empty waveguide, λ_g - the length of the electromagnetic wave of the waveguide filled with the investigated liquid, $tg\,\Delta/2$– the parameter characterizing the degree of damping of the electromagnetic waves in the waveguide filled with the liquid.

2. Discussion

According to the theory of waveguide transmission lines [6, 7], the coefficient of standing wave η in the waveguide is determined by the expression:

$$\eta = \frac{1 + |\hat{\rho}|}{1 - |\hat{\rho}|}$$

here: $|\hat{\rho}|$ – Modulus of complex reflection coefficient

$$\left\{|\hat{\rho}| = \left|\frac{z \cdot th\hat{\gamma} l - z_o}{z \cdot th\hat{\gamma} l + z_o}\right|;\right.$$

z_o and z – wave impedances, respectively, of an empty waveguide and a waveguide filled with the investigated medium.

Since the fixation of extreme points is carried out with a high degree of accuracy more reasonable to use as measured parameters the values l_m and η_m corresponding to the extremal values of the dependence η from l.

The extremal values of the standing wave coefficient in the waveguide η_m for the thickness of the liquid layer in the waveguide section equal to l_m are described by two equations after the transformations of equations (1) and (2):

$$\eta_m = \sqrt{\frac{cth(2\pi xy) + ytg(2\pi x)}{th(2\pi xy) - ytg(2\pi x)}}; \quad (4) \quad \text{and}$$

$$\eta'_m = \sqrt{\frac{th(2\pi xy) - ytg(2\pi x)}{cth(2\pi xy) + ytg(2\pi x)}} \quad (5)$$

for η_m =1 both equations are reduced to form:

$$sh(\pi xy) = -y\sin(\pi x) \quad (6)$$

here: $x = l_m/\lambda_g$, $y = tg\,\Delta/2$;

The obtained equations (3)-(6) contain only the functions of the two auxiliary parameters x and y and in principle have established a connection between the permittivity ε', the dielectric losses ε'' and the length of the electromagnetic wave of liquid λ_g and the experimentally determined value of the liquid layer thickness in the cell l_m, at which the extremum $|\hat{\rho}|$ or η_m have been detected at this fluid thickness, provided that the values of λ and λ_b are known. However this relation can not be obtained explicitly due to the presence of transcendental functions in the initial equations (5) and (6). As a result new variational method of measuring of dielectric parameters in the ultrahigh frequencies diapason are proposing a new graphical method (by nomograms) which not only eliminated this lack of existing methods, and also opened up new possibilities for studying polar liquids with large losses.

Since in such liquids was obtained only one maximum in the dependence of η from l, and one maximum allowed to determine the values ε' and ε'' by already existing methods. These techniques required knowledge of three or more maxima in η = f (l) [2,3] by the following nomograms:

1) Nomograms to the graphical method of calculating λ_g and $tg\,\Delta/2$ on the experimental values l_m and η_m for the thickness of the liquid layer in the waveguide cell at which the first minimum of the dependence η from l in the coordinate plane takes place:

$[x = l_m/\lambda_g;\ y = tg\,\Delta/2]$

2) Nomograms to the graphical method of calculating λ_g and $tg\,\Delta/2$ on the experimental values of l_m and η_m for the thickness of the liquid layer in the waveguide cell at which the first minimum of the dependence η from l in the coordinate plane takes place:

$[\lambda_g/\lambda_b : tg\,\Delta/2]$

3) Nomograms to the graphical method of calculating ε' and ε'' by the experimental values of l_m and η_m for the thickness of the liquid layer in which the first minimum of the dependence η from l in the coordinate plane takes place [ε'; ε''], [1-5].

Cyclopentanone and its solutions in cyclopentane have been investigated by using the variational method. The results are given in Table 1.

Table 1

Permittivity ε' and the refractive index of solutions cyclopentanone-cyclopentane for λ = 7,10mm and their temperature dependences

Temp. t°C	The concentration of cyclopentanone in mole fractions										
	0	0,1724		0,3572		0,5556		0,7692		1,0	
	ε'	ε'	ε''	ε'	ε''	ε'	ε''	ε'	ε''	ε'	ε''
-40	2,05	2,76	0,94	3,38	1,87	3,65	2,75	3,56	3,25	3,40	3,00
-30	2,04	2,78	0,97	3,43	1,90	3,72	2,83	3,70	3,44	3,51	3,25
-20	2,02	2,81	1,01	3,48	1,93	3,80	2,91	3,86	3,63	3,68	3,49
-10	2,01	2,84	1,05	3,53	1,98	3,89	2,98	4,07	3,82	3,88	3,81
0	2,00	2,88	1,08	3,59	2,02	3,98	3,06	4,28	4,00	4,13	4,26
10	1,98	2,91	1,11	3,68	2,09	4,10	3,13	4,40	4,07	4,38	4,61
20	1,97	2,94	1,14	3,78	2,16	4,22	3,20	4,52	4,14	4,70	4,76
30	1,96	3,01	1,16	3,80	2,21	4,25	3,33	4,64	4,14	5,02	4,79
40	1,94	3,08	1,19	3,83	2,27	4,28	3,46	4,75	4,15	5,33	4,70

Cyclopentane is not a polar liquid ($\varepsilon'' = 0$). Values of ε' and ε'' gradually increase with the addition the temperature and also the concentrated cyclopentanon.

References

[1]. Kasimov R.M., Nagizade N.S. Bulletin of the Moscow State University, ser. chem., 2, 1967, p.101 (by russian)
[2]. Kasimov R.M., Useynova S.M. Measuring technique, 2, 1975, pp. 76-82 (by russian)
[3]. Kasimov R.M., Useynova S.M. Ed. of AS of Azerb. SSR, series of physics-tech. and math. sciences, I, 1973, pp.111-117 (by russian)
[4]. Useynova S.M. About the variational method for studying the dielectric properties of liquids and solutions. BSU, Proc. of V Resp. konf., Baku, 2011, pp. 200-202 (by russian)
[5]. Useynova S.M. Graphical methods of application of the variational method. BSU, Proc. of V Resp. conf., Baku, 2011, pp. 202-205 (by russian)
[6]. Brandt A.A. Investigations of dielectrics on ultrahigh frequencies. M., fizmatgiz, 1963 (by russian)
[7]. Harvey A.F. The technique of ultrahigh frequencies, M. Publ. "Sov.radio", 1965
[8]. Useynova S.M. Development of a variational method for measuring the dielectric parameters of polar liquids in the ultrahigh frequencies diapason.1. Theoretical principles of the variational measurement method. Bulletin of the Baku State University, Baku, 1,2015, pp.176-184
[9]. Useynova S.M. Development of a variational method for measuring the dielectric parameters of polar liquids in the ultrahigh frequencies diapason. 2.Graphical method for solving initial equations. Bulletin of Baku State University, Baku, 1,2016, pp.177-188

The simplified construction of the Schrödinger functional scheme with the Möbius domain wall fermions

Y. MURAKAMI[1], K-I. ISHIKAWA[1,2]
[1]*Graduate school of science, Hiroshima University, Higashi-Hiroshima, Hiroshima 739-8526, Japan*
[2]*Core of Research for Energetic Universe, Hiroshima University, Higashi-Hiroshima, Hiroshima 739-8526, Japan*

We try to simplify the construction of the Schrödinger functional (SF) scheme with the Möbius domain wall fermions (MDWFs). In the previous work, we constructed this scheme and confirmed that our method reproduced the one-loop beta function by introducing a SF boundary term in the MDWF action to satisfy the SF boundary condition. However, our previous construction prevents us to analytically investigate the temporal boundary effect which is introduced by the SF boundary term. We construct a simplified SF boundary term for the MDWFs and discuss the universality for the fermionic part of the one-loop beta-function in the SF scheme.
Key words: Lattice Field Theory; Lattice Chiral Symmetry; Renormalization

1. Introduction

Quantum Chromodynamics (QCD) is the theory of the strong interaction that works among quarks and gluons and is a part of the Standard Model. The interaction strength among quarks and gluons becomes weaker as the interaction energy becomes higher due to the so called "asymptotic freedom" property of QCD. From this property, we can analytically investigate the QCD phenomena in the high-energy region via the weak coupling expansion of the perturbation theory. In the low-energy region, however, the interaction strength becomes strong, so we cannot apply the perturbation theory to investigate QCD analytically. Lattice quantum chromodynamics (LQCD) is a non-perturbative formulation to explore the phenomena in the low-energy region. LQCD is defined in a finite lattice space-time box and regularized by the lattice cut-off to have gauge symmetry, and is applicable to the computer simulation directly. LQCD has been applied to investigate the hadron physics and successfully reproduced the low energy hadron spectrum. However, there are still some problems in precisely computing hadron matrix elements using the LQCD technique.

The chiral symmetry is one of the important properties of the massless quarks in QCD and plays an important role in the calculation of quantities of hadron physics. We cannot construct lattice fermion actions with the chiral symmetry in LQCD due to the Nielsen-Ninomiya's No-Go theorem. P. H. Ginsparg and K.G. Wilson extracted a relation for the chiral symmetry remnant after the coordinate space renormalization group transformation in the quantum field theory, and this relation is known as the so-called "Ginsparg-Wilson (GW) relation" [1]. Lüscher proved that the GW relation shows the alternative symmetry on the lattice to the chiral symmetry [2] and this symmetry is called "the lattice chiral symmetry". The lattice chiral fermions are the lattice fermions that satisfy the lattice chiral symmetry and some expressions have been proposed; the overlap fermion [3], the domain wall fermion [4], and the Möbius domain wall fermions (MDWFs) [5]. The overlap fermion realizes the GW relation completely; however, it requires a huge computational cost. The domain wall fermion or the MDWFs realizes the GW relation at a controllable accuracy so that it requires a lower computational cost than that for the overlap fermion.

Renormalization is always required in the quantum field theory, and it is preferable to use a renormalization scheme suitable for LQCD to compute precise hadron matrix elements. We focus on the Schrödinger functional (SF) scheme [6], where the renormalization scale is introduced by the finite box size of the space-time with a special temporal boundary condition. The SF scheme has an advantage that a quantity calculated in the SF scheme at the low-energy scale can be related to that in the MS-bar scheme through the finite box size scaling method. The SF scheme is independent from the UV-regularization and has been applied successfully to LQCD with lattice fermions without the lattice chiral symmetry [7].

It was difficult to apply the SF scheme to the lattice chiral fermion actions since the temporal boundary condition introduced in the SF scheme breaks the lattice chiral symmetry explicitly, and there are some studies for the application to the lattice chiral fermions. It has been proposed for the overlap fermion in Refs. [8, 9], for the domain wall fermions [10]. We extended the work by Takeda to the MDWFs and confirmed the universality at the one-loop level [9]. We found that the effective four-dimensional fermion propagator induced from the MDWF in the SF scheme requires a temporal boundary renormalization due to the SF boundary condition. We could not show the explicit form for the effective four-dimensional Dirac operator induced from the MDWF in the SF scheme to investigate the SF boundary effect analytically. In this paper, we propose a simplified SF boundary setup for the MDWF to investigate the boundary effect analytically. We investigate the universality of the one-loop beta function of the MDWF with the simplified boundary term at the one-loop level.

This paper is organized as follows. In Section 2, we introduce the SF scheme and the properties of the chiral symmetry with the SF boundary condition. The details of the Moebius domain wall fermion and the modifications to the MDWF for the SF scheme are also introduced. The numerical results for the fermionic part of the one-loop effective action with the SF boundary, from which we can extract the one-loop beta function in the SF scheme, are shown in Section 3. The universality of the one-loop beta

function extracted from the numerical results is discussed in Section 4. In the last section, we conclude this paper.

2. The detail of the Möbius domain wall fermion

The Schrödinger functional (SF) scheme [6] is defined in a finite lattice box with the size of L for the spatial direction and T for the time direction respectively. For the time direction in the SF scheme, the fermion field exists from $x_0 = 0$ to $x_0 = T$ and satisfies the following Dirichlet boundary condition at the temporal boundary;

$$P_+\psi(x)|_{x_0=0} = 0,\ P_-\psi(x)|_{x_0=T} = 0 \quad (1)$$

$$\bar{\psi}(x)\,P_-|_{x_0=0} = 0,\ \bar{\psi}(x)\,P_+|_{x_0=T} = 0 \quad (2)$$

where $P_\pm = (1 \pm \gamma_4)/2$ and $(\bar{\psi})\,\psi$ is the (anti-) fermion field. The boundary condition in the spatial direction is usually periodic.

The SF boundary condition is incompatible with the chiral symmetry. The massless Dirac operator in the continuum theory always anti-commutes with γ_5, while the propagator does not anti-commute as follows [9].

$$\gamma_5 S(x,y) + S(x,y)\gamma_5 = \int_{z_0=0} dz\, S(x,z)\gamma_5 P_- S(z,y) + \int_{z_0=T} dz\, S(x,z)\gamma_5 P_+ S(z,y) \quad (3)$$

On the lattice, the MDWF's operator that satisfies the GW relation does not satisfy the boundary condition Eqs. (1), (2) and Eq. (3). Therefore, we must modify the MDWF operator on the lattice to properly reproduce the relation Eq. (3) in the continuum limit. This modification should break the GW relation for the lattice Dirac propagator at the temporal boundary only. The strategy and the required conditions of the modification and has been described in Ref. [9], and the conditions are (i) keeping the space-time discrete symmetries; the charge conjugation, the parity, the time reversal, and γ_5-Hermiticity, which are required by the quantum field theory, and (ii) breaking the lattice chiral symmetry locally near the temporal boundary. We need to check that the propagator satisfies Eq. (3) in the continuum limit.

The Möbius domain wall fermion (MDWFs) is defined in the five-dimensional lattice, where the four-dimensional fermions are coupled each other in the extra dimension so as to decouple left and right massless modes in the distant boundary in the fifth dimension. Combining the left and right modes from the boundary, we can construct massless fermions satisfying the lattice chiral symmetry. The number of lattice sites in the fifth direction is denoted as N_5 in this paper. We use the case of $N_5 = 4$ for the MDWFs to display the equations as examples. The matrix form of the original MDWFs is as follows,

$$D_{MDWF} = \begin{pmatrix} D_1^{(+)} & D_1^{(-)}P_L & & -m_f D_1^{(-)}P_R \\ D_2^{(-)}P_R & D_2^{(+)} & D_2^{(-)}P_L & \\ & D_3^{(-)}P_R & D_3^{(+)} & D_3^{(-)}P_L \\ -m_f D_1^{(-)}P_L & & D_4^{(-)}P_R & D_4^{(+)} \end{pmatrix}_{(n,m)} \quad (4)$$

$$\begin{cases} D_j^{(+)} = b_j D_w + 1, \\ D_j^{(-)} = c_j D_w - 1, \ (j = 1,2,\dots,N_5), \end{cases} \quad (5)$$

where (n,m) is the four-dimensional lattice indexes, $P_{L/R}$ is the chiral projection defined by $P_{L/R} = (1 \pm \gamma_5)/2$, m_f is the fermion mass, and D_w is the Wilson-Dirac operator.

The parameters b_j and c_j are Möbius parameters and to be tuned to reproduce the Dirac operator in the continuum limit. The MDWF operator (4) has discrete symmetries; the parity symmetry, the charge conjugation, the time reversal, and the Γ_5-Hermiticity which is an extension of the γ_5-Hermiticity to the domain wall type fermions. The effective four-dimensional operator induced form Eq. (4) does satisfy the GW-relation [12]. This, however, contradicts with Eq. (3) even after imposing the Dirichlet boundary condition on D_w. To reproduce Eq. (3) in the continuum limit we must add a SF boundary term to the MDWFs so as to break the lattice chiral symmetry explicitly. We have introduced the boundary term in Ref. [11] and investigated the property at the one-loop level. In this paper, we introduce the following the MDWF operator including a simplified boundary term in the SF scheme,

$$D_{MDWF}^{SF} = \begin{pmatrix} D_1^{(+)} & D_1^{(-)}P_L & & -m_f D_1^{(-)}P_R - c_{SF} D_1^{(-)} B_{SF} \\ D_2^{(-)}P_R & D_2^{(+)} & D_2^{(-)}P_L & \\ & D_2^{(-)}P_R & D_2^{(+)} & D_2^{(-)}P_L \\ -m_f D_1^{(-)}P_L + c_{SF} D_1^{(-)} B_{SF} & & D_1^{(-)}P_R & D_1^{(+)} \end{pmatrix}_{(n,m)}, \quad (6)$$

$$B_{SF}(n,m) = \delta_{n,m}\gamma_5\left(\delta_{n_4,1}P_- + \delta_{n_4,N_T-1}P_+\right). \quad (7)$$

B_{SF} is the SF boundary term and c_{SF} is a tuneable parameter. Compared this form to that introduced in Ref. [11], the SF boundary term is only located at the both ends of the fifth-dimensional lattice index. The effective four-dimensional operator, D_q is defined by

$$D_q = \epsilon^\dagger P^\dagger (D_{PV})^{-1} D_{MDWF} P \epsilon, \quad (8)$$

$$\epsilon^\dagger = (1,0,0,0),\ P = \begin{pmatrix} P_L & P_R & & \\ & P_L & P_R & \\ & & P_L & P_R \\ P_R & & & P_L \end{pmatrix} \quad (9)$$

Here D_{PV} is the Pauli-Villars contribution defined with D_{MDWF} with $m_f = 1$. Without the SF boundary term B_{SF}, D_q can be written as

$$D_q = \frac{1+m_f}{2} - \frac{1-m_f}{2}\gamma_5(1-T)(1+T)^{-1}. \quad (10)$$

the SF boundary effect analytically. Since the term B_{SF} is introduced in the simpler form, the investigation on the boundary effect in an analytic manner still remains for our future works.

Before investigating the boundary effect explicitly, we have to check the universality of the operator introduced by Eq. (6). This is done by computing the one-loop effective action from which we can extract the renormalized coupling in the SF scheme. In this paper, we focus on the fermionic contribution to the effective action at the one-loop level.

3. Numerical results

Before showing numerical results for the effective action, we explain the properties of the MDWF operator itself. The eigenvalues and functions of the effective four-dimensional operator D_q have to converge to those in the continuum theory in the SF scheme. To see this condition holds we investigate the lowest ten eigenvalues of the effective four-dimensional operator. After validating this operator property, we investigate the fermionic contribution to the one-loop beta function from the effective action. We employ the classical background gauge field described in Ref. [13]. We set the Möbius parameter as $(b_i, c_i) = (1,0)$ (the Shamir DWF), the domain wall height, $m_0 = 1$, the domain wall fermion mass, $m_f = 0$, and the spatial boundary phase, $\theta = \pi/5$.

We show the continuum limit of the lowest ten eigenvalues of the effective four-dimensional operator, $L^2 D_q^\dagger D_q$. The coefficient of the SF boundary term is fixed to $c_{SF} = 1$. We calculate the eigenvalues in the cases of the lattice size, $L/a = 8, 12, 16, 20, 24, 32$ and 48 with the fifth-dimensional lattice size at $N_5 = 8$ and 16.

Figure 1 shows the cut-off dependence of the ten eigenvalues of the effective four-dimensional operator. The red solid points are the eigenvalues of the continuum Dirac operator with the SF boundary condition [14]. The eigenvalues from the MDWF are consistent with those in the continuum limit.

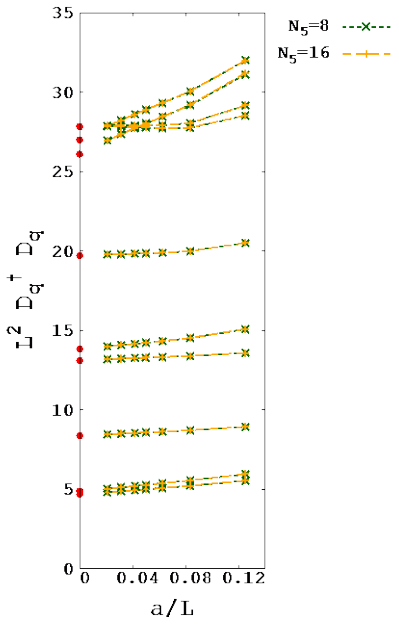

Figure 1 The cut-off dependence of the eigenvalues of the effective four-dimensional operator derived from the MDWFs.

We next show the fermionic contribution to the one-loop beta function in the SF coupling constant. The renormalized coupling constant in the SF scheme, g_{SF}^2, is defined by

$$\frac{1}{g_{SF}^2} = \frac{1}{k}\frac{\partial \Gamma}{\partial \eta}\Big|_{\eta=0}, \Gamma = -\log Z(\eta), \tag{11}$$

where $Z(\eta)$ is the partition function and Γ is the effective action. The effective action can be expanded by the bare coupling, g_0^2, as

$$\Gamma = \frac{1}{g_0^2}\Gamma^{(0)} + \Gamma^{(1)} + \cdots \tag{12}$$

The SF coupling constant is expanded as

$$g_{SF}^2 = g_0^2 + p_1 g_0^4 + \cdots, \quad p_1 = p_{1,0} + N_f p_{1,1}. \tag{13}$$

Using the MDWF operator, $p_{1,1}$ is calculated by

$$p_{1,1} = \frac{1}{k}\sum_p \mathrm{Tr}\left[\frac{\partial \tilde{D}_{MDWF}^{SF}}{\partial \eta}\left(\tilde{D}_{MDWF}^{SF}\right)^{-1} - \frac{\partial \tilde{D}_{PV}^{SF}}{\partial \eta}\left(\tilde{D}_{PV}^{SF}\right)^{-1}\right]\Big|_{\eta=0} \tag{14}$$

where $\tilde{D}_{Op.}^{SF}$ are the momentum representation of the MDWF operators. The trace in Eq. (14) is worked for the five-dimensional lattice sites, colour, and spinor indexes. Taking $p_{1,1}$ to the continuum limit $a \to 0$, $p_{1,1}$ has the following asymptotic form;

$$p_{1,1} \sim \sum_{k=0}^{\infty}[r_k + s_k \ln(L/a)](L/a)^k. \tag{15}$$

The coefficient s_0 corresponds to the one-loop beta function $s_0 = -1/(12\pi^2) \cong -0.00844343\cdots$, and the constant r_0 is related to the Λ-parameter. As we work in the bare coupling expansion, we employ the relation between the couplings in the SF scheme and in the $\overline{\mathrm{MS}}$ scheme to verify the value of r_0. In this case the constant r_0 determined at $N_5 = \infty$ for the Shamir DWF with $m_0 = 1$ is expected to be $r_0 = 0.0010886(51)$ [15].

We calculate $p_{1,1}$ for the Shamir DWF at $N_5 = 8, 16$ on each $L/a = 4, 6, 8, \cdots, 48$ with $c_{SF} = 0.6702$. The SF boundary term, c_{SF}, is tuned with the $O(a)$-improvement method to remove the discretization error coming from the temporal boundary [16]. We investigated $p_{1,1}$ as a function of a/L using Eq. (14) up to the order of $(a/L)^2$. However, we cannot confirm the consistency on s_0 numerically. In order to check the value of r_0, we check the cut-off dependence of $f(a/L) = p_{1,1} + 1/(12\pi^2)\ln(a/L)$ where the consistency on s_0 is assumed. Figure 2 shows the cut-

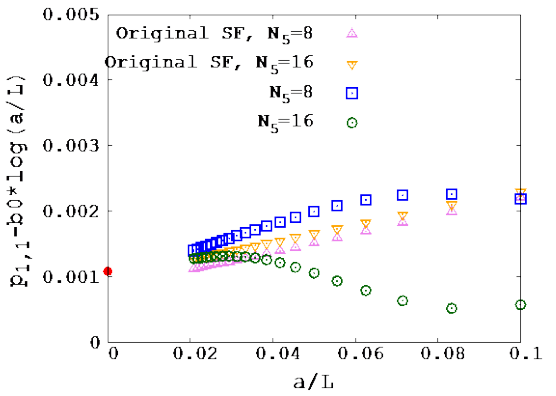

Figure 2 The cut-off dependence of the fuction of f(a/L).

off dependence of $f(a/L)$. The red point in Figure 2 is the value of r_0 expected from the universal coupling-relation between the SF scheme and $\overline{\text{MS}}$ scheme. The blue squares and the green circles are obtained with Eq. (6) (with simplified SF boundary term) and red up/down triangles are the data obtained with a different SF boundary term from previous works [11]. We find that $f(a/L)$ with the MDWFs approaches to the expected value in the continuum limit irrespective of the form of the SF boundary term added.

4. Discussions

From data of ten lowest eigenvalues of the effective four-dimensional operator in Section 3, our operator with the finite size of N_5 properly realizes the continuum massless Dirac operator in the SF scheme at the tree-level. From investigation of the fermionic contribution to the one-loop effective action in the SF scheme, we could not extract the proper beta-function as it shows the large cut-off dependence and the fit result of s_0 is unstable for the fit range we employed. When $s_0 = -1/(12\pi^2)$ is assumed, the fit result of r_0 is consistent to the value of the universal Λ-parameter relation between the couplings in the SF scheme and in the $\overline{\text{MS}}$ scheme. To further confirm the consistency of our construction, we need a wider range for L/a with finer lattices to stabilize the fitting for s_0 to extract the beta-function.

In order to find out the origin of the cut-off dependence and the effect of the SF boundary term, analytic investigations on the effective four-dimensional operator with the SF boundary term are required. As we could not obtain any simple forms for the effective operator, this remains as our future work.

5. Conclusions

In this paper, we investigated the Möbius domain wall fermions (MDWF) with the simplified SF boundary term in the Schrödinger functional (SF) scheme at the one-loop level. We confirmed that our operator with the simplified SF boundary term is consistent with the SF continuum Dirac operator at the tree-level. At the one-loop level, however, it was difficult to see the consistency on the fermionic contribution to the one-loop beta function. Assuming the consistency of the one-loop beta function, we could see the validity of the universal Λ-parameter relation between the couplings in the SF scheme and the $\overline{\text{MS}}$ scheme even at finite sizes of N_5.

Acknowledgements The numerical computations have been done on the workstations of the INSAM (Institute for Nonlinear Sciences and Applied Mathematics) at Hiroshima University. This work was partly supported by JSPS KAKENHI Grant Numbers 24540276 and 16K05326, and Core of Research for the Energetic Universe (CORE-U) at Hiroshima University.

References

[1] P. H. Ginsparg and K. G. Wilson, Phys. Rev. D **25**, 2649(1982).
[2] M. Lüscher, Nucl. Phys. B **254**, 52(1985).
[3] R. Narayanan and H. Neuberger, Nucl. Phys. B **412**, 574(1994).
[4] D. B. Kaplan, Phys. Lett. B **288**, 342(1992).
[5] R. C. Brower, H. Ne and K. Orginos, Nucl. Phys. Proc. Suppl. 140, 686(2005).
[6] M. Lüscher, R. Narayanan, P. Weisz and U. Wolff, Nucl. Phys. B **384**, 168(1992).
[7] M. Lüscher, S. Sint, R. Sommer and H. Wittig, Nucl. Phys. B **491**, 344(1997).
[8] Y. Taniguchi, JHEP 0512, 037(2005).
[9] M. Lüscher, JHEP 0605, 042(2006).
[10] S. Takeda, Phys. Rev. D 87, no. 11, 114506 (2013)
[11] Y. Murakami and K-I. Ishikawa, arXiv:1702.01526(2017).
[12] Y. Kikukawa and T. Noguchi, Nucl. Phys. Proc. Suppl. 83, 630(2000).
[13] M. Lüscher, R. Sommer and P. Weisz, Nucl. Phys. B **413**, 481(1994).
[14] S. Sint, Nucl. Phys. B **421**, 135(1994).
[15] S. Aoki and Y. Kuramashi, Phys. Rev. D **68**, 034507(2003).
[16] M. Lüscher and P. Weisz, Nucl. Phys. B **479**, 429(1996).

Y. MURAKAMI: d152338@hiroshima-u.ac.jp,
K-I. ISHIKAWA: ishikawa@theo.phys.sci.hiroshima-u.ac.jp.

Transverse momentum physics in $^{12}C^{12}C$ interactions at the momentum 4.2AGeV/c

Y.H.HUSEYNALIYEV, L.Y.HUSEYNALIYEVA

Azerbaijan State Pedagogical University

Abstract. The properties of proton and negative π -meson production are studied in CC - interactions using pp -reference data at 4.2AGeV/c to extract information on the collective phenomena, i.e., the formation of the Δ^0 -baryon resonance in the nucleus. Nuclear modification factor, $R(p_t)$ as a function of transverse momentum is computed for these comparisons. The data used are from the $2m$ -propane bubble chamber of Joint Institute for Nuclear Research, Dubna, Russia.

Keywords: carbon-carbon interaction, 4.2GeV/c, transverse momentum, baryon resonances, collective phenomena.

1. Introduction

The transverse momentum (p_T) physics is of great interest. J.D.Bjorken has shown that transverse momentum, p_t is a constant variable [1]. Using the Heisenberg's uncertainty principle, $p_t \times A \sim h/2\pi$, one can find the size of particle emission area (A), where h is the Plank constant. p_t is used as applicability region of different models (for example, recombination, fragmentation, etc). In a collision the p_t plays crucial role, when: i) the nuclei barely graze each other ("peripheral" collision), a high-p_t parton (quark and gluon) quickly escapes the medium and it emerges after losing less energy and ii) the collision might be almost head-on ("central" collision), high-p_t partons have larger in-medium path-lengths and thus lose more energy (in average). The transverse momentum of a particle being a Lorentz invariant quantity has been accepted as a useful parameter in the study of strong interaction dynamics [2].

Experimental results and theoretical calculations suggest distinction of three p_T regions [3]: bulk (or low), intermediate and high-p_t. It is a rough distinction, because if in 90th years a start value of high-p_t was 2GeV/c, now a days it is around 6GeV/c, with the starting of first HIC in Large Hadron Collider (LHC) of European Organization for Nuclear Research (CERN) experiment, it is expected to be 13GeV/c. Thus, above mentioned p_t regions change with increasing incident energy. The bulk region (p_t<2GeV/c) seems to be driven by the thermal properties of the matter created in hA -, AA -interactions and HIC. Majority of the particles (about 99% of produced hadrons at the Relativistic Heavy Ion Collider (RHIC) of Brookhaven National Laboratory (BNL) have p_t of less than 1GeV) emitted in HIC appear in the low-p_y region. In the intermediate-p_t region (2<p_t<6GeV) one can investigate the interactions between the hard probes and the bulk matter created in hA -, AA -interactions and HIC. In the high-p_t (p_t>6GeV/c) region measured particle spectra are well described by perturbative Quantum Chromo-Dynamics (pQCD) calculations. High-p_t particles suppression is one of the signatures of quark-gluon plasma (*QGP*), i.e., a thermalized phase in which partons are the relevant degrees of freedom.

The study of hadron production at high-p_t is a sensitive tool to characterize the matter created in ultra-relativistic HIC, and in particular, to detect the possible formation of QGP. Particles at high-p_t result from parton scatterings with high momentum transfer ("hard scattering"). The scattered partons will traverse the created medium as they fragment into the observable hadrons. High-p_t particle production in proton+nucleus (pA) and AA - interactions was predicted to be suppressed [4] as a consequence of the energy loss of the scattered projectile partons (or hadrons) in the hot and dense medium (a phenomenon known as "jet quenching") before the particle production process. Such suppression was observed by experiments at RHIC in central Au+Au and Cu+Cu collisions at a center-of-mass energy of up to $\sqrt{s_{NN}}$ =200GeV/nucleon [5]. Particles are suppressed not equally. Another phenomenon, called "Cronin enhancement" [6] is presented in d+Au and peripheral Au+Au collisions. It is believed to be due to multiple nucleons scattering within the nucleus. Neither of these are clearly understood thus require further experimental and theoretical study.

The hard scatterings are still present in the heavy-ion data, but resulting distributions are found to be modified due to medium interactions. Thus, understanding modifications to the high-p_t particle distributions can lead to qualitative conclusions on the energy loss mechanisms within the medium.

2. The Experimental method

The experimental data were obtained using the 2m propane bubble chamber of the Laboratory of High Energies of Joint Institute for Nuclear Research (JINR) (Dubna, Russia) exposed to a beam of protons, helium and carbon nuclei at the momentum 4.2AGeV/*c* per nucleon at Dubna Synchrophasotron [7]. In table 1 a specification of CC and pp- interactions is given. In this experiment the impurity of the charged strange particles does not exceed 1%. Therefore all negative particles, except for identified electrons, were considered as negative pions. The impurity not identified electrons in studied collisions practically is absent. The average density of δ electrons on tracks of protons with length of a trace is more 5 mm made 0.021 $\pm 0.001 cm^{-1}$.

Table 1: *Features of the experiments*

Type of interaction	Momentum of beam, GeV/c	Accelerator	Year	No. of inelastic interactions
CC	4.2	Synchrophazotron, LHE, JINR, Russia	1976	21090
pp	4.2	Synchrophazotron,	1976	4753

Positive particles include in themselves positive pions, protons and heavier single charged fragments of nuclei (deuteron, tritium). Observable fragments with $Z \geq 2$ concerned to fragments of a nucleus-projectile. For allocation of fragments from a set of all positively charged particles different procedures were used. A fraction of a positive pions in the general number of positive particles in momentum interval p_{π^+}=(0.5-2.0) GeV/c did not exceed 13.5%.

Protons, deuterons and heavier fragments in propane bubble chamber one can possible divide on density of ionization on traces only in a momentum interval (1.0-2.0)GeV/c. Experimentally certain value of the contribution of deuterons and heavier fragments in the general number of fragments was equaled ~2.2% in a considered momentum interval. It allows making the assumption, that in our experiment positively charged particles (except for identified positive pions) presented, basically, protons.

Protons used for the figures used in the paper were taken with p>0.15GeV/*c* and negative pions with p>0.080GeV/*c*, since 0,15GeV/*c* and 0,08GeV/*c* are average lower momentum thresholds of registration of protons and pions respectively in propane chamber. Below of these threshold values the efficiency of registration of these particles is very low. So called stripping protons (spectator protons from projectile-nucleus) having p>3GeV/*c* and θ (emission angle) <4 degrees (in laboratory frame) for interactions at initial momentum of 4.2*A*GeV/*c* were excluded.

We have analyzed 4753 inelastic pp -interactions at momentum 4.2GeV/c and 21090 inelastic CC-interactions at 4.2AGeV/c. The properties of proton and negative π -meson production have been studied in CC-interactions, using pp reference data at 4.2GeV/c to extract information on the collective phenomena, for example formation of the Δ^0 resonance in the nucleus. Particle yield dN/dp_t is calculated and then nuclear modification factor R is constructed by comparing *AA* yield with *pp* yield.

Now let's present the experimental results from carbon + carbon interactions taken from 2m propane bubble chamber. To analyze the results the Nuclear Modification Factor has been used. The general formula of it is the following:

$$R = \frac{[1/N^{tot}_{events}\,(dN_{\pi^-,proton}/dp_t)]^{CC}}{[1/N^{tot}_{events}\,(dN_{\pi^-,proton}/dp_t)]^{pp}}$$

It should be noted that the integration of nominator (and denominator) gives us the mean multiplicity (it is a number of particles per event) CC and pp-interactions. Mean multiplicity is one of the important characteristics to take important information from hadron+nucleus and nucleus+nucleus interactions.

3. Experimental results

In Figure 1, the values of

$$R = \frac{[1/N^{tot}_{events}\,(dN_{prot}/dp_t)]^{CC}}{[1/N^{tot}_{events}\,(dN_{prot}/dp_t)]^{pp}}$$

for protons are given. Momentum of the incident particle is 4.2AGeV/c. It is seen that:

1. The variable R approximately is constant within error bars in low p_t region (p_t<1.2GeV/c). It should be noted that the enhancement of the R were observed in low p_t region (p_t<0.3GeV/c) in pC -interactions at 4.2GeV/*c*[8]. So, one can say that in case of CC interactions we have the highest number of nucleon-nucleon collisions per event (and the highest number of participant nucleons and thus the lowest number of spectator nucleons) and the highest degree of carbon disintegration among pC and CC interactions and thus the enhancement at p_t<0.3GeV/c due to spectator protons in CC interactions smears out and disappears.

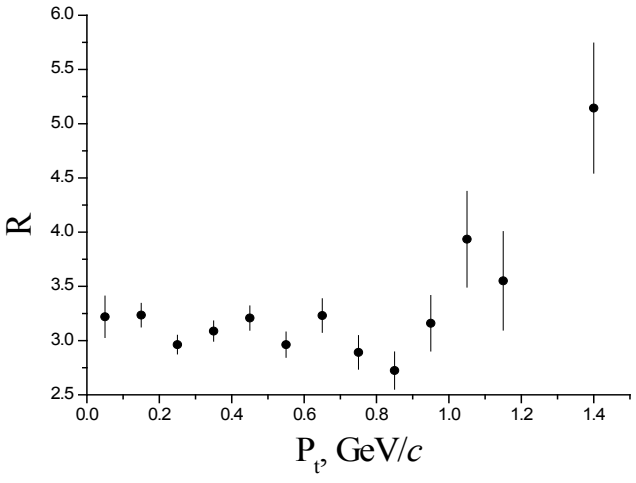

Fig. 1. The ratio R (protons) for CC-interactions at 4.2GeV/c per nucleon

2. One can see the clear enhancement at p_t>1.2GeV/c. This enhancement is due to collective phenomena, i.e. due to the contribution from central-central collisions, where the p_t enhancement can be explained as due to the processes of hard scattering in central nucleus-nucleus collisions [9].

In Figure 2 the values of

$$R = \frac{[1/N^{tot}_{events}\,(dN_{\pi^-}/dp_t)]^{CC}}{[1/N^{tot}_{events}\,(dN_{\pi^-}/dp_t)]^{pp}}$$

for negative pions are given. Momentum of the incident particle is 4.2AGeV/c per nucleon. It is seen that:

1. There are two different regions for emission of π^- mesons: p_t<0.45GeV/c and p_t>0.45GeV/c, which was seen for pC -interactions at 4.2GeV/c. The values of R in both regions increase;

2. At p_t≈0.45GeV/c we see minimum, that was found for pC -interactions at the same point;

3. There is a tendency in increase of the mean multiplicity of negative pions in low-p_t region (p_t<0.45GeV/c) in CC -interactions compared to pp -interactions at the incident energy of 4.2GeV/c per nucleon. An average number of interacting nucleons in CC -collision is 8.64±0.14 [10]. The mean multiplicity of π^- -mesons increases in high-p_t region (p_t>0.45GeV/c) with the mass of the colliding system too. These high-p_t pions, most probably, are direct pions. The slow protons are direct protons too, because they are not participated in interaction. But the low p_t pions and high-p_t protons are correlated. In paper [11] has shown that, according to the Quark Gluon String Model (QGSM) [12], contributions of resonance and direct pions strongly depend on the p_t. At p<0.3GeV/c, most pions (64%) are from Δ^- and Δ^0 decay, while at momenta higher than 0.5GeV/c, direct pions dominate (52%) in CC and C-Ta interactions at 4.2GeV/c per nucleon. Besides, paper [13] confirms that Δ^0 decay is a dominant mechanism of pion production in C + C collisions at 4.2GeV/c per nucleon and the ratio of pion production from Δ decay and direct pion creation was estimated to be at the level of (50±5)% for Δ^0 .

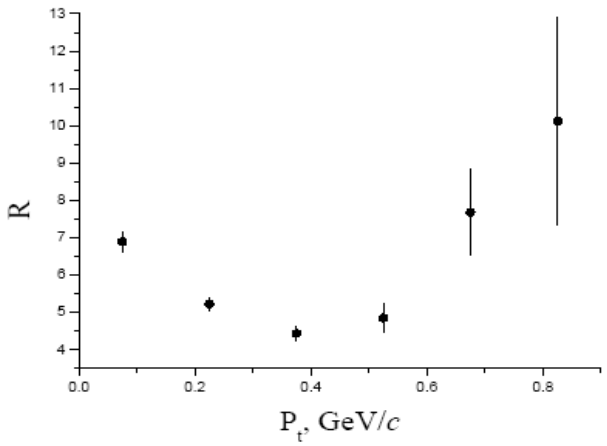

Fig. 2. The ratio R (negative pions) for CC -interactions at 4.2GeV/c per nucleon

4. Conclusions

In R(p_t) dependence, in low-p_t region (p_t<0.3GeV/c) for protons, with increasing mass number of projectile (beginning from pC up to CC interactions) the enhancement of the R smears out and disappears due to spectator protons. On the other hand, one can see the clear enhancement at high-p_t (p_t>1.2GeV/c), which is the highest in case of CC-collisions at 4.2AGeV/c. This enhancement is due to collective phenomena, i.e. due to the contribution from central-central collisions, where the p_t enhancement can be explained as due to the processes of hard scattering in central nucleus-nucleus collisions.

The mean multiplicity of π^- mesons increases in high p_t region (p_t > 0.45GeV/c) with the mass of the colliding system too. These high p_t pions and slow protons are direct particles. Another dominant mechanism for the emission of the low p_t negative pions and high p_t protons is the Δ^0 resonance decay.

It is our pleasure to express the gratitude to all the members of the former collaboration who took part in data processing from 2m propane bubble chamber of the Laboratory of High Energies of JINR.

References

1. J.D.Bjorken, FERMILAB-Pub-82/59-THY, 1982

2. Ramona Vogt, "Ultrarelativistic Heavy ion collisions", ELSEVIER, Netherland, 2007

3. Levente Molnar, arxiv: 0801. 2715v1 [nucl-ex] 17 Jan 2008

4. X.-N. Wang, M. Gyulassy, arxiv: 0708.2630v2 [nucl-ex] 17 Jun 2008

5. J. Adams et al., Nucl. Phys. A**757**, 102 (2005)

6. J. Adams et al, Phys. Lett. B**637**, 161 (2006)

7. D. Armutlisky et al., Z. Phys. A**328**, 455 (1987)

8. Y.H. Huseynaliyev, L.Y. Huseynaliyeva, F.C. Rasulova, Z.M. Hashimov, Journ. of Qafqaz Univer., **33,** 71 (2012)

9. A.I. Bondarenko, et al., Physics of Atomic Nuclei, **65**(1), 90 (2002)

10. Lj. Simic, M. Vranjes Milosavljevic et al., Phys. Rev. C**80**, 017901 (2009)

11. Lj.Simic, S.Backovic et al., Phys. Rev. C**52**, 356 (1995)

12. V.D. Toneev et al., Nucl. Phys. **A** (519), 463 (1990)

13. P.Seyboth for NA49 Collaboration. 23rd Winter Workshop on Nuclear Dynamics, Big Sky, February 12-17, (2007)

Email: yashartur@yahoo.com

Spectroscopic study of the stars HD142983 and HD187982

Y.M.MAHARRAMOV, A.R.HASANOVA, A.M.KHALILOV, A.SH.BALOGLANOV, G.M.HAJIYEVA

Shamakhy Astrophysical Observatory named after N.Tusi, Azerbaijan National Academy of Sciences
y_meherremov@rambler.ru

Abstract

Profile variations in the Hα and Hβ lines in the spectra of the stars HD142983 and HD187982 are investigated from observations acquired in 2011, 2013 and 2014. It has been determined that profile of the Hα line of HD142983 are consist of two changeable emission with double peak and absorption in its. The intensity of emission and absorption components of the Hβ line changes quickly. We suppose that all of these changeabilities are explained with the characteristic feature of the star which this peculiarity is nature of the Be-type stars. In addition, it was revealed that when Hα line from a form P Cyg to the pure absorption in the spectra of HD187982, the Hβ line moves to the red side, and its radial velocity changes sharply.
Keywords: *Hα line, P Cyg profile, the radial velocities*

Introduction

HD142983. According to latest scientific data the parameters of the star HD142983 are: the spectral class B8Ia/ab, the mass $M_* = 4.1M_\odot$, the radius $R_* = 3.2R_\odot$, the effective temperature $T_{eff} = 12860$ K, the rotational velocity $\vartheta \sin i = 390$ km/s [1].

The spectroscopic investigations of the "Be-shell" star HD142983 has been studied particularly by A.B.Underhill, R.Faraggiana and H.G.Geuvernik [2-4].

Underhill (1953) discovered that the underlying star of HD142983 is a rapidly rotating B-type star. Intensity tracings show that in 1950 stellar Hα was obliterated by emission from the shell and a sharp absorption core, and that in 1951 the same was true for stellar Hβ. In 1953 the stellar Hα was still not visible but a stellar feature could be observed at Hβ underlying the emission and absorption core from the shell [2]. Observations of the line of Hα and Hβ are shown that the shape and strength of the emission features at Hα and Hβ change with time. The wings of the emission at Hα are symmetrical, the apparent slight asymmetry of the red wing in 1953 being caused by a flaw on the plate. The emission and sharp absorption core at Hβ are superimposed on a diffuse, shallow stellar feature [2].

Radial velocities of Hα line have been measured on spectra of HD142983 taken in the period 1950 – 1962 [3]. Faraggiana (1969) noted that the radial velocities of the Hα absorption core do not fit on the mean radial velocity curve but indicate that the material from which this line is formed is expanding with a constant velocity of about -25 km/s. The profiles of Hα line change during the radial velocity cycle.

It was noted that in the works done by Geuverink (1970) the great width of the Hα emission line may be due to chaotic motions of the material emitting this line or it may be due to radiation damping [4].

HD187982. It is a supergiant of spectral type A2Ia with the following parameters [5-9]: $m_v = 5^m.58$, $M_* = 15M_\odot$, $R_* = 78R_\odot$, $T_{eff} = (9300 \pm 250)$ K and $\vartheta \sin i = (15 \pm 6)$ km/s.

In [7-8, 10-11] the study of Hα and other lines observed in the atmospheres of the supergiant HD187982 is presented. It is noted that generally the profiles of the Hα line are observed in absorption. Sometimes in the red wing of the profile of Hα line is observed weak emission component. A more complete explanation of appearance and disappearance of these components require additional observations.

In the present study, which can be considered a continuation of the above studies, we analyze variations of the Hα and Hβ lines in the spectra of HD142983 and HD187982 with the aim to study their peculiarities.

Observations, data processing and discussion

Spectral observations of the stars HD142983 and HD187982 in 2011, 2013, and 2014 were carried out using the echelle spectrometer in the Cassegrain focus of the 2-m telescope of the Shamakhy Astrophysical Observatory with CCD detector [12]. The spectral resolution R was equal to 15000 and the spectral range was λλ4700-6700 ÅÅ. The Echelle spectra were processed by the standard technique using the DECH20 and DECH20t software[13].

Two spectra of the target star were obtained during each night of observation. These spectra summed up before measuring. The signal-to-noise ratio was S/N =150÷200 for the average exposure of 600 s (depending on the image quality). In addition to the observations of these stars we also obtained numerous spectra of standard stars, day and night background, as well as comparison spectra to enable analysis of the stability of the instruments and telescope-receiver complex. The measurement error for the radial velocity is ± 2 km/s.

HD142983. The Figure 1 shows the fragments of Hα and Hβ lines in selected epochs in 2011 and 2014. The spectral observations showed that the most variability in the spectra of HD142983 is found in the intensity and profiles of the Hα and Hβ lines.

As seen the Hα profile appears as a double emission peak. The violet emission component obviously becomes weaker than red one (Fig.1a). We measured the residual intensities and radial velocities of Hα line.

Measurements showed that the residual intensity and radial velocity of the absorption and violet and red

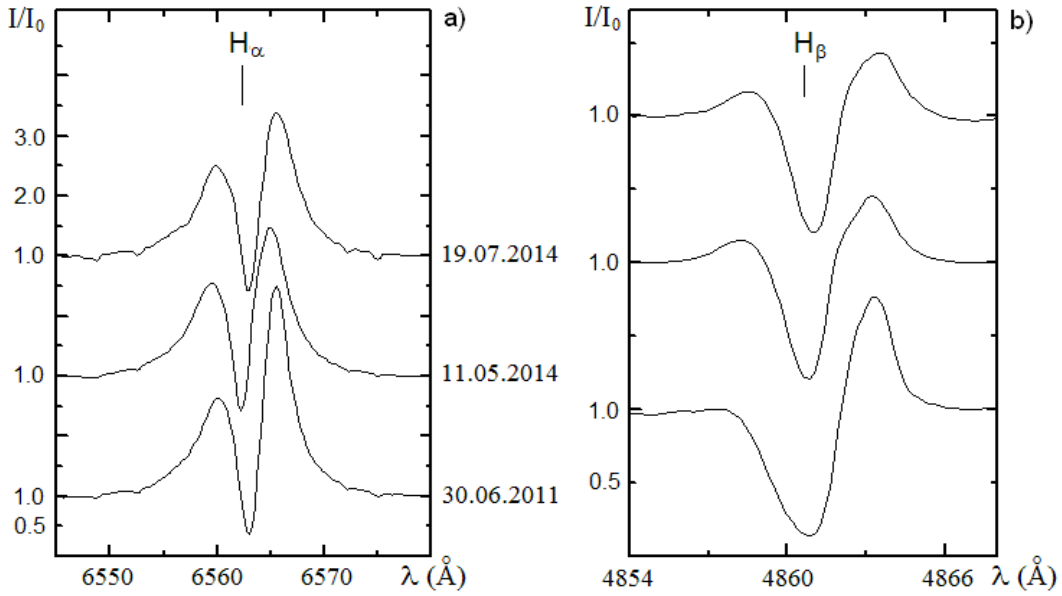

Fig.1. *Hα and Hβ profiles in spectra of HD142983 obtained at various epochs.*

emission peaks of Hα line change in 0.36 ÷ 0.59, 2.46 ÷ 2.63, 3.38 ÷ 4.49 and -24 ÷ -10 km/s, -156 ÷ -139 km/s, 96 ÷ 108 km/s intervals respectively. It is apparent that the shape and spectral measurements of the emission features at Hα change with time. The values of the V/R (ratio of continuum-subtracted fluxes in violet and red peak, respectively) ratio changes from 2011 to 2014 and are quite homogeneous. In addition, our observations showed that the Hβ profile is observed in P Cyg shape (the absorption and emission components) in 2011 (Fig.1b). But, in 2014, Hβ appeared in double emission with a deep central shell absorption. The changes in shape and strength of these emission features vary with the velocity changes. The great width of the emission feature at Hα is significant. The remarkable change in the Hα profile observed on 2011 and 2014 implies the possible occurrence of the violent activity in the stellar emission envelope.

We may infer that these changes, especially the Hα line-profile variations could be due to the non-uniform distribution of the circumstellar matter. The non-uniform distribution of the circumstellar envelope is possibly related to the violent activity of the emission envelope in the star. We investigated the changeability of radial velocity of the lines with time. It was not found short-term periodicity. We suppose that these changes may be a long-term periodicity.

HD187982. Profile of the Hα line is P Cyg type. The profile of this line has a variable structure. The radial velocities, residual intensities and half-widths of the studied lines are determined. The analysis of the absorption and emission components of the Hα line shows that the radial velocities change with time. In the spectra of HD187982 observed on 01.09.2013 and 06.09.2013, the profiles of the Hα lines consist of a strong absorption component and a weak emission component which is observed on the red wing of the Hα line (Fig. 2a). It is also interesting that in the red side of emission component of the Hα line, there is a weak absorption component again. But on 02.10.2013 and 03.10.2013, the Hα line is visible only in absorption and there are no accompanying components.

We noted above that (Fig.2a) the profile of Hα line has variable structure in the spectrum of the star HD187982 depending on the activity phase of the atmosphere. This profile is observed in two following forms:

a) the profile of the Hα line consists of a strong absorption component and a weak emission component which is observed on the red wing of the Hα line.

b) the profile of the Hα line is observed in pure absorption.

On the other hand, apparently from Fig. 2b, the strongly structural changes in the profiles of the Hβ line are not observed. But our measurement showed that the radial velocities of Hβ line varied with time. So, on 01.09.2013, 06.09.2013, 02.10.2013, and 03.10.2013, the radial velocity of the Hβ line were -33 km/s, -33 km/s, -18 km/s and -19 km/s, respectively. Apparently, upon transition of the Hα profile from a form a) to the b) case the Hβ line moves to the red side, and the radial velocity changes sharply. So, we revealed that change of the radial velocity in the Hβ line shows interesting similarity to the shape of Hα profile.

The further spectra of this star are observed between 21.06.2014 and 09.08.2014.

In the spectra observed on 21.06 – 09.08.2014, the radial velocity of Hα and Hβ changed (-13÷-5 km/s, and -16÷-8 km/s, respectively) on average on ±4 km/s. But

strong changes in the profiles of these lines are not observed. We did not find periodicity in these changes.

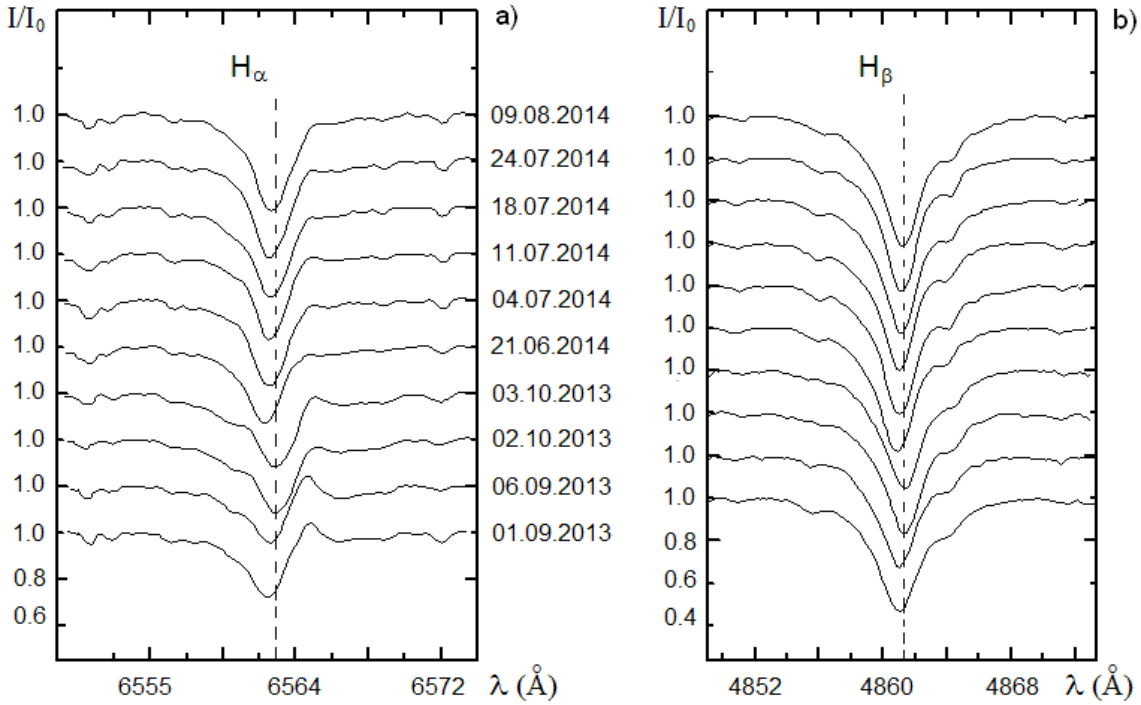

Fig.2. *Profiles of the Hα and Hβ lines in the spectra of HD187982 observed in 2013 and 2014.*

Hence, we revealed that the profile of Hα line of the star HD187982 has a normal P Cyg type in the active phase of the star atmosphere. The emission component in the red wing of this line forms and disappears.

We supposed that all these variations in the atmosphere of HD187982 may be due to non-stationary and strong flow substance in the atmosphere of this star.

Conclusions

Our observations showed that the Hα and Hβ profiles had dramatic moving features in the spectra of HD142983. We may infer that these changes, especially the Hα line-profile variations could be due to the non-uniform distribution of the circumstellar matter. The non-uniform distribution of the circumstellar envelope is possibly related to the violent activity of the emission envelope in the star.

All the data considered here indicate strong variability of the atmosphere of HD187982. The emission component in the red wing of the Hα profile forms and disappears. In addition, we revealed that when the Hα line is observed in pure absorption in 2013, the Hβ line moves to the red side, and therefore its radial velocity changes sharply. We supposed that such variations may be due to non-stationary and strong flow substance in the atmosphere of this star.

References

1. G.Catanzaro, Astronomy and Astrophysics, **550**, A79, 1 (2013).
2. A.B.Underhill, Publications of the Dominion Astrophysical Observatory, **IX**, No.12, 363 (1953).
3. R.Faragiana, Astronomy and Astrophysics, **2**, 162 (1969).
4. H.G.Geuverink, Astronomy and Astrophysics, **5**, 341 (1970).
5. C.J.Evans, Ian D.Howarth, MNRAS, **345**, 1223 (2003).
6. N.Przybilla, M.Firnstein, M.F.Nieva, G.Meynet, A.Maeder, Astronomy and □ Astrophysics, **517**, 1 (2010).
7. E.Verdugo, A.Talavera, A.I.Gomez de Castro, Astronomy □ Astrophysics, **346**, 819 (1999).
8. E.V.Verdugo, A.Talavera, A.I.Gomez de Castro, Astronomy □ Astrophysics, **137**, 351 (1999).
9. E.M.Hendry, The Astronomical Journal, **86**, 1540 (1981).
10. A.A.Helmut, N.I.Morrell., Astrophysical Journal, Suppl. Ser., **99,** 135 (1995).
11. R.L.Snell, P.A.Vanden Bout, Astrophysical Journal, **244**, 844 (1981).
12. Kh.M.Mikailov, V.M.Khalilov, I.A.Alekberov, Tsirkulyar ShAO, **109**, 21 (2005).
13. G.A.Galazutdinov, Prepint SAO RAS, **92**, 1 (1992)

The interactional nature of nanoparticles with plant cell surface

I.S.AHMADOV, M.A. RAMAZANOV, V.N. RAMAZANLI, N.J.AGAYEVA

Department of Chemical Physics of Nanomaterials, Baku State University, Azerbaijan

Under the microscope dynamic nature of the adsorption of the nanoparticles on the surface of the plant cell, depending on the exposure time and concentration of nanoparticles in solution was investigated. The toxicity of nanoparticles primarily connected with their ability to absorption, transport and interaction with the cell wall and plasma membrane in plants. Surface properties of plasma membrane partially controlled by the ionic composition of the exposure medium, play significant roles in the distribution of nanoparticles on the surface of plant cells. It was suggested that by the nature of adsorption of nanoparticles on the surface of plant cells can determine the type of charge on their surface.
Key words: plant cell, nanoparticles, adsorption, cell surface, interaction, toxicity

1. Introduction

The unique physicochemical properties of nanoparticles (NPs) that have given rise to applications in many fields, including drug delivery [1], cancer therapy [2], biosensors [3], food additives and cosmetics [4], may also increase the risk of toxicity to humans or the environment [5]. Many in vitro studies have demonstrated that certain NPs are cytotoxic and can cause oxidative stress and DNA damage, which has raised human health concerns [5]. As more NPs and NP-containing products are developed and brought into commercial use, it is generally assumed that NPs will enter the environment [6]. Industrial production of NPs is increasing in scale and diversity, raising additional concerns of environmental exposure to nanomaterials. The potential for human and ecological toxicity associated with nanomaterials is thus a growing area of investigation [7]. The toxic effects of a wide range of sizes of silica NPs have been tested and despite the NPs showing fast agglomeration upon contact with cell culture media, smaller sized silica NPs have been shown to be more cytotoxic than larger ones, [8]. It is critical to understand fundamental mechanisms underlying any biological responses to NPs, be they desirable or not. Understanding the principles of how NPs can transmigrate into cells could enable greater control over cellular uptake and would improve prediction of possible toxic effects. There have been reports that some NPs are taken up by cells via non-endocytic pathways [6], and model membranes have indicated possible mechanisms for non-endocytic uptake [9]. For instance, Banerji et al. showed that citrate-capped gold particles (7 to 15 nm diameter) do not diffuse through a lipid membrane and can be encapsulated by vesicles. In contrast, hydrophobic alkane-thiol coated gold NPs of 2 nm diameter become located inside the hydrophobic core of the lipid bilayer (whereas larger hydrophobic particles tend todisrupt lipid vesicles) . A range of behaviours has been observed with amorphous silica particles. Particles up to 5 μm diameter have been shown to enter the cytoplasm of cells and although they are considered to have good biocompatibility, they have been shown to have haemolytic activity (see [10] and references therein). NPs cause haemolysis of mammalian red blood cells through interaction between the surface of the NPs with the cell membrane [10]. NPs of less than 100 nm can induce endocytosis-dependent reactive oxygen species generation, DNA damage [11] and aberrant nucleoplasmic protein aggregation [12]. Furthermore, particles of 15–20 nm can bind to lipid vesicles, while larger particles (up to 190 nm) can transmigrate into giant unilamellar vesicles (GUV) [9]. In the latter case the nanoparticles were coated with a lipid membrane in the process. Membrane disruption by nanoparticles has also been identified by electrophysiological methods [13]. If such disruption were to enable uptake directly into the cytoplasm, without significant damage to the cell, nanoparticles would be potential vehicles for drug delivery applications. The biocompatibility of NPs, its amenability to surface modification and the fact that it is not electro-active in aqueous media has already led others to consider it for application in gene and drug delivery [14,15]. The affinity of NPs for lipid bilayers and the potential for 'passive' uptake in vesicles makes NPs an intriguing target for toxicological as well as drug-delivery studies.

The rate of uptake and intracellular localization of nanoparticles have been studied by many research groups, and several review articles summarizing the published data are available; see e.g. [16]. These reviews reveal that it is difficult to draw general conclusions about how to produce particles for optimal cellular uptake, as the rate and mechanism of uptake turns out to be cell-type dependent and vary between nanoparticles with different size, charge, and other surface properties. There are, however, several reports showing that nanoparticles of 20—50 nm are taken up more rapidly than smaller or larger particles . Because particles with a positive charge will bind to the negatively charged cell surface, one would expect positively charged particles to be endocytosed more efficiently than negatively charged particles. In fact, a study in HeLa cells with positively and negatively charged nanoparticles of equal size (80 nm) showed a 2-fold higher uptake of the positively charged particles . In contrast, a

higher uptake of negatively charged nanoparticles has been reported in HEK cells .

The interaction of nanoparticles with cells surface is critical in many applications such as adsorption, uptake, transport and localization of nanoparticles in plants. These applications require a firm control over nanoparticle–cell interactions, which are mainly dictated by surface properties of nanoparticles and cells. This thesis work presents an understanding of how nanoparticles interact with plant surfaces. Have been analyzed the data in field of cell wall, cell surface, surface structure, the electrical properties of cell surface and interaction of some nanoparticles with plant cell surface.

2. Experimental materials and methods

The objects of study were aquatic plant *Trianea bogotensis karst*. Trianea very beautiful stemless floating plant of the family *Hydrocharideae*. Its leaves almost round, thick, light green top, convex, smooth, covered with shiny waxy coating; pale beneath, depressed, covered with a mass of cells with glassy air bubbles that support them on the water. Trianea is one of the few floating plants that retain their leaves are sometimes of the winter, but of course, these leaves, reaching the size of the 3-penny coin in the summer , in the winter begin to diminish. Trianea multiplies very quickly and easily. From one instance of a few weeks, you can get a whole ten, but only in the summer and provided to keep it in a sunny spot. In the same greenhouse aquariums it multiplies and winter. It is best to keep it at this time, as it turns out, in aquariums, heated lamp. Here it continues to not only grow and reach a large size, but also provides a variety of branches. Root hairs of the plant have a diameter of 70-80 mm 2-4 mm in length, which allows for different experiments with nanoparticles. Large cells allow these plants to conduct experiments for a long time without disturbing their physiological state and undamaged of the membranes. In addition, cells electro genesis aquatic plants has been thoroughly studied, and it is often used in electrophysiology.

In experiments used different kind of nanoparticles such as copper oxide (CuO), titanium oxide (TiO2), iron oxide (Fe3O4), zinc oxide (ZnO), aluminum nano powder (Al2O3), zirconium oxide (ZrO2) with different sizes.

3. Results and discussion

If to observe fresh leaves or roots of plant in a conventional SEM, we will be surprised to find that in the surface of leaves or roots there are many interesting structures in nanosized (Fig.1). These structures are the surface structures of primary cell wall. This cell wall is part of the apoplast which itself is largely self-contiguous and contains everything that is located between the plasma membrane and the cuticle. The primary wall and middle lamella account for most of the apoplast in growing tissue. The symplast is another unique feature of plant tissues. This self-contiguous phase exists because tube-like structures known as plasmodesmata connect the cytoplasm of nearby cells. The main chemical components of the primary plant cell wall include cellulose (in the form of organized microfibrils), a complex carbohydrate made up of several thousand glucose molecules linked end to end. In addition, the cell wall contains two groups the pectins and cross-linking glycans. In the networks of branched polysaccharides, thre are a small amount of protein can be found in all plant primary cell walls. Some of this protein is thought to increase mechanical strength and part of it consists of enzymes, which initiate reactions that form, remodel, or breakdown the structural networks of the wall.

Fig. 1. SEM picture of Lotus leaf (Nelumbo nucifera) surface. Treated with CP-drying preparation methods (H. J. Ensikat et all., 2010).

Cell walls are the first barriers which limit the entry of rigid particles (also nanoparticles with high sizes), large molecules that may be toxic to the cell. Cell walls creation of stable osmotic environments by preventing osmotic lysis and helping to retain water. At now it is good investigated that the plant cell wall is a complex biomatrix with porosity on the scale of 5–10 nm. For example, in root hairs of Raphanus the diameter of pores was 3.8 nm, which was determinated by solute exclusion [19]. The porosity of plant cell wall depends of types of plant cells and is changing during development of plants. The porosity of cell wall allow diffuse small nanoparticles freely to the face of plasmatic membrane. But negative charges at cell membrane surfaces which create a surface electrical potential ($\psi 0$) also hinders on diffusion of nanoparticles to the plasmatic membrane. During uptake of nanoparticles in plant cells there are specific interactions between cells and nanoparticles. These interactions includes mechanical, electrical and osmotic interactions. Therefore it is interesting to investigate the nature of adsorption processes nanoparticles on the plant cell surface.

Fig. 2. The adsorption of CuO nanoparticles on the root hair

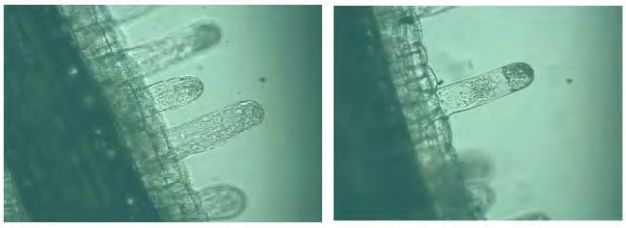

surface of Trianea

In preliminary experiments have been explored the adsorption of nanoparticles on the surface of plant cells depending on the exposure time. For this purpose, roots of

Trianea were maintained in the solution of colloidal nanoparticle in different times. The adsorption of nanoparticles were observed under a microscope depending on the exposure time. Figure 2 shows the adsorption of CuO nanoparticles for 10 minutes on the cell surface of root hairs Trianea. The concentration of CuO nanoparticles in solution was 1mg/ml. As seen from figure nanoparticles were adsorbed rapidly mainly on the tip of the cell.

In the next experiments have been studied the adsorption of different nanoparticles on the surface of root hairs. For this the plant of *Trianea bogotensis* with roots was exposed in the colloidal solutions of nanoparticles during 24 h. After the expositions the root of trianea was separated from plants and observed under microscope. It is clear seen from microscope's pictures that nanoparticles adsorbed on the surface of root hairs form agglomerates and do not rinse for a long time and remain on the cell surface. On the figure 3 are shown the adsorption of ZnO, CuO, TiO2 and Fe2O3 nanoparticles on the root hair surface of *Trianea bogotensis*. It was interesting that during 24 h expositions adsorption of iron nanoparticles still does not seen. It is maybe they no form agglomerates

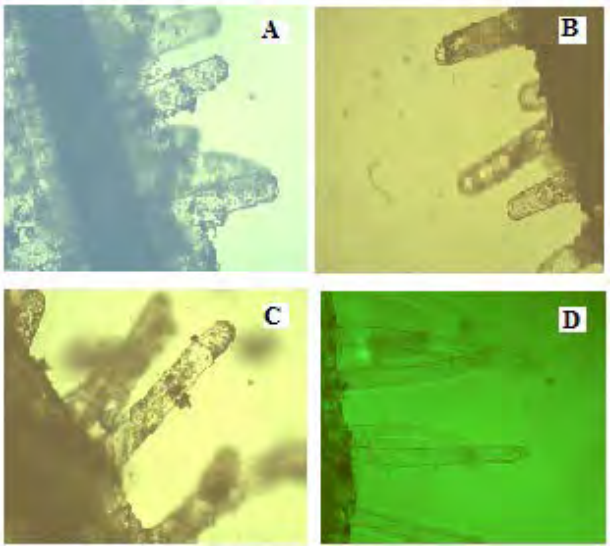

Fig. 3. The adsorption of ZnO (A), CuO (B), TiO2 (C) and Fe2O3 (D) nanoparticles on the root hair surface of Trianea bogotensis

In the another experiments are studied the cell surface adsorption's of nanoparticles dependence on their concentration in solutions. The concentration of nanoparticles was 0.01 mg/ml, 0.1 mg/ml and 1 mg/ml. The concentration's dependence of adsorption was studied for the all given nanoparticles. In the figure 4 was shown the concentration's dependence of adsorption for the ZnO nanoparticles. As seen from the picture 4 the adsorption rate and density of nanoparticles increase with increasing the concentrations of nanoparticles.

Despite the widely investigation works interaction of nanoparticles with plants still many questions remain concerning the fate and behavior of nanoparticles in plant systems such as the role of sizes, dose, environmental conditions, surface area or surface activity of nanoparticles on phytotoxicity, the potential route of entrance to plant cell and the role of plant cell walls in internalization of nanoparticles. The toxicity of nanoparticles primarily connected with their ability to adsorption, transport and interaction with the cell wall, plasma membrane and intracellular membrane of organelles system in plants. NPs have to penetrate cell walls and plasma membranes of epidermal layers in roots to enter vascular tissues (xylem) in order to be taken up and translocate through stems to leaves.

Cell walls, through which water molecules and other solutes must pass to enter into roots, are a porous network of polysaccharide fiber matrices. The pore sizes of plant walls are typically in the range of 3–8 nm, which is much smaller than many tested NPs [17]. Navarro et al. hypothesized that cell walls typically with the thickness of about 5 to 20 nm function as natural sieves. NPs aggregates with a size smaller than the largest pore are expected to pass through and reach the plasma membrane and the larger particle aggregates will not enter into plant cells. But the authors also admitted that ENPs may induce the formation of new and large size pores which allow the internalization of large ENPs through cell walls [18].

Thus, from the literature data and from results of these experiments, it is clear that when nanoparticle adsorption in the surface of the plant cell there is appear agglomeration of NPs. The adsorbed nanoparticles diffuse through cell wall and reach to plasmatic membrane. During diffuse the nanoparticles are interacting with cell wall's cellulose, hemicellulose, pectin, with memrane proteins, ions and a surface electrical potential ($\psi 0$). Therefore the interaction of NPs has a complex characters and depends of structure and physiological condition of cell wall and plasmatic membrane, depends on the sizes, forms, surface electric charges of NPs. This process play important role for the determination of nanoparticle's toxicity. It can be assumed that if the nanoparticle adsorption on surface of the cell continues for a long time there is occur important changes in the cell metabolism. The results of given research showed that with adsorption of NPs on the cell surface the movement of protoplasm slows down and eventually stops.

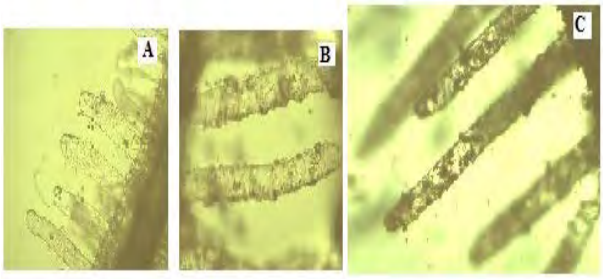

Fig. 4. The adsorption of ZnO nanoparticles on the root hair surface of Trianea bogotensis: A – 0.01 mg/ml; B – 0.1 mg/ml; C – 1 mg/ml

4. Conclusion

The toxicity of nanoparticles primarily connected with their ability to absorption, transport and interaction with the cell wall, plasma membrane and intracellular

membrane of organelles system in plants. Under the light microscope dynamic nature of the adsorption of the nanoparticles on the surface of the plant cell, depending on the exposure time and concentration of nanoparticles in solution was observed. It was found that the adsorption of nanoparticles depends on their size, type and exposure time. The nanoparticles were adsorbed rapidly mainly on the tip of the root hairs cell. Electrical properties of plasma membranes play significant roles in the adsorption and distribution of nanoparticles at the cell wall and exterior surface of plasma membrane. It can be assumed that negatively charged nanoparticles pass difficult through cell wall and the surface electrical layer of membrane strongly effects on the adsorption of nanoparticles. Positively charged nanoparticles are adsorbed mainly actively growing parts of cells.

References

[1]. Hu L, Mao ZW, Gao CY: Colloidal particles for cellular uptake and delivery. J Mater Chem, 19:3108–3115,(2009).
[2]. Peer D, Karp JM, Hong S, FaroKhzad OC, Margalit R, Langer R: Nanocarriers as an emerging platform for cancer therapy. Nat Nanotechnol, 2:751–760, (2007)
[3]. Lord H, Kelley SO: Nanomaterials for ultrasensitive electrochemical nucleic acids biosensing. J Mater Chem, 19:3127–3134,(2009)
[4]. Nohynek GJ, Lademann J, Ribaud C, Roberts MS: Grey goo on the skin? Nanotechnology, cosmetic and sunscreen safety. Crit Rev Toxicol, 37:251–277,(2007)
[5]. Nel A, Xia T, Madler L, Li N: Toxic potential of materials at the nanolevel. Science, 311:622–627,(2006)
[6]. Geiser M, Rothen-Rutishauser B, Kapp N, Schurch S, Kreyling W, Schulz H, Semmler M, Hof VI, Heyder J, Gehr P: Ultrafine particles cross cellular membranes by nonphagocytic mechanisms in lungs and in cultured cells. Environ Health Perspect, 113:1555–1560,(2005)
[7]. Geiser M, Rothen-Rutishauser B, Kapp N, Schurch S, Kreyling W, Schulz H,Semmler M, Hof VI, Heyder J, Gehr P: Ultrafine particles cross cellular membranes by nonphagocytic mechanisms in lungs and in cultured cells. Environ Health Perspect, 113:1555–1560,(2005)
[8]. Napierska D, Thomassen LCJ, Lison D, Martens JA, Hoet PH: The nanosilica hazard: another variable entity. Part Fibre Toxicol, 7:39, (2010)
[9]. Le Bihan O, Bonnafous P, Marak L, Bickel T, Trepout S, Mornet S, De Haas F, Talbot H, Taveau JC, Lambert O: Cryo-electron tomography of nanoparticle transmigration into liposome. J Struct Biol, 168:419–425,(2009)
[10]. Slowing II, Wu CW, Vivero-Escoto JL, Lin VSY: Mesoporous silica nanoparticles for reducing hemolytic activity towards mammalian red blood cells. Small, 5:57–62,(2009)
[11]. Nabeshi H, Yoshikawa T, Matsuyama K, Nakazato Y, Tochigi S, Kondoh S, Hirai T, Akase T, Nagano K, Abe Y, et al: Amorphous nanosilica induce endocytosis-dependent ROS generation and DNA damage in human keratinocytes. Part Fibre Toxicol, 8:1,(2011)
[12]. Chen M, Singer L, Scharf A, von Mikecz A: Nuclear polyglutaminecontaining protein aggregates as active proteolytic centers. J Cell Biol, 180:697–704,(2008)
[13]. de Planque MRR, Aghdaei S, Roose T, Morgan H: Electrophysiological characterization of membrane disruption by nanoparticles. ACS Nano, 5:3599–3606,(2011)
[14]. Coti KK, Belowich ME, Liong M, Ambrogio MW, Lau YA, Khatib HA, Zink JI, Khashab NM, Stoddart JF: Mechanised nanoparticles for drug delivery. Nanoscale, 1:16–39,(2009)
[15]. Vinu A, Hossain KZ, Ariga K: Recent advances in functionalization of mesoporous silica. J Nanosci Nanotechnol, 5:347–371,(2005)
[16]. D. Maysinger, J. Lovric, A. Eisenberg, R. Savic, Eur. J. Pharm. Biopharm. 65 270—281, (2007)
[17]. Carpita NC, Gibeaut DM. Structural models of primary cell walls in flowering plants: consistency of molecular-structure with the physical properties of walls during growth. Plant J;3:1-30, (1993)
[18]. Navarro E, Baun A, Behra R, Hartmann NB, Filser J, Miao A, et al. Environmental behavior and ecotoxicity of engineered nanoparticles to algae, plants and fungi. Ecotoxicology;17:372–86.,(2008a)
[19]. Stephen M. Read and Antony Bacic. Cell wall Porisity and its Determination. Modern Methods of Plant Analysis, Vol.17. Plant Cell Wall Analysis.Edit by H.F.Linskens and J.F.Jackson, Springer-Verlag Berlin Heidelberg 1996.

ismetahmadov@mail.ru

Some parameters of planetary nebulae and determination of the total energy flux radiated by them in the region λ>912Å

A.G.ALILI, K.I.ALISHEVA

Astrophysical department, Baku State University, AZ1148, 23, Z.Khalilov str., Baku, Azerbaijan

In this paper a more precise method of determination of the total energy flux emitted by the planetary nebulae which optically thick in the Lyman-continuum (LyC) in the region λ> 912 Å is given. It made possible to estimate the radii of central stars. Comparison of the values of the radii obtained by the method earlier developed by authors where the filling factor accepted equal to unity, with the ones estimated by the method proposed in given paper, permitted to estimate filling factor as well.

Keywords: *planetary nebulae, filling factor, radii of the central stars.*
Pacs 98.58 Ly, ***97.20.Rp***

1. INTRODUCTION

As it was mentioned in the[1], after the revealing of the important role of the study of planetary nebulae in the star evolution, interest to these objects was increased as well. Furthermore, possibilities of observation of planetary nebulae in all bands of electromagnetic radiation permitted to expand the number of explored questions.

In our study, we choose nebulae whichoptically thickin theLyC. All used parameters, such asthe electron concentration n_e, the electron temperature T_{el}, the angular radius θ of nebulae, the flux in the lines of H_β -$F(H_\beta)$, E_{B-V} for the taking into account the absorption in the interstellar medium, the temperature of nucleus T and the distance to nebulae d are taken from [1].

In this paper, the more exact method for the estimation of the total energy flux radiated by the nebulae whichoptically thick in theLyC, both in the lines and in the continuum in the region of wavelengths λ> 912 Å is proposed. It is possible to find the luminosity of the central star by the method suggested in [1], using more precise flux.

The estimation of the radius of the central stars in itself has a great interest. As is known, from the Hertzsprung-Russel diagram it follows that the central stars form an evolutionary sequence; the star, located in the right part of this diagram usually is the youngest, it will evolve, moving on the diagram to the left-hand side; this process will accompanied by the temperature increasing at a constant luminosity [1]. From here, of course, it follows that such evolutionary scenario should accompanied by the corresponding decrease of the radius of the central star. In our previous papers [2,3]are calculated the radii of the central stars, for which the Hertzsprung-Russel diagram is constructed. The conclusion made in [1] about the fact that the temperature increasing at a constant luminosity is accompanied by the corresponding decrease of the radius of the central star, has proved to be true.

Nevertheless, the method of determination of radii of the central stars, proposed by us in[2], has a disadvantage; the formula for the radius estimation includes a so-called filling factor, which accepted equal to unity. As this coefficient in reality ≤1, in the presented work we proposea new method for the estimation of the radius of central stars where the filling factor is absent.

Therefore, from the equality of two expressions obtained in our study for the radii of the central stars, we have estimated the filling factor. Since some relations given in [2] used in given paper, the basic concepts of [2] soon shortly specified in the beginning.

2. DETERMINATION METHOD OF RADII OF THE CENTRAL STARS OF PLANETARY NEBULAE IN THE ABSENT OF THE FILLING FACTOR

The basicconcept of thismethod, was as follows: if the nebulae is optically thick in theLyC, then referring to [4], the number of photons emitted by the central star in the LyC, (L_c) is equal to the number of photons emitted by the central star by the nebula in Balmer series, $N_{L_c} = N_{Ba}$ or

$$\int_{x_o}^{\infty} \frac{x^2 dx}{e^x - 1} = \sum_{Ba} A_i \frac{x_i^3}{e^{x_i} - 1}, \qquad (1)$$

where $x = \frac{h\nu}{kT_*}, x_i = \frac{h\nu_i}{kT_*}, x_o = \frac{h\nu_o}{kT_*}$, ν_o is the boundary frequency of theLyC, ν_i is the frequency of i- thBalmer lines, T_* is the effective temperature of the central star. The dimensionless quantity A_i expressed through the total energy emitted by the nebulae in i-thBalmer line and the energy, emitted by a star in a unit interval of frequency near this line and has the following form:

$$A_i = \frac{n_i A_{i2} hV}{4\pi^2 I^*_{\nu_i} R_*^2}, \qquad (2)$$

Here A_{i2} is the Einstein coefficient of the spontaneous transitions, V is the volume of the nebulaeemittingin hydrogen lines, n_i is the concentration of the hydrogen atoms in i-th level, R^* is the radius of the central star, and $I^*_{\nu_i}$ is the average Plank intensity of radiation of the central star at the frequency ν_i which is expressed as:

$$I^*_{\nu_i} = \frac{2k^3 T_*^3}{c^2 h^2} \frac{x_i^3}{e^{x_i} - 1}, \qquad (3)$$

As a first approximation, we consider the nebula as a sphere containing ionized matter with constant value of theelectron concentration. The filling degree of this sphere by ionized matter described by the filling factor ε [1]. If

ε=1, then the sphere with the radius R is uniformly filled by ionized matter, and the condition ε<1 means that the density distribution of matter is nonhomogeneous. As it was mentioned in [1] though it is only simplified the model, it apparently well represents the true picture. So, it is accepted, that $V = 4/3\,\pi R^3 \varepsilon$. Using the formulas (2) and (3), and taking into account the expression for V, the right-hand side of an equation (1) one can presented as:

$$\sum_{Ba} A_i \frac{x_i^3}{e^{x_i}-1} = 5.4\cdot 10^{-12}\frac{\varepsilon R^3}{T_*^3 R_*^2}\sum n_i A_{i2}\,, \qquad (4)$$

where

$$\sum_{i=3}^{\infty} n_i A_{i2} = 3.2\cdot 10^{-16}\frac{n_e^2}{T_e^{3/2}}\sum_{i=3}^{\infty} i^2 A_{i2} e^{\chi_i/kT_e}\,.$$

Therefore,

$$\sum_{Ba} A_i \frac{x_i^3}{e^{x_i}-1} = \frac{2\cdot 10^{-27} n_e^2 \varepsilon R^3 \sum_{i=3}^{\infty} i^2 A_{i2} b_i e^{\chi_i/kT_e}}{T_*^3 T_e^{3/2} R_*^2}\,. \qquad (5)$$

The multiplier $b_i e^{\chi_i/kT_e}$ in the equation (5) taken from the table by Sitton [4].

As to the left-handside of the equation (1), so keeping in the mind, that $\frac{1}{e^{x_i}-1} = \sum_{n=0}^{\infty} e^{-(n+1)x}$ and being restricted with first three terms, (the contribution of the subsequent terms is small enough), it is possible to present it in the following way

$$\int_{x_0}^{\infty}\frac{x^2dx}{e^x-1} = \sum_{n=0}^{\infty}\int_{x_0}^{\infty} e^{-(n+1)x}x^2dx \approx \sum_{n=0}^{2} e^{-(n+1)x_0}\left[\frac{x_0^2}{n+1}+\frac{2x_0}{(n+1)^2}+\frac{2}{(n+1)^3}\right].$$

Thus for the estimation of the radius of the central star, the following formula can obtained:

$$R_*^2 = \frac{2\cdot 10^{-27} n_e^2 \varepsilon R^3 \sum_{i=3}^{\infty} i^2 A_{i2} b_i e^{\chi_i/kT_e}}{T_*^3 T_e^{3/2}\sum_{n=0}^{2} e^{-(n+1)x_0}\left[\frac{x_0^2}{n+1}+\frac{2x_0}{(n+1)^2}+\frac{2}{(n+1)^3}\right]}\,. \qquad (6)$$

In this formula the sum in the numerator consists of terms relating to the first eight spectral lines of hydrogen Balmer series (as the contribution of following spectral lines is considerably small and can be neglected) and Balmer continuum which numerical value, as is known from [4], is equal to the emission energy in H_β line. As to the sum in the denominator, even at very high temperatures of the central star, it is enough to take the sum of the first three terms. In the formula (6), the radius of nebulae is R=dθ, where d is the distance to nebulae, $\theta$is theangular radius of the nebulae.

On the basis of the fact that for the homogeneous model the electron concentrations obtained else by the recombination lines or by the radio continuum show good correlation with the values of concentration obtained by the analysis of the forbidden lines, the estimation of radii in [2] were provided by applying of the formula (6), where we accept ε=1.

However, as it was noted in [1,5], large nebulae with small bright areas in the forbidden lines on which the electron concentration is calculated are also observed. In this case, the electron concentration appears much more than that of estimated on recombination lines. It should be noted that there is also the opposite case - the electron concentration obtained on recombination lines may be more than that of determined on the forbidden lines.

Thus, it is necessary to keep in mind that in the real situationε≤1. Moreover, it is known that the value of n_e is often determined only with an accuracy of up 2 times, and θhave an error that is not less than 20% [1].

Due to above-mentioned, the formula for calculation of radius R* needs to enter correction. For this purpose, we tried to choose the nebula, whose parameters had no considerablemistakes and were optically thick in the LyC.

3. DEFINITION OF RADII OF THE CENTRAL STARS, WITH TAKING INTO ACCOUNT THE FILLING FACTOR

Referring to the [1], the luminosity of the central star of the nebula which optically thick in the LyC

$$L = 4\pi d^2 100 F(H_\beta) \quad [\text{Erg/s}].$$

Here d is the distance, 100 $F(H_\beta)$ is the total flux of energy emitted by the nebula in the lines and in the continuum at the wavelengths λ> 912 Å and it is believed that this flux exceeds that of in H_β lines approximately 100 times. As it was noted in[1], the value 100 $F(H_\beta)$may differ from true one no more than two times, except for cold stars for which this quantity is too underestimated. With taking into account it, we will get a formula for estimating of the total flux, with a more accurate factor instead of 100. Having designated this factor as (through), H_β we have,

$$L = 4\pi d^2 H_\Sigma F(H_\beta) \qquad (7)$$

On the other hand, as

$$(5) = 4\pi R_*^2 \sigma T_*^4\,.$$

Moreover, with taking into account (6) and bearing in mind that $R = d\sin\theta = \frac{d\theta''}{206265''}$, we can get the expression for L:

$$L = \frac{1.62\cdot 10^{-46} n_e^2 \varepsilon d^3 \theta^3 T_* \sum_{i=3}^{10} i^2 A_{i2} b_i e^{-\chi_i/kT_e}}{T_e^{3/2}\sum_{n=0}^{2} e^{-(n+1)x_0}\left[\frac{x_0^2}{n+1}+\frac{2x_0}{(n+1)^2}+\frac{x_0}{(n+1)^3}\right]}. \qquad (8)$$

From the equations (7) and (8) we obtain

$$d = \frac{7.7\cdot 10^{46} F(H_\beta) T_e^{3/2} H_\Sigma \sum_{n=0}^{2} e^{-(n+1)x_0}}{n_e^2 \varepsilon \theta^3 T_* \sum_{i=3}^{10} i^2 A_{i2} b_i e^{-\chi_i/kT_e}} x$$

$$x\left[\frac{x_0^2}{n+1}+\frac{2x_0}{(n+1)^2}+\frac{x_0}{(n+1)^3}\right]. \qquad (9)$$

At the determination of the distance to planetary nebulae by comparison of the electron concentration obtained on the forbidden lines and on the energy flux measured in recombination lines, we have (see [1]):

$$n_e\varepsilon^{1/2} = 2.74\cdot 10^4\left[F(H_\beta)\, t^{0.88}/\theta^3 d\right]^{1/2},$$

where $F(H_\beta)$ - in terms of 10^{-11} erg/sm^2, θ-in seconds of an arc, d - distance in kpc and $t=10^{-4}T_e$.

By expressing d in centimeters and inserting $F(H_\beta)$ according to observations (with taking into account the interstellar absorption), for the previous equality, we will obtain:

$$n_e\varepsilon^{1/2} = \left\{2.33\cdot 10^{41}\left[F(H_\beta)\, t^{0.88}/\theta^3 d\right]\right\}^{1/2},$$

or

$$d = \frac{2.33\cdot 10^{41} F(H_\beta) t^{0.88}}{\theta^3 n_e^2 \varepsilon} \qquad (10)$$

From equations (9) and (10) for H_Σ we get

$$H_\Sigma = \frac{3\cdot 10^{-6} t^{0.88} T_* \sum_{i=3}^{10} i^2 A_{i2} b_i e^{\chi_i/kT_e}}{T_e^{3/2}\sum_{n=0}^{2} e^{-(n+1)x_0}\left[\frac{x_0^2}{n+1}+\frac{2x_0}{(n+1)^2}+\frac{2}{(n+1)^3}\right]} \qquad (11)$$

The results of H_Σ evaluations for the chosen nebulae is given in Table 1 where besides of the logarithms of radiation flux in H_β (with the correction for interstellar absorption), n_e –electron concentration, d – distance to planetary nebula taken from [2, 4, 6, 8, 10, 12, 13], T_* - the temperature of central star, T_e- electron temperature are given also.

Table 1

Some dates of planetary nebulae

#	Nebulae	LgF(Hβ)	n_e, sm^{-3}	d, kps	T_*, K	Te, K	H_Σ
1.	NGC 40	-9,92	1300	0,8[12]	35000	8500	129,7
2.	NG 246	-10,17	90	0.5[6]	10000	12000	72,4
3.	NGC1360	-9,95	50	0,38[6]	100 000	18000	71,2
4.	NGC1535	-10,31	4200	2,1[12]	73000	11000	68,3
5.	NGC2022	-10,72	1400	1,8[12]	72000	14000	67,0
6.	NGC2371	-10,88	1300	1,41[6]	92000	14500	69,8
7.	NGC2392	-11,23	3400	1,5[12]	89000	13000	69,2
8.	NGC2438	-10,55	200	1,42[6]	134000	12000	84,3
9.	NGC2440	-10,02	2500	2[12]	190 000	14000	107,2
10.	NGC2452	-10,90	2000	2,84[13]	100 000	12000	72,4
11.	NGC2792	-10,40	3000	1,9[12]	95000	14000	70,3
12.	NGC2867	-10,17	2500	2[8]	107 000	12000	74,5
13.	NGC3132	-10,23	1000	0,81[6]	85000	9500	70,8
14.	NGC3211	-10,74	900	1,91[6]	115 000	12000	77,2
15.	NGC3242	-9,70	3300	0,55[12]	68000	11000	68,6
16.	NGC3587	-10,27	200	0,76[6]	117 000	10000	79,5
17.	NGC3918	-9,63	3200	1,84[6]	112000	11000	76,8
18.	NGC 4361	-10,48	300	0,95[6]	80 000	23000	67,6
19.	NGC 5189	-10,78	450	1,44[6]	100 000	12000	72,4
20.	NGC 5315	-9,81	30000	2[12]	46000	9000	83,0
21.	NGC 5882	-9,97	4000	1,2[12]	61000	9000	72,2
22.	NGC 6210	-9,96	7500	1,57[12]	55000	10000	74,2
23.	NGC 6302	-9,17	7300	0,74[10]	270000	16500	144
24.	NGC 6445	-9,94	700	1,8[12]	160 000	13000	94,5
25.	NGC 6537	-9,72	17500	2[2]	165000	12000	97,2
26.	NGC 6543	-9,51	4000	1 [12]	58000	8300	74,6
27.	NGC 6563	-10,62	900	1,67[6]	100 000	12000	78,2
28.	NGC 6565	-10,77	7000	4,66[10]	67 000	8000	72,2
29.	NGC 6572	-9,39	20000	1,86[6]	67000	10500	69,1
30.	NGC 6629	-9,98	2100	2[6]	41000	9000	98,9
31.	NGC 6644	-10,23	2100	3[2]	95000	12500	70,8
32.	NGC 6720	-9,96	600	0,7[6]	100 000	10000	73,9
33.	NGC 6741	-10,19	10 000	3,73[4]	210 000	11600	118,1
34.	NGC 6772	-10,58	200	1,26[2]	120000	12000	78,9
35.	NGC 6781	-10,33	350	1,57[2]	100000	12000	72,4
36.	NGC 6751	-9,97	15000	2[6]	80 000	12000	69,9
37.	NGC 6818	-10,28	2800	2[12]	120000	12000	78,9
38.	NGC 6826	-9,94	2500	1,4[12]	42000	10700	93,5
39.	NGC 6853	-9,38	200	0,38[6]	103 000	12000	73,3
40.	NGC 6886	-10,47	12000	2,6[12]	163 000	13000	95,7
41.	NGC 6905	-10,8	1100	1,58[6]	85000	12000	68,9
42.	NGC 7008	-10,13	300	0,7[6]	80 000	23000	67,6
43.	NGC 7009	-9,62	8000	1,45[6]	74000	9000	70,2
44.	NGC 7026	-9,91	9500	2,35[4]	60 000	9500	71,9
45.	NGC 7027	-8,82	80000	0,9[12]	295 000	14000	156,9
46.	NGC 7293	-9,35	160	0,16[13]	116 000	12000	76,9
47.	NGC 7354	-9,76	2100	0,17[4]	87000	12000	68,7
48.	NGC 7662	-9,82	4500	1,2[12]	100 000	12500	72,1
49.	Hb 12	-9,8	400000	1[4]	46000	13000	82,8
50.	J 320	-11,06	8700	6,3[2]	69000	12000	67,9
51.	J 900	-10,45	7000	4,3[4]	135000	11500	85,0
52.	IC 418	-9,30	14000	1[12]	32000	8500	157,1
53.	IC 1747	-10,48	3800	2,99[4]	67000	10000	69,5
54.	IC 2149	-10,09	4000	1,52[6]	33000	10500	141,9
55.	IC 2165	-10,34	5000	1,5[12]	116000	13000	77,0
56.	Hu 1-2	-10,52	9000	1,5[12]	100000	16000	71,2
57.	He 2-131	-9,91	18000	3,67[13]	25000	7000	338,6
58.	BD+30	-9,66	0 000	1[12]	31 000	8000	171,5
59.	Me2-1	-11,07	2400	2,3[12]	135 000	23000	83,9
60.	Ps-1	-12,02	2000	12,3[13]	23 000	12000	430,1
61.	A24	-10,82	60	0,53[13]	99 000	12000	71,6
62.	A31	-10,54	30	0,48[6]	112 000	12000	75,6
63.	A 71	-10,64	140	2,8[4]	131000	12000	82,5
64.	A84	-11,74	110	1,68[6]	100 000	12000	71,8
65.	PW-1	-10,85	25	0,37[6]	105000	12000	73,3
66.	Jn-1	-11,06	30	0,9[6]	93000	12000	70,0
67.	K 1-22	-11,13	65	1,33[6]	100000	12000	71,8

As seen from the formula (11) and Table 1,H_Σ varies in a small range, since the weak dependence of $H_\Sigma$on both temperatures. This dependence is appreciable strong when the temperature of the star and electronic temperature of nebula are too small (for example, for nebulae He 2-131 and Cn 3-1 T * = 25000 K, T_e=7000-8000 K and H_Σ= 338). In this case $H_\Sigma$considerably differs from the value which accepted in the literature H_Σ = 100 and sometimes reaches to H_Σ =300 and more (calculations for nebula Ps-1 (it was not included in Table 1) show, that for this nebula $H_\Sigma \cong$ 500, at T * = 23000 K, T_e=9000 K).

The comparison of expression (7) for luminosity with standard expression $L = 4\pi R_*^2 \sigma T_*^4$ leads to the following formula to determine R*:

$$R_* = \frac{1.33\cdot 10^2 d\left[F(H_\beta) H_\Sigma\right]^{1/2}}{T_*^2} \qquad (12)$$

As it was expected, the values of radiiare calculated by the formula (6) whichare basically considerable more than that of calculated by the formula (12), because in the formula (6) the filling factor is accepted equal to unit. From the ratio of the radii calculated by the formulas (6) and (12) we have estimated the filling factor of the nebulae as well.

The results of these calculations are presented in the last column of Table 2. As seen from this table only for some nebulae, the filling factor is hardly more than the unit which reason can be in small errors in the used values.

For an example, we consider the nebula IC 418. For this nebula from the literature two values of n_e are known: n_e=2,0·10^4 sm^{-3} and n_e=1,4·10^4 sm^{-3}. The first valuecalculated on hydrogen lines and the second one on the forbidden lines. From the Table 2 it is seen that for this nebula at then_e=1,4·10^4 sm^{-3},ε=1,67 and n_e=2,0·10^4 sm^{-3} , the filling factor ε= 0,75. Therefore, it is possible to come to such conclusion, that the electronic concentration obtained by using of hydrogen lines can be more real. To the similar conclusions, we can come when the calculated

value of $\varepsilon > 1$. In this case plausible (admissible) correction in value n_e leads to the true value of ε. Here it is necessary to notice once again, that the value of n_e is often determined only with an accuracy of up 2 times. [5].

Table 2.

	Nebulae	$R_* R_0$	R_* / R_0
1.	NGC 40	0.4830	0.683
2.	NGC 246	0.0205	-
3.	NGC 1360	0.0200	-
4.	NGC 1535	0.1331	0.519
5.	NGC 2022	0.0726	0.099
6.	NGC 2371	0.0294	-
7.	NGC 2392	0.0224	0.845
8.	NGC 2438	0.0227	-
9.	NGC 2440	0.0337	0.037
10.	NGC 2452	0.0503	-
11.	NGC 2792	0.0653	0.079
12.	NGC 2867	0.0725	-
13.	NGC 3132	0.0426	-
14.	NGC 3211	0.0317	-
15.	NGC 3242	0.0816	0.14
16.	NGC 3587	0.0212	-
17.	NGC 3918	0.1151	-
18.	NGC4361	0.0410	-
19.	NGC 5189	0.0290	-
20.	NGC 5315	0.5784	0.306
21.	NGC 5882	0.1676	0.231
22.	NGC 6210	0.2731	0.36
23.	NGC 6302	0.0185	-
24.	NGC 6445	0.0430	0.0348
25.	NGC 6537	0.0617	0.0147
26.	NGC 6543	0.2651	0.457
27.	NGC 6563	0.0303	-
28.	NGC 6565	0.2123	-
29.	NGC 6572	0.4086	-
30.	NGC 6629	0.7102	-
31.	NGC 6644	0.1256	-
32.	NGC 6720	0.0370	-
33.	NGC 6741	0.0315	0.184
34.	NGC 6772	0.0232	-
35.	NGC 6781	0.0535	-
36.	NGC 6751	0.1259	-
37.	NGC 6818	0.0520	0.048
38.	NGC 6826	0.4811	0.98
39.	NGC 6853	0.0366	-
40.	NGC 6886	0.0329	0.038
41.	NGC 6905	0.0417	-
42.	NGC 7008	0.0406	-
43.	NGC 7009	0.2014	-
44.	NGC 7026	0.2319	-
45.	NGC 7027	0.0298	0.0716
46.	NGC 7293	0.0129	-
47.	NGC 7354	0.0831	-
48.	NGC 7662	0.0735	0.118
49.	Hb 12	0.3284	-
50.	J 320	0.1876	-
51.	J 900	0.0757	-
52.	IC 418	1.6080	1.3
53.	IC 1747	0.0821	
54.	IC 2149	0.8702	-
55.	IC 2165	0.0389	0.0774
56.	Hu 1-2	0.0406	0.0335
57.	He 2-131	7.0395	
58.	BD+30	1.1806	1.42
59.	Me2-1	0.0197	0.0273
60.	Ps-1	2.7633	-
61.	A24	0.0104	-
62.	A31	0.0105	-
63.	A 71	0.0415	-
64.	A84	0.0112	-
65.	PW-1	0.0063	-
66.	Jn-1	0.0151	-
67.	K 1-22	0.0180	-

4. CONCLUSIONS

As seen from Table 2, the radii of the central stars located in the range from $1R_\odot$ up to a little bit more than $0{,}01R_\odot$. As is known (see [1,5]) during the time from 20 000 till 40 000 years the effective temperature of the central star increases, at least, ten times, and then the star starts to be cooled and during all this process its radius decreases, approximately from $1R_\odot$ or a little more to less than $0{,}01\ 1R_\odot$.

Our calculations obviously show that really with the increasing of the temperature of the star its radius decreases in such manner that the luminosity remains constant, and then luminosity and temperature and radius decrease simultaneously and the star turns into a white dwarf.

REFERENCES

1. Alisheva K.I. Some aspects of central stars evolution of planetary nebulae. Transactions of the NAS of Azerbaijan, № 4, 2000.
2. Bensby T. and Lundström L.The distance scale of Planetary Nebulae. A&A, 07 June 2001.
3. Pottash S.R, Planetary nebulae 1987.
4. Giammanco C., Sale S.E., Corradi R.L., Barlow M.J. etc. IPHAS extinction distances to Planetary Nebulae, A&A, № 4, 07 July, 2010
5. Guseinov R.E., AlishevaK.I.. Determination of the nuclear radius and some parameters of planetary nebulae,Fizika. 6, 1, .60-63, 2000
6. Jacob R., Schönberner D., Steffen M. The evolution of planetary nebulae. VIII. True expansion rates and visibility times. A&A, № 21532, September 18, 2013
7. Sobolev V.V., Kursteoreticheskoyastrofiziki, 1987
8. Krzysztof G., Agnes A., Albert A. Kinematics, turbulence and evolution of planetary nebulae. A&A no. MS3219, February 2, 2008.
9. Kwok S., The origin and evolution of planetary nebulae, 2000
10. Ortiz R., Copetti M.V.F. and Lornz-Martins S. A distance scale of planetary nebulae based on mid-infrared data, R.Astron. Soc. 000, 12 August 2011

11. Pottash S.R. and Bernard-Salas J. Planetary nebulae abundances and stellar evolution II. A&A, no.vol 2. V7, May 19, 2010.

12. Pottash S.R. and Bernard-Salas J. Planetary nebulae abundances and stellar evolution II. A&A, no.vol 2. V7, January 19,2014.

13. Stanghellini L., Shaw R. A. and Villaver E. Magellanic cloud calibration of the galactic planetary nebulae distance scale. December 10, 2008.

(E-mail:galaktika2002@mail.com)

Solar Spin-Orbit Interaction: Tidal Torque

J.S. ALIYEV

Shamakhy Astrophysical Observatory, Azerbaijan National Academy of Sciences, AZ5618, Shamakhy, Azerbaijan
Email: jascience@yahoo.com

Abstract

It is created a program-package SolAct that solves a system of equations of the spin-orbit interaction and allows to follow the sun's angular momentum change over time. Also it has been created a program-package TiTor which calculates the tidal torque exerted on the Sun taking into account the solar rotation, computes the spectra of the sampled or averaged data, searches for the spurious periods. Using SolAct and the TiTor it is proved that the torques exerted on the Sun change its spin, but a contribution into total torque by the tidal torque is insignificant.

Keywords: solar activity: spin-orbit coupling – tidal torque

1. Planetary hypotheses: Third period of the development

Planetary hypotheses have passed three periods of development, from the supposition that the solar activity has a causal connection with the orbital motion of the planets [16], more, solar activity correlates with the movement of the Sun around the center of mass of the solar system [15], to the idea that there is an interaction between the solar spin momentum and the solar orbital angular momentum [2-5, 12-13]. As a continuation of these ideas, in 2012 Abreu et al. have published a paper entitled "*Is there a planetary influence on solar activity*?", in which the authors have put forward the idea that long-term fluctuations of solar activity are probably connected with the oscillations caused by a planetary tidal torque exerted on solar tachocline. The last may be included into the third period of the development of ideas about the spin-orbit interaction, of course, after some reprocessing and specifications, which we are going to do in this note.

2. Spin-orbit coupling

Let's first shortly concern a mechanics of motion of the Sun. During the motion around the barycenter, the trajectory of the solar center is so complex that even the torsion changes not only the value and sign too. Moreover, the radius of the sun's trajectory around the barycenter is comparable to the radius of the sun, which means that the trajectory of Sun's center is strongly curved. To think that a gyroscope as the sun during such a walking will not be subjected to any influence and will preserve its state is not reasonable.

The picture is as follows: The sun is immersed into the non-inertial system and, therefore, will be under the influence of additional forces. The sun is a gyroscope, which rotates, oscillates and spirals with variable torsion. One of the forces must be arisen because of that, the solar gyroscope is forced to simultaneously rotate around the center of the Sun and the center of mass. If we remember that the center of mass of the solar system is inside the sun, it is quite clear that the force with the moment arm equal to the distance between the solar center and the center of mass, certainly, will generate torque that changes the solar spin. There are other torques (for example, $[\boldsymbol{L}, \boldsymbol{\Omega}]$, where $\boldsymbol{L}$ is the spin momentum of Sun and $\boldsymbol{\Omega}$ the instantaneous orbital angular velocity) to change the solar rotational momentum, but this torque plays a major role in the spin-orbit interaction. For example, the center of mass of the relative motion of the Sun, Jupiter and Saturn is inside the Sun, and the torque components at this point, for $t = 2000$, have the values:

$$K_x/M_\odot = 6.98 \cdot 103; \quad K_y/M_\odot = -1.37 \cdot 104;$$
$$K_z/M_\odot = -1.24 \cdot 105 \ (\textit{units in } cm^2/s^2), \qquad (1)$$

where $M_\odot$ is the solar mass. The main problem, in our view, is how to take the influence of forces on the sun into account.

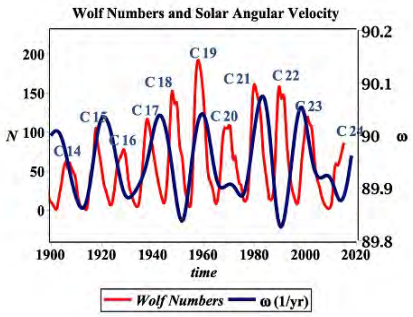

Fig. 1. Solar angular velocity, $\omega = (\omega_x^2 + \omega_y^2 + \omega_z^2)^{1/2}$ (blue), and Wolf numbers, N (red): the case of the constant coefficients of interaction ('C' means 'Cycle').

This vision opens the window to look at the old astrophysical problems again, for example, such as why close binary systems, in general, multi-body systems are so active. In the notes [6, 8, 9] we have reported on the program - package *SolAct* (Module ***Solar Activity***), which was created to generate the motion of the Sun and the planets around the solar system barycenter, to calculate the angular momenta and orbital parameters. Moreover, *SolAct* solves a system of equations of the spin-orbit interaction and allows us to follow the sun's angular

momentum change over time. We call the rotating system of the Sun and Jupiter, with embedded all other planets, as the solar system catastrophe machine because of the similarity to the Zeeman catastrophe machine. However, the solar system catastrophe machine is very complex than that. The main problem, as discussed above, is how to determine the torque, moreover how to compute it. For this purpose, a new version of the module *SolAct* was created. *SolAct* takes into account the torques exerted on the interior of the sun (more precisely, on rigidly rotating part of the sun) from the outer planets. Assume that the sun is under the influence of the torques of outer planets and coefficients of coupling are constant. The torque of type [$\boldsymbol{L}$, $\boldsymbol{\Omega}$] is also added. As seen from Fig. 1, after 1954 the extrema of the two curves are in a good match. However, there is a phase shifting between them in the time interval from 1900 to 1954. To fix this we take a time-dependent coefficient for the spin-orbit interaction with the time-dependent phase. Using time-dependent coefficient for the spin-orbit coupling, we again carry out a calculation.

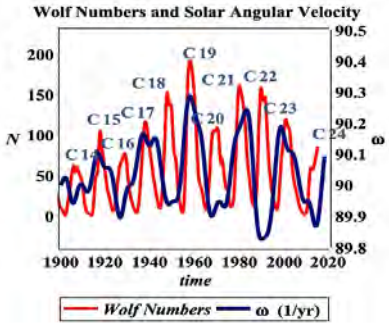

Fig. 2. Solar angular velocity, ω (blue), and Wolf numbers, N (red): the case of the variable coefficients of coupling.

From Fig. 2 it is seen that the solar angular velocity and Wolf numbers show a remarkable correlation (anti-correlation).

So far, we considered only mechanics of the Sun, and the theory, which establishes connection between the variations of solar spin and the electromagnetic phenomena waits its development. To have primary view, it can be used already existing dynamo theories together with the equations of the spin-orbit coupling. However, even the suggested mechanical model of the spin-orbit coupling allows to have some notions concerning the observable phenomena of solar activity, for example, why there is the *north-south asymmetry* (the gyroscope inside the sun changes the plane of rotation due to a precession with 11 year cycle, at the same time the oblate tachocline which is responsible for the solar activity, changes its rotation plane that leads to spatial asymmetry with respect to the solar equator), why *even and odd cycles* are different from each other (odd cycles correspond to maxima of the solar spin momentum, but the even cycles to minima), why *torsional oscillations* arise and change the direction of torsion from east to west and vice versa with periods of 11 years (torsion of the solar center trajectory changes the direction with increasing and decreasing of the solar spin momentum), as well some other phenomena.

For example, this model easily explains also why the solar activity correlates with syzygies of planets (see, e.g., [5, 14]). During syzygies the solar spin momentum passes the extrema (see Fig. 2) and two moments of time, in these cases, define the bifurcation points, which are the solutions of equation of $d\boldsymbol{L}/dt = 0$. When the system (temporarily and spatially) approaches nearer to bifurcation points, it goes to become unstable, which is transformed into chaos inside the sun.

The data analysis carried out by Javaraiah [11] (see also [14]), has shown that the rate of solar equatorial rotation is relatively lower in even cycles than in odd cycles. The above theoretical model of the spin-orbit coupling also shows the same result (see Fig. 2). Thus, experiment confirms that the theoretically modeled spin-orbit coupling is believable. With the lapse of time, the idea that the planetary torque governs the solar rotation will not raise doubts. Here the matter is that, how much we can correctly model this complex challenge. We think that it is only the commencement, and the theory will pass many tests. The theoretical calculations require to know how much hard the planetary torques are coupled to the Sun. In this way, the helioseismic analysis of variation of solar deep rotation would be the best helper for calibration. Again, the matter is that how much hard the torques are coupled to the Sun. This is similar to the case, when Foucault pendulum is not hard connected to the dome, and therefore, the Coriolis force must be introduced into the equations with some coefficient. Some cases of such a consideration are realized using the module *SolAct*, which is briefly described in Section 2 (see also [6, 8, 9]).

3. Tidal torque

It is necessary to emphasize the remarkable idea about the tidal torque advanced by [1], but at the same time, it should be stressed that the model proposed by them, is an exotic:

(a) the assumption that the solar tachocline has the ellipsoidal shape is not hard proven;
(b) spatial orientation of the ellipsoid is not linked to realistic position of the solar rotational axis and the exact sizes of the ellipsoid are unknown;
(c) the solar rotation is not taken into account.

Moreover, in that article in our opinion, the tidal torque has not been entered completely. In the paper of Abreu et al., the solar rotation is ignored, and as a result, the rotation of the tachocline ellipsoid is not considered. The program-package *TiTor* (***Ti****dal* ***Tor****que*) will help us to take into account a rotation of the Sun in calculation of the tidal torque. Note that *TiTor* considers a spatial position of the solar rotational axis ($i = 7.25^{\circ}$, $\Omega = 75.76^{\circ}$) only in a case when the solar rotation is taken into account. It is obvious that in the case (when the solar rotation is ignored) of the prolate ($R_x = R_y$, R_z, $R_x < R_z$) or oblate (Rz < R_x) Sun, N_z component of the tidal torque will equal to zero (this is the same with that designated

(3) by Abreu et al.). Therefore, for a theoretical experiment when solar rotation is disregarded, we consider the case of R_x, $R_y = R_z$, $R_x > R_z$, like to the case (1) by Abreu et al. [1]. Fig. 3a compares the full tidal torque (all planets, z-component) in two cases: with the Sun's rotation (red) and without one (blue). It is interesting, as seen from Fig. 3b, that the tidal torque with the solar rotation averaged over the solar rotational period (red) is almost negligible. The physics of such result is that for one quarter of the solar rotational period the tidal torque will accelerate the tachocline, and during other quarter one will slow it down, which is clearly seen, for example, for the tidal torque of Venus, which is depicted in Fig. 3c.

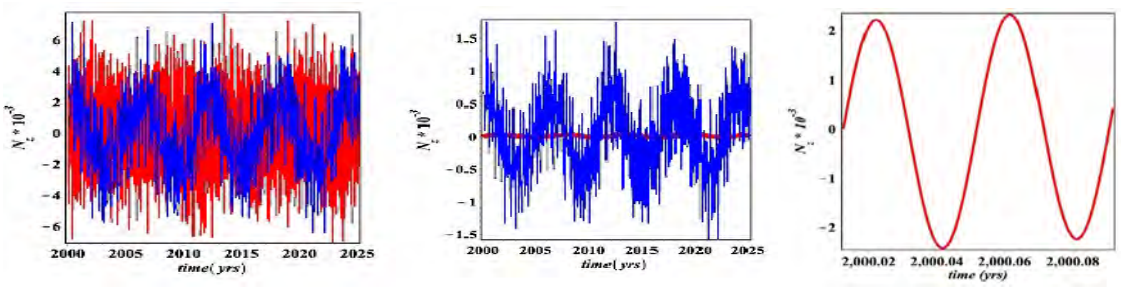

(a) (b) (c)

Fig. 3. a) Total tidal torque with the solar rotation (red) and without one (blue), b) Total tidal torque with the solar rotation averaged over the solar rotational period (red) and the same (but not averaged) without solar rotation (blue), c) Tidal torque with the sun's rotation for Venus at the time interval comparable with the solar rotational period. Tidal torques are calculated for 1g solar mass and unit is [g cm^2/s^2].

Moreover, short-term modulation will transform slow long-term oscillations into noise (see Fig. 3a), and such a slight tidal torque with nearly zero short-term mean value (see Fig. 3b), together with the other randomly added noises in tachocline region, can hardly bear the memory.

However, the case is different. Abreu et al. consider, in fact, the tidal torque without short-term modulation (see [1]):

$$N_{z,i} \propto m_i x_i y_i/|\boldsymbol{r}_i|^5 \propto m_i/a_i^3 f(t), \quad (2)$$

where m_i, x_i and y_i denote the mass and heliocentric coordinates of the ith planet, respectively, and a_i and $\boldsymbol{r}_i$ are the semi-major axis and the position vector of the ith planet; f is some function of t. If we go back to history, such a formula is already met, although to describe another quantity. Wolf is the first ([16, 10]) to introduce the formula for the quantitative description of the evolution of sunspots over time. In 1859 he gave a formula for the sunspot number, M,

$$M = 50.31 + 3.73 \cdot \sum_{i=1}^{4} m_i/r_i^2 \sin(2\pi t/T_i), \quad (3)$$

where m_i, r_i and T_i being the planetary masses, mean distances and orbital periods of Venus, Earth, Jupiter, and Saturn, are normalized to the earth's mass, the earth-sun mean distance and the earth's orbital period, respectively. However, in these cases of formulae (2) and (3), the long-term periodicity is preserved.

Note that, despite the aforementioned remarks, it is necessary to appreciate remarkable vision of Abreu et al. of such thin effect as the planetary tidal torque. In the above remark 1 we have generalized their formula to a case of the solar rotation and in order that it has ceased to be exotic and entered into the equations of the spin-orbit interaction (Section 2) it is sufficient that rigidly rotating part of the sun has the ellipsoidal shape. The problem becomes more realistic thanks to observations that show on the oblate spheroidal shape of the Sun, $R_x = R_y$, R_z, $R_z < R_x$, with $R_z = R_x - 6$ (km). It is slight difference between the semi-major axes, but it (together with an inclination of the Sun's rotational axis to the ecliptic) does the N_x, N_y and N_z different from zero. Thus, we assume that,

(a) Sun's rotational axis is tilted with respect to the ecliptic for $i = 7.25^\circ$, the longitude of the ascending node of the intersection of the Sun's equatorial plane with the ecliptic is accepted to be $\Omega = 75.76^\circ$;

(b) Sun consists of rigidly rotating internal part and the convective external one. It is supposed that the tidal torque is applied to the rigidly rotating interior and the convective exterior separately, at that the densities of the internal and external parts are assumed, for a first approximation, to be constant and equal to the mean ρ_r and ρ_c, consequently (rigorous approach needs to know coordinate dependence of the density and the differential rotation of the convection zone);

(c) the shape of the rigidly rotating part of the Sun is an oblate ellipsoid, and the semi-major axes of thereof are taken to be $R_x \equiv R_y = 0.71\ R_\odot$ and $R_z = R_x - 100$ (km).

Calculation for the case of an oblate sun with unvarying rotation (only for tidal torque exerted on rigidly rotating part) is shown in Fig. 4. If we compare the tidal torque (see the ordinates of Fig. 4) with the torque from Equation (1), we observe that the tidal torque is incomparably small. Changing the value of Z in $R_z = R_x - Z$ (km) from 100 to 1000 results in a slight increase of the tidal torque. Drawing attention to the two cases, as depicted in Fig. 4 and Fig. 3a, we will be convinced that in

case of the rotating oblate sun short-term modulation of N_z is absent.

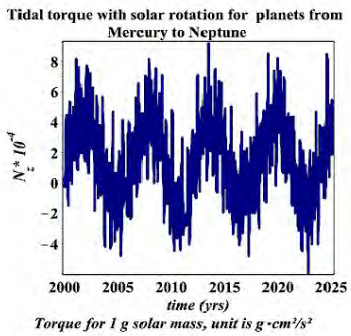

Fig. 4. Total tidal torque for the rotating oblate sun.

Now, the tidal torque can be included into system of the equations of spin-orbit coupling, but we know that its contribution into total torque will be insignificant.

2. Concluding remarks

So far, the influence of planets on the Sun was only a hypothesis. Now the certain mechanisms for the spin-orbit interaction of the Sun and planets have been suggested. It is only the first step in transformation of a hypothesis into the theory. Copernicus' revolution has not only shifted the center of control of the solar system from a geocentric to a heliocentric in the world outlook of people, but also created a new style of thinking that recognizes the sun as the sole ruler of the solar system. Wolf tried to restore the 'rights' of the planets for control in the solar system, drawing attention to their possible impact on the solar activity. These attempts are still going on, and it becomes clear that 'the planets have a claim' to take part in control of both the mechanics and the physics of the Sun.

References

[1] J. A. Abreu, J. Beer, A. Ferriz-Mas, K. G. McCracken, F. Steinhilber, A&A, **548**, A88 (2012)
[2] J. S. Aliyev, Circ. ShAO, **94**, 19 (1998a)
[3] J. S. Aliyev, Int. Conf. "N. Tusi - 800", ShAO, 5 (1998b)
[4] J. S. Aliyev, L. Kh. Salmanova, Int. Conf. "N. Tusi and Modern Astronomy", Baku, 23 (2001)
[5] J. S. Aliyev, Actual Problems of Physics **II**, BSU, Baku, 7 (2001)
[6] J. S. Aliyev, Modern Problems of Physics **VI**, BSU, Baku, 300 (2012a)
[7] J. S. Aliyev, Modern Problems of Physics **VI**, BSU, Baku, 297 (2012b)
[8] J. S. Aliyev, Modern Problems of Physics **VII**, BSU, Baku, 343 (2013)
[9] J. S. Aliyev, Modern Problems of Physics **VIII**, BSU, Baku, 279 (2014)
[10] P. J. Charbonneau, Journal for the History of Astronomy, **33**, 4, 113, 351 (2002)
[11] J. Javaraiah, Solar Phys., **212**, 23 (2003)
[12] D. A. Juckett, Solar Phys., **191**, 201 (2000)
[13] D. A. Juckett, A&A, **399**, 731 (2003)
[14] I. R. G. Wilson, B. D. Carter, I. A. Waite, Pub. Astron. Soc. Austral, **25**, 85 (2008)
[15] P. D. José, AJ, **70**, 193 (1965)
[16] R. Wolf, MNRAS, **19**, 85 (1859)

Thermoelectric properties of $(InTe)_{1-x}$-$(HoTe)_x$ solid solutions

YU.G. NURULLAYEV[1], B.SH. BARKHALOV[2], R.M. ISMAYILOV[3], K.I. MAGERRAMOVA[2], H.O. SADIG[4], N.B. MUSTAFAYEV[2]

[1] *Baku State University, Azerbaijan, Baku*
[2] *Institute of Physics of ANAS, Azerbaijan, Baku*
[3] *Sumgait State University, Azerbaijan, Sumgait*
[4] *Azerbaijan State University of Oil and Industry, Azerbaijan, Baku*

The thermoelectric properties of of the InTe-HoTe system solid solutions have been investigated. It is shown that an increase in the content of HoTe in a solid solution $(InTe)_{1-x}$-$(HoTe)_x$ leads to a significant improvement in thermoelectric parameters, which makes them suitable for use in the manufacture of thermoelectric energy converters.

Keywords: solid solution, solubility, Hall coefficient, electrical conductivity, thermal e.m.f.

1. Introduction

The investigation of the thermoelectric properties of indium telluride is of scientific interest, which is connected both with a layered structure having a strong anisotropy of physical properties and practical one - since on the basis of its solid solutions it is possible to create efficient materials for thermoelectric energy converters [1-4].

In the present work the influence of holmium telluride (HoTe) on the thermoelectric properties of indium telluride (InTe) with the purpose of revealing the prospects of this material for use in thermoelectric energy converters was investigated.

According to the results of the physico-chemical analysis of the InTe-HoTe system, the solubility of HoTe in indium telluride does not exceed 1.5 mol % at 300 K. The present work is devoted to the study of the thermoelectric properties of $(InTe)_{1-x}$-$(HoTe)_x$ solid solutions, where x = 0.3, 0.5 and 1.1.

2. Experimental results and discussion

Fig. 1 shows the concentration dependences of the thermal e.m.f. α and Hall coefficient R_H at room temperature. It can be seen that the coefficient of thermal e.m.f. with an increase in the content of HoTe in alloys $(InTe)_{1-x}$- $(HoTe)_x$ with x = 0.3; 0.5 and 1.1 increases, and for an alloy of 99.9 mol % HoTe - 0.1 mol % InTe reaches a value of 165 μV/K. The Hall coefficient R_H for indium telluride is 0.15 cm^3/C, and for an alloy of 99.9 mol % HoTe - 0.1 mol % InTe is 0.47 cm^3/C, i.e. three times higher. In this case, the electrical conductivity increases more than twofold (Fig. 2, curve 1), while the carrier density n calculated from the Hall coefficient R_H decreases more than threefold (Fig. 2, curve 2).

The mobility of charge carriers μ, calculated from the ratio $\mu = R_x \cdot \sigma$, analogously to the electrical conductivity σ and the coefficient of thermal e.m.f. α, increases continuously with increasing content of the dissolved HoTe component (Fig. 2, curve 3). When studying the temperature dependence of the thermoelectric parameters and the Hall effect in $((InTe)_{1-x}$- $(HoTe)_x$ solid solutions, the main attention was paid to those alloys that are of interest from a practical point of view.

Investigations of the temperature dependence of the thermoelectric parameters and the Hall effect for both indium telluride (parallel to the crystallographic "C" axis) and for solid solutions $(InTe)_{1-x}$- $(HoTe)_x$ with x = 0.3; 0.5 and 1.1 showed, that for these solid solutions and indium telluride the temperature dependence in the temperature range 77-300 K is identical, but at higher temperatures for the solid solution is steeper.

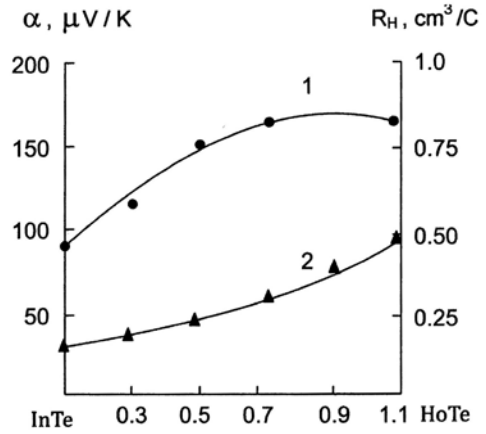

Fig. 1. Concentration dependence of the thermal e.m.f. α (1) and the Hall coefficient R_H (2) at room temperature.

In the temperature range 77-300 K, the thermal e.m.f. coefficient for InTe is 40 to 90 μV/K, for the alloy $(InTe)_{1-x}$-$(HoTe)_x$ with x = 0.5 from 60 to 150 μV/K, and at higher temperatures (300-670 K) it is in the range from 90 to 120 μV/K and from 150 to 360 μV/K, respectively.

In this case, a continuous increase in the maximum value of α and minimum value of σ was observed with an increase in the percentage of HoTe and a shift of the maximum toward higher temperatures, which is apparently

due to a change in the total concentration of charge carriers.

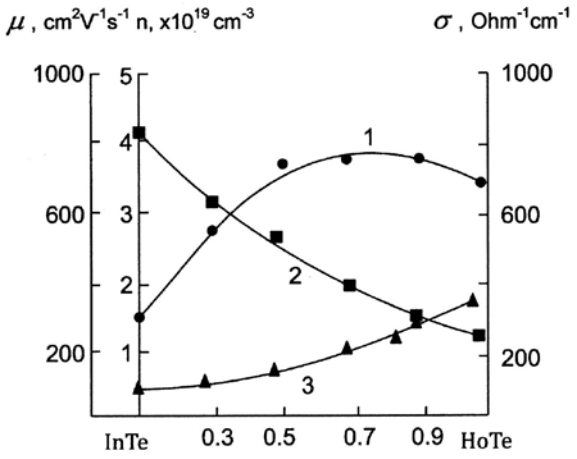

Fig. 2. Concentration dependence of the electrical conductivity σ (1), concentration n (2) and the mobility of the charge carriers μ (3) at room temperature.

As studies have shown, the nature of the change in the electrical conductivity of solid solutions as a function of the temperature regions and the concentration of HoTe, unlike indium telluride, tends to linear. The results of the study of the thermo-e.m.f. and electrical conductivity coefficients showed that in HoTe - InTe system, alloys with a composition 99.5 mol% HoTe-0.5 mol% InTe may be thermoelectrically more efficient, and therefore a measurement of the thermal conductivity with the purpose of determining the temperature range of the maximum thermoelectric efficiency (thermoelectric figure of merit) Z of the given material have been carried out.

The temperature dependences of the thermal conductivity coefficient for InTe and the alloy 99.5 mol % HoTe - 0.5 mol % InTe are shown in Fig. 3 (curve 1). Thermal conductivity studies were carried out in a steady-state regime. It can be seen, that for indium telluride in the temperature range 77-300 K the thermal conductivity changes linearly with temperature, which agrees well with the results of [1], and for 99.5 mol % HoTe-0.5 mol % InTe alloy, in comparison with InTe, the thermal conductivity decreases sharply with increasing temperature (Fig. 3, curve 2).

It is noteworthy that for a given alloy, if the electrical conductivity and the thermo-e.m.f. coefficient increase continuously with an increase in the content of the dissolved component of HoTe, the total thermal conductivity decreases in this case.

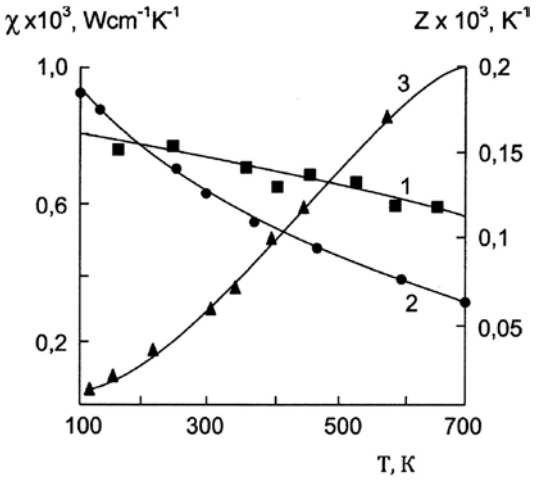

Fig. 3. Temperature dependence of the thermal conductivity χ for InTe (1), the alloy 99.5 mol % HoTe - 0.5 mol % InTe (2) and the thermoelectric efficiency Z for 99.5 mol % HoTe-0.5 mol % InTe (3).

All this leads ultimately to an increase in the thermoelectric efficiency for this solid solution. Thus, from the above experimental results it follows that an increase in the content of HoTe in indium telluride leads to a marked increase in thermoelectric parameters even at room temperature.

Based on the temperature dependence of electrical conductivity σ, thermo-e.m.f. α and thermal conductivity χ, Z values were calculated for an alloy of 99.5 mol% HoTe - 0.5 mol% InTe in the temperature range 100-700 K. The parameter Z for this alloy increases with increasing temperature, reaching a maximum value of $Z_{max} = 2x10^{-4}$ K^{-1} at 700 K (Fig. 3, curve 3), whereas for InTe at the same temperature the value of Z does not exceed $Z_{max} = 2x10^{-5}$ K^{-1}.

References

[1] E.V. Osipov, "Solid-state cryogenics", Naukova Dumka, Kiev, 234 p., 1977 (in Russian).

[2] L.I. Anatychuk, "Thermoelements and thermo-electric devices", Naukova Dumka, Kiev, 768 p., 1979 (in Russian).

[3] A.L. Weiner, "Cascade thermoelectric sources of cold", Soviyet radio, Moscow, 136 p., 1976 (in Russian).

[4] V.A. Kutasov, M.V. Vedernikov, P.N. Konstantinov, Thermoelectric materials and cooling modules based on tellurides and selenides, Proceedings of the IV Interstate Seminar on Materials for Thermoelectric Converters. St. Petersburg, November, 1995, p. 16.

E-mail: nurullayev.yusif@rambler.ru